Global Approximations of Agent-Based Model State Changes

by

Michael A. Yereniuk

A Thesis

Submitted to the Faculty
of the
WORCESTER POLYTECHNIC INSTITUTE
In partial fulfillment of the requirements for the
Degree of Doctor of Philosophy
in
Mathematical Sciences
by

April 2020

APPROVED:

Professor Sarah D. Olson
Worcester Polytechnic Institute
Major Thesis Advisor

Professor Andrea N. Arnold
Worcester Polytechnic Institute

Professor Michael J. Lee
University of Massachusetts Medical School

Professor Burt S. Tilley
Worcester Polytechnic Institute

Professor Homer Walker
Worcester Polytechnic Institute

Abstract

How can we model global phenomenon based on local interactions? Agent-Based (AB) models are local rule-based discrete method that can be used to simulate complex interactions of many agents. Unfortunately, the relative ease of implementing the computational model is often counter-balanced by the difficulty of performing rigorous analysis to determine emergent behaviors. Calculating existence of fixed points and their stability is not tractable from an analytical perspective and can become computationally expensive, involving potentially millions of simulations. To construct meaningful analysis, we need to create a framework to approximate the emergent, global behavior.

Our research has been devoted to developing a framework for approximating AB models that move via random walks and undergo state transitions. First, we developed a general method to estimate the density of agents in each state for AB models whose state transitions are caused by neighborhood interactions between agents. Second, we extended previous random walk models of instantaneous state changes by adding a cumulative memory effect. In this way, our research seeks to answer how memory properties can also be incorporated into continuum models, especially when the memory properties effect state changes on the agents. The state transitions in this type of AB model is primarily from the agents' interaction with their environment. These modeling frameworks will be generally applicable to many areas and can be easily extended.

Acknowledgments

"Ever tried. Ever failed. No matter. Try again. Fail again. Fail better."
– Samuel Beckett, *Worstward Ho*

Many people contributed to and helped me fashion this dissertation. First and foremost, I would like to thank Professor Olson, the best boss I ever had. Thank you for your patience, trust, and tireless effort on my behalf. The questions you raised during our weekly meetings definitely helped clarify this work, pushing it to avenues I never would have considered. I looked forward to our weekly meetings in anticipation of how you would respond to my new, undeveloped ideas. I also would like to thank my dissertation committee members: Professor Andrea Arnold, Professor Michael Lee, Professor Burt Tilley, Professor Homer Walker. I am honored that you agreed to participate with me on this adventure and am grateful for all the help and humor you gave me during my time studying at WPI.

My friends and colleagues were instrumental in my studies, especially Dr. Lucia Carichino, Dr. Simone Cassani, Zackary Crosley, Dr. Eyob Demeke, Dr. Kyle Dunn, Dr. David Earles, Dr. Brian Kodalen, Krystine Powell, and Pooya Yousefi. I equally appreciated our jokes and serious mathematical discussions.

I would not have considered studying mathematics if not for Professor Maureen Eckert, Professor Negash Yusuf, and Professor Maria Basterra who, after graduating with my philosophy degree, prodded me to encounter and embrace this field. Negash, you taught me the greatest lesson for a young mind, that the answer is never as important as the way it is attained.

My family was very supportive during this process, knowing when I needed guidance and humor. This document is due, in no small part, to the pithy aphorisms my parents espoused and ingrained in me during my cerebral development. Thank you Mom, Dad, and Anne for conditioning me to enjoy learning, encouraging me to be creative, and teaching me to not be fearful when subjects were difficult. Lindsay, the love of my life, thank you for your intellectual and emotional support and for the sacrifices you made so I could finish this dissertation.

Your lessons and wisdom were heeded, your fervor resonated, and for that any successes I achieve are your successes as well.

"Attitude is everything."
– Anton Yereniuk

"If you can read, then you can do anything."
– Jo-Anne Yereniuk

For Mr. Pike

Contents

List of Figures

List of Tables

List of Symbols and Notation

- $\mathbf{x} = (x_1, x_2, \ldots, x_n)^T$: *vectors are denoted in bold face (when* $\mathbf{x} \in \mathbb{R}^n$ *the superscript* T *denotes the vector transpose)*
- L^p: *space defined by generalizing the p-norm for vector spaces in* $\mathbb{R}^n$
- N: *the number of agents in agent-based model simulation*
- $\mathcal{X}$: *the collection of agents (indexed as* $1, 2, \ldots, N$*)*
- $\mathbf{x}_t^k$: *the location of agent* k *at time* t
- Σ: *agent state space*
- s_t^k: *the state of agent* k *at time* t
- U_t: *the number of agents in state* $\mathcal{U}$ *at time* t
- $\mathcal{N}_t^k$: *neighborhood of agent* k *at time* t
- $f : \mathcal{X} \to \Sigma$: *the transition rule that assigns each agent at time* t *to a unique state at time* $t + 1$
- $B_t^{\mathcal{V},\mathcal{U}}$: *the* $\mathcal{V} \to \mathcal{U}$ *transition region*
- $W_t(\mathcal{V} \to \mathcal{U})$: *the probability an agent in state* $\mathcal{V}$ *transitions to state* $\mathcal{U}$
- Ω: *the spatial domain*
- $\partial\Omega$: *the boundary of domain* Ω
- $\triangle x$: *simulation spatial step-size along* x*-coordinate*
- $\triangle y$: *simulation spatial step-size along* y*-coordinate*
- $\triangle r$: *simulation spatial step-size in radial direction*
- $\triangle t$: *simulation time step-size*

- $||\cdot||_1 \equiv \int_\Omega \int_0^\infty |\cdot| \, d\xi \, dV$*: 1-norm*
- $||\cdot||_2 \equiv \sqrt{\int_\Omega \int_0^\infty (\cdot)^2 \, d\xi \, dV}$*: 2-norm*
- $B(x,d) = \{y : ||x-y||_1 < d\}$*: the 1-norm ball of radius* d *centered at* x
- δx*: numerical discretization size in spatial coordinate*
- δt*: numerical discretization size in time coordinate*
- $\delta \xi$*: numerical discretization size in absorption coordinate*
- $\omega_{i,k} = B(x_i, \delta x/2) \times [\xi_k, \xi_{k+1})$*: the cell volume used to discretize the numerical cumulative absorption PDE*
- $\mathcal{C}^k$*: the space for continuously differentiable functions up to the* k^{th} *derivative*
- $\nabla = \left(\frac{\partial}{\partial x}, \frac{\partial}{\partial y}\right)^T$*: the gradient operator*
- $f * g = \int_{\mathbb{R}} f(x-y)g(y) \, dy$*: the convolution of two functions* f *and* g*. In this paper all convolutions are done in the spatial domain*
- $f *^m g = \underbrace{f * f * \ldots * f}_{m \text{ times}} * g$*: multiple convolution of the same function*
- $\delta(\cdot)$*: the Dirac delta distribution*
- $erf(z) \equiv (2/\sqrt{\pi}) \int_0^z e^{-t^2} \, dt$*: the error function*
- $\lfloor d \rfloor$*: greatest integer less than or equal to* d
- $|S|$*: the cardinality of set* S

Chapter 1

Introduction

How can we understand a complex system of interacting and decision-making entities? Mathematical modeling translates real-world physical dynamics into abstract mathematical language. Once encoded, analysis allows the structure of the specific modeling language to expose information not readily apparent. However, a mathematical model cannot include everything from the physical world, so the translation from the real-world to mathematics requires making assumptions or simplifications. Knowing when and how to impose those decisions, balancing model fidelity with analytical tractability, transforms mathematical modeling into an art form.

There are several different modeling frameworks from which to choose, but each structure decides the ease (or even tractability) of answering specific types of questions about the model. Often, if the focus is on understanding and capturing each of the interactions and movement, an individual-based approach such as an Agent-Based (AB) model is used [59, 60, 72, 100]. When we are interested in global dynamics, or we are more interested in how the field is evolving, density-based approaches are utilized, e.g. difference equations or systems of differential equations [21, 27, 81]. For each of these frameworks, there are different pros and cons with respect to the ability to formalize and analyze a model, as well as the ease with which one can simulate the dynamics [93]. There are many challenges, which can arise due to noise, nonlinearities, and other spatial or temporal variations in the system [111].

In AB models, the agents are each individually assessing their surrounding environment, potentially moving or changing state at each time increment based on a given set of rules [17]. The state-dependent rules could be deterministic or stochastic, and are quite often nonlinear functions based on information (e.g. other agents, states, or environmental factors) in a locally defined interaction neighborhood [34]. The movement can be on-lattice, where the spatial domain is a graph, or off-lattice, where the spatial domain is a continuum, as depicted in Fig. 1.1a and Fig. 1.1b, respectively. In on-lattice movement, an agent occupies a discretely defined node, from which it can move to occupy other nodes only by traveling along graph edges. For example, if a lattice is a regular, two-dimensional grid, the on-lattice movement of a given agent could be either horizontal or vertical movement to an adjacent lattice node at each time increment [52, 119]. Conversely,

in off-lattice movement, an agent is located in a continuous space and new locations can be determined via specified rules or determined by solving systems of differential equations [55]. Often, questions of interest concern the emergent behavior of a large number of interacting agents, which can be hard to capture at the continuous scale [60]. We note that since this modeling framework is quite general, the agent could represent any feature of interest in a given system [106], which is why these types of models are frequently used for social, biological, financial, and military applications [4, 17, 24, 31, 35, 52, 62, 99, 119]. In terms of biological applications at the cellular level, AB models have been used to investigate tumor growth where the agents are the individual cells that make up the tumor [62], sperm cell motility where the sperm are the individual agents [19, 20], and signaling pathways within and on the membrane of cells where agents are molecules and receptors [17].

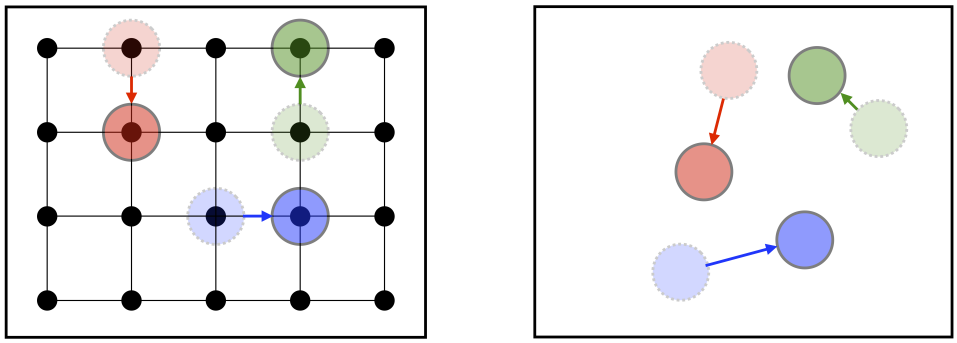

(a) On-Lattice Movement (b) Off-Lattice Movement

Figure 1.1: Diagram depicting types of movement. Agents are denoted as colored disks, with the shading denoting agent location before (lighter) or after (darker) movement. The arrows denote movement direction. **(a)** On-lattice movement, where agents move to established nodes along graph edges. **(b)** Off-lattice movement, where agents can move on a continuum in the domain.

Each agent in an AB model is initialized with its own set of static or variable features, which may consist of goals, data, properties (including a behavioral state), or memory. The flowchart in Fig. 1.2 loosely demonstrates how the agent and environmental influences, which are local to a particular agent, determine the agent's action in a generic AB model. As the simulation progresses, the agent's location or goals may update these features. This update may be deterministic, such as how social-force AB models solve a differential equation [5, 57, 84] or probabilistic, such as a random walk (RW) model [29, 98]. If an agent interacts and undergoes property changes due to some connection with other agents, then it does so through an interaction neighborhood, which is a physical space surrounding an agent where another agent's features can exercise an influence. Additionally, environmental factors, such as resources or topographical considerations, may also update an agent's properties or memory. An agent may only perceive and interact with local environmental information, in which case the agent's features would be

updated according to the data within the agent-environment neighborhood.

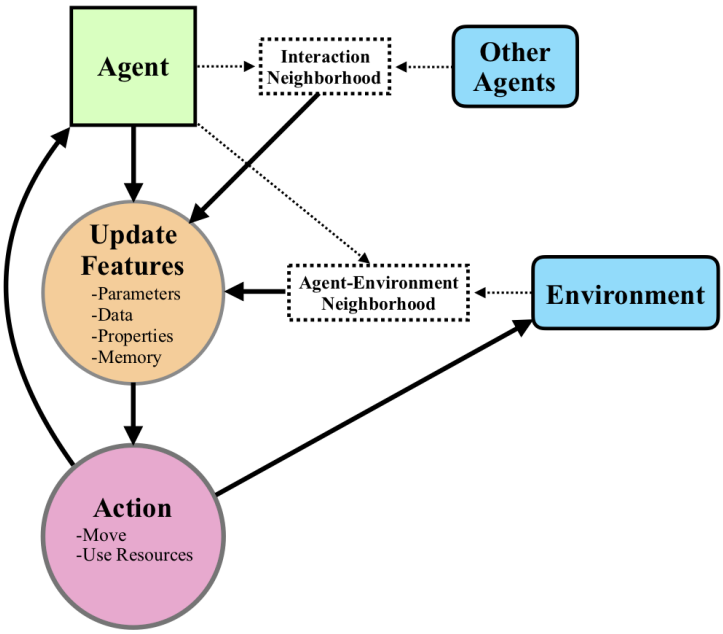

Figure 1.2: Flowchart for depicting various aspects of a generic AB model

The agent's updated features determine the agent's action, such as updating an agent's velocity or determining how an agent alters the environment, through some specified algorithm. Some AB models can be more complex by adding agents during simulation run time from birth or some estimated domain boundary flux, whereas other AB models may not exhibit all these elements. However, Fig. 1.2 illustrates the basic structure we investigate and exploit in this dissertation.

AB models allow the modeler the ability to readily define and control local interactions regardless of the amount of heterogeneity. However, we can see from the flowchart of a single time-step for one agent in Fig. 1.2 that as the number of agents in a system increases, the computational cost increases. In fact, investigating long-term dynamics solely from simulations may become intractable due to the computational cost involved with the increased amount of interactions with other agents and the environment as well as any additional feature updates [60]. With current computer architectures, simulating many agents is feasible but is offset by the computational time required to compute a sufficient number of simulations for analysis [2, 32, 110, 132]. Even with advanced computer architectures such as graphical processing units (GPUs) and parallel processing, the computational time could become prohibitive as the number of agents increases [104]. Additionally, there is generally a desire to understand how model outcomes change with respect to varying parameter values [25], which again would necessitate many simulations. Since continuum models generally model global dynamics, they have difficulty incorporating local interaction rules without making homogeneous assumptions. As such, continuum models can easily model dense populations, but have difficulty modeling dy-

namics when populations are sparse or the interacting heterogeneous populations have densities of different orders of magnitude.

The computational time or tractability of using realistic, complex domain geometries also exhibits the differences between AB models and continuum models. Since AB models track agents individually, this framework can adapt to boundaries that are time dependent, non-convex, or contain cusps relatively easily. However, due to their global framework, continuum Partial Differential Equation (PDE) models may not be well-posed under certain boundary conditions, such as when singularities exist at cusps [115]. Moreover, although domain discretization and numerical methods exist for intricate domains, the computational cost may be prohibitive even if the PDE is proved to be well-posed [26]. Further comparison between AB models and continuum PDE models can be found in Table 1.1. With this comparison in mind, it is important for a modeler to be able to have

Agent-Based Model		**Continuum Model**	
Pros	Cons	Pros	Cons
Local Solution	Must run sufficiently many times or with sufficiently many agents	Many established solution methods	Analytic solution difficult (or impossible) with complex boundaries
Easy to code (even with complex geometries)	Expensive to find global solution	Closed form solution may exist with simple geometries	May be difficult to couple with other equations
Relatively easy to couple with other equations	Difficult to analyze parameter effects	Can calculate parameter sensitivity, stability, ...	Numerical schemes for full solution can be computationally expensive

Table 1.1: Comparison between using AB models and using continuum models.

a bridge to connect AB models with continuum models, and be able to construct statistically similar models using either framework. Further development will enable modelers to use the best tools available in order to answer their questions of interest.

It is worth noting that much work has been done analyzing the data generated by AB models. For example, using the field of topological data analysis with AB data new tools have been developed such as the "Contour Realization Of Computed k-dimensional hole Evolution in the Rips complex" (CROCKER) plot to analyze pattern persistance in time [15, 126]. Moreover, many hybrid models exist, using PDE models within an AB model framework to increase fidelity and decrease computational cost. An example of such a model is fluid flow animation, where the flow particles are treated as agents and the pressure equation is solved as a PDE [107]. These methods and models are interesting

and certainly expand the usefulness of AB models as legitimate tools for the scientific and mathematical community. However, in this dissertation, we are solely interested in how to derive global approximations of AB models and examining the additional analytic tools such approximations make possible.

Part I of this dissertation deals with developing background material on AB models as well as deriving and providing an example of a new general method for estimating state densities. We want to use the explicit local interaction rules of AB models to develop methods that generate equations to approximate the AB model's global dynamics.

Random walk models, a simple case of AB models, consist of sequential random steps of movement; they have been widely used to investigate cellular motility, often in a spatially homogeneous environment [12, 29, 87, 135, 136]. Assuming the moving agent or cell is memoryless, an equation governing the spatiotemporal evolution of the density of cells can be determined. It corresponds to a standard diffusion equation if there is no bias in the motion or an advection-diffusion equation if there is bias in the motion [12, 29, 87, 136]. The derivation of this is detailed in **Chapter 2**. The advection-diffusion equation can capture different *taxis*, biasing the probability of movement based on chemical profiles (chemotaxis), temperature gradients (thermotaxis), fluid flow (rheotaxis), or environmental mechanical stiffness (durotaxis) [3, 21, 96, 98, 99]. The continuum limit of the stochastic process is often formulated in the case of cell motility since it is tractable from an analytical perspective and we have existing computational methods to easily solve these governing equations. The continuum derivation and applications (e.g. first passage time density and splitting probability) are introduced in this chapter and are necessary for the derivation and analysis of the absorption model in Part II.

Of special interest is how local state change dynamics can be captured in a global model. **Chapter 3** explains this in further detail as well as providing elucidating examples. In the existing random walk framework, accounting for different cell states would correspond to a system of coupled PDEs where local sinks or sources would describe leaving one cell state and entering another cell state. The two main methods with which AB models can precipitate state changes are agent-agent neighborhood interaction or agent-environment interaction. Here, we also codify the AB notation used in the remainder of the dissertation. This notation can also be found in the *List of Symbols* section preceding this chapter. Currently, our research has developed two different global approximation methods, which are detailed in Chapter 4 and Part II.

Through developing a precise definition of an off-lattice AB model with a specified interaction neighborhood, in **Chapter 4**, we develop a general method to determine a Global Recurrence Rule (GRR). This allows estimates of the state densities in time, which can be easily calculated for a range of parameters in the model. The utility of this framework is tested on an Epidemiological Agent-Based (E-AB) model where agents correspond to people that are in the susceptible, infected, or recovered states. The interaction neighborhoods of agents are determined in a mathematical formulation that allows the GRR to accurately predict the long term behavior and steady states. The GRR calculates the density of cells in particular states, but does not provide additional spatial information. In order to have our global approximation predict densities at spatial locations, we need

a method to derive a PDE from the AB model framework.

Part II develops a framework to describe and simulate stochastic cellular processes that are coupled to the environment and use this history to determine state changes. The classical PDE approximation of random walk models cannot account for cells changing states due to a cumulative environmental coupling, so we propose an extension to this methodology. Specifically, through upscaling, in **Chapter 5** we derive a novel continuum governing PDE equation from an AB model that considers the cell density as a function of time, space, and a cumulative variable that is coupled to the environmental conditions. By using the AB model to guide the continuum model, the model parameters have explicit and quantifiable physical meanings. For this new governing equation, we consider the stability through an energy analysis, as well as proving well-posedness. To solve the governing equations in free-space, we propose an operator-splitting numerical method that uses fundamental solutions after discretizing the space using uniform volumes. As an application, we study a cell moving in an infinite domain that contains a spatially heterogeneous toxic chemical, where a cumulative exposure above a critical value results in cell death. We illustrate the validity of this new modeling framework and associated numerical methods by comparing the spatiotemporal density of live cells to results from the corresponding AB model.

Chapters 6 and **7** expand on this basic free-space cumulative absorption model. First, we examine the absorption model in a bounded spatial region. Then we incorporate a fluid flow into the model, biasing and advecting the agent. Diffusion and the fluid velocity profile also creates a dynamic chemical density. Solving these more complex models requires further adaptations to the operator-splitting numerical method. Since the cumulative absorption model is the focus of the entirety of Part II, **Chapter 8** only focuses on the conclusions and future work of that research. There is a discussion section at the end of Chapter 4 that focuses on implications and future work for the GRR.

Finally, **Part III** includes additional derivations, proofs, plots, and discussions related to various sections in Parts I and II. These sections are appropriately referenced within the main body of the dissertation. However, including these sections within the main body would interrupt the flow for the reader and are better served within a standalone appendix.

Part I

Background Material and Global Recurrence Rule

Chapter 2

Random Walks

Although random walk (RW) models are a relatively simple type of agent-based model, the modeling framework is used extensively when modeling population dynamics [27], movement ecology [109, 28], and stock share prices [42]. RWs are also used to depict small particle motion, such as Brownian motion [65], and can be applied to add random noise to algorithms, such as evolutionary algorithms [56, 38] and ensemble Kalman filters [6], to avoid convergence to non-global extrema.

An agent is initialized in a spatial domain. At a time increment $\triangle t$ an agent moves to a location drawn from a movement probability distribution. In this dissertation, the RWs move at a constant spatial step, $\triangle x$, so the movement probability distribution determines the direction an agent moves. This constant spatial step essentially makes the RW occur on a fixed lattice. Denoting RWs as unbiased or biased relate to the type of movement probability distribution. Unbiased random walks (URWs) follow a symmetrical movement distribution, where each movement direction occurs with equal probability (1/number of directions). Contrarily, biased random walks (BRWs) usually follow an asymmetrical distribution. The movement probability distribution may account for the fact that an agent may remain in the same location, rather than move. We denote the waiting probability as the probability an agent remains in the same location. Generally, URWs have zero waiting probability.

The RWs used in this dissertation are mainly URWs and BRWs, as can be seen in Figs. 2.1 and 2.2. However, we briefly discuss correlated RWs in Section 2.3 since one could apply Chapters 5-7 to those. There are other types of RWs, such as Lévy walks, where the step-size is drawn from a probability distribution and can be approximated by fractional PDEs [85, 140], but these fall outside the purview of this dissertation since we are mainly interested in RWs with constant spatial step-size $\triangle x$.

A RW simulation iterates the above process until a terminating condition is encountered. RW processes are Markovian, in that agents only require information from the current time-step (e.g. location and orientation) to determine their next iteration [23]. Additionally, the Markov property and the simplicity of the model behavior allows us the ability to more easily approximate global RW behavior and predict useful statistical measures about RWs from the initial condition, movement probability, and step sizes.

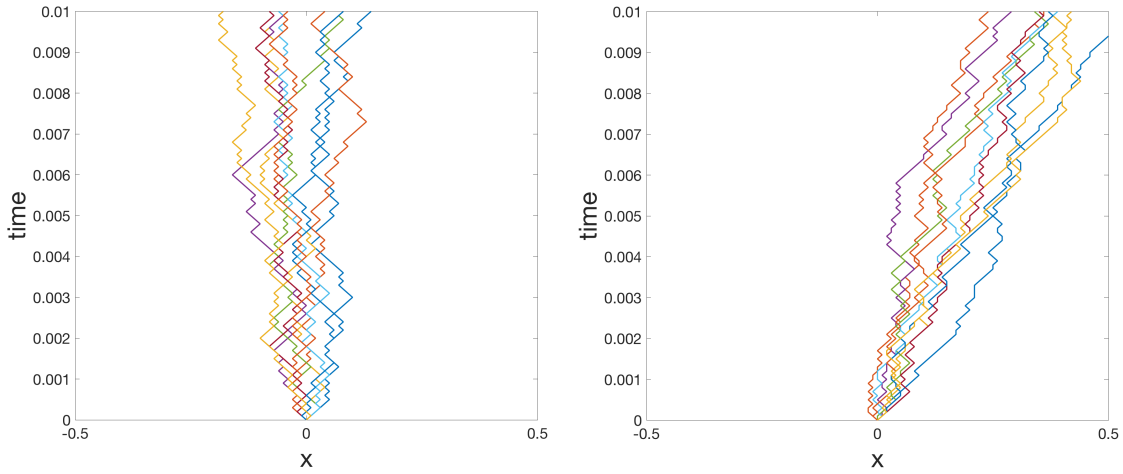

(a) Unbiased Random Walk

(b) Biased Random Walk
($\ell = 0.25, r = 0.65$)

Figure 2.1: Examples of RWs in one spatial dimension (1-d). Each graph shows 10 different RWs initialized at $x = 0$ with spatial step-size $\triangle x = 0.01$ and time step-size $\triangle t = \triangle x^2$. The variables ℓ and r denote the probabilities of moving left and right, respectively. The horizontal axis is the spatial dimension, whereas the vertical axis denotes the time dimension.

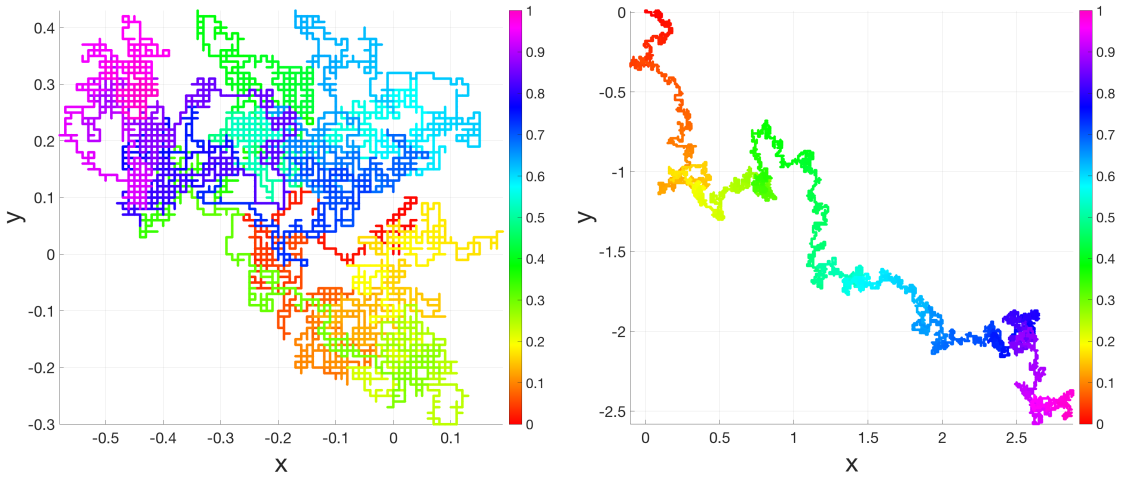

(a) Unbiased Random Walk

(b) Biased Random Walk
($\ell = 0.22, r = 0.25, u = 0.25, d = 0.28$)

Figure 2.2: Example of RWs in two spatial dimensions (2-d) for 10^4 iterations with spatial step size $\triangle x = 0.01$, $\triangle t = \triangle x^2$ and initialized at the point $(0, 0)$. Each graph shows one agent performing a RW. The variables ℓ, r, u, and d denote the probabilities of moving left, right, up, and down, respectively. The color of the line denotes the time since initialization (as shown in the colorbar).

There are two perspectives from which one may view RW movement, illustrated in Fig. 2.3, which are appropriated from the field of fluid mechanics: Lagrangian and Eulerian. We can frame the RW with a Lagrangian description, according to Fig. 2.3a, where we define and track individual agents and compute their next location. In fact, due to the Markovian (memoryless) nature of a RW, this is a natural framework for simulations, since we compute the location of each agent independently. We can also frame the RW with an Eulerian description, according to Fig. 2.3b, where we pick a location in time and determine all the possible ways an agent can occupy that location at that particular time. This is a more straightforward framework for deriving the global approximation, where we solve for the probability or density of agents at a particular location in time. We can still utilize the Markovian property by tracking only the possible paths originating from one prior time-step, rather than every possible path from the initial condition. This distinction becomes more apparent in the derivation of the global approximation within the following subsection.

2.1 Unbiased Random Walk (URW)

An URW is a subset of RWs, where the agent has an equal chance of moving left or right with zero waiting probability. So, in terms of Fig. 2.3a, we assign movement probabilities $\ell = r = 1/2$. We also assume that agents performing an URW do not hit or interfere with the motion of other agents. In fact, the only thing that would affect the unbiased motion of an agent would be if the spatial domain were bounded (or contained obstructions) and the simulation enforced reflecting boundary conditions. Examples of simulated runs of URWs can be seen in one spatial dimension (1-d) in Fig. 2.1a and two spatial dimensions (2-d) in Fig. 2.2a. In the 1-d case, the horizontal axis denotes the spatial coordinate and the vertical axis denotes time. We see that the agents move left or right each iteration and the distribution of agents tends to be symmetrical about the initial location. In the 2-d case, the axes denote the x and y spatial coordinates, while the color of the line denotes time. A single agent's RW is shown in Fig. 2.2a having equal probability of moving up, down, left, or right at each iteration.

As we demonstrate when developing its global approximation in Section 2.1.1, the URW is a symmetric, diffusive process. This is useful when adding random motion to a model or adding random noise to an algorithm, such as a random mutation to an evolutionary algorithm [112].

2.1.1 Global Approximation

Here, we use the method outlined in [29, 98] to derive the governing partial differential equation (PDE) that, when solved, produces the global approximation of the probability density function (pdf) of an agent performing an URW. Suppose an agent moves according to an URW; that is, at each time-step, of length $\triangle t$, the agent moves a distance $\triangle x$ to the left or right with equal probability $1/2$ (as seen in Fig. 2.3a with $\ell = r = 1/2$). We

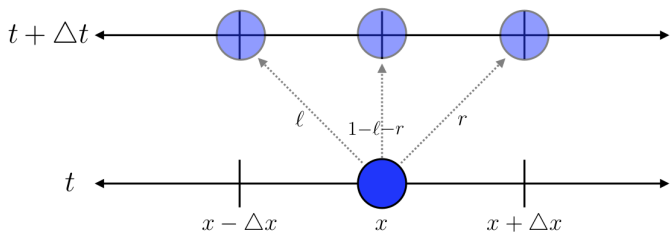

(a) Lagrangian Description of RW

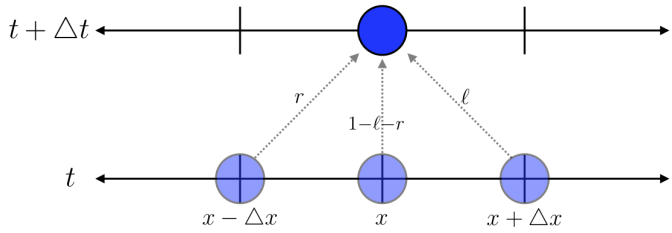

(b) Eulerian Description of RW

Figure 2.3: Two perspectives on how to define RW movement. **(a)** Simulations track each agent at time t and use the movement probabilities to determine where the agent can be located at $t+\triangle t$. **(b)** Global approximations track all the possible ways an agent can arrive at location x at time $t+\triangle t$.

want to derive a global approximation of the location of an agent in time. To do this, we must transition from the discrete lattice and discrete time-steps to a continuum approximation. We denote $U(x,t)$ as the probability an agent is at location x at time t.

To approximate a global solution of a discrete simulation in continuous space, we first set up a difference equation. We equate the probability an agent is at location x at time $t+\triangle t$, $U(x,t+\triangle t)$, with all the different ways the agent can arrive at that point (as seen in Fig. 2.3b with $\ell = r = 1/2$). The agent could begin at $x+\triangle x$ at time t and move left (with probability $1/2$), which we denote as $\frac{1}{2}U(x+\triangle x,t)$. Or the agent can begin at $x-\triangle x$ at time t and move right (with probability $1/2$), which we denote as $\frac{1}{2}U(x-\triangle x,t)$. The difference equation modeling an URW is then

$$U(x,t+\triangle t) = \frac{1}{2}U(x+\triangle x,t) + \frac{1}{2}U(x-\triangle x,t). \tag{2.1}$$

By assuming $U \in \mathcal{C}^2(\mathbb{R},[0,\infty))$ and $0 < \triangle x, \triangle t \ll 1$, we can expand these terms in a Taylor series centered at (x,t) by

$$\begin{aligned} &U + \triangle t\frac{\partial U}{\partial t} + \mathcal{O}(\triangle t^2) = \\ &\frac{1}{2}\left[U + \triangle x\frac{\partial U}{\partial x} + \frac{\triangle x^2}{2}\frac{\partial^2 U}{\partial x^2}\right] + \frac{1}{2}\left[U - \triangle x\frac{\partial U}{\partial x} + \frac{\triangle x^2}{2}\frac{\partial^2 U}{\partial x^2}\right] + \mathcal{O}(\triangle x^3). \end{aligned} \tag{2.2}$$

Simplifying the above equation results in the governing PDE of an URW:

$$\frac{\partial U}{\partial t} = \frac{\triangle x^2}{2\triangle t}\frac{\partial^2 U}{\partial x^2} + \mathcal{O}(\triangle t, \triangle x^3).$$

Traditionally [29], we say that the diffusion coefficient[1] is $D = \lim_{\triangle x, \triangle t \to 0} \frac{\triangle x^2}{2\triangle t}$, given that $\triangle t$ is proportional to $\triangle x^2$. Then, in the limit, the global continuum approximation of URW movement is

$$\frac{\partial U}{\partial t} = D\frac{\partial^2 U}{\partial x^2}. \tag{2.3}$$

However, one can also make the asymptotic argument that as long as the condition $0 < \triangle x, \triangle t \ll 1$ holds, then Eq. (2.3) with the diffusion coefficient $D = \triangle x^2/(2\triangle t)$ is a global continuum approximation of URW behavior. The distinction here may not seem necessary, but it is when addressing biased RW behavior in Section 2.2.

We can interpret the solution to Eq. (2.3) in two ways. If the initial condition to PDE (2.3) is a point source at x_0, then the solution $U(x,t)$ is the probability an agent initialized at x_0 is at location x at time t. However, if we have an arbitrary initial spatial distribution of agents $\phi(x) \geq 0$, then the solution $U(x,t)$ is the expected density of agents at location x at time t.

The above 1-d derivation of Eq. (2.3) can easily be extended to higher spatial dimensions. In that case, the governing PDE for an URW in n spatial dimensions is:

$$\frac{\partial U}{\partial t} = \frac{\triangle x^2}{2n\triangle t}\nabla^2 U, \tag{2.4}$$

where the spatial step in each spatial dimension is the constant $\triangle x$. If the spatial step is non-constant, then the governing PDE is:

$$\frac{\partial U}{\partial t} = \sum_{k=1}^{n} \frac{\triangle x_k^2}{2n\triangle t}\frac{\partial^2 U}{\partial x_k^2},$$

where the agent moves a step size $\triangle x_k$ in the k^{th} coordinate.

As we move to spatial dimensions higher than 1-d, we have more options for defining fixed spatial-step RW movement [58, 29]. Suppose in a 2-d domain we define the RW by choosing an angle along a continuum, rather than simply moving along a rectangular lattice as seen in Fig. 1.1a. That is, at each time-step the agent chooses an angle $\theta \in [0, 2\pi)$ and moves a distance $\triangle r$ in that direction. Since the RW is unbiased, the angle is a random variable drawn from $p(\theta) = 1/2\pi$, the pdf for a continuous uniform distribution on $[0, 2\pi]$. Because the angle is on a continuous (as opposed to discrete) distribution, we need to use an integral in the difference equation. Therefore, our difference equation becomes

$$U(x, y, t + \triangle t) = \int_0^{2\pi} \frac{1}{2\pi} U(x + \triangle r\cos(\theta), y + \triangle r\sin(\theta), t)\, d\theta.$$

[1] It is interesting to note that the diffusion coefficient is reminiscent of the CFL condition for solving the diffusion equation by forward Euler finite-difference methods, namely $\frac{\triangle t}{\varphi \triangle x^2} < 1$ for some constant φ [75, Ch.9]. This similarity is due to the fact that the formulation of the forward Euler method essentially reverses the above derivation by using Taylor expansions to discretize the PDE.

Expanding with a Taylor series and simplifying terms results in the governing PDE

$$\frac{\partial U}{\partial t} = \frac{\triangle x^2}{4\triangle t}\nabla^2 U + \mathcal{O}(\triangle x^3, \triangle t).$$

Note that this is the same result as if we performed the URW on a 2-d lattice, as seen in Eq. (2.4).

Comparison with Normal Distribution

If we want to model the pdf of a RW of a single agent starting at location x_0, we need to solve the following PDE:

$$\begin{cases} \frac{\partial U}{\partial t} = D\frac{\partial^2 U}{\partial x^2}, & x \in \mathbb{R},\, t > 0, \\ U = \delta(x - x_0), & x \in \mathbb{R},\, t = 0, \\ \lim_{|x|\to\infty} U = 0, & x \in \mathbb{R},\, t > 0, \end{cases} \tag{2.5}$$

where the diffusion constant is $D = \triangle x^2/(2\triangle t)$ and the initial condition $\delta(x - x_0)$ is the Dirac delta distribution centered at x_0. By using Fourier transformations detailed in Appendix A.1.2, we derive the analytical solution to Eq. (2.5),

$$U(x,t) = \frac{1}{\sqrt{4\pi D t}} \exp\left\{-\frac{(x - x_0)^2}{4Dt}\right\}. \tag{2.6}$$

We know that the pdf of a normal distribution with mean μ and variance σ^2 is

$$f(x|\mu,\sigma^2) = \frac{1}{\sqrt{2\pi\sigma^2}} \exp\left\{-\frac{(x-\mu)^2}{2\sigma^2}\right\}. \tag{2.7}$$

Relating Eq. (2.6) and (2.7), we see that the pdf of an agent's RW that begins at x_0 is a normal distribution with mean $\mu_{PDE} = x_0$ and time-dependent variance $\sigma^2_{PDE}(t) = 2Dt = \triangle x^2 t/\triangle t$.

This should not be surprising, since the probability a given lattice point of an URW is occupied at a particular time step essentially follows a binomial distribution. According to the central limit theorem, as the lattice step size decreases, the binomial distribution approaches a normal distribution. In fact, it has been shown in [29] that one can obtain (2.6) through this process. Thus, we can apply theory about normal distributions to RWs.

Comparing URW and PDE Approximation

We need to compare the analytic solution (2.6) with RW simulations. As an example, we initialize 10^5 agents at $x_0 = 0$ and perform independent RWs with step sizes $\triangle x = 0.01$ and $\triangle t = \triangle x^2$ for 100 iterations. After normalization (by dividing each bin by the total number of agents), this data generates a histogram of the proportion of agents at particular locations. To compare the PDE solution to this histogram data, we observe

that the RW simulation occurs on a lattice with a constant bin width of $\triangle x$. We calculate the PDE solution over each histogram bin by integrating (2.6) over each bin. Here, $u_k(t)$ denotes the integrated solution over the k^{th} bin. Thus, the exact PDE solution over each bin is

$$\begin{aligned} u_k(t) &= \int_{x_k-\triangle x/2}^{x_k+\triangle x/2} U(x,t)\,dx \\ &= \int_{x_k-\triangle x/2}^{x_k+\triangle x/2} \frac{1}{\sqrt{4\pi Dt}} \exp\left\{-\frac{x^2}{4Dt}\right\} dx \\ &= \frac{1}{2}\left\{ erf\left(\frac{x_k+\triangle x/2}{\sqrt{4Dt}}\right) - erf\left(\frac{x_k-\triangle x/2}{\sqrt{4Dt}}\right)\right\}, \end{aligned}$$

where x_k is the center of the k^{th} histogram bar and $erf(x) = (2/\sqrt{\pi})\int_0^x e^{-t^2}\,dt$ is the error function. This data is depicted in Fig. 2.4(a)-(d) for 4 distinct times.

We see a difference in the relative magnitude between the simulation and PDE approximation at each spatial location in Fig. 2.4(a)-(d) due to the fact that the URW does not have a waiting probability and the PDE smooths the RW dynamics[2]. The difference in magnitude is not due to the spatial step-size being too large. We could try decreasing the spatial step-size, since the diffusion coefficient is same when the spatial and temporal step-sizes, $\triangle x$ and $\triangle t$, scale according to $D = \frac{\triangle x^2}{2\triangle t}$. That is, the PDE models the same dynamics as a RW with step sizes $\widehat{\triangle x} = a\triangle x$ and $\widehat{\triangle t} = a^2\triangle t$ for any $a > 0$. However, our PDE values are calculated on intervals $(x-\triangle x/2, x+\triangle x/2)$ and would still calculate positive values where we know the simulation histograms have values of 0, since the RW does not have a waiting probability (as seen in Fig. 2.4(e)-(h), where $\triangle x = 0.005$).

If the relative magnitude at each spatial location is important, we have a few different options to smooth the URW data. We could fit the non-zero simulation data with a spline, enforcing 0 at the endpoints, and then normalize the results so that the approximation integrates to 1. Another option to smooth the RW histogram is to average neighboring bins, but we would have to alternate the bin groupings each iteration since the empty lattice points alternate between each time-step. Alternatively, a better option that would result in smooth RW graphs is to change the RW initial condition from a point source to a random location chosen from a normal distribution with mean x_0 and standard deviation $\triangle x$ (that is, the agent is initialized with a value drawn from $N(x_0, \triangle x)$). The magnitudes at specific time-points can be seen in Fig. 2.4(i)-(l). At early times, the PDE, with point source initial condition, overestimates the magnitude of the URW; however, it quickly recovers a similar magnitude.

Depicting the exact initial location may be a necessary requirement of the model. Another way to smooth the graphs is to take the notion of a BRW from Section 2.2 and insert a waiting probability. This is seen in Fig. 2.5(e)-(h) where the movement probabilities of the RW simulations and PDE approximations are unbiased with a 10%

[2]Because of the inherent discontinuities in the URW behavior, choosing to truncate the Taylor series at later terms does not sufficiently correct the magnitude difference to make the URW directly comparable with the PDE solution.

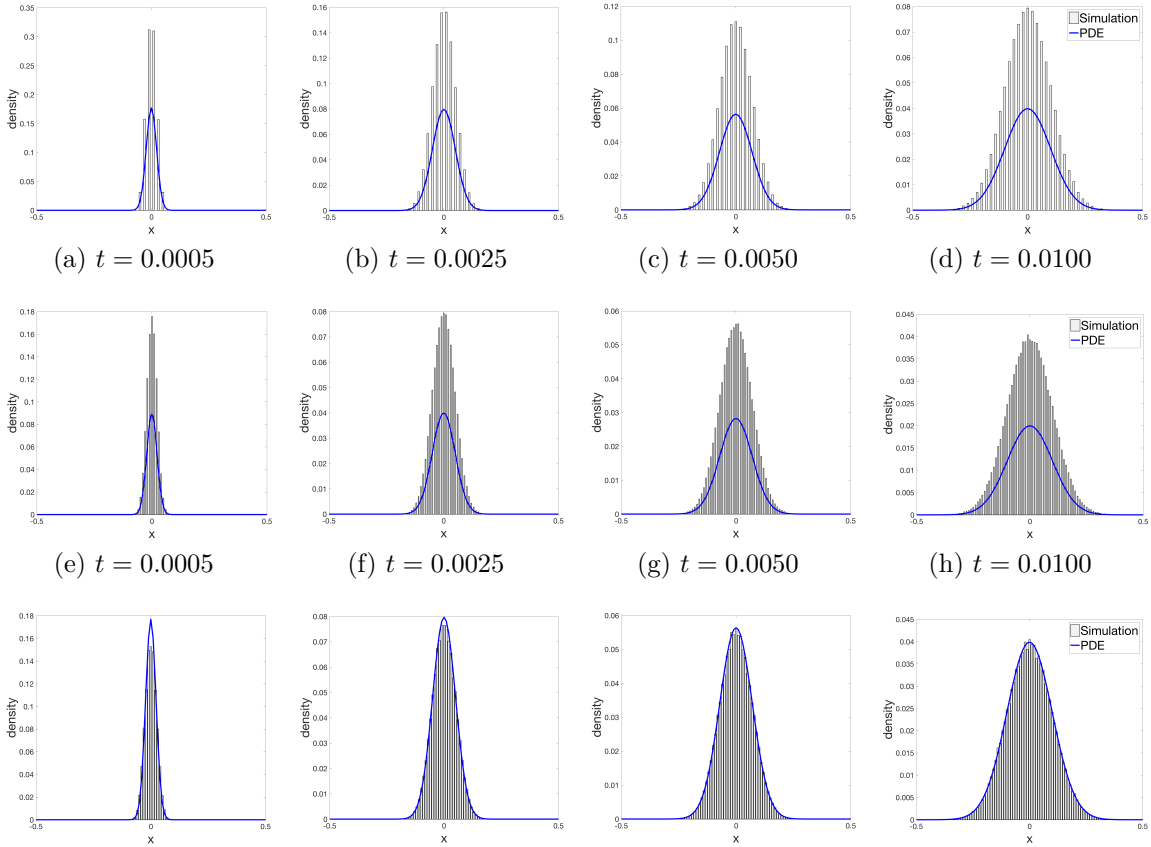

(a) $t = 0.0005$ (b) $t = 0.0025$ (c) $t = 0.0050$ (d) $t = 0.0100$

(e) $t = 0.0005$ (f) $t = 0.0025$ (g) $t = 0.0050$ (h) $t = 0.0100$

(i) $t = 0.0005$ (j) $t = 0.0025$ (k) $t = 0.0050$ (l) $t = 0.0100$

Figure 2.4: Comparison of URW and PDE approximation. RW density is the average of 10^5 simulations and denoted as a histogram with bin size $\triangle x$. **(a)-(d)** step size $\triangle x = 0.01$, $\triangle t = \triangle x^2$, with URW initialized at $x_0 = 0$. **(e)-(h)** step size $\triangle x = 0.005$, $\triangle t = \triangle x^2$, with URW initialized at $x_0 = 0$. **(i)-(l)** step size $\triangle x = 0.01$, $\triangle t = \triangle x^2$, with URW initialized at $x_0 \sim N(0, \triangle x)$.

waiting probability. The derivation of this PDE is in Section 2.2.1. Note that, unlike the URW with normal initial condition, this PDE underestimates the RW magnitude at early time-steps. The RW with waiting time requires some time to elapse before smoothing the simulation histogram. The amount of time is dependent on the value of the waiting probability.

However, we are not solely interested in comparing the magnitude of the URW and PDE solution graphs. Of arguably greater importance are the statistical measures of mean, μ, and standard deviation, σ. We know the analytic solutions of these statistical measures from comparing the PDE solution with the normal distribution. From Figs. 2.6a, 2.6b we see that the shape of the solution surface plots, showing the probability distribution of location of agents in time and space, appear similar. We see in Fig. 2.6c that the mean values between the two graphs are minimally different (a small percentage of the

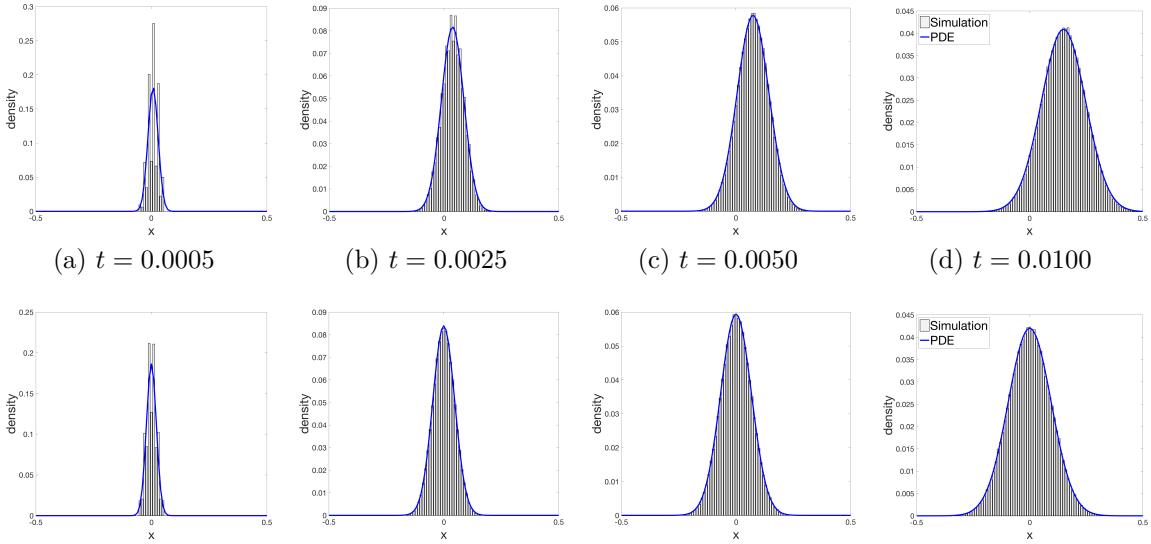

(a) $t = 0.0005$ (b) $t = 0.0025$ (c) $t = 0.0050$ (d) $t = 0.0100$

(e) $t = 0.0005$ (f) $t = 0.0025$ (g) $t = 0.0050$ (h) $t = 0.0100$

Figure 2.5: Comparison of BRW and PDE approximation. BRW initialized at $x_0 = 0$ with step sizes $\triangle x = 0.01$ and $\triangle t = \triangle x^2$. RW density is the average of 10^5 simulations and denoted as a histogram with bin size $\triangle x$. **(a)-(d)** probabilities of moving left $\ell = 0.4$ and moving right $r = 0.55$. **(e)-(h)** probabilities of moving left $\ell = 0.45$ and moving right $r = 0.45$.

width of a step size) due to some stochastic variation. Adding more agents to the simulation decreases this noise. Further, the standard deviation graphs in Fig. 2.6d appear very similar. Now that we are confident the PDE (2.3) approximates URW densities, we can use (2.3) to further explore URW behavior.

The PDE derivation assumes averaging over an infinite number of agents, that is, $N \to \infty$. Each URW simulation example above is the average of 10^5 agents. If we only used 10 agents, we would expect the error between the simulation mean and PDE mean to be much larger due to its small sample size. So, we may be interested in the relation between the number of random walk agents and the error in our statistical metrics. To get a sense of the trends, we find the total mean error for a simulation with N agents,

$$E_\mu(N) = \sum_{t_i} |\mu_{URW}(t_i) - \mu_{PDE}(t_i)|\,,$$

as the summation over each iteration of the absolute difference between the URW simulation mean and the PDE mean in the time interval $t_i \in [0, 0.01]$. We know analytically that $\mu_{PDE} = x_0$, where x_0 is the initial location of agents. Similarly, we find the total standard deviation error as

$$E_\sigma(N) = \sum_{t_i} |\sigma_{URW}(t_i) - \sigma_{PDE}(t_i)|\,,$$

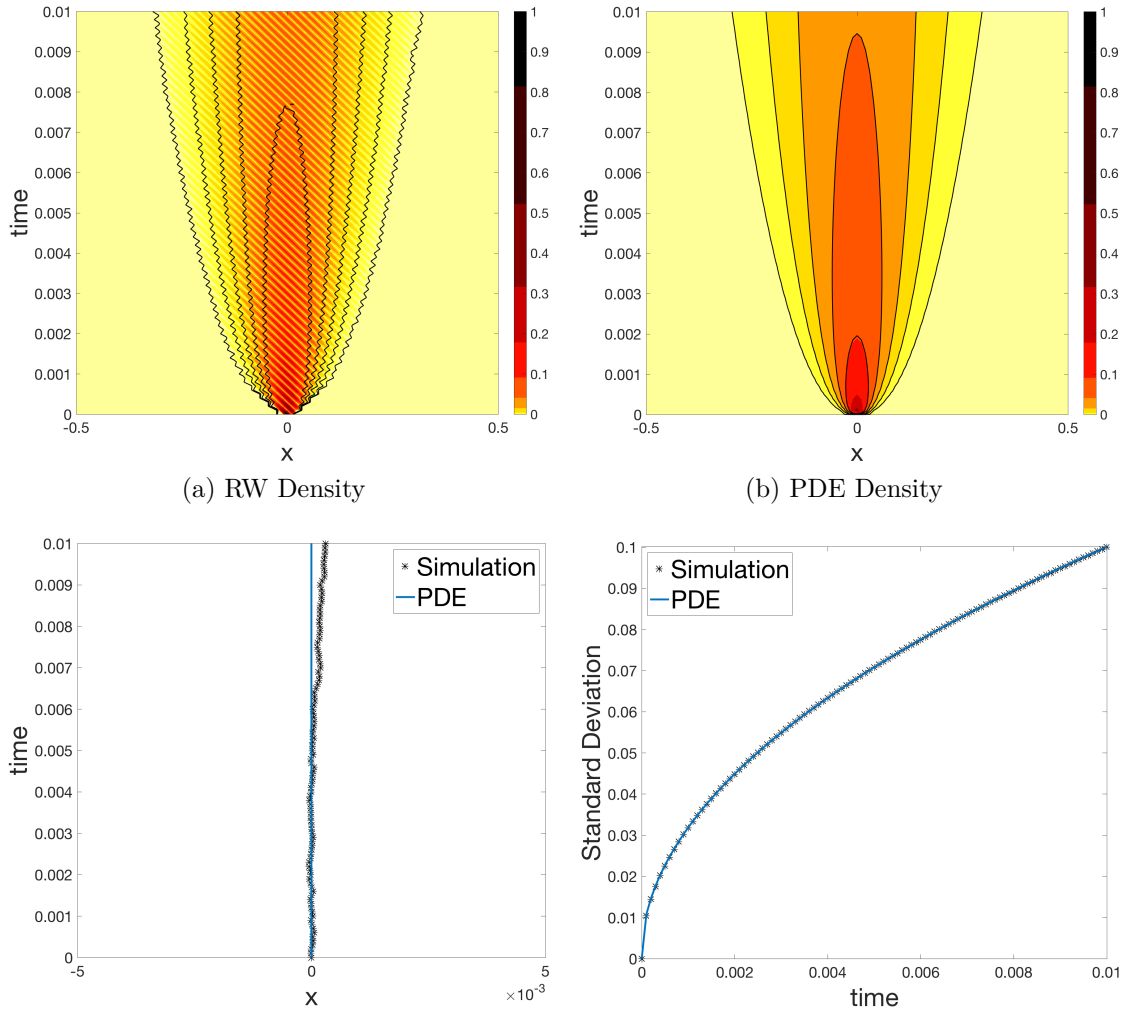

(a) RW Density (b) PDE Density

(c) Mean Location (d) Location Standard Deviation

Figure 2.6: Comparison of URW and PDE approximation initialized at $x_0 = 0$ with step sizes $\triangle x = 0.01$, $\triangle t = \triangle x^2$. RW density is average of 10^5 simulations. **(a)-(b)** Contour lines denote the same surface height for each graph. **(c)** The URW mean location is close to the PDE mean, $\mu = 0$. The spatial axis for the mean values is the narrow interval $[x_0 - \triangle x/2, x_0 + \triangle x/2]$. **(d)** URW and PDE location standard deviation graphs.

where the PDE standard deviation is $\sigma_{PDE}(t_i) = \sqrt{2Dt_i}$. These functions are graphed in Fig. 2.7, where both the number of agents and error axes are stretched using log scale. Clearly, the relation between the number of agents and the mean error graph is log-linear. That is, $\log(E_\mu) = a\log(N) + b$ for some $a, b \in \mathbb{R}$, where N is the number of agents. Using least-squares approximation with the data as derived in Appendix B, we find $E_\mu(N) \approx e^{1.6231} N^{-0.5135}$. So the convergence rate for the mean location error is approximately $1/\sqrt{N}$. This experimental convergence rate is unsurprising, since this is the order of convergence for the central limit theorem by the Berry-Esseen theorem [44]. Moreover, it

is interesting that the slope relating the number of agents and error in Figs. 2.7a and 2.7b is similar. In fact, the least-squares approximation is $E_\sigma(N) \approx e^{1.1474} N^{-0.4932}$, where the order of convergence is approximately $1/\sqrt{N}$. The experimental order of convergence is also found to be $1/\sqrt{N}$ for subsets of the time domain $[0, 0.01]$.

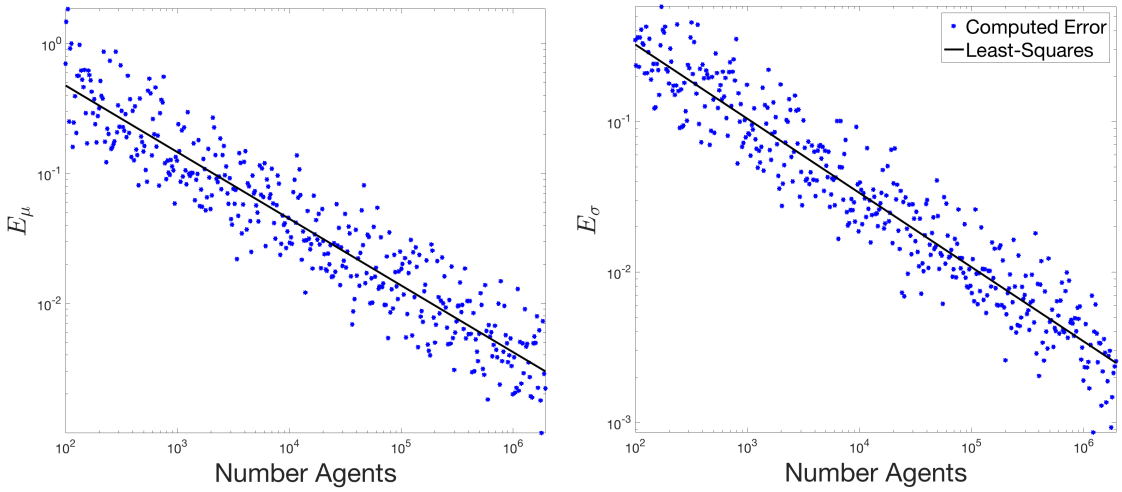

(a) Mean Location Error (b) Standard Deviation Error

Figure 2.7: Total error between URW simulation and PDE approximation depending on the number of URW agents. **(a)** Total mean location error $E_\mu = \sum_{t_i} |\mu_{URW}(t_i) - \mu_{PDE}|$ **(b)** Total standard deviation error $E_\sigma = \sum_{t_i} |\sigma_{URW}(t_i) - \sigma_{PDE}(t_i)|$.

2.1.2 First Passage Time Density (FPTD)

One particular measure of interest is the time it takes an agent to enter (or exit) a particular region, also known as the first passage time (FPT) or first hitting time. Suppose an agent is initialized at x_0 and we want to know the probability distribution for the time that agent first passes the location x^*. That is, we want to find the first passage time density (FPTD) function $f(t)$. Let us assume that $x_0 < x^*$. As demonstrated in [14, 79], we begin by setting up a PDE with the same governing equation and initial condition as (2.5), but with an absorbing boundary condition at x^*:

$$\begin{cases} \lim_{x \to -\infty} U(x,t) = 0, & t > 0, \\ U(x^*, t) = 0, & t > 0. \end{cases}$$

We use (2.6) in conjunction with the method of images (as further detailed in Section 6.1.1) to obtain an exact solution with an absorbing wall at x^*:

$$U(x,t) = \frac{1}{\sqrt{4\pi D t}} \left[\exp\left(-\frac{(x - x_0)^2}{4Dt} \right) - \exp\left(-\frac{(x + x_0 - 2x^*))^2}{4Dt} \right) \right]. \tag{2.8}$$

The probability that the agent is still in the region $(-\infty, x^*)$ at time t is

$$S(t) = \int_{-\infty}^{x^*} U(x,t)\,dx.$$

We call $S(t)$ the survival probability. Then the probability that an agent passes x^* between time t and $t+\tau$, for any time $\tau > 0$ is $f(t)\tau = S(t) - S(t+\tau)$. We can rewrite this as $f(t) = -\frac{S(t+\tau)-S(t)}{\tau}$. If we take the limit as $\tau \to 0$, then by the definition of a derivative we obtain the relation between the FPTD and survival probability, $f(t) = -\frac{dS}{dt}$. Using the definition of $S(t)$, we know $f(t) = -\frac{d}{dt}\int_{-\infty}^{x^*} U(x,t)\,dx$. Inserting Eq. (2.8) into $f(t)$ gives us

$$f(t) = \frac{|x^* - x_0|}{\sqrt{4\pi D t^3}} \exp\left(-\frac{(x^* - x_0)^2}{4Dt}\right), \tag{2.9}$$

the FPTD function that an agent travels across point x^*.

We can also try to solve for the mean first passage time (MFPT), the average time for the agent to travel across x^* by solving for the first moment of $f(t)$. That is,

$$M = \int_0^\infty t f(t)\,dt = -\int_0^\infty t\frac{dS}{dt}\,dt.$$

Using integration by parts, $M = -tS\Big|_{t=0}^{\infty} + \int_0^\infty S\,dt$. If the survival probability approaches 0 for large times (i.e. $S(t) \to 0$ as $t \to \infty$), then the MFPT exists and we can calculate it by $M = \int_0^\infty S\,dt$. It is shown in [39, 53] that $S(t) \nrightarrow 0$ as $t \to \infty$ for bounded domains in 3-d. Hence, the MFPT is guaranteed to exist in 1-d or 2-d, but not necessarily in higher dimensions. This property is a direct consequence of the form of the fundamental solution of the diffusion equation in n-d (2.6) and that there is a non-zero survival probability as $t \to \infty$ for $n > 2$.

2.1.3 Splitting Probability

Suppose our agent is initialized in a bounded domain, Ω. If there are finitely many regions in which the agent can escape along the boundary of the domain, $\partial\Omega$, we may be interested in the probability that the agent exits the domain from a particular region. This is known as the splitting probability. Such information is useful in applications such as chemical sensing [37] and escape dynamics [92]. There are multiple methods to solve the splitting probability such as Kramers method, the absorbing boundary method, and the normal mode method [50, 130]. Here, we demonstrate the absorbing boundary method since we adapt this method in Section 6.2. Moreover, it further elucidates the effectiveness of obtaining the global approximation Eq. (2.3).

Suppose our 1-d domain is a bounded interval $\Omega = [x_1, x_2]$ and we want to know the probability that an agent exits Ω through x_1 instead of x_2. We begin by deriving the

FPTD for the following PDE:

$$\begin{cases} \frac{\partial U}{\partial t} = D\frac{\partial^2 U}{\partial x^2}, & x \in (x_1, x_2),\ t > 0 \\ U = \delta(x - x_0), & x \in [x_1, x_2],\ t = 0, \\ U = 0, & x \in \{x_1, x_2\},\ t > 0, \end{cases}$$

where $x_0 \in (x_1, x_2)$. Since the agent can exit out of x_1 and x_2, the PDE has absorbing boundary conditions at both endpoints. By our previous derivations, we know that the survival probability at time t is $S(t) = \int_{x_1}^{x_2} U(x,t)\,dx$ and the FPTD is $f(t) = -\frac{d}{dt}S(t)$. It follows that

$$\begin{aligned} f(t) &= -\frac{d}{dt}\int_{x_1}^{x_2} U(x,t)\,dx \\ &= -\int_{x_1}^{x_2} \frac{\partial U}{\partial t}\,dx \\ &= -\int_{x_1}^{x_2} D\frac{\partial^2 U}{\partial x^2}\,dx \\ &= D\frac{\partial U}{\partial x}\bigg|_{x=x_1} - D\frac{\partial U}{\partial x}\bigg|_{x=x_2}. \end{aligned}$$

Let us define $J_1(t) = D\frac{\partial U}{\partial x}\Big|_{x=x_1}$ and $J_2(t) = -D\frac{\partial U}{\partial x}\Big|_{x=x_2}$. Then the expected density to exit $[x_1, x_2]$ is $f(t) = J_1(t) + J_2(t)$. Thus, J_1 and J_2 at time t compute the expected fluxes out of the endpoints x_1 and x_2, respectively. The signs of J_1 and J_2 are opposite since the agents move across the endpoints in opposite directions.

By our derivation, we know that the total flux out of x_1 is $\int_0^\infty J_1(t)\,dt$. Similarly, $\int_0^\infty J_2(t)\,dt$ is the total flux out of x_2. Since the initial condition is a point source and integrates to 1, and since we know that $\lim_{t\to\infty} S(t) = 0$, it follows that $\int_0^\infty f(t)\,dt = 1$. Therefore, the probability that an agent initialized at x_0 escapes out of x_1 is $\int_0^\infty J_1(t)\,dt$.

This absorbing boundary method can be extended to higher dimensions. The boundary conditions are changed to absorbing where an agent can exit the simulation, and reflecting otherwise. Further work has been done developing methods to solve for moving escape regions [128] and asymptotically small escape regions [70].

2.2 Biased Random Walk (BRW)

For more realistic models, the RW movement may depend on internal or external influences, such as bound cellular receptors [127], established goal locations [11], fluid flow forces [58], or attracting chemical profile gradients [3]. These influences may cause an agent to prefer moving in one direction rather than another. This movement biasing may depend on an agent's internal state or an agent's location. In this subsection, we extend the derivation of Section 2.1.1 to approximate a RW where the agent's location biases its movement by using the method illustrated in [29]. In Section 3.3.3, we briefly discuss approximating RWs where an agent's internal state biases its movement.

2.2.1 Global Approximation

For spatially-dependent biasing probabilities, it is important to be clear as to the meaning of the spatial dependence. The term $\ell(x)$ could refer to the probability of an agent, who currently occupies location x, to move left. However, it could also refer to the probability of an agent, who currently occupies a location to the right of x, to move left to occupy location x at the next time-step. This section investigates both interpretations. In either case, $1-\ell(x)-r(x)$ is the waiting probability, the probability an agent remains in the same location.

Suppose $\ell(x)$ and $r(x)$ are the probabilities an agent, currently occupying location x, moves left or right, respectively. As in Section 2.1.1 we set up a difference equation:

$$U(x,t+\triangle t)=\ell(x+\triangle x)U(x+\triangle x,t)+r(x-\triangle x)U(x-\triangle x,t)+[1-\ell(x)-r(x)]U(x,t).$$

Unlike the URW, there may be a non-zero probability that the agent remains in its current location (i.e. $0<\ell(x)+r(x)<1$). The expression $1-\ell(x)-r(x)$ in the last term denotes the waiting probability at location x. The expected waiting time is $\triangle x/(1-\ell(x)-r(x))$, which is the expected time an agent stays in the same location. We assume $U\in\mathcal{C}^2\left(\mathbb{R},[0,\infty)\right)$, $\ell\in\mathcal{C}^2(\mathbb{R})$, and $r\in\mathcal{C}^2(\mathbb{R})$. As in Section 2.1.1, we expand each term in a Taylor series, which simplifies to:

$$\frac{\partial U}{\partial t}=\frac{\triangle x}{\triangle t}\frac{\partial(\ell(x)-r(x))U}{\partial x}+\frac{\triangle x^2}{2\triangle t}\frac{\partial^2(\ell(x)+r(x))U}{\partial x^2}+\mathcal{O}(\triangle t,\triangle x^3). \tag{2.10}$$

Note that the coefficient before the first spatial derivative is $\frac{\triangle x}{\triangle t}$, the speed of the agent.

If we make the same limiting argument as Section 2.1.1 for our parameters, then

$$a=\lim_{\triangle x,\triangle t\to 0}\frac{\triangle x}{\triangle t},\qquad D=\lim_{\triangle x,\triangle t\to 0}\frac{\triangle x^2}{2\triangle t},$$

with $\triangle x^2\propto\triangle t$. However, unless we add a caveat that $0<r(x)-\ell(x)\ll 1$ for all x, then we cannot reasonably assert that the limit for a exists. If we suppose that $\triangle x\propto\triangle t$, then we can argue that, in the limit, $D=0$. So our PDE simplifies to a transport equation with velocity a. But that simplification results in a model that does not explain any of the diffusive spread. To overcome this oversimplification, we make an asymptotic argument by assuming that our RW step sizes obey $0<\triangle x,\triangle t\ll 1$. Then we propose that we define the variables

$$a=\frac{\triangle x}{\triangle t},\qquad D=\frac{\triangle x^2}{2\triangle t}$$

as the parameters for our BRW approximation. The general equation for a BRW becomes

$$\frac{\partial U}{\partial t}=a\frac{\partial(\ell(x)-r(x))U}{\partial x}+D\frac{\partial^2(\ell(x)+r(x))U}{\partial x^2}. \tag{2.11}$$

If we do notice that either $0<\ell(x)-r(x)\ll 1$ or $|\ell(x)-r(x)|\approx 1$, then we can solve Eq. (2.11) using regular perturbation methods, where the leading order solution is in

the diffusive or advective regime, respectively. Note that Eq. (2.11) is the Fokker-Planck equation [50].

However, we can also consider $\ell(x), r(x)$ the probabilities of moving left or right, respectively, to location x from some location other than x. This is subtly different than the previous derivation, where $\ell(x), r(x)$ were the probabilities of moving left or right when the agent is at location x. We then obtain the difference equation

$$U(x, t+\triangle t) = \ell(x)U(x+\triangle x, t) + r(x)U(x-\triangle x, t) + [1-\ell(x)-r(x)]U(x,t).$$

Expanding in a Taylor series and simplifying results in the following equation:

$$\frac{\partial U}{\partial t} + (r(x)-\ell(x))\frac{\triangle x}{\triangle t}\frac{\partial U}{\partial x} = (\ell(x)+r(x))\frac{\triangle x^2}{2\triangle t}\frac{\partial^2 U}{\partial x^2} + \mathcal{O}(\triangle t, \triangle x^3).$$

As we did when deriving (2.11), we can make an asymptotic argument for defining the parameters[3]

$$a(x) = (r(x)-\ell(x))\frac{\triangle x}{\triangle t}, \qquad D(x) = (\ell(x)+r(x))\frac{\triangle x^2}{2\triangle t}.$$

In this case, the general equation approximating a BRW is

$$\frac{\partial U}{\partial t} + a(x)\frac{\partial U}{\partial x} = D(x)\frac{\partial^2 U}{\partial x^2}. \tag{2.12}$$

With the movement probabilities defined this way, Eq. (2.12) is the advection-diffusion equation.

The choice of (2.11) or (2.12) depends on which more easily fits the RW modeling framework. We can change (2.11) to (2.12) by changing the expressions for ℓ and r. We also note that if ℓ and r are constant, then (2.11) and (2.12) are equivalent. If necessary, we can have ℓ and r depend on time, t as well. The resulting governing equations for time-dependent parameters would be similar to (2.11) or (2.12).

Comparison with Normal Distribution

Suppose an agent is initialized at x_0 and performs a BRW with constant movement biases $\ell = \ell(x)$ and $r = r(x)$. The global approximation of the probability the agent is at location x at time t is

$$\begin{cases} \frac{\partial U}{\partial t} = a\frac{\partial U}{\partial x} + D\frac{\partial^2 U}{\partial x^2}, & x \in \mathbb{R},\ t > 0, \\ U = \delta(x - x_0), & x \in \mathbb{R},\ t = 0, \\ \lim_{|x|\to\infty} U = 0, & x \in \mathbb{R},\ t > 0, \end{cases} \tag{2.13}$$

[3] Note that if we were given the advection coefficient, $a(x)$, and the diffusion coefficient, $D(x)$, and were interested in knowing the probabilities of moving left and right, then we solve the following equations:

$$\ell(x) = \frac{\triangle t}{\triangle x}\left[\frac{D}{\triangle x} - \frac{a}{2}\right], \quad r(x) = \frac{\triangle t}{\triangle x}\left[\frac{D}{\triangle x} + \frac{a}{2}\right].$$

where $a = (\ell - r)\frac{\triangle x}{\triangle t}$ and $D = (\ell + r)\frac{\triangle x^2}{2\triangle t}$. Utilizing the Fourier transformation, as detailed in Appendix A.1.3, we can calculate the analytical solution to Eq. (2.13) as

$$U(x,t) = \frac{1}{\sqrt{4\pi Dt}} \exp\left\{-\frac{(x + at - x_0)^2}{4Dt}\right\}. \tag{2.14}$$

Comparing the solution (2.14) with the normal distribution pdf (2.7) shows us that the pdf of the location of the BRW agent follows a normal distribution with a time-dependent mean $\mu(t) = x_0 - at = x_0 - (\ell - r)\triangle x t/\triangle t$ and variance $\sigma^2(t) = 2Dt = (\ell + r)\triangle x^2 t/\triangle t$. Note that the variance depends on the waiting probability. If the agent does not have a waiting probability ($\ell + r = 1$), then the variance of (2.14) is the same as the variance of (2.6).

Comparing BRW and PDE Approximation

We compare the simulation and PDE approximations of the BRW in the same way as the URW. Initialize 10^5 agents at $x_0 = 0$ with step sizes $\triangle x = 0.01$, $\triangle t = \triangle x^2$, and movement probabilities $\ell = 0.4$, $r = 0.55$. Note that the magnitude of the histograms and PDE solutions in Fig. 2.5(a)-(d) match better than the URW in Fig. 2.4(a)-(d). In this case, there is a 5% waiting probability, which smooths the RW histogram. This waiting time smoothing is also the reason that the early-time approximation does not match the magnitude as well as the later-time approximations, a result that is also shown in Fig. 2.5(e)-(h) where $\ell = r = 0.45$. Similar to the URW, the mean and standard deviation graphs demonstrate similarity, as shown in Figs. 2.8c and 2.8d, respectively.

For larger biasing, such as that shown in Fig. 2.9 with $\ell = 0.6$ and $r = 0.3$, the standard deviation does not match as well as smaller biasing. The standard deviation error accumulates in time due to the asymptotic parameter approximations. We can see the error is greater when $|\ell - r| = 0.3$ than in Fig. 2.8d when $|\ell - r| = 0.15$.

We can calculate the total mean error, $E_\mu(N)$, and total standard deviation error, $E_\sigma(N)$ in a similar way as Section 2.1.1 to determine if the BRW distribution converges to the PDE solution. Here, since the movement probabilities are constant, the PDE mean is $\mu_{PDE}(t_i) = (\ell - r)t_i/\triangle t$ and the PDE standard deviation is $\sigma_{PDE}(t_i) = \sqrt{2Dt_i}$. These functions are graphed in Fig. 2.10, where both the number of agents and error axes use log-scales. Clearly, the relation between the number of agents and the mean error graph is log-linear. Using least-squares approximation with the data as derived in Appendix B, we find $E_\mu(N) \approx e^{1.5994} N^{-0.5138}$. So, just like the URW, the experimental convergence rate for the mean is approximately $1/\sqrt{N}$. In contrast, the standard deviation approaches a horizontal asymptote around $E_\sigma(N) = 0.078$ for $N \geq 10^5$. This is due to the parameter assumptions mentioned above. However, the variance in the data of the error plot in Fig. 2.10b informs us that one should perform simulations with $N \geq 10^5$ to obtain reliable results.

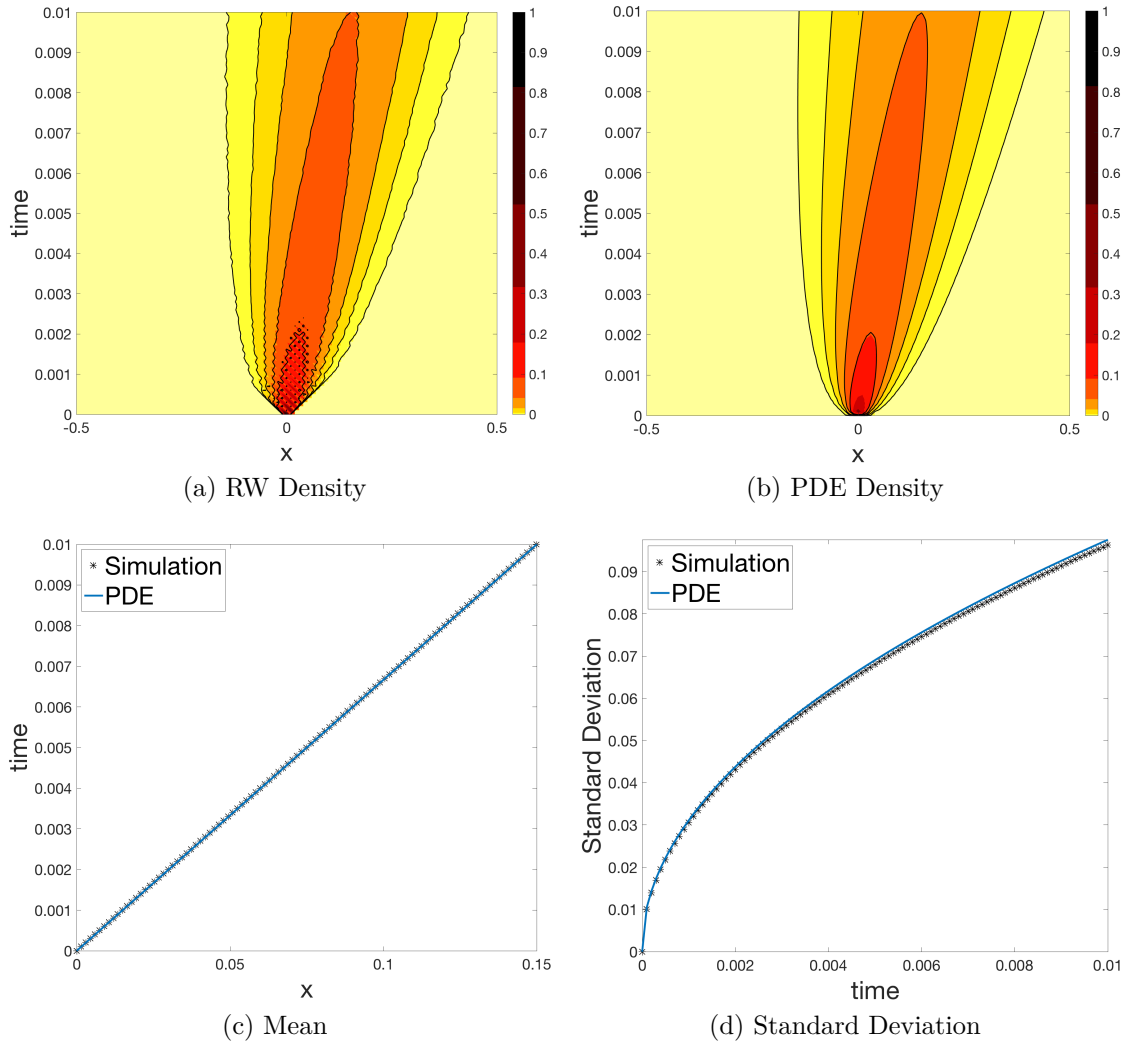

(a) RW Density (b) PDE Density

(c) Mean (d) Standard Deviation

Figure 2.8: Comparison of BRW and PDE approximation initialized at $x_0 = 0$ with probability moving left $\ell = 0.4$ and probability moving right $r = 0.55$. Simulation step sizes are $\triangle x = 0.01$ and $\triangle t = \triangle x^2$. RW density is the average of 10^5 simulations. **(a)-(b)** Contour lines denote the same surface height for each graph. **(c)** The mean location of the simulation and PDE. **(d)** The standard deviation graphs.

2.2.2 Further Analysis

One can calculate the FPD and MFPT in a manner similar to the unbiased RW. It is important to note that even in 1-d the MFPT may not exist for a BRW (consider the case where $\ell = 1, r = 0$ and the initial location, x_0, of the agent is to the left of the target location, x^*) [29].

Now we have an understanding of how to relate BRW and Fokker-Planck (or advection-diffusion equations), as well as an understanding of how the errors originate. With this

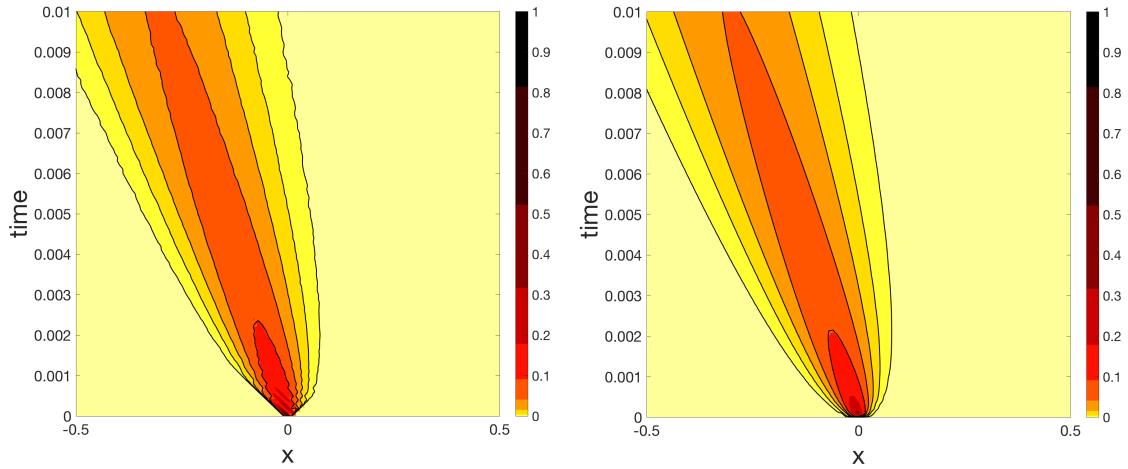

(a) RW Density

(b) PDE Density

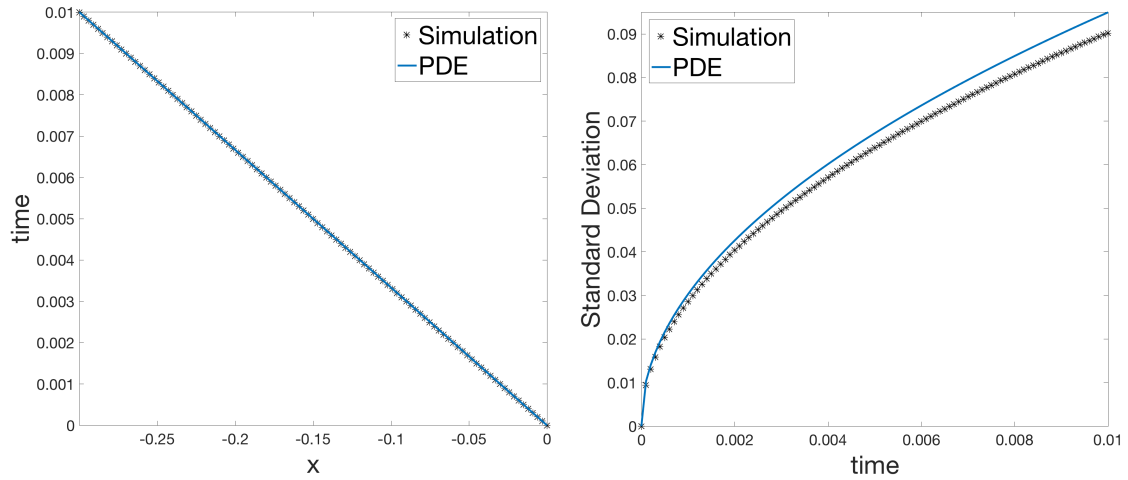

(c) Mean Location

(d) Location Standard Deviation

Figure 2.9: Comparison of RW and PDE approximation initialized at $x_0 = 0$ with probability moving left $\ell = 0.6$ and probability moving right $r = 0.3$. Simulation step sizes are $\triangle x = 0.01$ and $\triangle t = \triangle x^2$. RW density is the average of 10^5 simulations. **(a)-(b)** Contour lines denote the same surface height for each graph. **(c)** The mean location of the simulation and PDE. **(d)** The standard deviation graphs.

knowledge, we can solve a reverse problem. Suppose we have an advection-diffusion equation that needs to be solved inside a complex geometry. We can approximate the PDE solution by running RW simulations. In Part II, we adapt the continuum derivation as well as the various applications (e.g. FPTD and splitting probability) of URWs and BRWs for the cumulative absorption model.

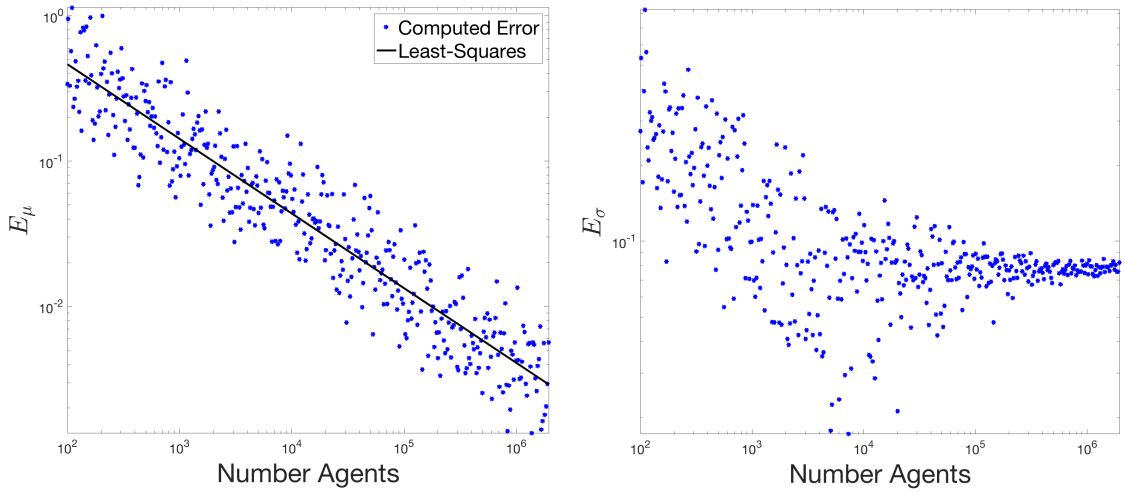

(a) Mean Location Error

(b) Standard Deviation Error

Figure 2.10: Total error between BRW simulation and PDE approximation depending on the number of BRW agents. **(a)** Total mean location error $E_\mu = \sum_{t_i} |\mu_{BRW}(t_i) - \mu_{PDE}(t_i)|$ **(b)** Total standard deviation error $E_\sigma = \sum_{t_i} |\sigma_{BRW}(t_i) - \sigma_{PDE}(t_i)|$.

2.3 Correlated Random Walk (CRW)

The URWs and BRWs are purely Markovian, in that the probability of moving in a particular direction does not require any information outside of an agent's current state. However, realistic portrayal of certain phenomena may also require knowledge of an agent's current heading. For example, Eschericia coli (E. coli) have flagella that can turn the bacterium clockwise or counter-clockwise. When the flagella turns clockwise, then the E. coli swims foreward. However, when the flagella turns counter-clockwise, then the E. coli tumbles, reorienting itself [63]. Even a BRW cannot naturally account for the turning rate. However, there is a type of RW, called a correlated random walk (CRW) or persistent RW, where an agent continues to move forward until a stochastic switch causes the agent to turn. Although CRWs are not featured in subsequent chapters of this dissertation, we mention them here for completeness.

2.3.1 Analytical Approximation

We develop a global approximation of the pdf of a CRW according to the method used in [29]. Suppose we have a 1-d CRW. Denote $U^+(x,t)$ and $U^-(x,t)$ the probability an agent is moving right or left, respectively, and is at location x at time t. Then $U(x,t) = U^+(x,t) + U^-(x,t)$ is the probability an agent is at location x at time t, regardless of movement heading. Further, we assume that the turning rates are Poisson processes, and are denoted as λ^+ and λ^- when initially moving right or left, respectively.

We first define the difference equation for right moving agents. The density of agents

that change direction from left to right during the time interval $[t, t+\triangle t)$ is $\lambda^- \triangle t$. Moreover, the proportion of agents that continue moving right during that same time interval is $1 - \lambda^+ \triangle t$. Thus, the difference equation for right moving agents is:

$$U^+(x, t+\triangle t) = (1 - \lambda^+ \triangle t) U^+(x - \triangle x, t) + \lambda^- \triangle t U^-(x - \triangle x, t).$$

Assuming $U^+ \in \mathcal{C}^2(\mathbb{R}, [0, \infty))$, expanding in a Taylor series and simplifying gives us the PDE

$$\frac{\partial U^+}{\partial t} + \frac{\triangle x}{\triangle t} \frac{\partial U^+}{\partial x} = \lambda^- U^- - \lambda^+ U^+ + \mathcal{O}(\triangle t, \triangle x^2).$$

Next, we can follow the same logic to derive the difference equation for left moving agents:

$$U^-(x, t+\triangle t) = (1 - \lambda^- \triangle t) U^-(x + \triangle x, t) + \lambda^+ \triangle t U^+(x + \triangle x, t).$$

By expanding in a Taylor series, we have the continuum PDE,

$$\frac{\partial U^-}{\partial t} - \frac{\triangle x}{\triangle t} \frac{\partial U^-}{\partial x} = \lambda^+ U^+ - \lambda^- U^- + \mathcal{O}(\triangle t, \triangle x^2),$$

describing the movement of left-moving agents. Using the same asymptotic argument as in Section 2.1.1 that $0 < \triangle x, \triangle t \ll 1$, we obtain the following hyperbolic PDE system to describe the 1-d CRW:

$$\begin{cases} \frac{\partial U^+}{\partial t} + v \frac{\partial U^+}{\partial x} = \lambda^- U^- - \lambda^+ U^+, \\ \frac{\partial U^-}{\partial t} - v \frac{\partial U^-}{\partial x} = \lambda^+ U^+ - \lambda^- U^-, \end{cases} \tag{2.15}$$

where $v = \frac{\triangle x}{\triangle t}$, the agent's speed.

2.3.2 Similarity to Previous Derivations

For the 1-d case where $\lambda^+ = \lambda^-$, we can perform simplifying arithmetic on the system of equations in (2.15) to solve for $U(x,t) = U^+(x,t) + U^-(x,t)$ as:

$$\frac{\partial^2 U}{\partial t^2} + 2\lambda \frac{\partial U}{\partial t} = v^2 \frac{\partial^2 U}{\partial x^2}, \tag{2.16}$$

a type of Telegrapher's equation. In general, for more heterogeneous turning rates or in higher dimensions, finding a single PDE to define the CRW is intractable. In those cases, we would have to solve a system of high-order hyperbolic PDEs.

In this case, the turning rate is equal in each direction. So this model is similar to an URW. However, it appears that Eq. (2.16) is wholly different than (2.3), especially considering the former is a hyperbolic equation, whereas the latter is a parabolic equation.

We can expand the left-hand side of the difference equation (2.2) to include the second-order time derivative,

$$\begin{aligned} &U + \triangle t\frac{\partial U}{\partial t} + \frac{\triangle t^2}{2}\frac{\partial^2 U}{\partial t^2} = \\ &\frac{1}{2}\left[U + \triangle x\frac{\partial U}{\partial x} + \frac{\triangle x^2}{2}\frac{\partial^2 U}{\partial x^2}\right] + \frac{1}{2}\left[U - \triangle x\frac{\partial U}{\partial x} + \frac{\triangle x^2}{2}\frac{\partial^2 U}{\partial x^2}\right] + \mathcal{O}(\triangle x^3, \triangle t^3). \end{aligned} \tag{2.17}$$

Rearranging the terms of (2.17) and dividing by $\triangle t^2/2$ yields the PDE

$$\frac{\partial^2 U}{\partial t^2} + \frac{2}{\triangle t}\frac{\partial U}{\partial t} = \frac{\triangle x^2}{\triangle t^2}\frac{\partial^2 U}{\partial x^2} + \mathcal{O}(\triangle x^3, \triangle t). \tag{2.18}$$

We see that Eq. 2.18 is the same as Eq. 2.16 with turning rate $1/\triangle t$ and velocity $\triangle x/\triangle t$.

We can also see that rearranging terms of (2.17) and dividing by $\triangle t$ yields

$$\frac{\triangle t}{2}\frac{\partial^2 U}{\partial t^2} + \frac{\partial U}{\partial t} = \frac{\triangle x^2}{2\triangle t}\frac{\partial^2 U}{\partial x^2}. \tag{2.19}$$

The particular RW regular asymptotic solution depends on the order of the coefficient $\triangle x/\triangle t$. If $\triangle x/\triangle t = \mathcal{O}(\triangle t)$, then

$$U(x,t) \approx G(x - x_0, t) - \varepsilon \int_0^t \int_{\mathbb{R}} G(x - y, t - s)\frac{\partial^2 G}{\partial t^2}(y - x_0, s)\, dy\, ds$$

is the asymptotic solution, where it solves the diffusion equation at leading order with a 2nd order time derivative correction term. The function $G(x,t)$ is the fundamental solution to the diffusion equation as derived in Appendix A.1.2. However, if $\triangle x/\triangle t = \mathcal{O}(1)$, then the asymptotic solution is

$$U(x,t) \approx \delta(x - x_0) + \varepsilon v^2 \frac{\partial^2 \delta(x - x_0)}{\partial x^2} t.$$

Since the solution does not represent the model behavior for $\varepsilon \ll 1$, it demonstrates that considering the parameter regime is important for developing a reasonable model. These solutions are derived in Appendix A.3.

Hyperbolic PDEs have finite wave-speed, which matches the physical limitations of early-time RW dynamics. However, some parabolic PDEs (such as the advection-diffusion equation), which are often easier to solve, have infinite wave speeds that can approximate later-time RW dynamics after sufficient spread has occurred. Work has been done to determine how and when one can approximate systems of hyperbolic PDE models of CRWs as a single parabolic advection-diffusion equation [54, 123]. Now that we have an understanding about RWs and their PDE approximations, the next section contains an overview of AB model state changes.

Chapter 3

State Changes

We denote the amalgam of specific properties and behaviors belonging to an agent as a particular state. To model realistic dynamics, it is not sufficient to simply initialize an agent in a particular state; there must be possible mechanisms during the simulation for an agent to change state. Undergoing such a process can change the mobility and interactions of an agent. It can also change an agent's internal processes, such as the rate of resource consumption [60, 99]. State transitions can be a consequence of: random mutation, interactions between an agent and the environment (agent-environment), interactions between agents (agent-agent), or an agent's internal machinations. State changes can be deterministic, such as waiting for a specific length of time, or they can be stochastic, such as a probabilistic contact tolerance. Section 3.3 provides an example of the latter.

From a certain perspective, the correlated random walk (CRW) model analyzed in Section 2.3 could be perceived as a two-state system, where the state is the direction of movement. There, the state change is due to a probabilistic turning parameter. Other examples of models that simulate state changes are: epidemiological models [121, 138], cell taxis (based on the number of available receptor binding sites) [92], animal movement [64], and cellular chemical absorption [139]. The latter example is the focus of Chapters 5-7.

States are often described as being a discrete set of possible agent properties or behaviors, but they can also be defined on a continuum scale. Discrete states are useful when a model compartmentalizes behavior, such as an epidemic model, where the infected agents may act completely different than susceptible agents. The well-mixed epidemic ordinary differential equation model is well-known [80]. However, adapting such a model to an agent-based (AB) model, it is natural to define an agent as having one of three states: susceptible ($\mathcal{S}$), infected ($\mathcal{I}$), or recovered ($\mathcal{R}$) [61, 108, 133]. Continuum states are useful when a state refers to internal dynamics, where those properties influence an agent's behavior on a continuum [54].

The random walk (RW) models of Chapter 2 only consisted of an agent and fixed rules for motion. Now we are discussing more intricate AB models, where the agent's properties or behavior can change in time due to encoded transition rules. As these AB models increase in complexity, we require precise notation to detail an agent's actions and

responses in an exacting manner.

3.1 State Change Notation

We first need to create a precise definition of the properties of the agents and their interactions in order to determine the correct governing equations and hence be able to mathematically analyze the model. We define a bounded region of interest Ω in which we track the agents. We suppose that we have a finite collection, $\mathcal{X}$, of N agents indexed by $1, 2, \ldots, N$. At every time $t \geq 0$ in the simulation, each agent k is assigned to a particular location $\mathbf{x}_t^k$ and discrete state s_t^k. We denote states as $\mathcal{U}_i$ and define the set containing all possible discrete agent states as the state space $\Sigma = \{\mathcal{U}_1, \mathcal{U}_2, ...\}$, which may have infinite or finite cardinality. That is, for each agent k and time t, we necessitate that $s_t^k = \mathcal{U}_i$ for exactly one state $\mathcal{U}_i \in \Sigma$. In this dissertation, discrete agent states are denoted with calligraphic font (e.g. $\mathcal{U}$, $\mathcal{S}$, etc.) and continuous agent states are denoted by ξ.

The domain, Ω, may be either a graph or network consisting of a discrete set of nodes connected by edges or it may be a continuous, bounded subset of $\mathbb{R}^d$ for some spatial dimension $d \in \mathbb{N}$ (as seen in Fig. 1.1). If Ω is discrete, we say these agents exist on-lattice, where they occur on nodes and travel along the graph edges. Otherwise, if Ω is continuous, we say these agents exist off-lattice. In either case, the agents can either be stationary or move. The model keeps track of individual agents performing a deterministic movement or a RW, governed by a model specific probability distribution over a bounded domain [24, 33, 99]. It is important to note that the scalings and distributions may be spatially, temporally, or state dependent.

An individual-based model is defined by a set of state change rules and a set of interaction neighborhoods, denoted as the pair $\mathcal{A} = (f, \mathcal{N})$. The local transition rule, f, defines how agents transition to other states. The interaction neighborhoods are the areas in which an agent can interact with the environment or other agents. We denote the collection of neighborhoods for each agent as $\mathcal{N} = \left\{\mathcal{N}^1, \mathcal{N}^2, ..., \mathcal{N}^N\right\}$, where $\mathcal{N}^k$ is the neighborhood of agent k [34]. One can visualize the agents and neighborhoods in Fig. 3.1, which are further detailed later in this section. If the model specifies that each neighborhood is temporally or state dependent, we define $\mathcal{N}_t^k$ as the neighborhood of agent k in state s_t^k at iteration t. Since we assume the agents move in time, these neighborhoods are time dependent.

3.1.1 Agent-Environment State Change

Agent-environment state changes require agents to interact with the environment through an interaction region surrounding each agent. The location of an agent $\mathbf{x}_t^k$ is an infinitesimally small point, which is a useful way to track an agent's location but does not represent the physical nature of the agent as it interacts with the environment. To this end, we endow each agent with a neighborhood, $\mathcal{N}_t^k$, that has non-zero area, the geometry of which is model-dependent. If the agent represents a cell, the perimeter of the neighbor-

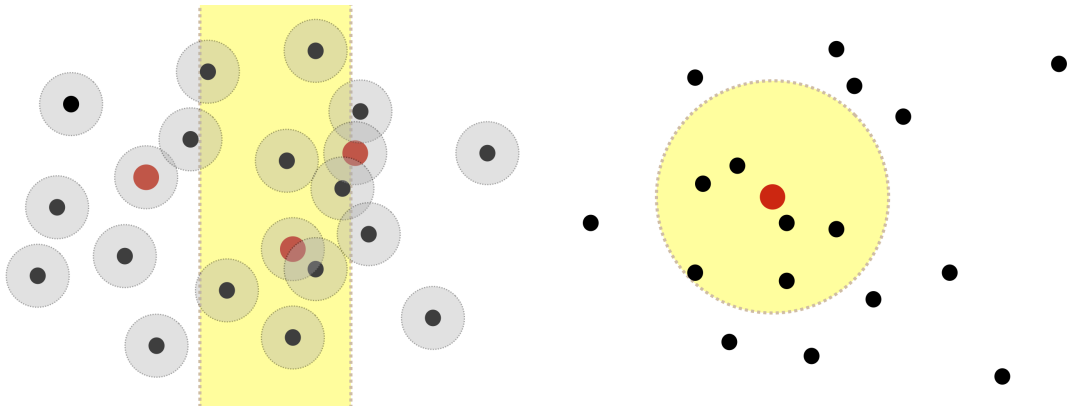

(a) Agent-Environment Transition Region (b) Agent-Agent Transition Region

Figure 3.1: We illustrate examples of a $B_t^{\mathcal{U},\mathcal{V}}$ transition region as the shaded **yellow** region. The solid **red** circle represents an agent in state $\mathcal{V}$ and the solid **black** circles represent agents in state $\mathcal{U}$. The only agents in state $\mathcal{U}$ that have a non-zero probability of transitioning to state $\mathcal{V}$ are located inside the shaded region. Agents outside this yellow region are not in the $B_t^{\mathcal{U},\mathcal{V}}$ transition region and, therefore, cannot transition to state $\mathcal{V}$. **(a)** Example of an agent-environment transition region, where the $B_t^{\mathcal{U},\mathcal{V}}$ depends on the spatial location only and not the agents' locations. The neighborhoods surrounding each agent are **gray** disks. **(b)** Example of an agent-agent transition region, where the $B_t^{\mathcal{U},\mathcal{V}}$ is the shaded **yellow** disk centered at the red agent.

hood could correspond the cell membrane or wall [101]. Whereas, if the agent represents a soldier, the neighborhood could be the agent's field of regard [118]. In some models, the neighborhood shape may be dependent on other factors such as time or an agent's internal state dynamics. In Fig. 3.1a the neighborhoods, $\mathcal{N}_t^k$, are depicted as gray circles.

The local transition rule is a function $f : \mathcal{X} \to \Sigma$, assigning each agent a particular state. Since each agent belongs to one and only one state, the local transition rule f is well-defined. The function assignment $s_{t+1}^k = f(s_t^k)$ depends conditionally on the regions in which the neighborhood $\mathcal{N}_t^k$ is contained. Define $B_t^{\mathcal{U},\mathcal{V}}$ as the $\mathcal{U} \to \mathcal{V}$ agent-environment transition region at time t. That is, $B_t^{\mathcal{U},\mathcal{V}}$ is the region such that if, at time t, there is some agent k such that $s_t^k = \mathcal{U}$ and $\mathcal{N}_t^k \cap B_t^{\mathcal{U},\mathcal{V}} \neq \emptyset$, then agent k can transition to state $\mathcal{V}$ at time $t+1$. In Fig. 3.1a the agent-environment transition region, $B_t^{\mathcal{U},\mathcal{V}}$, is depicted as the yellow region. We formally define the agent-environment transition region as follows:

Definition. The $\mathcal{U} \to \mathcal{V}$ agent-environment transition region at time t is

$$B_t^{\mathcal{U},\mathcal{V}} = \left\{ \mathbf{x} \in \Omega \middle| \, \forall k \text{ such that } 1 \leq k \leq N, s_t^k = \mathcal{U}, \text{ and } \mathbf{x} \in \mathcal{N}_t^k, \text{ then } \mathbb{P}\left(f(s_t^k) = \mathcal{V}\right) > 0 \right\}.$$

3.1.2 Agent-Agent State Change

In some models, agents change states through agent-agent interactions rather than their interaction with the environment. These interactions also occur through neighborhoods, but with subtly different dynamics. Traditional Cellular Automaton (CA) agent-agent state change model definitions define the neighborhood $\mathcal{N}_t^k$ as the region in which other agents exert state changes to agent k. Density analysis has been previously studied using this neighborhood definition [34]. However, since we want to focus on locations of moving individuals that can influence state changes to others in a region, we assert the opposite—$\mathcal{N}_t^j$ is the region in which agent j can exert state changes to other agents (including agent k). Shifting our interpretation of neighborhoods in this way allows us greater freedom to model more realistic state and property-dependent neighborhoods. Define $B_t^{\mathcal{U},\mathcal{V}}$ as the $\mathcal{U} \to \mathcal{V}$ agent-agent transition region at time t. That is, $B_t^{\mathcal{U},\mathcal{V}}$ is the region such that if, at time t, there is some agent k such that $s_t^k = \mathcal{U}$ and $\mathbf{x}_t^k \in B_t^{\mathcal{U},\mathcal{V}}$, then agent k can transition to state $\mathcal{V}$ at time $t+1$. We can formally define the agent-agent transition region in terms of our neighborhoods of influence as follows:

Definition. The $\mathcal{U} \to \mathcal{V}$ agent-agent transition region at time t is

$$B_t^{\mathcal{U},\mathcal{V}} = \bigcup_{j \in \mathcal{A}} \mathcal{N}_t^j,$$

with indexing set

$$\mathcal{A} = \left\{ j \,|\, \exists k \text{ such that } 1 \leq k \leq N, s_t^k = \mathcal{U}, \text{ and } \mathbf{x}_t^k \in \mathcal{N}_t^j, \text{ then } \mathbb{P}\left(f(s_t^k) = \mathcal{V}\right) > 0 \right\}.$$

We define the agent-agent transition region in this way, since, in general, agents in states other than $\mathcal{V}$ can cause agents to transition to state $\mathcal{V}$. Leveraging our new neighborhood perspective in the agent-agent transition region, we require agent k to be located in the neighborhood $\mathcal{N}_t^j$ (for some agent j) in order to change states. Our explicit definition of the transition region $B_t^{\mathcal{U},\mathcal{V}}$ for each $\mathcal{U}, \mathcal{V} \in \Sigma$ allows us to clearly define $f(s_t^k)$. A visual example of an agent-agent transition region can be found in Fig. 3.1b. We are interested in calculating the expected density of agents in a state at each iteration throughout Ω. We denote $W_t(\mathcal{V} \to \mathcal{U})$ to be the transition probability that an agent in state $\mathcal{V}$ at iteration t transitions to state $\mathcal{U}$ at time $t+1$. If the transition probability is fixed in time, then we can ignore the t subscript. We summarize our AB notation in the *List of Symbols*.

3.2 Correlated Random Walk as State Change

We can restate the description of the CRW, introduced in Section 2.3.1, as an AB model with probabilistic state changes. Let $\mathcal{U}^+$ denote the state of an agent moving right and $\mathcal{U}^-$ the state of an agent moving left. Agents in state $\mathcal{U}^+$ move at a constant speed

$v^+ = \triangle x/\triangle t$ to the right, and agents in state $\mathcal{U}^-$ move at a constant speed $v^- = \triangle x/\triangle t$ to the left. The probabilities of an agent changing state are denoted as $W(\mathcal{U}^+ \to \mathcal{U}^-) = \triangle t\lambda^+$ and $W(\mathcal{U}^- \to \mathcal{U}^+) = \triangle t\lambda^-$, where λ^+ (λ^-) is the turning rate of an agent initially traveling to the right (left). Here, W does not have a t subscript since the transition probability is fixed in time. We can then state an equivalent, but notationally different, system of difference equations

$$\begin{aligned} U^+(x, t+\triangle t) &= [1 - W(\mathcal{U}^+ \to \mathcal{U}^-)]U^+(x - v^+\triangle t, t) \\ &\quad + W(\mathcal{U}^- \to \mathcal{U}^+)U^-(x - v^-\triangle t, t), \\ U^-(x, t+\triangle t) &= W(\mathcal{U}^+ \to \mathcal{U}^-)U^+(x + v^+\triangle t, t) \\ &\quad + [1 - W(\mathcal{U}^- \to \mathcal{U}^+)]U^-(x + v^-\triangle t, t). \end{aligned}$$

Using this notation, it is easier to see how we could add more complicated dynamics to a CRW model.

3.3 Probabilistic RW State Changes

3.3.1 Spatial Region for Change

Here, we produce a simple elucidating example of probabilistic state change from an agent-environment interaction, and a global approximation of an agent's pdf in space and time. This model has a live state, $\mathcal{U}$, and a dead state, $\mathcal{V}$. Suppose a single agent in live state $\mathcal{U}$ is performing an URW in a bounded 1-d domain $\Omega = [0, 1]$ with spatial step size $\triangle x$ and time step size $\triangle t$. We implement reflective boundary conditions such that

$$x_t \leftarrow \begin{cases} -x_t & : \text{ if } x_t < 0, \\ 1 - (x_t - 1) & : \text{ if } x_t > 1. \end{cases}$$

Moreover, if the agent is located at x at time t, the agent's neighborhood is the interval centered at x with width $\triangle x/2$. That is, we define $\mathcal{N}_t = (x - \triangle x/2, x + \triangle x/2)$. Since this model has only one agent[1], we do not need to use superscript to denote the index of the particular agent. If the agent's neighborhood intersects with the transition region $B^{\mathcal{U},\mathcal{V}} = [\alpha, \beta] \subset \Omega$ at time t, then the agent has a probability κ of transitioning to the dead state $\mathcal{V}$ during the interval $[t, t + \triangle t)$. That is, the time-independent transition probability is $W(\mathcal{U} \to \mathcal{V}) = \kappa \in [0, 1]$. For this example, we are not interested in agents in state $\mathcal{V}$, so we can assume that agents in state $\mathcal{V}$ exit the simulation.

Although this model includes more complex dynamics than an URW, it is clear that this AB model is still Markovian. As such, we can use a process similar to that detailed in Section 2.1.1 to find a global approximation of this model. Denote $U(x, t)$ the probability the agent is alive and centered at location x at time t. To develop a continuum equation,

[1] The model itself depicts only one agent. However, statistical measures are acquired when the AB model is run over multiple realizations.

we construct a difference equation similar to that in Eq. (2.1), but with the addition of a sink term denoting agent death. If the agent dies, it must be in the subregion $B^{\mathcal{U},\mathcal{V}} \subset \Omega$ and the simulation must draw a random variable $X \sim \mathit{Uniform}(0,1)$ such that $X < \kappa$. We represent this dynamic with the expression $\mathbf{1}_{B^{\mathcal{U},\mathcal{V}}}(x)\kappa U(x,t)$, where

$$\mathbf{1}_{B^{\mathcal{U},\mathcal{V}}}(x) = \begin{cases} 1 & : \text{ if } x \in B^{\mathcal{U},\mathcal{V}} \\ 0 & : \text{ otherwise} \end{cases}$$

denotes the indicator function. We can make the simplifying assumption that the indicator function only depends on x (and not the neighborhood interval) since the neighborhood interval width is half the spatial step-size. Thus, the difference equation is:

$$U(x, t+\triangle t) = \frac{1}{2}U(x-\triangle x, t) + \frac{1}{2}U(x+\triangle x, t) - \mathbf{1}_{B^{\mathcal{U},\mathcal{V}}}(x)\kappa U(x,t). \tag{3.1}$$

Expanding in a Taylor series and simplifying gives us

$$\frac{\partial U}{\partial t} = \frac{\triangle x^2}{2\triangle t}\frac{\partial^2 U}{\partial x^2} - \mathbf{1}_{B^{\mathcal{U},\mathcal{V}}}(x)\frac{\kappa}{\triangle t}U(x,t) + \mathcal{O}(\triangle x^3, \triangle t). \tag{3.2}$$

Using the asymptotic argument that $0 < \triangle x, \triangle t \ll 1$, we define the diffusion parameter $D = \frac{\triangle x^2}{2\triangle t}$ and state change proportion parameter $q(x) = \mathbf{1}_{B^{\mathcal{U},\mathcal{V}}}(x)\frac{\kappa}{\triangle t}$ to obtain the pdf that the agent is alive and at location x at time t:

$$\frac{\partial U}{\partial t} = D\frac{\partial^2 U}{\partial x^2} - q(x)U. \tag{3.3}$$

Note that Eq. (3.3) is a reaction-diffusion PDE.

Assuming the agent is initialized at location x_0, the PDE system that we solve is:

$$\begin{cases} \frac{\partial U}{\partial t} = D\frac{\partial^2 U}{\partial x^2} - q(x)U, & x \in (0,1),\ t > 0, \\ U = \delta(x - x_0), & x \in [0,1],\ t = 0, \\ \frac{\partial U}{\partial x} = 0, & x \in \{0,1\},\ t > 0. \end{cases} \tag{3.4}$$

We can also solve for the probability an agent is in the live state at time t by $p(t) = \int_\Omega U(x,t)\,dx$.

We compare example simulations of the AB model and PDE approximation in Figs. 3.2(a)-(b) and 3.2(c)-(d) for initial location, $x_0 = 0.40$ and $x_0 = 0.65$, and transition probabilities, $\kappa = 0.25$ and $\kappa = 0.2$, respectively. In both cases we perform 10^5 realizations of the single agent AB model. Agents are initialized at location x_0 and perform an URW with step size $\triangle x = 0.01$, $\triangle t = \triangle x^2$. The transition region is the interval $B^{\mathcal{U},\mathcal{V}} = [0.4, 0.6]$. In either case the behavior is similar, even though differences in the magnitudes may be off due to the lack of waiting time. Note that agents outside of $B^{\mathcal{U},\mathcal{V}}$ diffuse like an URW, but agents in $B^{\mathcal{U},\mathcal{V}}$ tend to change state after sufficiently many iterations. In fact, given the relative size of the spatial step to the transition region width, $\triangle x/0.2 = 0.05$ and transition probability $\kappa = 0.25$, no agent survives diffusion to the other edge of the transition region $B^{\mathcal{U},\mathcal{V}}$.

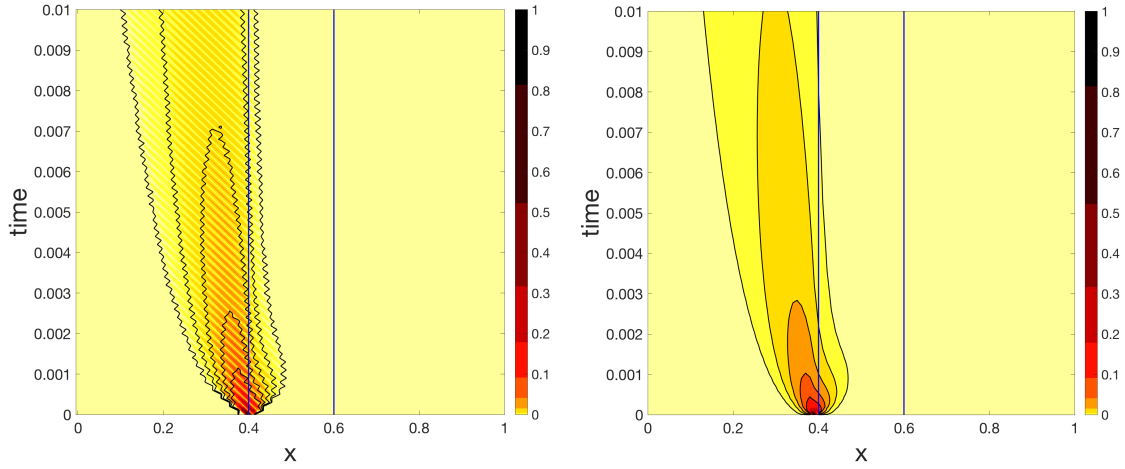

(a) AB Model Density
($x_0 = 0.40$, $\kappa = 0.25$)

(b) PDE Density
($x_0 = 0.40$, $\kappa = 0.25$)

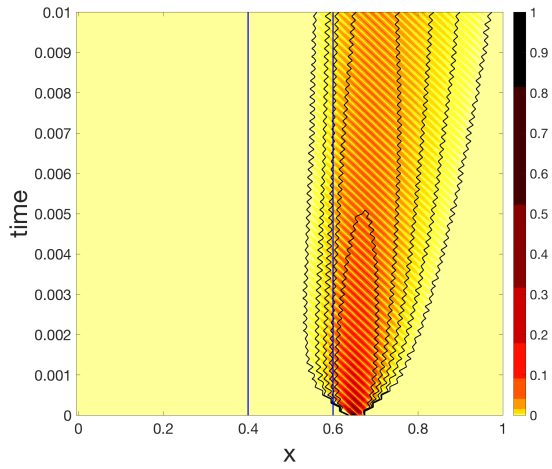

(c) AB Model Density
($x_0 = 0.65$, $\kappa = 0.20$)

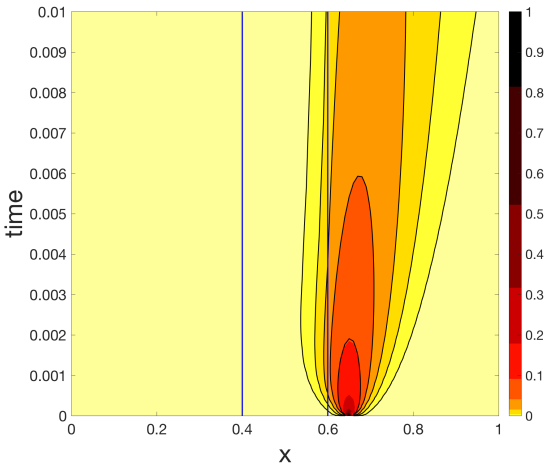

(d) PDE Density
($x_0 = 0.65$, $\kappa = 0.20$)

Figure 3.2: Comparison of AB model histogram and PDE solution of state $\mathcal{U}$ in space and time. AB model is average of 10^5 realizations. Agents are initialized in state $\mathcal{U}$ at x_0 and move according to an URW with step size $\triangle x = 0.01$, $\triangle t = \triangle x^2$ and free-space boundary conditions. The agent-environment interaction region is the interval $B^{\mathcal{U},\mathcal{V}} = [0.4, 0.6]$ and its boundaries are depicted in the graphs as **blue** lines. Agents in $B^{\mathcal{U},\mathcal{V}}$ change state with probability κ. Contour lines denote the same surface height for AB model (left) and PDE (right) graphs.

3.3.2 Moving Region for Change

We can develop the pdf for the above model in the case that the state-transition region $B^{\mathcal{U},\mathcal{V}}$ changes in time. Thus, rather than have $B^{\mathcal{U},\mathcal{V}}$ be a fixed interval, we denote the state-transition region as the time-dependent function $B_t^{\mathcal{U},\mathcal{V}}$. Our PDE system is generally

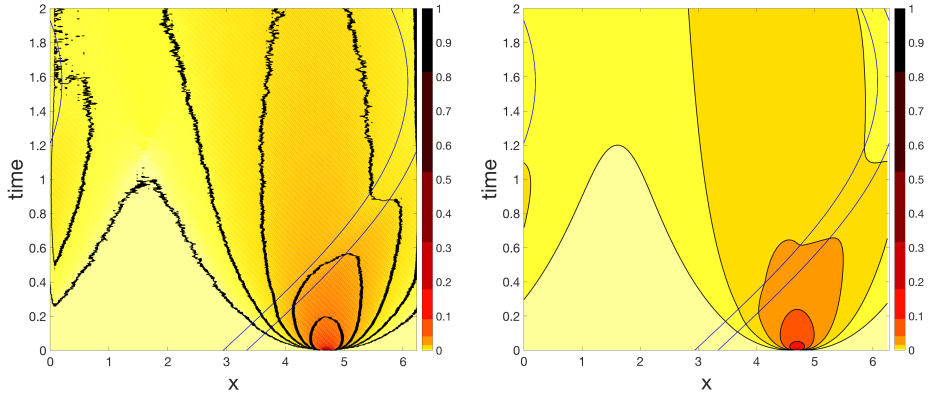

(a) AB Model Density
($x_0 = 3\pi/2$)

(b) PDE Density
($x_0 = 3\pi/2$)

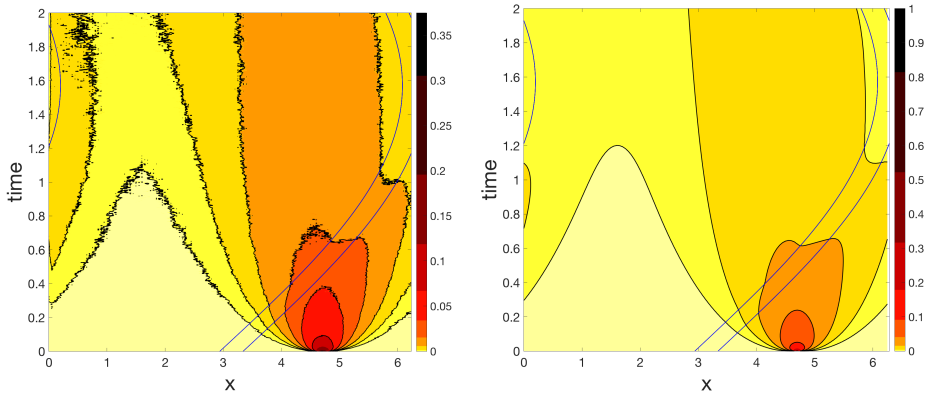

(c) AB Model Density
($x_0 \sim N(3\pi/2, \triangle x)$)

(d) PDE Density
($x_0 \sim N(3\pi/2, \triangle x)$)

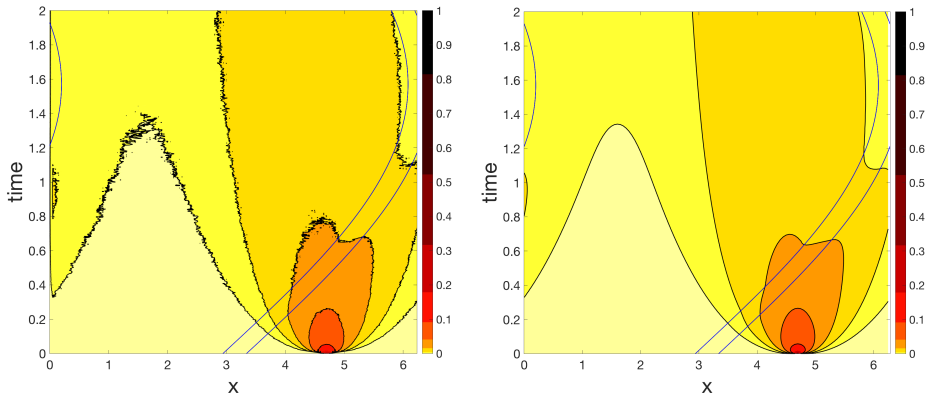

(e) AB Model Density
($x_0 = 3\pi/2$, $\ell = r = 0.45$)

(f) PDE Density
($x_0 = 3\pi/2$, $\ell = r = 0.45$)

Figure 3.3: Comparing AB model density with PDE approximation with a moving transition region, $B_t^{\mathcal{U},\mathcal{V}}$ (denoted by **blue** lines). AB model is an average of 10^5 realizations. Agents initialize at x_0 and move according to an URW with step size $\triangle x = 0.05$, $\triangle t = \triangle x^2$ and periodic boundary conditions. Agents in $B_t^{\mathcal{U},\mathcal{V}}$ transition with probability κ.

of the form:

$$\begin{cases} \frac{\partial U}{\partial t} = D\frac{\partial^2 U}{\partial x^2} - q(x,t)U, & x \in (0, 2\pi),\ t > 0, \\ U = \delta(x - x_0), & x \in [0, 2\pi],\ t = 0, \end{cases} \tag{3.5}$$

where $q(x,t) = \mathbf{1}_{B_t^{\mathcal{U},\mathcal{V}}}(x)\frac{\kappa}{\triangle t}$ and boundary conditions are model-dependent.

For an example, suppose that the agent-environment transition region is a time-dependent interval of length 0.4 centered at $\pi(\sin(t) + 1)$. That is, $B_t^{\mathcal{U},\mathcal{V}} = [\pi(\sin(t) + 1) - 0.2, \pi(\sin(t) + 1) + 0.2]$. The agent then has a probability κ of transitioning to state $\mathcal{V}$ during the interval $[t, t + \triangle t)$. Just like Section 3.3.1, an agent in $B_t^{\mathcal{U},\mathcal{V}}$ has probability κ of transitioning to state $\mathcal{V}$ during the interval $[t, t + \triangle t]$. We add periodic boundary conditions, so agents exiting one end of the simulation enter the other

$$U(0,t) = U(2\pi,t), \qquad t > 0.$$

In Fig. 3.3(a)-(b), the URW simulation's lack of smoothness affects the shape of the solution more than previously. This is especially due to the jump discontinuity between being in and out of the transition region. Note that the boundary of $B_t^{\mathcal{U},\mathcal{V}}$ is denoted by blue lines in the figures. For comparison, in Fig. 3.3(c)-(d) we initialize the agents with locations drawn from a normal distribution with mean $3\pi/2$ and standard deviation $\triangle x$. We see a smoother RW solution surface, with behavior (solution surface shape) that appears similar to the PDE model. We further compared the RW model and PDE approximation in Fig. 3.3(e)-(f), where the movement probability of RW agents are $\ell = 0.45$ and $r = 0.45$. The agents have equal probability of moving left or right, but now there is a probability of 0.1 that an agent remains in the same location. This waiting time smooths the RW histogram sufficiently for a clear comparison with the PDE solution in terms of both solution surface shape and magnitude.

3.3.3 Internal State Changes Biasing Movement

We characterize internal state changes differently than the previously detailed state changes, since they are usually on a continuum scale and may affect agent behavior along a continuum. Internal state changes can affect movement. For example, the turning parameter of CRW approximations can depend on the agent's internal state. Some examples of this behavior in E. coli and foraging models can be found in [102, 54, 43]. Additionally, internal state changes can directly cause external discrete state transitions. A cell immersed in a chemical bath may die if the cell absorbs chemical above a specific tolerance [88]. In this case, the internal state change is the cumulative absorption amount and the external states are live or dead. We examine this model in further detail in Chapter 5. Chapters 2 and 3 provide the relevant theoretical background and notation for us to further contribute to this mathematical field of developing global approximations of AB models in subsequent chapters.

Chapter 4

Global Recurrence Rule

The focus of this Chapter is providing an introduction of a new[1] theoretical formalism and subsequent analysis of an off-lattice AB model where agents exhibit stochastic behavior when moving and changing states through agent-agent neighborhood interactions. The analysis of the off-lattice AB model relies heavily on a precise definition of the interaction neighborhoods between agents. In contrast to other, more traditional approaches [34], we view the interaction neighborhood as a region where an agent potentially exerts state changes to other agents. Specifically, the necessary notation for the AB model is outlined in Section 3.1, which is similar to previous work on Cellular Automaton[2] (CA) models [34, 59]. In Section 4.1, we detail how to derive a Global Recurrence Rule (GRR) to determine the expected value for the number of agents in each state when assuming that an agent's state and movement are solely determined by the agent's current status. To show the applicability of this formalism, in Section 4.2, we illustrate how a GRR can be derived for an Epidemiological-AB (E-AB) model that captures the spread of an infection such as influenza or COVID-19 (Novel Coronavirus). In addition, we illustrate with the E-AB how to use additional information about the dynamics to develop a more refined local approximation of the neighborhoods, with reduced error. In Section 4.2.5, we compare the different models and emphasize which assumptions need to be satisfied in order for the GRR to be a valid approximation for the E-AB model.

4.1 Global Recurrence Rule Defined

With the notation developed in Chapter 3 and some basic probability theory, we have the necessary background material to derive the expected density of agents in a state at any given time. The state of an agent k at time $t+1$ only depends on its state (s_t^k) and location ($\mathbf{x}_t^k$) at time t, making this a Markovian process [23]. Recall that the probability an agent transitions from state $\mathcal{V}$ to state $\mathcal{U}$ at time t is denoted as $W_t(\mathcal{V} \to \mathcal{U})$. Hence,

[1] We recently published portions of this work in [138].

[2] CA models are a sub-category of AB models, where the agents are generally fixed in a discrete space and the state changes of an agent are generally determined based on the states of the neighboring agents.

the probability that agent k is in state $\mathcal{U}$ at time $t+1$ given that the agent was in state $\mathcal{V}$ at time t reduces to

$$\mathbb{P}\left(s_{t+1}^k = \mathcal{U} \middle| s_t^k = \mathcal{V}\right) = \mathbb{P}\left(\mathbf{x}_t^k \in B_t^{\mathcal{V},\mathcal{U}}\right) W_t(\mathcal{V} \to \mathcal{U}), \tag{4.1}$$

the product of the probability that agent k is located in a $\mathcal{V} \to \mathcal{U}$ transition region with the probability that agent k transitions from state $\mathcal{V}$ to state $\mathcal{U}$. The equality in 4.1 is what allows our GRR derivation to link global densities with local rules.

The discrete random variable denoting the number of agents in state $\mathcal{U}$ at time t is U_t. We can then find $\mathbb{E}(U_{t+1})$, the expected number of agents in state $\mathcal{U}$ at iteration $t+1$, by

$$\mathbb{E}(U_{t+1}) = \mathbb{E}\left(\left|\{k : s_{t+1}^k = \mathcal{U}\}\right|\right) \tag{4.2}$$

$$= \sum_{k=1}^{N} \mathbb{P}\left(s_{t+1}^k = \mathcal{U}\right) \tag{4.3}$$

The first equality is by definition of U_{t+1}, and the second equality is by definition of expected value. Note that we can partition the collection of agents $\mathcal{X}$ by the distinct states in Σ. That is, we can change the summation over all the agents into a double summation over all the states and every agent in each state. In order for the double summation to make sense, we use the Bayesian property to rewrite the summed probability in terms of a prior state $\mathcal{V}$:

$$\sum_{k=1}^{N} \mathbb{P}\left(s_{t+1}^k = \mathcal{U}\right) = \sum_{\mathcal{V}\in\Sigma} \sum_{\{k:s_t^k=\mathcal{V}\}} \mathbb{P}\left(s_{t+1}^k = \mathcal{U} \middle| s_t^k = \mathcal{V}\right) \tag{4.4}$$

$$= \sum_{\mathcal{V}\in\Sigma} \sum_{\{k:s_t^k=\mathcal{V}\}} \mathbb{P}\left(\mathbf{x}_t^k \in B_t^{\mathcal{V},\mathcal{U}}\right) W_t(\mathcal{V} \to \mathcal{U}). \tag{4.5}$$

Finally, from Eq. (4.1), we replace the conditional probability that an agent is in state $\mathcal{U}$ given that the agent was in state $\mathcal{V}$ at the prior time-step, $\mathbb{P}\left(s_{t+1}^k = \mathcal{U} \middle| s_t^k = \mathcal{V}\right)$, with the local mechanism for the state change to occur. We can see in the derivation a transition from the global model view of (4.2) to the local model view of (4.5). In the global view we treat U_{t+1} as a random variable from an unknown underlying probability distribution, on which we perform a mean approximation over all the finitely many agents. However, in the local view we acknowledge the states and properties of individual agents as well as the local dynamics which allow state changes. This leads us to the definition of the GRR.

Definition. Let $\mathcal{U}, \mathcal{V} \in \Sigma, U_t = |\{k : s_t^k = \mathcal{U}\}|$, and $B_t^{\mathcal{V},\mathcal{U}}$ be the $\mathcal{V} \to \mathcal{U}$ transition region at time t. We define the Global Recurrence Rule (GRR) as

$$\mathbb{E}(U_{t+1}) = \sum_{\mathcal{V}\in\Sigma} \sum_{\{k:s_t^k=\mathcal{V}\}} \mathbb{P}\left(\mathbf{x}_t^k \in B_t^{\mathcal{V},\mathcal{U}}\right) W_t(\mathcal{V} \to \mathcal{U}).$$

Thus, to find expected values of the number of agents in each state analytically, one just needs a framework to calculate both the probability of being in a transition region, $B_t^{\mathcal{V},\mathcal{U}}$, as well as the probability that an agent in the transition neighborhood can transition to a particular state, $W_t(\mathcal{V} \to \mathcal{U})$. These probabilities are model-dependent, since they provide the GRR with the specific model dynamics. In the following section, we use this framework with an epidemiological agent-based (E-AB) model to elucidate its usefulness as well as certain challenges that may arise when deriving a GRR.

4.2 Application to Disease Dynamics

Disease dynamics provides an interesting application to determine the validity of the GRR. Assume there are infected individuals in a population. For simplicity, we can divide the remaining population into two classes, those who are susceptible to infection and those who were infected but cannot currently infect other individuals. We denote these classes "susceptible" and "recovered," respectively. Further, suppose that after a finite time the recovered can become susceptible to infection again. That is, an individual in the recovered state is temporarily conferred immunity before returning to the susceptible state. This is often referred to as a Susceptible-Infected-Recovered (SIR) Epidemiological model, where simulations and analysis have been an active research area for many years [61, 108, 133], especially with respect to endemic equilibrium sizes [81, 86, 134] and infectivity wave speed [49, 83].

In terms of the AB framework presented in Section 3.1, it is relatively straightforward to implement an E-AB model. There are only three states: $\mathcal{S}$ (susceptible), $\mathcal{I}$ (infected), and $\mathcal{R}$ (recovered). In addition, the only agent-agent state change is when susceptible agents are near infected agents. Thus, the only neighborhoods of interest are those belonging to the infected agents since only infected agents, within a fixed distance, can influence the state change of susceptible agents. All other state changes are either probabilistic or time-dependent.

4.2.1 Epidemiological Agent-Based (E-AB) Model

To simplify, we let the continuous domain, Ω, of the E-AB be the unit square. The agents remain in the infected and recovered states for T_i and T_R iterations, respectively. Thus, our state space for the E-AB is $\Sigma = \{\mathcal{S}, \mathcal{I}_1, \mathcal{I}_2, ..., \mathcal{I}_{T_I}, \mathcal{R}_1, \mathcal{R}_2, ..., \mathcal{R}_{T_R}\}$. This dynamic is also referred to as an $SI^{T_I}R^{T_R}$ model [81].

We initialize N agents in Ω such that $N-1$ agents are in state $\mathcal{S}$ ($S_0 = N-1$) and one agent is in state $\mathcal{I}_1$ ($I_0 = 1$), where $S_t = |\{k : s_t^k = \mathcal{S}\}|$ and $I_t = \cup_{j=1}^{T_I} |\{k : s_t^k = \mathcal{I}_j\}|$ for each time t. We index the initially infected agent as $k = 1$ and initialize its location in the center of the region Ω. The susceptible agents are randomly initialized following a uniform random distribution (i.e. $\mathbf{x}_0^k \sim \mathit{Uniform}(\Omega)$ for $k = 2, 3, \ldots, N$).

Each agent[3] moves by an unbiased random walk (URW) inside Ω. If $\mathbf{x}_t^k = (x, y)$, then

[3] For simplicity, every agent in this model moves according to the same rules. However, one could

$\mathbf{x}_{t+1}^k = (x + \triangle r \cos\theta, y + \triangle r \sin\theta)$, where $\theta \sim$ *Uniform* $[0, 2\pi)$ and $\triangle r \ll 1$ is the constant radial spatial step. A simple reflective boundary condition is enforced along $\partial\Omega$. If an agent hits the boundary (or is about to move outside of Ω), it is shifted a distance $\triangle r$ into Ω along the direction normal to the boundary. That is, $\mathbf{x}_t^k = \left(\hat{x} + \triangle r \cos\hat{\theta}, \hat{y} + \triangle r \sin\hat{\theta}\right)$, where $(\hat{x}, \hat{y})$ is the point the agent would have crossed along the boundary and $\hat{\theta}$ is the direction normal to the boundary at that point.

For our E-AB, we assume that the infectivity neighborhood of any infected agent k is radially symmetric with radius ρ_0. That is, $\mathcal{N}_t^k = \left\{\mathbf{y} \in \Omega : ||\mathbf{y} - \mathbf{x}_t^k||_2 \leq \rho_0\right\}$, the collection of all points of a distance less than ρ_0 away from agent k, is the area in which susceptible agents can become infected by agent k.

Now consider any agent k such that $s_t^k = \mathcal{S}$. In order for agent k to become infected, we require $\mathbf{x}_t^k$ to be in an infected neighborhood, regardless of the iteration of infectivity (i.e. $\mathcal{I}_1, \mathcal{I}_2, \ldots, \mathcal{I}_{T_I}$). We define the $\mathcal{S} \to \mathcal{I}_1$ transition region as $B_t^{\mathcal{S},\mathcal{I}_1} = \bigcup_{\{k:s_t^k=\mathcal{I}_j, \exists j\}} \mathcal{N}_t^k$. Recall that the $\mathcal{S}$ to $\mathcal{I}_1$ transition region is the region in which an agent in state $\mathcal{S}$ can transition to state $\mathcal{I}_1$. The susceptible agent has the potential to become infected when in at least one neighborhood of an infected agent at any state of the infection (for $j = 1, \ldots, T_I$). In this simple E-AB model, the number of infectivity neighborhoods in which agent k is located does not affect the probability of agent k being infected. The susceptible agents located inside $B_t^{\mathcal{S},\mathcal{I}_1}$ become infected with probability $1 - \kappa$, where $\kappa \in [0, 1]$ is the contact tolerance. For simplification, we assume that ρ_0 and κ are scalar constants[4] and the transition rules between states are given below.

Definition. The local transition rule $f : \mathcal{X} \to \Sigma$, such that $s_{t+1}^k = f(s_t^k)$ is given as follows:

$$\text{If } s_t^k = \mathcal{S}: \quad f(s_t^k) = \begin{cases} \mathcal{I}_1 & : \text{ if } \mathbf{x}_t^k \in B_t^{\mathcal{S},\mathcal{I}_1} \text{ and } \kappa > X, \text{ where } X \sim \textit{Uniform}\,[0,1], \\ \mathcal{S} & : \text{otherwise,} \end{cases} \tag{4.6}$$

$$\text{If } s_t^k = \mathcal{I}_j, \text{ for some } j = 1, 2, ..., T_I: \quad f(s_t^k) = \begin{cases} \mathcal{I}_{j+1} & : \text{ if } 1 \leq j < T_I, \\ \mathcal{R}_1 & : \text{ if } j = T_I, \end{cases} \tag{4.7}$$

$$\text{If } s_t^k = \mathcal{R}_m, \text{ for some } m = 1, 2, ..., T_R: \quad f(s_t^k) = \begin{cases} \mathcal{R}_{m+1} & : \text{ if } 1 \leq m < T_R, \\ \mathcal{S} & : \text{ if } m = T_R. \end{cases} \tag{4.8}$$

Recall from Section 3.1 that $\mathcal{X}$ is the collection of agents and Σ is the collection of states. Thus, the local transition rule, f, assigns each agent to a particular state at each iteration.

Figure 4.1 illustrates the off-lattice E-AB simulation as outlined above using $N = 10^4$ agents, where the susceptible, infected, and recovered agents are colored as black, red, and blue, respectively. We implemented each iteration by first determining the region

produce a model where each state moves differently. For example, the infected agents could move at a larger or smaller spatial step than the susceptible or recovered agents due to the disease's effect on the territoriality or the physicality of the infected agent [45, 51].

[4] Our E-AB is a toy example to demonstrate the efficacy of the GRR. For simplification, ρ_0 and κ are constants. In practice, ρ_0 and κ should be random variables drawn from specific probability distributions, such as the models found in [80].

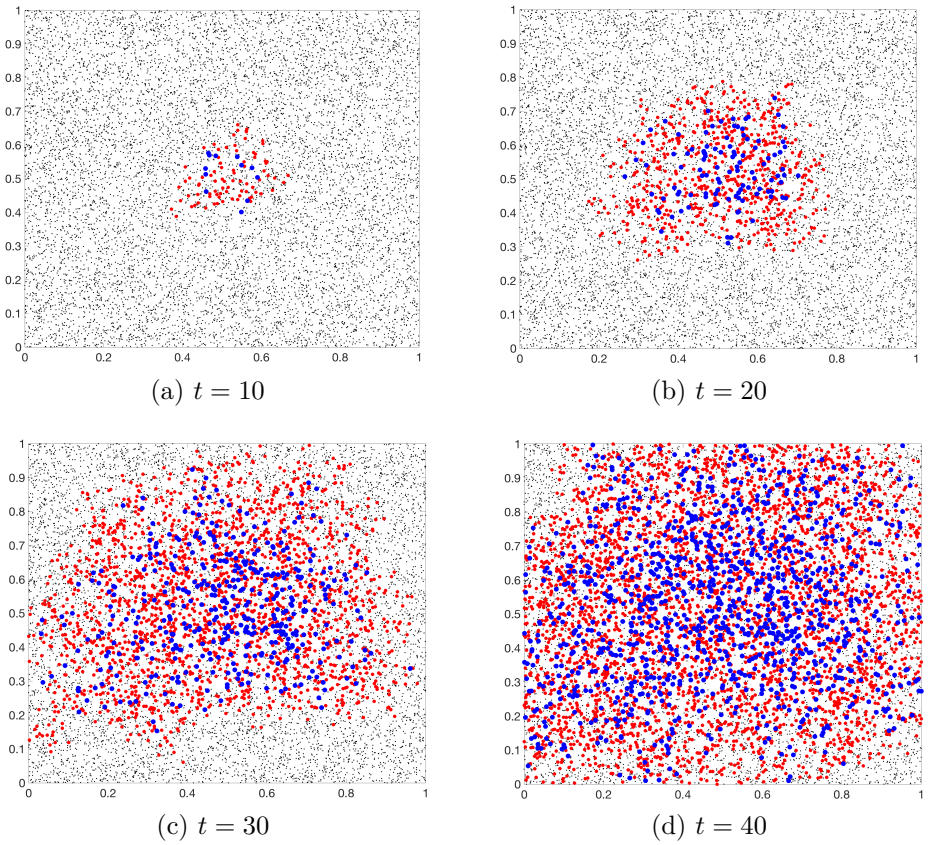

(a) $t = 10$ (b) $t = 20$

(c) $t = 30$ (d) $t = 40$

Figure 4.1: Simulation of 10^4 agents at various time steps with a single agent infected initially, which is located at (0.5,0.5). The states are denoted as ■ Susceptible, ■ Infected, ■ Recovered. The simulation parameters are defined as: contact tolerance = $\kappa = 0.95$, infectivity radius = $\rho_0 = 0.04$, infection time = $T_I = 30$, recovered time = $T_R = 30$, and spatial step = $\triangle r = 0.001$. As time increases, the epidemic spreads as a wave throughout the domain.

of infectivity from a constant infectivity radius of $\rho_0 = 0.04$. We then updated the agent states according to the above transition rules (4.6)–(4.8) with contact tolerance $\kappa = 0.95$. This "high" contact tolerance relates to a "low" probability of a susceptible agent becoming infected. Moreover, the time spent in the infective state and the time spent in the recovered state are $T_I = T_R = 30$. Finally, the agent's location is updated by performing an URW with spatial step-size $\triangle r = 0.001$.

4.2.2 Globally Homogeneous GRR

To reduce the number of equations, we can assume a Markovian (time-independent) process. We further simplify the number of states in our analysis by defining $\mathcal{I} = \bigcup_{i=1}^{T_I} \mathcal{I}_i$ as the infected state, which is independent of the amount of time spent in the infected

state. Similarly, we define $\mathcal{R} = \bigcup_{i=1}^{T_R} \mathcal{R}_i$, the total number of recovered agents, regardless of the amount of time spent in the recovered state. We reduce the number of states in this way when calculating the GRR because we are primarily interested in calculating the expected total number of infected and recovered agents at each particular iteration t, not the particular stage of the infection or recovery.

Adapting equation (4.5) to our E-AB model, we have the system

$$S_{t+1} = \sum_{\{k:s_t^k=\mathcal{S}\}} W(\mathcal{S} \to \mathcal{S}) + \sum_{\{k:s_t^k=\mathcal{R}\}} W(\mathcal{R} \to \mathcal{S}), \tag{4.9}$$

$$I_{t+1} = \sum_{\{k:s_t^k=\mathcal{S}\}} \mathbb{P}\left(\mathbf{x}_t^k \in B_t^{\mathcal{S},\mathcal{I}}\right) W(\mathcal{S} \to \mathcal{I}) + \sum_{\{k:s_t^k=\mathcal{I}\}} W(\mathcal{I} \to \mathcal{I}), \tag{4.10}$$

$$R_{t+1} = \sum_{\{k:s_t^k=\mathcal{I}\}} W(\mathcal{I} \to \mathcal{R}) + \sum_{\{k:s_t^k=\mathcal{R}\}} W(\mathcal{R} \to \mathcal{R}). \tag{4.11}$$

Recall from Section 3.1 that $W_t(\mathcal{V} \to \mathcal{U})$ denotes the probability an agent in state $\mathcal{V}$ transitions to state $\mathcal{U}$ at time t. However, since the transition probabilities do not vary in time, we do not need the subscript t. The total number of agents is constant, so $S_t = N - (I_t + R_t)$. This allows the reduction of the above system to just two equations, namely, (4.10) and (4.11). Now that we have the GRR framework for this model, we can determine the expressions for the probabilities.

We further simplify the derivation by ignoring the effect of the boundary on the infectivity neighborhood, which allows the assumption that the area of the region $\mathcal{N}_t^j$ is independent of j and t. Let $\mu(\mathcal{N})$ denote the area of any neighborhood $\mathcal{N}_t^j$. Since our simulation is two-dimensional, we then make the approximation[5] that $\mu(\mathcal{N}) := \mu(\mathcal{N}_t^j) = \pi\rho_0^2$ for all j and t. It follows that the probability that the k^{th} agent is located in the neighborhood of the j^{th} agent is

$$\mathbb{P}(\mathbf{x}_t^k \in \mathcal{N}_t^j) = \frac{\mu(\mathcal{N})}{\mu(\Omega)}, \quad \forall j, \tag{4.12}$$

the ratio of the area of the infectivity neighborhood and the area of the region.

For any susceptible agent k to transition to state $\mathcal{I}$, it is sufficient that $\mathbf{x}_t^k \in B_t^{\mathcal{S},\mathcal{I}}$. If we assume that the transition probability $W(\mathcal{S} \to \mathcal{I})$ does not depend on the number of infectivity neighborhoods, then it follows that $W(\mathcal{S} \to \mathcal{I}) = 1 - \kappa$, where $\kappa \in [0, 1]$ is the contact rate. Moreover, if we assume that the infectivity neighborhoods are uniformly distributed within Ω, then by the multiplication rule of independent events,

$$\mathbb{P}(\mathbf{x}_t^k \notin B_t^{\mathcal{S},\mathcal{I}}) = \left(1 - \frac{\mu(\mathcal{N})}{\mu(\Omega)}\right)^{I_t}. \tag{4.13}$$

[5] Any agent neighborhood sufficiently close to the boundary has smaller area, since, by definition, the neighborhood is contained in Ω. However, since we assume that the initially infected agent is located in the center of the region as well as the fact that the spatial step size and ρ_0 are much smaller than the size of Ω, there are sufficiently many infected agents away from the boundary to make this simplification reasonable.

It follows that the probability of $\mathbf{x}_t^k$ being located in an $\mathcal{S} \to \mathcal{I}$ transition neighborhood is then

$$\mathbb{P}(\mathbf{x}_t^k \in B_t^{\mathcal{S},\mathcal{I}}) = 1 - \left(1 - \frac{\mu(\mathcal{N})}{\mu(\Omega)}\right)^{I_t}. \tag{4.14}$$

Then, for any k such that $s_t^k = \mathcal{S}$, by inserting (4.14) into (4.10) we have:

$$\begin{aligned}\mathbb{P}(s_{t+1}^k = \mathcal{I}) &= \mathbb{P}(\mathbf{x}_t^k \in B_t^{\mathcal{S},\mathcal{I}}) W(\mathcal{S} \to \mathcal{I}) \\ &= \underbrace{\left\{1 - \left(1 - \frac{\mu(\mathcal{N})}{\mu(\Omega)}\right)^{I_t}\right\}}_{\substack{\text{probability in at least} \\ \text{one infectivity region}}} \underbrace{(1-\kappa)}_{\substack{\text{probability} \\ \text{becoming} \\ \text{infected}}}.\end{aligned} \tag{4.15}$$

Moreover, by assuming the cumulative time spent in infected states is uniformly distributed, we have for any agent k such that $s_t^k = \mathcal{I}$,

$$W(\mathcal{I} \to \mathcal{R}) = 1/T_I, \tag{4.16}$$

$$W(\mathcal{I} \to \mathcal{I}) = 1 - 1/T_I, \tag{4.17}$$

where T_I is the time spent in the infective state. This assumption is valid for a large number of agents and for a sufficiently large number of iterations. Inserting equations (4.15), (4.16), and (4.17) into (4.10), we have

$$\underbrace{I_{t+1}}_{\substack{\text{total} \\ \text{infected} \\ \text{agents} \\ \text{at time } t+1}} = \underbrace{(N - I_t - R_t)}_{\substack{\text{total} \\ \text{susceptible} \\ \text{agents} \\ \text{at time } t}} \underbrace{\left\{1 - \left(1 - \frac{\mu(\mathcal{N})}{\mu(\Omega)}\right)^{I_t}\right\}}_{\substack{\text{probability in at least} \\ \text{one infectivity region}}} \underbrace{(1-\kappa)}_{\substack{\text{probability} \\ \text{becoming} \\ \text{infected}}} + \underbrace{\left\{1 - \frac{1}{T_I}\right\}}_{\substack{\text{probability remain} \\ \text{in infected state}}} \underbrace{I_t}_{\substack{\text{total} \\ \text{infected} \\ \text{agents} \\ \text{at time } t}}. \tag{4.18}$$

That is, the expected number of infected agents at $t+1$ is the sum of two terms. The first term is the product of the expected number of susceptible agents at time t multiplied by the probability a susceptible agent transitions to state $\mathcal{I}$. The second term is the expected number of infected agents at t times the probability that an infected agent remains in state $\mathcal{I}$. Similarly, by assuming the time in recovered states is uniformly distributed, we have for any agent k such that $s_t^k = \mathcal{R}$, the probability of staying in state $\mathcal{R}$ is

$$W(\mathcal{R} \to \mathcal{R}) = 1 - 1/T_R. \tag{4.19}$$

Then, inserting (4.16) and (4.19) into (4.11) we have

$$R_{t+1} = \frac{1}{T_I} I_t + \left(1 - \frac{1}{T_R}\right) R_t, \tag{4.20}$$

and the expected number of recovered agents at iteration $t+1$ is the sum of two terms. The first term is the expected number of infected agents at time t times the probability an infected agent transitions to state $\mathcal{R}$. The second term is the expected number of recovered agents at t times the probability a recovered agent remains in state $\mathcal{R}$.

Since T_I and T_R are scalar values, we can easily find a $q \in \mathbb{R}$ such that $T_R = qT_I$. We then have the following E-AB GRR:

$$I_{t+1} = (N - I_t - R_t)\left\{1 - \left(1 - \frac{\mu(\mathcal{N})}{\mu(\Omega)}\right)^{I_t}\right\}(1-\kappa) + \left(1 - \frac{1}{T_I}\right) I_t := H(I_t, R_t), \quad (4.21)$$

$$R_{t+1} = \frac{1}{T_I} I_t + \left(1 - \frac{1}{qT_I}\right) R_t := G(I_t, R_t). \quad (4.22)$$

Since $S_t = N - (I_t + R_t)$, we have recurrence formulas for the expected agent densities in each state at each iteration. With our GRR, we now have a general framework to further analyze the behavior of the system. Note that we identify (4.21)-(4.22) as globally homogeneous since we have assumed the infectivity neighborhoods are uniformly distributed in the domain with the same constant area.

4.2.3 Fixed Point Analysis for Globally Homogeneous GRR

We can now calculate the stability of the fixed points of the globally homogeneous GRR by finding all solutions to the system that simultaneously solve $I_{t+1} - I_t = 0$ and $R_{t+1} - R_t = 0$. That is, we need to find all solutions to the system

$$\begin{bmatrix} (N - I_t - R_t)\left\{1 - (1 - \mu(\mathcal{N}))^{I_t}\right\}(1-\kappa) - \frac{1}{T_I} I_t \\ \frac{1}{T_I} I_t - \frac{1}{qT_I} R_t \end{bmatrix} = \begin{bmatrix} 0 \\ 0 \end{bmatrix}. \quad (4.23)$$

We have two fixed points. One is the trivial fixed point, $(I, R) = (0, 0)$. The other is the point along the line $R = qI$ that solves the fixed point problem

$$(N - (1+q)I)\left\{1 - (1 - \mu(\mathcal{N}))^{I}\right\}(1-\kappa) - \frac{1}{T_I} I = I. \quad (4.24)$$

This second fixed point has to be computed numerically.

We analyze the fixed point $(0, 0)$ using two-dimensional perturbation theory, where details can be found in Appendix C. The Jacobian matrix of the E-AB GRR is

$$J = \begin{bmatrix} -(1-\kappa)\Big\{(N - I - R)K \ln(1 - \mu(\mathcal{N})) + (1 - K)\Big\} - \frac{1}{T_I} & -(1-\kappa)(1-K) \\ \frac{1}{T_I} & 1 - \frac{1}{qT_I} \end{bmatrix},$$

where we define $K = (1 - \mu(\mathcal{N}))^I$ for ease of reading. Evaluating at $(0, 0)$ gives us

$$J\Big|_{(I,R)=(0,0)} = \begin{bmatrix} -N(1-\kappa)\ln\left(1 - \mu(\mathcal{N})\right) - \frac{1}{T_I} & 0 \\ \frac{1}{T_I} & 1 - \frac{1}{qT_I} \end{bmatrix}. \quad (4.25)$$

The eigenvalues are $\lambda_1 = 1 - \frac{1}{qT_I}$ and $\lambda_2 = -N(1-\kappa)\ln(1 - \mu(\mathcal{N})) - \frac{1}{T_I}$. Clearly, since $qT_I = T_R > 0$ we know $|\lambda_1| < 1$. Now, suppose $\lambda_2 < 1$. It follows that $\alpha > 1 - \exp\left(\frac{1+1/T_I}{N(1-\kappa)}\right)$. That is, $\frac{\mu(\mathcal{N})}{\mu(\Omega)} > 1 - \exp\left(\frac{1+1/T_I}{N(1-\kappa)}\right)$. We know $\mu(\mathcal{N}) \ll \mu(\Omega)$ and it is

reasonable to assume that N is sufficiently large such that $N(1-\kappa) > 2$. This contradicts the inequality. It must follow that $\lambda_2 > 1$. Thus, we have that $(0,0)$ is a saddle point that is only stable along the nullcline $I = 0$.

Since we do not have an explicit solution of the second fixed point, we cannot perform the same computation as we did for $(0,0)$. However, we know that the following are bounded: H and all derivatives of H, the expected number of infected agents at the next time step from equation (4.21), and the domain. Additionally, since I is repelled by $(0,0)$, we can infer that the second fixed point is stable. Thus, we can prove that this E-AB has a stable endemic equilibrium ($I > 0$) as $t \to \infty$, which we can see in Fig. 4.4.

Similar to a differential equation SIR model, we are able to obtain fixed points. However, the fixed points are different and there are not direct comparisons since we assume a moving population with dynamic contacts that allow for infection whereas a differential equation assumes a well-mixed population.

4.2.4 Locally Homogeneous GRR

When deriving the globally homogeneous E-AB GRR, (4.21) and (4.22), we assume that the infectivity neighborhoods are uniformly distributed throughout Ω. For this test case, we initialize one infected agent, $s_0^1 = \mathcal{I}$, such that it is initially located in the center of the region $\mathbf{x}_0^1 = (0.5, 0.5)$. However, from observation of simulations, such as in Figure 4.1, we know there is a wave of infectivity propagating from this initial infected agent. The susceptible agents that agent 1 infects must be located in its neighborhood $\mathcal{N}^1$. Some future infected agents may be located in those neighborhoods of the newly infected agents. As time progresses, newly infected agents can be located farther from the initially infected agent until the domain boundary is reached. Thus, the edge of the region containing infected agents propagates outward at finite speed, a feature also seen in spatial SIR PDE models [90]. So rather than generalize a uniform distribution of infected agents, we should modify the GRR to account for the infection wave front.

We then need to create a sequence of regions $\left\{\tilde{B}_0^{\mathcal{S},\mathcal{I}}, \tilde{B}_1^{\mathcal{S},\mathcal{I}}, ...\right\}$, where $\tilde{B}_0^{\mathcal{S},\mathcal{I}} = \mathcal{N}^1$ and $\tilde{B}_t^{\mathcal{S},\mathcal{I}}$ is the smallest connected region containing the infection front at time t. We know such a region exists since the model initially has one infected agent and the neighborhoods of infected agents have finite radii. For notation, we use tildes above variables to denote variables and functions specifically defined for the locally homogeneous case.

Definition. $\tilde{B}_t^{\mathcal{S},\mathcal{I}} = \inf_A \left\{A \subset \Omega : A \text{ is connected and } \cup_{\{k:s_t^j=\mathcal{I}\}} \mathcal{N}_t^j \subset A\right\}$.

Suppose agent k is such that $s_t^k = \mathcal{S}$ at iteration t. We have the following conditional probability that an agent is located in the $\mathcal{S} \to \mathcal{I}$ transition neighborhood, $B_t^{\mathcal{S},\mathcal{I}}$, given that the agent is within the infection front, $\tilde{B}_t^{\mathcal{S},\mathcal{I}}$:

$$\mathbb{P}\left(\mathbf{x}_t^k \in B_t^{\mathcal{S},\mathcal{I}} \middle| \mathbf{x}_t^k \in \tilde{B}_t^{\mathcal{S},\mathcal{I}}\right) = 1 - \left(1 - \frac{\mu(\mathcal{N})}{\mu\left(\tilde{B}_t^{\mathcal{S},\mathcal{I}}\right)}\right)^{I_t}. \tag{4.26}$$

In general, for regions $\mathcal{N}$ and $\tilde{B}_t^{\mathcal{S},\mathcal{I}}$, the probability is given as $\mathbb{P}\left(\mathbf{x}_t^k \in \tilde{B}_t^{\mathcal{S},\mathcal{I}}\right) = \frac{\mu\left(\tilde{B}_t^{\mathcal{S},\mathcal{I}}\right)}{\mu(\Omega)}$.

Using Bayes' theorem [124], we have that the locally homogeneous probability of an agent being in the $\mathcal{S} \to \mathcal{I}$ transition neighborhood is

$$\begin{aligned}\mathbb{P}\left(\mathbf{x}_t^k \in B_t^{\mathcal{S},\mathcal{I}}\right) &= \mathbb{P}\left(\mathbf{x}_t^k \in B_t^{\mathcal{S},\mathcal{I}} \middle| \mathbf{x}_t^k \in \tilde{B}_t^{\mathcal{S},\mathcal{I}}\right) \mathbb{P}\left(\mathbf{x}_t^k \in \tilde{B}_t^{\mathcal{S},\mathcal{I}}\right), \\ &= \left\{1 - \left(1 - \frac{\mu(\mathcal{N})}{\mu\left(\tilde{B}_t^{\mathcal{S},\mathcal{I}}\right)}\right)^{I_t}\right\} \frac{\mu\left(\tilde{B}_t^{\mathcal{S},\mathcal{I}}\right)}{\mu(\Omega)}.\end{aligned} \tag{4.27}$$

Inserting (4.27) into (4.15), our locally homogeneous E-AB GRR is

$$\begin{aligned}\tilde{I}_{t+1} &= \left(N - \tilde{I}_t - \tilde{R}_t\right)\left\{1 - \left(1 - \frac{\mu(\mathcal{N})}{\mu\left(\tilde{B}_t^{\mathcal{S},\mathcal{I}}\right)}\right)^{I_t}\right\} \frac{\mu\left(\tilde{B}_t^{\mathcal{S},\mathcal{I}}\right)}{\mu(\Omega)}(1-\kappa) \\ &\quad + \left(1 - \frac{1}{T_I}\right)\tilde{I}_t =: \tilde{H}(\tilde{I}_t, \tilde{R}_t), \\ \tilde{R}_{t+1} &= \frac{1}{T_I}\tilde{I}_t + \left(1 - \frac{1}{qT_I}\right)\tilde{R}_t =: \tilde{G}(\tilde{I}_t, \tilde{R}_t).\end{aligned} \tag{4.28}$$

Recall that the tilde denotes values associated with the locally homogeneous GRR.

We derived this GRR by focusing on early dynamics. But how does the non-uniform assumption of the infection front affect the stability using the locally homogeneous GRR compared with the globally homogeneous GRR?

Theorem 1. *If $\tilde{B}_t^{\mathcal{S},\mathcal{I}} \to \Omega$ as $t \to +\infty$ and α is a fixed point of H, then α is a fixed point of $\tilde{H}$. Moreover, α has the same stability conditions for H and $\tilde{H}$.*

Proof. Suppose that $\lim_{t\to+\infty} I_t = \alpha$ and suppose that $\lim_{t\to+\infty} \tilde{I}_t$ exists. Then, since $\mu\left(\tilde{B}_t^{\mathcal{S},\mathcal{I}}\right) \to \mu(\Omega)$ as $t \to +\infty$, we have that $\lim_{t\to+\infty}\left(1 - \frac{\mu(\mathcal{N})}{\mu\left(\tilde{B}_t^{\mathcal{S},\mathcal{I}}\right)}\right)^{\tilde{I}_t} = \lim_{t\to+\infty}\left(1 - \frac{\mu(\mathcal{N})}{\mu(\Omega)}\right)^{\tilde{I}_t}$. Plugging into (4.21) and taking the limit,

$$\begin{aligned}\lim_{t\to+\infty} \tilde{H}(\tilde{I}_t) &= \lim_{t\to+\infty}\left[(N - \tilde{I}_t)\left(1 - \frac{\mu(\mathcal{N})}{\mu(\Omega)}\right)^{\tilde{I}_t}(1-\kappa) + \left(1 - \frac{1}{qT_I}\right)\tilde{I}_t\right] \\ &= \lim_{t\to+\infty} H(\tilde{I}_t) = \alpha.\end{aligned}$$

Moreover, $\mu(\tilde{B}^t_{\mathcal{S},\mathcal{I}}) \to \mu(\Omega)$ for fixed α and it is clear that $\left.\frac{\partial\tilde{H}}{\partial\tilde{I}}\right|_\alpha \to \left.\frac{\partial H}{\partial I}\right|_\alpha$, $\left.\frac{\partial\tilde{H}}{\partial\tilde{R}}\right|_\alpha \to \left.\frac{\partial H}{\partial R}\right|_\alpha$, $\left.\frac{\partial\tilde{G}}{\partial\tilde{I}}\right|_\alpha \to \left.\frac{\partial G}{\partial I}\right|_\alpha$, and $\left.\frac{\partial\tilde{G}}{\partial\tilde{R}}\right|_\alpha \to \left.\frac{\partial G}{\partial R}\right|_\alpha$. Since the stability condition depends on the Jacobian, and the Jacobian of the locally homogeneous region approaches the Jacobian of the globally homogeneous region as $t \to +\infty$, the long term stability conditions must be the same. □

From Theorem 1 we know that $(\tilde{H}, \tilde{G})$ has the same fixed points as found in Section 4.2.3 with the same stability conditions. We thus reduced the problem to capturing an explicit formula for $\mu\left(\tilde{B}_t^{\mathcal{S},\mathcal{I}}\right)$. Before, we made the simplifying assumption that the infected agents were distributed uniformly throughout the region, so we did not need to incorporate any spatial characteristics into the globally homogeneous GRR. Now, we need to capture the infection front dynamics in order to explicitly calculate the area of the infectivity region, $\mu\left(\tilde{B}_t^{\mathcal{S},\mathcal{I}}\right)$, in the locally homogeneous case.

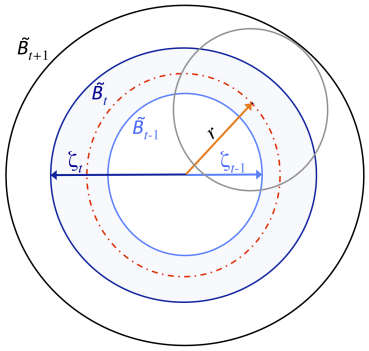

Figure 4.2: Diagram demonstrating how the locally homogeneous $\tilde{B}_{t+1}^{\mathcal{S},\mathcal{I}}$ region depends on $\tilde{B}_t^{\mathcal{S},\mathcal{I}}$ and $\tilde{B}_{t-1}^{\mathcal{S},\mathcal{I}}$ regions. The initially infected agent at $t = 0$ is located in the center of the $\tilde{B}_t^{\mathcal{S},\mathcal{I}}$ regions, which expand outward with radii ζ_t. We make the simplifying assumption that newly infected agents lie on the radial center of mass of the region $\tilde{B}_t^{\mathcal{S},\mathcal{I}} \setminus \tilde{B}_{t-1}^{\mathcal{S},\mathcal{I}}$, denoted with the dashed line, which is a distance r from the initially infected agent.

To construct our formula, we make the simplifying assumption that newly infected agents are expected to be in the region $\tilde{B}_t^{\mathcal{S},\mathcal{I}} \setminus \tilde{B}_{t-1}^{\mathcal{S},\mathcal{I}}$ and are moving a fixed distance $\triangle r$. Further, we assume the expected location of the newly infected agents lie on the circle that is the radial center of mass of $\tilde{B}_t^{\mathcal{S},\mathcal{I}} \setminus \tilde{B}_{t-1}^{\mathcal{S},\mathcal{I}}$, a distance r from the initially infected agent location as shown in Figure 4.2. The radius of the infectivity front region $\tilde{B}_t^{\mathcal{S},\mathcal{I}}$ at time t is denoted as ζ_t. We then have the following expected radius of $\tilde{B}_{t+1}^{\mathcal{S},\mathcal{I}}$:

$$\zeta_{t+1} = \rho_0 + \sqrt{\frac{(\zeta_t + \delta_{out}(\triangle r))^2 + (\zeta_{t-1} - \delta_{in}(\triangle r))^2}{2}}, \tag{4.29}$$

where δ_{in} and δ_{out} are functions of the expected distance an infected agent travels towards the center of $\tilde{B}_t^{\mathcal{S},\mathcal{I}}$ and out of the region $\tilde{B}_t^{\mathcal{S},\mathcal{I}}$, respectively. For our simulations and derivation, we assume $\delta_{out} = \triangle r$ and $\delta_{in} = \triangle r$. Even though the simulation is a Markov process, our analytical solution, which calculates the area $\mu\left(\tilde{B}_{t+1}^{\mathcal{S},\mathcal{I}}\right)$ using ζ_{t+1}, is not, since it relies on information at iterations t and $t-1$. Clearly, the simulation is a Markovian process but the GRR does not have to be for this analysis. In fact, it can belong to a larger class of processes than the underlying AB model.

By the following theorem, we know that equation (4.29) satisfies the premise of Theorem 1.

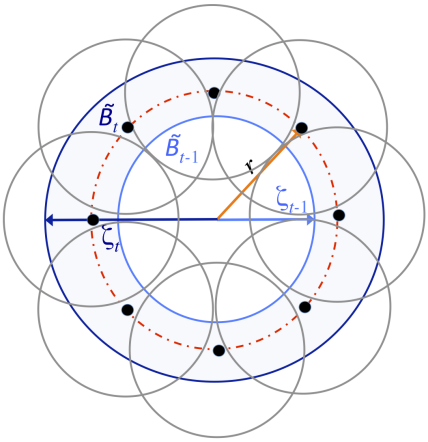

Figure 4.3: Infectivity neighborhood depends on the number n of newly infected agents. The radial center of mass of the region $\tilde{B}_t^{\mathcal{S},\mathcal{I}} \setminus \tilde{B}_{t-1}^{\mathcal{S},\mathcal{I}}$ (dashed line) is a distance r from the initially infected agent. Newly infected agents are distributed uniformly along the radial center of mass and the new infection front radius ζ_{t+1} depends on the total area of the infectivity neighborhoods outside $\tilde{B}_t^{\mathcal{S},\mathcal{I}}$.

Theorem 2. *If $\rho_0 > 0$ and for all iterations t_m such that $\mu\left(\tilde{B}_{t_m}^{\mathcal{S},\mathcal{I}}\right) \neq \mu(\Omega)$ there exists an agent k with $s_{t_m}^k = \mathcal{S}$ such that $\mathbf{x}_{t_m}^k \notin \tilde{B}_{t_m}^{\mathcal{S},\mathcal{I}}$, then $\exists \hat{t} \in \mathbb{N}$ such that $\mu\left(\tilde{B}_t^{\mathcal{S},\mathcal{I}}\right) = \mu(\Omega)$ for all $t > \hat{t}$ with radius ζ_t as defined in (4.29).*

The above theorem essentially states that if the infection does not "die out," then the $\mathcal{S} \to \mathcal{I}$ transition neighborhood, $\tilde{B}_{t_m}^{\mathcal{S},\mathcal{I}}$, eventually covers the entire region of interest Ω. The proof is clear, since Ω is bounded. As we see in Section 4.2.5, we are able to approximate early behavior more accurately with the locally homogeneous GRR, while still being able to evaluate and determine the stability of fixed points with the simpler equations of the globally homogeneous GRR.

Extensions to More Complex Neighborhoods

As long as the infection front in the E-AB approaches $\partial\Omega$ and $\tilde{B}_t^{\mathcal{S},\mathcal{I}} \to \partial\Omega$, Theorem 1 holds. One could derive a formula for $\tilde{B}_t^{\mathcal{S},\mathcal{I}}$ that more closely approximates the initial phases of the infection spread. Rather than assume that the new infection front extends approximately $\triangle r$ from the mean center of mass as in Figure 4.2, we can assume that the infectivity radius expansion depends on the number of newly infected agents in $\tilde{B}_t^{\mathcal{S},\mathcal{I}} \setminus \tilde{B}_{t-1}^{\mathcal{S},\mathcal{I}}$, as shown in Figure 4.3.

Further details regarding the calculation and derivation for this case of $\tilde{B}_t^{\mathcal{S},\mathcal{I}}$ can be found in Appendix D. In this example, we illustrate that, by relaxing assumptions, one can derive other expressions calculating the area of the infectivity front radius ζ_t that may decrease the error of the locally homogeneous GRR during the early stages of the

epidemic. Moreover, we know that as long as the new formulation of ζ_t maintains the suppositions of Theorem 1, the long term dynamics are captured.

4.2.5 Numerical Results

Results for the E-AB model with $N = 10^4$ initialized agents are shown in Figure 4.4. Note that each simulation curve on the plot is the average of 10^3 E-AB realizations, whereas the curves based on the globally and locally homogeneous GRRs are from solving (4.22) and (4.28), respectively. The realizations were run in parallel on a computing cluster using eight cores, requiring approximately 30 minutes of run time for each parameter regime. For comparison, the GRR calculations for each parameter regime required less than a second of run time. Thus, along with rigorous analysis, the GRR is much less computationally expensive. In the figure, we observe agreement of long term behavior of the simulations with both the globally and locally homogeneous GRRs. For example, in Figure 4.4, the left hand column of each row corresponds to the case where $\rho_0 = 0.02$. In the left column of (c), the average of the E-AB simulations for the fixed points or long term behavior is 3877.1 infected agents and 5790.9 recovered agents. Upon calculation, the relative error between the simulated fixed points and the GRR fixed points is $\mathcal{O}\left(10^{-4}\right)$. Further, the early time dynamics of the infected and recovered populations with the GRR estimates have behavior similar to that of the E-AB simulations.

However, the early infection dynamics of the GRRs do not exactly match the simulations for all cases. In Figure 4.4(a)-(b), for a contact tolerance $\kappa = 0.6$ and $\kappa = 0.8$ (characterizing how easily an agent becomes infected), we observe that as the infectivity radius increases, the GRRs are able to more accurately capture the early time dynamics of the E-AB simulations. For an infectivity neighborhood of radius $\rho_0 = 0.02$, it is likely that there is not a sufficient number of agents in the region to accurately capture the early time dynamics of infectivity. We do observe that the locally homogeneous GRR provides a better approximation to the E-AB simulations in comparison to the globally homogeneous GRR. Similar trends are observed in Figure 4.4(c), where the recovery time T_R is increased.

To explicitly define how much "better" the locally homogeneous GRR is relative to the globally homogeneous GRR at capturing the E-AB dynamics for a particular parameter set, we need to develop a metric. We have a sequence of points, $(1, U_1), (2, U_2), ..., (M, U_M)$, from the simulation, where U_t, as previously defined, is the number of agents in state $\mathcal{U}$ at iteration t for $t = 1, \ldots, M$. By linear spline interpolation of these points, we construct a function $g(t) = \frac{U_{m+1}-U_m}{t_{m+1}-t_m}(t - t_m) + U_m$, for $t_m \leq t \leq t_{m+1}$. We also have a sequence of points, $(1, \hat{U}_1), (2, \hat{U}_2), \ldots, (M, \hat{U}_M)$, from the GRR. Given the fact that some of the error is due to translation and that the number of agents is much larger than the number of iterations, we need to normalize the data. We scale the t-values so that $t_m \leftarrow t_m/M$ and $\hat{t}_m \leftarrow \hat{t}_m/M$, for $m = 1, 2, \ldots, M$. Additionally, we let $\gamma = \max\{U_1, U_2, ..., U_M\}$ and scale the U-values so that $U_i \leftarrow U_i/\gamma$ and $\hat{U}_i \leftarrow \hat{U}_i/\gamma$. Our error metric is a normalized least

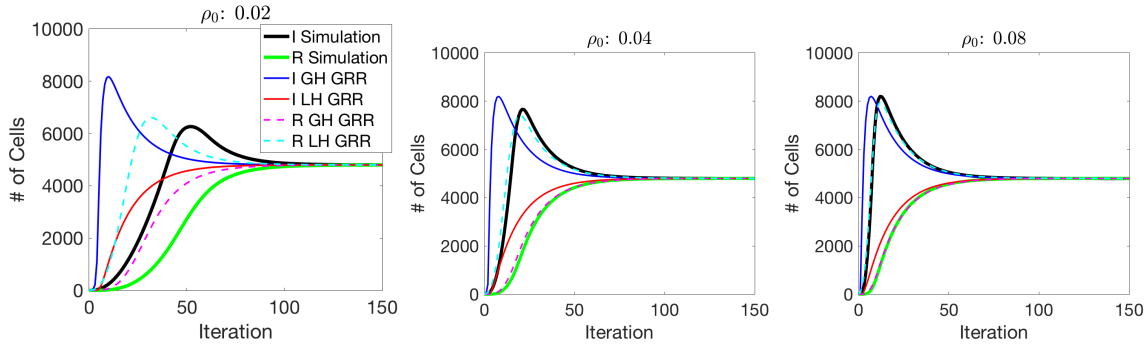

(a) $N = 10^4, \kappa = 0.6, T_I = T_R = 30$

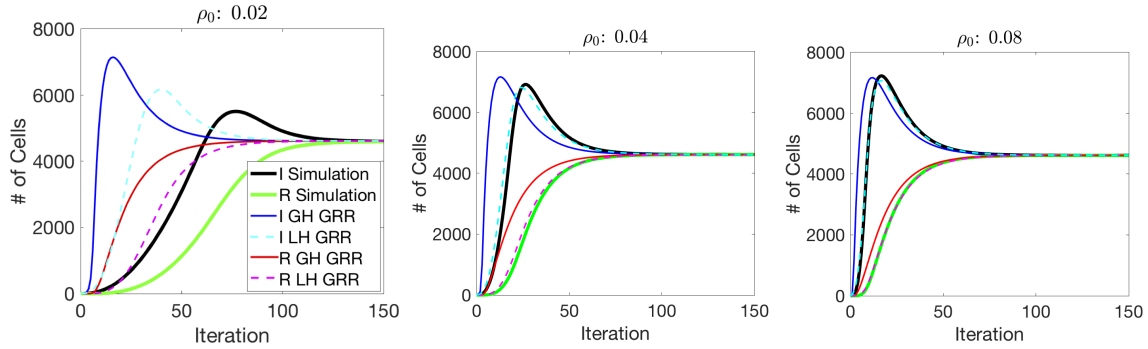

(b) $N = 10^4, \kappa = 0.8, T_I = T_R = 30$

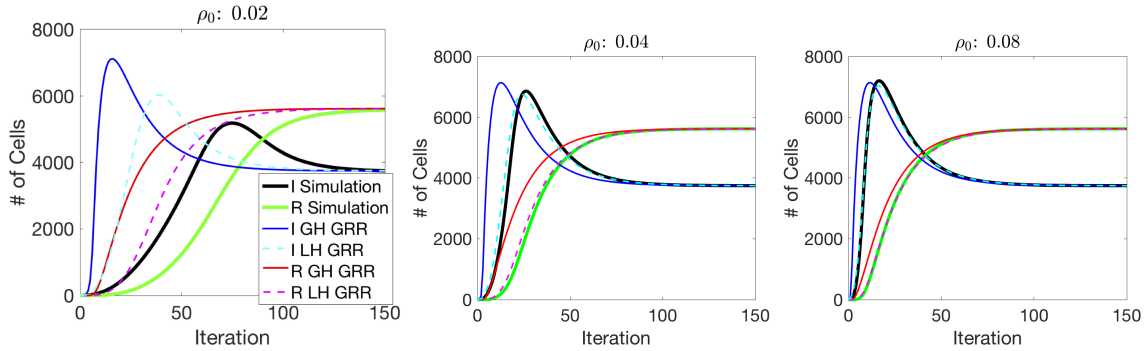

(c) $N = 10^4, \kappa = 0.8, T_I = 30, T_R = 45$

Figure 4.4: Comparing the average value of 10^3 E-AB realizations with results from the globally and locally homogeneous GRRs calculated from (4.22) and (4.28), respectively. The time to remain infected is set to $T_I = 30$, while the recovery time is $T_R = 30$ in **(a)-(b)** and $T_R = 45$ in **(c)**. Each plot corresponds to a different infectivity radii parameter ρ_0 with contact tolerance $\kappa = 0.6$ in **(a)** and $\kappa = 0.8$ in **(b)-(c)**. Note that for the globally homogeneous case (labeled as GH GRR), the infectivity neighborhood has fixed radius of ρ_0, whereas the locally homogeneous case (labeled as LH GRR) has a variable radii ζ_t at each iteration t as given in (4.29), which is a function of ρ_0.

square,

$$\nu = \frac{1}{M}\sum_{m=1}^{M} \inf_{t} \sqrt{(\hat{t}_m - t)^2 + (\hat{U}_m - g(t))^2}, \tag{4.30}$$

evaluating the average distance of each scaled GRR estimation to the scaled E-AB simulated curve. This metric is further detailed in Appendix E

$N = 10^4$	$T_I = T_R = 30$				$T_I = 30$, $T_R = 45$			
	$\kappa = 0.6$		$\kappa = 0.8$		$\kappa = 0.6$		$\kappa = 0.8$	
	Global	Local	Global	Local	Global	Local	Global	Local
$\rho_0 = 0.02$	0.036606	0.009573	0.052660	0.020494	0.035438	0.010552	0.059061	0.021560
$\rho_0 = 0.04$	0.008092	0.001398	0.007514	0.001237	0.008595	0.001687	0.008653	0.001444
$\rho_0 = 0.08$	0.004019	0.000652	0.003252	0.000360	0.004686	0.000692	0.003657	0.000391
$\rho_0 = 0.16$	0.002030	0.000798	0.001589	0.000545	0.002352	0.000859	0.001827	0.000608

(a) Error for number of infected agents.

$N = 10^4$	$T_I = T_R = 30$				$T_I = 30$, $T_R = 45$			
	$\kappa = 0.6$		$\kappa = 0.8$		$\kappa = 0.6$		$\kappa = 0.8$	
	Global	Local	Global	Local	Global	Local	Global	Local
$\rho_0 = 0.02$	0.022055	0.009537	0.027853	0.015889	0.028273	0.012485	0.036781	0.021142
$\rho_0 = 0.04$	0.008436	0.000831	0.008046	0.000817	0.010412	0.000895	0.010120	0.000937
$\rho_0 = 0.08$	0.003581	0.000126	0.003084	0.000104	0.004247	0.000138	0.003694	0.000103
$\rho_0 = 0.16$	0.001247	0.000176	0.001117	0.000154	0.001350	0.000189	0.001260	0.000184

(b) Error for number of recovered agents.

Table 4.1: Error between GRR and 10^3 E-AB simulations using metric ν from Equation (4.30) for infectivity radii ρ_0, contact tolerances κ, time in infected state T_I, and time in recovered state T_R.

We see from Figure 4.4, as well as Table 4.2a and Table 4.2b, that the locally homogeneous GRR approaches the E-AB with less error than the Global GRR. Despite the scaling and translation differences, the general behavioral trends of the Global GRR and locally homogeneous GRR emulate the E-AB agent state densities.

The surface plot in Figure 4.5 shows the mean error between the locally homogeneous GRR and the E-AB simulations with respect to the number of infected individuals. The horizontal axis represents the expected number of susceptible agents in the initial infected agents neighborhood and the vertical axis represents the contact tolerance κ for the mean error calculated from (4.30) using 150 iterations of data. We fixed the number of agents, N, and varied the infectivity radius, ρ_0, to generate the error surface plot in Figure 4.5; however, one can generate similar error surface plots by fixing N and varying ρ_0.

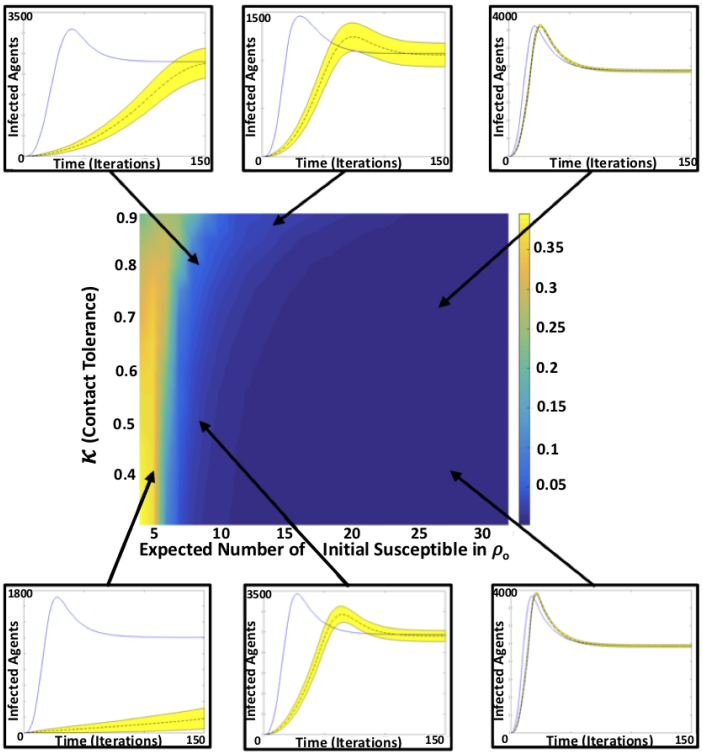

Figure 4.5: The surface plot in the center displays the error between the locally homogeneous GRR and the E-AB simulations with respect to the number of infected agents as a function of the contact tolerance and the expected number of susceptible agents located in the initial infected agent's neighborhood at $t = 0$. The 6 outside plots show the locally homogeneous GRR infected population solution (blue) and the simulated solution (black) with a bound of $\pm$ one standard deviation (yellow).

4.3 Discussion

We identified two classes of E-AB GRR: a globally homogeneous GRR, which assumes that the infected agents are uniformly distributed throughout the domain, and a locally homogeneous GRR, which assumes that there is an infectivity front expanding outward from the initially infected agent. With relaxed assumptions, the locally homogeneous GRR performs better than the globally homogeneous GRR with respect to early epidemic prediction. However, we demonstrated and proved that the much simplified globally homogeneous GRR can predict long-term behavior just as well as the locally homogeneous GRR.

Further, we demonstrated that the GRR is a generalized model, but is not unique in its application — certain choices must be made. The generalized GRR definition lends itself to be used as a framework when adapting similar models. For example, if the E-AB were three-dimensional or if the neighborhoods were a different geometry, then we could use our previously derived GRR equations 4.21, 4.22, and 4.28 while only simply having to

derive new expressions for $\mu(\mathcal{N})$ and ζ_t. Further, we assumed a constant number of cells, N, but we could derive a GRR to calculate S_t, I_t, and R_t that incorporates a dynamically varying number of agents in much the same way as we did in Section 4.2. The analysis would be similar, only in three-dimensional phase space instead of two-dimensional.

Previous analytical techniques, such as mean-field game theory, assumed the density of agents approaches infinity in order to calculate end behavior [22, 71]. Other approaches take continuum limits to approximate the dynamics of AB state distributions as a system of PDEs [24, 35, 99], which often corresponds to reducing the scales to infinitesimal time or spatial steps. In contrast, the GRR analysis allows for and takes into account a finite number of agents in a discrete spatial and temporal domain, which in some cases might more closely reflect the outcome of interest for a particular application. Moreover, the GRR incorporates the notion that the state changes are incurred through spatially defined neighborhoods. Traditional differential equation formulations of SIR models do not incorporate this feature since there is an assumption of a well-mixed population, but Fig. 4.5 demonstrated that these neighborhoods affect our steady state solutions. Since our GRR analysis incorporates movements of individuals, this causes the contacts between individuals to be dynamic. We note that it is not feasible to do a direct comparison with a differential equation SIR model but that previous AB models with individuals at fixed locations and fixed neighborhoods have done some comparisons for specific cases [49].

Our explicit GRR formulation for the E-AB model ultimately fails when the density of the infected population is zero. In general, the expansion of the wave of infectivity is caused by the infection spread, rather than the cell movement. However, when cell density is low, the early infectivity front growth relies on cell movement. For the infection to not "die out" in these cases, we require an increase in the ratio of the movement size to the neighborhood area to increase the probability that a susceptible cell encounters the infectivity region. In the future, we could develop continuum approximations of state changes in order to determine the probability that an infection eventually "dies out." We can use such probabilities to establish density and parameter bounds for when the E-AB GRR formulation is reliable. Early predictions of disease dynamics are necessary [103, 111], and the proposed framework can be extended to determine accuracy of these estimates for given parameter regimes.

Although the E-AB model used in this chapter is reasonable for use as a proof of concept for the GRR, it is not sophisticated enough to accurately model burgeoning epidemics to affect real world policy decisions. More accurate AB models using networks have already been developed [113, 114, 134]. It would be of interest to apply these realistic models to the GRR and compare the long term behaviors.

Part II

Cumulative Absorption Model

Chapter 5

Free-Space Cumulative Absorption Model

In this Chapter, we focus on our research to capture the continuum density of cells or agents in space, while accounting for the cumulative exposure to the environment as a continuous variable[1]. As a motivating example, consider a cell moving and absorbing chemicals from the domain; an agent-environment state change occurs when the cell has absorbed a critical (toxic) threshold of chemicals. We treat this state change as cell death. In Section 5.1, we show how the new governing equation is able to capture these dynamics. An analysis of this equation is detailed in Section 5.2 and the numerical method is outlined in Section 5.3. Representative numerical results are given in Section 5.4, comparing computation of our new governing equations with the corresponding agent-based (AB) model for the case of cells that randomly move and absorb chemical from the surrounding environment. We also consider two inverse problems using the numerical PDE solution. Additional commentary is given for several limiting cases in Section 5.5.

Suppose a spatial domain contains a spatially-varying (or time-varying) chemical concentration. For simplicity, we assume the chemical concentration is a positive, spatially-dependent distribution, $C(\mathbf{x})$, which is independent of time. We then insert a cell in this domain at an initial location $\mathbf{x}_0$. To avoid confusion and to divest the abstract dynamics from any particular example while developing our theory, we refer to this cell as an agent. A schematic of this setup is shown in Fig. 5.1. This agent has a given movement probability at each time point. In the 2-d setup, the agent may remain stationary or move left, right, up, or down as shown with the dotted arrows in Fig. 5.1. After moving, the agent absorbs a certain amount of chemical according to a function $\hat{\beta}(\mathbf{x})$, which depends on the local chemical concentration. To keep the model general, we are not fixing a specific form of the function $\hat{\beta}(\mathbf{x})$ for our analysis. However, we assert that this function preserves the property that if $C(\mathbf{x}) > 0$, then $\hat{\beta}(\mathbf{x}) > 0$. When the cumulative absorption within the agent reaches a critical threshold, the agent changes state (e.g. the agent dies). The flowchart of this model can be seen in Fig. 5.2.

[1] Portions of this chapter are published in [139].

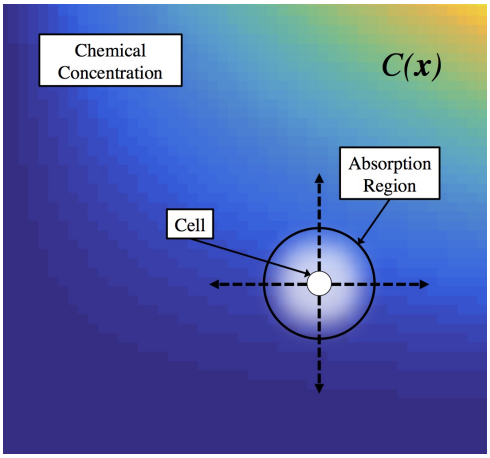

Figure 5.1: Schematic of an agent (the cell) in a 2-d domain that has a spatially dependent chemical profile. At each time step, the agent moves and then absorbs chemical from the local, surrounding absorption region.

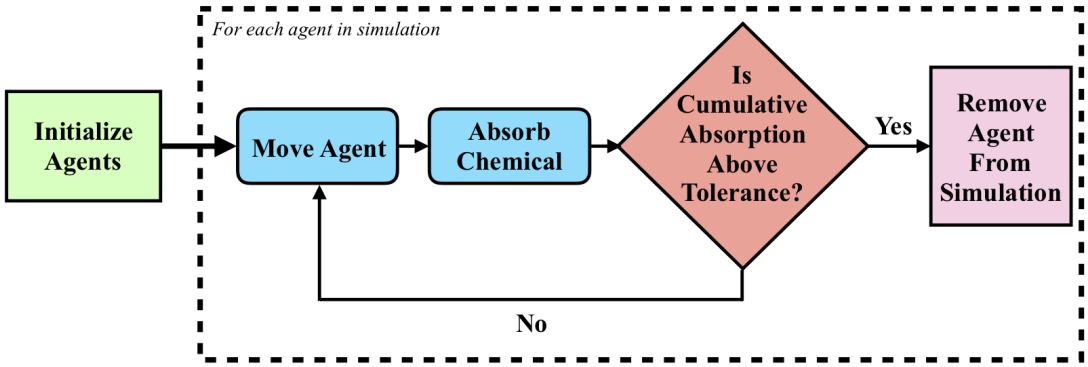

Figure 5.2: Flowchart of the AB absorption model. The algorithm demonstrating the logic for a single agent is in the dashed-line box.

At first glance, we may consider the agent in our absorption model as having only two states: live and dead. However, it is subtly more complicated since the cumulative absorption amount is a continuous internal state. Considering that the chemical concentration could be spatially and/or time-dependent, the particular path along which an agent travels may affect the amount of chemical the agent absorbs. For example, suppose there is no chemical concentration to the left of $\mathbf{x}_0$, but there is chemical to the right of $\mathbf{x}_0$. Further, consider two distinct paths the agent may travel: in one path, the agent is contained within the left side of the domain and terminates at $\mathbf{x}_0$ at time t, whereas in another path, the agent is contained within the right side of the domain and terminates at $\mathbf{x}_0$ at t. The agent traveling along the first path does not absorb any chemical by time t, but the agent traveling along the second path does absorb some chemical particles.

Since the model appears path dependent, the initial model formulation exploited this feature, which is derived and examined in Appendix F. However well it may model the

problem, the computational solution cost, the numerical errors, and the difficulties in extending the model induce us to find a different approach. This approach requires us to account for varying amounts of chemical concentration by treating the amount absorbed as distinct states.

As opposed to a compartmental model, we treat the chemical concentration as a continuous variable. In order to account for this, we need to consider cumulative absorption as a dimension orthogonal to both the temporal and spatial dimensions as seen in Fig. 5.3. That is, the agent is at a location $\mathbf{x}$, having a cumulative chemical absorption ξ, at a particular time t.

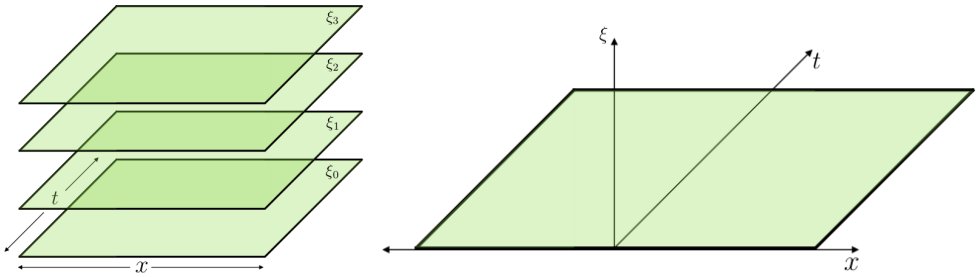

(a) Motivation for Coordinate System

(b) Absorption Model Coordinate System

Figure 5.3: **(a)** Motivation for absorption coordinate system by stacking discrete number of spatiotemporal coordinate systems, labeled by cumulative absorption amount. **(b)** Continuum absorption coordinate system, with cumulative absorption amount a continuous variable.

The cumulative amount absorbed is path dependent. However, we cannot say that ξ is dependent on space or time, just as we cannot say that $\mathbf{x}$ is dependent on time. All three variables are linked by our model, but should be considered independent.

5.1 The Continuum Model

Through upscaling, we derive the continuum absorption model. Using the same approach used for random walk (RW) models in Chapter 2, we develop a discrete difference equation from the AB model, and then take the continuum limit. At each iteration, our AB model agent moves in the domain with spatial-step $\triangle x$ and time-step $\triangle t$. Then, the agent absorbs chemical particles at its new location $\mathbf{x}$ based on a spatially-dependent function $\hat{\beta}(\mathbf{x})$ that depends on the distribution of chemical particles, $C(\mathbf{x})$. We interpret $\hat{\beta}(\mathbf{x})$ as the amount the cell absorbs during the time step of length $\triangle t$. This function may be a proportion of $C(\mathbf{x})$ or it may be the solution of realistic PDE dynamics [101].

5.1.1 Derivation of Single-State Absorption Model

Assume the AB model agent is initialized in the 1-D spatial domain $\mathbb{R}$. We define the variable $U(x,t,\xi)$ to denote the density of an agent centered at location x at time t, having absorbed ξ total particles. Suppose the agent moves a distance $\triangle x$ to the right to be at x at the next time increment, $t+\triangle t$. We then have that the agent absorbs $\hat{\beta}(x)$ chemical particles at x, yielding a cumulative absorption amount of $\xi+\hat{\beta}(x)$ particles at time $t+\triangle t$. Similarly, if the agent moves a distance $\triangle x$ to the left to be at x at the next time increment, then the agent cumulatively absorbs $\xi+\hat{\beta}(x)$ particles. Letting $\ell(x)$ and $r(x)$ be the probabilities of moving left or right at location x, respectively, we can assert a difference equation modeling this behavior:

$$\begin{aligned} U(x,t+\triangle t,\xi+\hat{\beta}(x)) &= \ell(x+\triangle x)U(x+\triangle x,t,\xi) \\ &\quad + r(x-\triangle x)U(x-\triangle x,t,\xi) + [1-r(x)-\ell(x)]U(x,t,\xi), \end{aligned} \tag{5.1}$$

where $\ell(x)+r(x)\leq 1$ for all $x\in\mathbb{R}$. The $U(x,t+\triangle t,\xi+\hat{\beta}(x))$ term expresses the fact that the agent absorbs an additional $\hat{\beta}(x)$ chemical particles at location x and time $t+\triangle t$. The right-hand side of (5.1) accounts for all the different possible ways (along with their respective probabilities) that agent $\mathfrak{u}$, having absorbed ξ total number of chemical particles at time t can be at location x at time $t+\triangle t$.

Assuming $U\in\mathcal{C}^2(\mathbb{R},[0,\infty),[0,\infty))$ and $q(x)\in\mathcal{C}^2([0,1])$ for $q(x)$ representing either $\ell(x)$ or $r(x)$, we can perform a Taylor expansion on U and the moving probability $q(x)$ in (5.1) and get

$$\begin{aligned} U(x,t+\triangle t,\xi+\hat{\beta}(x)) &= U(x,t,\xi)+\triangle t\frac{\partial}{\partial t}U(x,t,\xi)+\hat{\beta}(x)\frac{\partial}{\partial\xi}U(x,t,\xi) \\ &\quad +\mathcal{O}(\triangle t^2,\hat{\beta}(x)^2), \\ U(x\pm\triangle x,t,\xi) &= U(x,t,\xi)\pm\triangle x\frac{\partial}{\partial x}U(x,t,\xi)+\frac{\triangle x^2}{2}\frac{\partial^2}{\partial x^2}U(x,t,\xi) \\ &\quad +\mathcal{O}(\triangle x^3), \\ q(x\pm\triangle x) &= q(x)\pm\triangle x\frac{\partial}{\partial x}q(x)+\frac{\triangle x^2}{2}\frac{\partial^2}{\partial x^2}q(x)+\mathcal{O}(\triangle x^3). \end{aligned}$$

Inserting these expansions into (5.1) results in

$$\begin{aligned} U+\triangle t\frac{\partial U}{\partial t}+\hat{\beta}(x)\frac{\partial U}{\partial\xi}+\mathcal{O}\left(\triangle t^2,\hat{\beta}(x)^2\right) &= [\ell U]+\triangle x\frac{\partial(\ell U)}{\partial x}+\frac{\triangle x^2}{2}\frac{\partial^2(\ell U)}{\partial x^2} \\ &\quad +[rU]-\triangle x\frac{\partial(rU)}{\partial x}+\frac{\triangle x^2}{2}\frac{\partial^2(rU)}{\partial x^2} \\ &\quad +[1-\ell-r]U+\mathcal{O}\left(\triangle x^3\right). \end{aligned}$$

Rearranging terms and simplifying gives us

$$\triangle t\frac{\partial U}{\partial t}+\hat{\beta}(x)\frac{\partial U}{\partial \xi}=\triangle x\frac{\partial(\ell-r)U}{\partial x} + \frac{\triangle x^2}{2}\frac{\partial^2(\ell+r)U}{\partial x^2}+\mathcal{O}\left(\triangle x^3,\triangle t^2,\hat{\beta}(x)^2\right).$$

If we define $\beta(x)=\hat{\beta}(x)/\triangle t$ and rearrange terms, we have

$$\frac{\partial U}{\partial t}+\beta(x)\frac{\partial U}{\partial \xi}=\frac{\triangle x}{\triangle t}\frac{\partial(\ell-r)U}{\partial x}+\frac{\triangle x^2}{2\triangle t}\frac{\partial^2(\ell+r)U}{\partial x^2}+\mathcal{O}\left(\triangle x^3,\triangle t,\hat{\beta}(x)^2\right). \tag{5.2}$$

For simplification, we assume an unbiased random walk (URW). So we define $\ell(x)=r(x)=1/2$ for all $x\in\mathbb{R}$. Our equation then reduces to:

$$\frac{\partial U}{\partial t}+\beta(x)\frac{\partial U}{\partial \xi}=\frac{\triangle x^2}{2\triangle t}\frac{\partial^2 U}{\partial x^2}+\mathcal{O}\left(\triangle x^3,\triangle t,\hat{\beta}(x)^2\right). \tag{5.3}$$

We assume that $\triangle t\sim\triangle x^2$ and $\hat{\beta}(x)=\mathcal{O}(\triangle t)$. Taking the limit as $\triangle t,\triangle x\to 0$ results in the following governing continuum equation:

$$\frac{\partial U}{\partial t}+\beta(x)\frac{\partial U}{\partial \xi}=D\frac{\partial^2 U}{\partial x^2}, \tag{5.4}$$

where $D=\lim_{\triangle t,\triangle x\to 0}\triangle x^2/(2\triangle t)$. For this paper, we assume free-space boundary conditions and the initial condition depends on x and ξ.

Hence, our partial differential equation (PDE) for 1-d chemical absorption is as follows:

$$\begin{cases}\frac{\partial U}{\partial t}+\beta(x)\frac{\partial U}{\partial \xi}=D\frac{\partial^2 U}{\partial x^2}, & x\in\mathbb{R},\ \xi\in[0,\infty),\ t>0,\\ U=\phi(x,\xi), & x\in\mathbb{R},\ \xi\in[0,\infty),\ t=0,\\ \lim_{|x|\to\infty}U=0, & x\in\mathbb{R},\ \xi\in[0,\infty),\ t>0.\end{cases} \tag{5.5}$$

In a similar way, assuming that the spatial step $\triangle x$ is the same in every direction, we can derive a continuum PDE in n spatial dimensions. The resulting PDE is as follows:

$$\begin{cases}\frac{\partial U}{\partial t}+\beta(\mathbf{x})\frac{\partial U}{\partial \xi}=D_n\nabla^2 U, & x\in\mathbb{R}^n,\ \xi\in[0,\infty),\ t>0,\\ U=\phi(\mathbf{x},\xi), & x\in\mathbb{R}^n,\ \xi\in[0,\infty),\ t=0,\\ \lim_{|\mathbf{x}|\to\infty}U=0, & x\in\mathbb{R}^n,\ \xi\in[0,\infty),\ t>0,\end{cases} \tag{5.6}$$

where $D_n=\lim_{\triangle x,\triangle t\to 0}\triangle x^2/(2n\triangle t)$. Here we should note that the above equations (5.5) and (5.6) only model cumulative absorption, without taking into account any state transitions due to this cumulative absorption. We address two possible methods to account for absorption-based state changes in Section 5.1.2.

Units

Depending on the initial condition, we treat U slightly differently. If the initial condition for U is a point source, then $U(x,t,\xi)$ represents the probability an agent is at location $\mathbf{x}$ at time t having absorbed ξ chemical. It would then follow that U is in units of density. However, if U is something other than a point source, then $U(x,t,\xi)$ represents the number of agents at location $\mathbf{x}$ at time t having absorbed ξ chemical. In this case it would follow that U is in units of population. By construction, we know ξ is in units of chemical particles, and the function $C(\mathbf{x})$ is in units of chemical particles per length^n, where n is the spatial dimension of $\mathbf{x}$. From equation (5.6) we see that the absorption rate $\beta(\mathbf{x})$ is in units of chemical particles per time. Consequently, $\hat{\beta}(\mathbf{x})$ is also in units of chemical particles.

Classification

The PDE (5.5) may look like the advection-diffusion equation if we rewrite it in the form $\frac{\partial U}{\partial t} + \mathbf{a}\nabla U = \nabla \cdot \mathbf{D}\nabla U$, where $\nabla = \left(\frac{\partial}{\partial x}, \frac{\partial}{\partial \xi}\right)^T$, $\mathbf{a} = \begin{bmatrix} 0 \\ \beta(x) \end{bmatrix}$, and $\mathbf{D} = \begin{bmatrix} \triangle x^2/(2\triangle t) & 0 \\ 0 & 0 \end{bmatrix}$. The advection vector, $\mathbf{a}$, and the diffusion matrix, $\mathbf{D}$, each have different rows containing zeros. Work has been done on the advection-diffusion equation where $\mathbf{a}$ contains empty rows, but in those cases $\mathbf{D}$ does not contain any empty rows. The cumulative absorption PDE (5.5) is subtly different. Since the transport is only in the ξ-coordinate and diffusion is only in the spatial coordinates, we classify Eq. (5.5) as a mixed hyperbolic-parabolic PDE.

5.1.2 Absorption Threshold

Now that we have a governing equation for tracking the cumulative absorption property of an agent, we can address possible absorption-dependent state-changes. Suppose the agent changes state if the cumulative chemical absorption is greater than some absorption capacitance, ξ_c. That is, a cell is initially in the live state if $\xi < \xi_c$ and switches to a different state, possibly dying, if $\xi \geq \xi_c$. We denote the spatially-varying, total density of agents in the live state as $p(\mathbf{x},t)$. This value may be found through lab experimentation or through a toxicology database, such as PubChem [46].

We have two possible methods[2] for calculating the density of cells in a live state: by modifying our PDE model or by solving the PDE model and integrating ξ over the absorption domain of interest, $[0,\xi_c]$. First, we examine a modification of our PDE model and, in this case, we use the variable $V(x,t,\xi)$ to denote the density of agents in the live state (rather than the variable U to avoid confusion in later sections). Our difference

[2]We consider methods that keep β from being dependent on the cumulative absorption amount, ξ. One could derive a formula where β depends on both the chemical concentration, $C(x)$, and ξ to ensure that cells do not absorb chemical beyond the threshold. However, the derivation and resulting Taylor series would produce additional terms that could make the analysis and numerical solutions more difficult.

equation includes a Heaviside function centered at ξ_c in the sink term, since the agent switches state if $\xi \geq \xi_c$,

$$\begin{aligned} V(x, t+\triangle t, \xi + \hat{\beta}(x)) &= \ell(x+\triangle x)V(x+\triangle x, t, \xi) \\ &+ r(x-\triangle x)V(x-\triangle x, t, \xi) + [1 - r(x) - \ell(x)]V(x, t, \xi) \\ &- H(\xi - \xi_c)V(x, t, \xi), \end{aligned} \tag{5.7}$$

where $H(\xi - \xi_c) = \begin{cases} 1 & : \text{ if } \xi \geq \xi_c \\ 0 & : \text{ otherwise} \end{cases}$ denotes the Heaviside function centered at ξ_c. With the same assumptions as in the previous section and expanding in a Taylor series, we obtain the following PDE modeling live agents following an URW:

$$\begin{cases} \frac{\partial V}{\partial t} + \beta(x)\frac{\partial V}{\partial \xi} = D\frac{\partial^2 V}{\partial x^2} - \tilde{H}(\xi - \xi_c)V, & x \in \mathbb{R},\ \xi \in [0, \infty),\ t > 0, \\ V = \phi(x, \xi), & x \in \mathbb{R},\ \xi \in [0, \infty),\ t = 0, \\ \lim_{|x| \to \infty} V = 0, & x \in \mathbb{R},\ \xi \in [0, \infty),\ t > 0, \end{cases} \tag{5.8}$$

where $\tilde{H}(\xi - \xi_c) = \lim_{\triangle t \to 0} \frac{1}{\triangle t} H(\xi - \xi_c) = \begin{cases} +\infty & : \text{ if } \xi \geq \xi_c \\ 0 & : \text{ otherwise} \end{cases}$ is the result of taking the continuum limit. We can then calculate the spatially-variable, total density of cells in the live state as

$$p(x, t) = \int_0^\infty V(\mathbf{x}, t, \xi)\, d\xi. \tag{5.9}$$

This method offers us the ability to develop more complex models, such as when β can be negative, when the transition is stochastic (in which case we would substitute the Heaviside function with a probability distribution), or when we are interested in modeling agents in the secondary state. In this case, we can more easily separate different populations and capture additional state change driven dynamics (e.g. where movement rules could depend on the given state).

The alternate approach, which, other than a few comments, is the one used in the remainder of this dissertation. This is because it is simpler to analyze and it is suitable in the case where we are only interested in the live agents when there is a single deterministic state transition (when $\xi > \xi_c$) and positive chemical, $\beta > 0$ *a.e.*. In this case, it is possible to calculate the spatially-variable, total density, p, directly from the absorption model, U as

$$p(\mathbf{x}, t) = \int_0^{\xi_c} U(\mathbf{x}, t, \xi)\, d\xi. \tag{5.10}$$

If we initialize $\int_{\mathbb{R}^n} \int_0^\infty U(\mathbf{x}, 0, \xi)\, d\xi\, d\mathbf{x} = 1$, then we can consider $p(\mathbf{x}, t)$ the probability that an agent is at location $\mathbf{x}$ at time t and in the initial live state[3].

[3]If we want to find the probability an agent is at a particular location at a given time, given that the agent is in the initial live state, we can calculate:

$$\mathbb{P}(\mathbf{x}, t) = \frac{\int_0^{\xi_c} U(\mathbf{x}, t, \xi)\, d\xi}{\int_0^\infty U(\mathbf{x}, t, \xi)\, d\xi} = \frac{p(\mathbf{x}, t)}{\int_0^\infty U(\mathbf{x}, t, \xi)\, d\xi}.$$

We can rewrite (5.6) as a PDE of p. Let us integrate the terms from 0 to ξ_c with respect to ξ. This gives us

$$\int_0^{\xi_c} U_t \, d\xi + \int_0^{\xi_c} \beta(\mathbf{x}) U_\xi \, d\xi = \int_0^{\xi_c} D_n \nabla^2 U \, d\xi.$$

Since for any $t \geq 0$, $U \in L^1(\mathbb{R}^n \times [0, \infty))$, we can switch derivatives and integrals using Fubini's theorem. The above system reduces to a non-homogeneous diffusion equation

$$\begin{cases} \frac{\partial p}{\partial t} - D_n \nabla^2 p = f(\mathbf{x}, t), & \mathbf{x} \in \mathbb{R}^n, t > 0 \\ p = g(\mathbf{x}), & \mathbf{x} \in \mathbb{R}^n, t = 0 \\ \lim_{|\mathbf{x}| \to \infty} p = 0, & \mathbf{x} \in \mathbb{R}^n, t > 0, \end{cases} \tag{5.11}$$

where $f(\mathbf{x}, t) = -\beta(\mathbf{x}) U \Big|_{\xi = \xi_c}$ and $g(\mathbf{x}) = \int_0^{\xi_c} \phi(\mathbf{x}, \xi)$. If we know the value of f, then we have an explicit solution for p using the method of Green's functions (fundamental solutions). In most cases we do not have the explicit value of $f(\mathbf{x}, t)$, in which case we must first solve for $U(\mathbf{x}, t, \xi)$ before integrating to compute $p(\mathbf{x}, t)$.

We can use the value of p to calculate cellular properties of interest, such as flux out of the initial live state or the average time in the initial live state.

5.2 Well-Posedness

Through the derivation of this continuous approximation, higher order terms in the Taylor series expansions were neglected. We must still ensure that we are maintaining the proper physics with this new equation. For example, we wish that energy in the system is not increasing and that the total quantity of agents or cells is conserved. In addition, since the governing equation (5.6) is classified as a mixed Parabolic-Hyperbolic PDE, there is no generalized theorem we can apply to show it is well-posed. To this end, Theorems 5–7 in this section prove existence, uniqueness, and continuous dependence on initial data, respectively.

There are a few ways analysts prove the existence of a PDE, such as: by projection methods [41, Ch.7], using energy estimates [41, Ch.7], [125, Ch.6], and by discretization [7, 16]. Projection methods, like Galerkin approximation, project the PDE onto a finite n-dimensional subspace to convert the problem into a system of ODEs. If the limit of the solution as $n \to \infty$ exists, then the existence of the PDE is proven. Energy estimates, like viscosity techniques, are used for hyperbolic problems to reframe the PDE as solving for minimum energy, where the energy is a functional with specific assumptions. This method seeks to show that the limiting solution converges to and satisfies the original PDE by using regularization estimates of the minimization problem. Discretization methods, like the method of lines or Rothe method, discretizes one of the coordinates and rewrites the PDE as a system of difference quotients. If the limiting solution exists and solves the PDE, then existence is proven.

There are other methods for solving existence of PDEs, such as the Cauchy-Kowalevski theorem [41, Ch.4]. However, the three summarized methods all share the fact that rather than proving the existence of the PDE directly, the PDE is rewritten as a sequence of easier, solvable problems from which the limit proves existence. We use this framework to prove the existence of the cumulative absorption PDE (5.6).

5.2.1 Energy & Conservation

In order to prove uniqueness and the continuous dependence of the PDE solution on initial data, we show that there is some time-dependent functional $E(t)$, such that our solution U of (5.6) satisfies $0 \leq E(t) \leq E(0)$ for all $t > 0$. We refer to this functional as the energy of the solution at time t. This is a classical method used to prove uniqueness and stability in linear PDEs [41, Ch.2][125, Ch.2][73]. To match the physics of the AB model simulation, the energy of our PDE should be non-increasing, but we need to prove that our PDE does not lose this feature during the process of deriving the continuum approximation.

Theorem 3. *Suppose $\beta(\mathbf{x}) > 0$ for all $\mathbf{x} \in \mathbb{R}^n$. The PDE (5.6) with the energy functional [4] $E(t) = \frac{1}{2}||U||_2$ satisfies the inequality $0 \leq E(t) \leq E(0)$.*

Proof. Via a calculation,

$$\begin{aligned}\frac{dE}{dt} &= \int_{\mathbb{R}^n}\int_0^\infty U\frac{\partial U}{\partial t}\,d\xi\,dV = \int_{\mathbb{R}^n}\int_0^\infty U[-\beta(\mathbf{x})\frac{\partial U}{\partial \xi} + D_n\nabla^2 U]\,d\xi\,dV \\ &= -\int_{\mathbb{R}^n}\int_0^\infty \beta(\mathbf{x})U\frac{\partial U}{\partial \xi}\,d\xi\,dV + D_n\int_{\mathbb{R}^n}\int_0^\infty U\nabla^2 U\,d\xi\,dV.\end{aligned}$$

First, integration by parts in the variable ξ gives

$$\int_{\mathbb{R}^n}\int_0^\infty \beta(\mathbf{x})U\frac{\partial U}{\partial \xi}\,d\xi\,dV = \int_{\mathbb{R}^n}\left[\beta(\mathbf{x})U^2\Big|_{\xi=0}^{\infty}\right]dV - \int_{\mathbb{R}^n}\int_0^\infty \beta(\mathbf{x})U\frac{\partial U}{\partial \xi}\,d\xi\,dV.$$

We assume that for any finite $t > 0$ that $U = 0$ as $\xi \to \infty$. Given $\beta(\mathbf{x}) > 0$, then $U = 0$ at $\xi = 0$ for any $t > 0$. Thus, $\int_{\mathbb{R}^n}\int_0^\infty \beta(\mathbf{x})U\frac{\partial U}{\partial \xi}\,d\xi\,dV = 0$. Second, by the Divergence product rule,

$$\int_{\mathbb{R}^n}|\nabla U|^2\,dV = \int_{\partial\mathbb{R}^n} U\nabla U\cdot\hat{\boldsymbol{\eta}}\,dS - \int_{\mathbb{R}^n} U\nabla^2 U\,dV,$$

where $\hat{\boldsymbol{\eta}}$ is the unit outward normal vector. Considering $\lim_{|\mathbf{x}|\to\infty} U = 0$, we have that

$$\int_{\mathbb{R}^n}\int_0^\infty U\nabla^2 U\,d\xi\,dV = -\int_{\mathbb{R}^n}\int_0^\infty |\nabla U|^2\,d\xi\,dV.$$

Therefore, we have that for every $t > 0$,

$$\frac{dE}{dt} = -D_n\int_{\mathbb{R}^n}\int_0^\infty |\nabla U|^2\,d\xi\,dV \leq 0.$$

[4] The energy functional is not meant to be interpreted as physical energy (i.e. it is not kinetic or potential energy), it is a naming convention that is consistent with classical PDE theory [41].

Seeing that $\frac{dE}{dt} \leq 0$, we have $0 \leq E(t) \leq E(0)$.

□

Note that the energy functional $E_V(t) = \frac{1}{2}||V||_2$ also satisfies the inequality $0 \leq E_V(t) \leq E_V(0)$ since for every $t > 0$, $\int_{\mathbb{R}^n} \int_0^\infty \tilde{H}(\xi - \xi_c)U^2 \, d\xi \, d\mathbf{x} \geq 0$.

In the AB model simulation, no agent is removed from the system. Again, we want the PDE solution to match the important physics of the AB model simulation. We do so by proving that the solution U is conserved at each time t over the entire domain $\mathbb{R}^n \times [0, \infty)$.

Theorem 4. *(Conservation) Suppose for any fixed $t > 0$, $U \in L^1(\mathbb{R}^n \times [0, \infty))$ solves (5.6). And suppose $\beta(\mathbf{x}) > 0$ for all $\mathbf{x} \in \mathbb{R}^n$. Then $\int_{\mathbb{R}^n} \int_0^\infty U \, d\xi \, d\mathbf{x} = \int_{\mathbb{R}^n} \int_0^\infty \phi(\mathbf{x}, \xi) \, d\xi \, dV$ for any $t > 0$.*

Proof. By means of a calculation,

$$\begin{aligned}
\frac{\partial}{\partial t} \int_{\mathbb{R}^n} \int_0^\infty U \, d\xi \, dV &= \int_{\mathbb{R}^n} \int_0^\infty \frac{\partial U}{\partial t} \, d\xi \, dV \\
&= \int_{\mathbb{R}^n} \int_0^\infty \left\{ D_n \nabla^2 U - \beta(\mathbf{x}) \frac{\partial U}{\partial \xi} \right\} d\xi \, dV \\
&= \int_{\mathbb{R}^n} \int_0^\infty D_n \nabla^2 U \, d\xi \, dV - \int_{\mathbb{R}^n} \int_0^\infty \beta(\mathbf{x}) \frac{\partial U}{\partial \xi} \, d\xi \, dV \\
&= D_n \int_{\partial \mathbb{R}^n} \int_0^\infty \nabla U \cdot \hat{\boldsymbol{\eta}} \, d\xi \, dS - \int_{\mathbb{R}^n} \beta(\mathbf{x}) \left[U \Big|_{\xi=0}^{\infty} \right] dV.
\end{aligned}$$

Since $\lim_{|\mathbf{x}| \to \infty} U = 0$ we have that the first term is 0. Also, given $\beta(\mathbf{x}) > 0$ for all $x \in \mathbb{R}^n$, then for $t > 0$ we have $U(\mathbf{x}, t, \xi = 0) = 0$, and the second term is also 0. It follows that $\frac{\partial}{\partial t} \int_{\mathbb{R}^n} \int_0^\infty U \, d\xi \, dV = 0$. Therefore, U is conserved. □

5.2.2 Operator-Splitting Semi-Discrete Solution

Using operator-split, semi-discrete solutions is a useful way to prove the existence of solutions and provide additional insight into the PDE solution. In fact, the method of lines is used to prove existence by reformulating a problem by discretizing in spatial dimensions, while keeping the time dimension continuous [89]. Appendix A.2 demonstrates how operator-split, discrete in time formulations of the diffusion and advection-diffusion equations arrive at the fundamental solutions in the limit as the time-step approaches 0.

We approximate a solution to the PDE in (5.6) by splitting the linear operator and then solving the resulting system iteratively. This gives us a solution that is discrete in time and continuous in spatial and absorption dimensions, similar to the Rothe method [8]. We first derive this semi-discrete solution and then show that it is well-posed.

Let $U = \widehat{U}(\mathbf{x}, t|\xi)\overline{U}(\xi, t|\mathbf{x})$, where $\widehat{U}$ leaves ξ fixed and $\overline{U}$ leaves $\mathbf{x}$ fixed. We can see that $\overline{U}\frac{\partial \widehat{U}}{\partial t} + \widehat{U}\frac{\partial \overline{U}}{\partial t} + \beta(\mathbf{x})\widehat{U}\frac{\partial \overline{U}}{\partial \xi} = D_n \overline{U} \nabla^2 \widehat{U}$ and it follows that $\overline{U}\left(\frac{\partial \widehat{U}}{\partial t} - D_n \nabla^2 \widehat{U}\right) +$

$\widehat{U}\left(\frac{\partial \overline{U}}{\partial t} + \beta(\mathbf{x})\frac{\partial \overline{U}}{\partial \xi}\right) = 0$. Assuming that $\overline{U}$ and $\widehat{U}$ are not identically 0, we can then solve the following PDEs

$$\begin{cases} \frac{\partial \widehat{U}}{\partial t} - D_n \nabla^2 \widehat{U} = 0, & \mathbf{x} \in \mathbb{R}^n, t > 0, \\ \widehat{U} = \hat{\phi}(\mathbf{x}|\xi), & \mathbf{x} \in \mathbb{R}^n, t = 0, \\ \lim_{|\mathbf{x}|\to\infty} \widehat{U} = 0, & \mathbf{x} \in \mathbb{R}^n, t > 0, \end{cases} \tag{5.12}$$

$$\begin{cases} \frac{\partial \overline{U}}{\partial t} - \beta(\mathbf{x})\frac{\partial \overline{U}}{\partial \xi} = 0, & \xi \in [0, \infty), t > 0 \\ \overline{U} = \overline{\phi}(\xi|\mathbf{x}), & \xi \in [0, \infty), t = 0. \end{cases} \tag{5.13}$$

Since the PDE (5.6) is classified as having mixed-type, it seems natural to split the operator into a parabolic and a hyperbolic problem.

We solve the system in (5.12) using the method of Green's functions and convoluting[5] with the initial condition:

$$\widehat{U} = G(\mathbf{x}, t) * \hat{\phi}(\mathbf{x}|\xi), \quad \forall \xi \geq 0, t > 0, \tag{5.14}$$

where

$$G(\mathbf{x}, t) = \frac{1}{(4\pi D_n t)^{n/2}} \exp\left\{-\frac{|\mathbf{x}|^2}{4D_n t}\right\}, \qquad t > 0, \tag{5.15}$$

is the fundamental solution of the diffusion equation in $\mathbb{R}^n$ (as derived in Appendix A.1.2). We solve (5.13) using the method of characteristics:

$$\overline{U} = \overline{\phi}(\xi - \beta(\mathbf{x})t|\mathbf{x}), \quad \forall \mathbf{x} \in \mathbb{R}^n, \qquad t > 0. \tag{5.16}$$

Our solution of (5.6) alternates between (5.14) and (5.16) as the solution marches forward in time. As we are not solving the system simultaneously, we choose a length of time, $0 < \tau \ll 1$, in which each solution is valid. We denote the solution at time $t = m\tau$ as $U^m(\mathbf{x}, \xi)$. The following iterative algorithm solves the semi-discrete, operator splitting system:

- Initialize $U^0(\mathbf{x}, \xi) = \phi(\mathbf{x}, \xi)$
- For $m = 1, 2, \ldots$:
  - ◊ $\overline{U}^{m-1}(\mathbf{x}|\xi) = U^{m-1}(\mathbf{x}, \xi)$
  - ◊ $\widehat{U}^m(\xi|\mathbf{x}) = \overline{U}^{m-1}(\mathbf{x}|\xi - \beta(\mathbf{x})\tau)$
  - ◊ $U^m(\mathbf{x}, \xi) = G(\mathbf{x}, \tau) * \widehat{U}^m(\xi|\mathbf{x})$

Combining these solutions gives us the recurrence relation for the semi-discrete solution with time step τ:

$$U^{m+1}(\mathbf{x}, \xi) = G(\mathbf{x}, \tau) * U^m(\mathbf{x}, \xi - \beta(\mathbf{x})\tau). \tag{5.17}$$

Additionally, we can use our recurrence relation to rewrite the solution at $t = m\tau$ in terms of the initial condition $\phi(\mathbf{x}, \xi)$, given as

$$U^m(\mathbf{x}, \xi) = G(\mathbf{x}, \tau) *^m \phi(\mathbf{x}, \xi - \beta(\mathbf{x})m\tau), \quad \forall (\mathbf{x}, t) \in \mathbb{R}^n \times [0, \infty). \tag{5.18}$$

[5]We define the convolution of two functions $f, g \in L^1(\mathbb{R}^n)$ as the integral $f * g = \int_{\mathbb{R}^n} f(\mathbf{y})g(\mathbf{x} - \mathbf{y})\, d\mathbf{y}$

5.2.3 Existence

Our semi-discrete solution for $U^m(\mathbf{x}, \xi)$, given in (5.18), depends on the recurrence time step τ and the number of iterations m. So, we define

$$z_{m,\tau}(\mathbf{x}, \xi) \equiv G(\mathbf{x}, \tau) *^m \phi(\mathbf{x}, \xi - \beta(\mathbf{x})m\tau) \tag{5.19}$$

as the approximation[6] of $U(\mathbf{x}, m\tau, \xi)$, accounting for the choices of both τ and m (the same notation as used in [16]). We want to show that the $L^1(\mathbb{R}^n \times [0, \infty))$ limit, $\mathcal{U}(\mathbf{x}, t, \xi)$, of the sequence $\left\{z_{m,t/m}\right\}_{m\in\mathbb{N}}$ exists. That is, the limit of the recurrence relation for a time t exists when the recurrence time step, $\tau = t/m$, approaches 0. If this limit exists, it proves the existence of a solution, $U(\mathbf{x}, t, \xi)$, to the governing PDE, given in (5.6).

For the L^1 limit to make sense, we first need to show that $z_{m,\tau} \in L^1(\mathbb{R}^n \times [0, \infty))$.

Lemma 1. *Suppose $\phi \in L^1(\mathbb{R}^n \times [0, \infty))$ and $z_{m,\tau}(\mathbf{x}, \xi) = G(\mathbf{x}, \tau) *^m \phi(\mathbf{x}, \xi - \beta(\mathbf{x})m\tau)$ for all $m \in \mathbb{N}, \tau > 0$. Then $z_{m,\tau}(\mathbf{x}, \xi) \in L^1(\mathbb{R}^n \times [0, \infty))$, for all $\mathbf{x} \in \mathbb{R}^n, \xi \geq 0$.*

Proof. We know that $G(\mathbf{x}, \tau) \in L^1(\mathbb{R}^n \times [0, \infty))$. By reason that $L^1(\mathbb{R}^n \times [0, \infty))$ is closed under convolution, we have that $G(\mathbf{x}, \tau) *^m \phi(\mathbf{x}, \xi - \beta(\mathbf{x})m\tau) \in L^1(\mathbb{R}^n \times [0, \infty))$.

□

Lemma 2. *For any $t > 0$, $G(\mathbf{x}, t/m) *^m \delta(\xi) \to \delta(\mathbf{x}, \xi)$ as $m \to \infty$ in $L^1(\mathbb{R}^n \times [0, \infty))$.*

Proof. We know that $\lim_{m\to\infty} \int_{\mathbb{R}^n} |G(\mathbf{x}, t/m) - \delta(\mathbf{x})| \, d\mathbf{x} = 0$, so it follows that $\lim_{m\to\infty} ||G(\mathbf{x}, t/m) * \delta(\xi) - \delta(\mathbf{x}, \xi)||_1 = 0$. First, we show, via induction, that $\lim_{m\to\infty} ||G(\mathbf{x}, t/m) *^h \delta(\xi) - \delta(\mathbf{x}, \xi)||_1 = 0$ for any $h \in \mathbb{N}$.

As a base case, we show that $\lim_{m\to\infty} ||(G * G)(\mathbf{x}, t/m) * \delta(\xi) - \delta(\mathbf{x}, \xi)||_1 = 0$. By the Dominated Convergence theorem, we can see that

$$\begin{aligned}\lim_{m\to\infty} G * G(\mathbf{x}, t/m) &= \int_{\mathbb{R}^n} \left(\lim_{m\to\infty} G(\mathbf{x} - \mathbf{y}, t/m)\right)\left(\lim_{m\to\infty} G(\mathbf{y}, t/m)\right) d\mathbf{y} \\ &= \int_{\mathbb{R}^n} \delta(\mathbf{x} - \mathbf{y})\delta(\mathbf{x}) \, d\mathbf{y} = \delta(\mathbf{x}).\end{aligned}$$

By calculation,

$$\begin{aligned}\lim_{m\to\infty} ||(G * G)(\mathbf{x}, t/m) * \delta(\xi) - \delta(\mathbf{x}, \xi)||_1 &= || \lim_{m\to\infty} (G * G)(\mathbf{x}, t/m) * \delta(\xi) - \delta(\mathbf{x}, \xi)||_1 \\ &= ||\delta(\mathbf{x}, \xi) - \delta(\mathbf{x}, \xi)||_1 = 0.\end{aligned}$$

[6] We could also make a similar proof for approximating V with $z_{m,\tau}(\mathbf{x}, \xi) \equiv G(\mathbf{x}, \tau) *^m \left[\phi(\mathbf{x}, \xi - \beta(\mathbf{x})m\tau)\mathbf{1}_{[0,\xi_c)}(\xi - \beta(\mathbf{x})m\tau - \xi_c)\right]$. The indicator function is a result of solving the same operator splitting system as U with the additional equation

$$\begin{cases} \tilde{V}_t = -\tilde{H}(\xi - \xi_c)\tilde{V}, & \mathbf{x} \in \mathbb{R}^n, \xi \in [0, \infty), t > 0 \\ \tilde{V} = \bar{V}, & \mathbf{x} \in \mathbb{R}^n, \xi \in [0, \infty), t = 0. \end{cases}$$

Now, we can assume that $\lim_{m\to\infty}||G(\mathbf{x},t/m)*^h\delta(\xi)-\delta(\mathbf{x},\xi)||_1=0$ for some $h\in\mathbb{N}$. We can calculate that

$$\begin{aligned}\lim_{m\to\infty}||G*[G*^h(\mathbf{x},t/m)\delta(\xi)]-\delta(\mathbf{x},\xi)||_1 &= ||\lim_{m\to\infty}G*[G(\mathbf{x},t/m)*^h\delta(\xi)]-\delta(\mathbf{x},\xi)||_1\\ &= ||\delta(\mathbf{x},\xi)-\delta(\mathbf{x},\xi)||_1=0\end{aligned}$$

by the inductive assumption. It follows that

$$\begin{aligned}\lim_{m\to\infty}||G(\mathbf{x},t/m)*^{h+1}\delta(\xi)-\delta(\mathbf{x},\xi)||_1 &= \lim_{m\to\infty}||G*[G(\mathbf{x},t/m)*^h\delta(\xi)]-\delta(\mathbf{x},\xi)||_1\\ &= ||\lim_{m\to\infty}G*[G(\mathbf{x},t/m)*^h\delta(\xi)]-\delta(\mathbf{x},\xi)||_1\\ &= ||\delta(\mathbf{x},\xi)-\delta(\mathbf{x},\xi)||_1=0\end{aligned}$$

for all $h\in\mathbb{N}$.

If we define $h=m$ for $m\in\mathbb{N}$, then $\lim_{m\to\infty}||G(\mathbf{x},t/m)*^m\delta(\xi)-\delta(\mathbf{x},\xi)||_1=0$. □

Lemma 3. *Suppose $\phi\in L^1(\mathbb{R}^n\times[0,\infty))$ and $z_{m,t/m}(\mathbf{x},\xi)=G(\mathbf{x},t/m)*^m\phi(\mathbf{x},\xi-\beta(\mathbf{x})t)$ for any $m\in\mathbb{N},t>0$, as defined in (5.19). Then $\left\{z_{m,t/m}\right\}_{m\in\mathbb{N}}$ is a Cauchy sequence in $L^1(\mathbb{R}^n\times[0,\infty))$.*

Proof. We want to show

$$\lim_{p,q\to\infty}||z_{p,t/p}(\mathbf{x},\xi)-z_{q,t/q}(\mathbf{x},\xi)||_1=0.$$

From Lemma 2 we know that, for any $m\in\mathbb{N}$, $\lim_{m\to\infty}||G(\mathbf{x},t/m)*^m\delta(\xi)-\delta(\mathbf{x},\xi)||_1=0$. Then

$$\begin{aligned}\lim_{m\to\infty}||z_{m,t/m}(\mathbf{x},\xi)-\phi(\mathbf{x},\xi-\beta(\mathbf{x})t)||_1 &=\\ &= \lim_{m\to\infty}||G(\mathbf{x},t/m)*^m\phi(\mathbf{x},\xi-\beta(\mathbf{x})t)-\delta(\mathbf{x},\xi)*\phi(\mathbf{x},\xi-\beta(x)t)||_1\\ &\le \lim_{m\to\infty}||G(\mathbf{x},t/m)*^m\delta(\xi)-\delta(\mathbf{x},\xi)||_1||\phi(\mathbf{x},\xi-\beta(\mathbf{x})t)||_1=0.\end{aligned}$$

It follows that

$$\begin{aligned}\lim_{p,q\to\infty}||z_{p,t/p}(\mathbf{x},\xi)-z_{q,t/q}(\mathbf{x},\xi)||_1 &=\\ &= \lim_{p,q\to\infty}||z_{p,t/p}(\mathbf{x},\xi)-\phi(\mathbf{x},\xi-\beta(\mathbf{x})t)+\phi(\mathbf{x},\xi-\beta(\mathbf{x})t)-z_{q,t/q}(\mathbf{x},\xi)||_1\\ &\le \lim_{p\to\infty}||z_{p,t/p}(\mathbf{x},\xi)-\phi(\mathbf{x},\xi-\beta(\mathbf{x})t)||_1+\lim_{q\to\infty}||z_{q,t/q}(\mathbf{x},\xi)-\phi(\mathbf{x},\xi-\beta(\mathbf{x})t)||_1.\end{aligned}$$

Therefore, $\lim_{p,q\to\infty}||z_{p,t/p}(\mathbf{x},\xi)-z_{q,t/q}(\mathbf{x},\xi)||_1=0$. □

Theorem 5. *(Existence) Suppose $\phi\in L^1(\mathbb{R}^n\times[0,\infty))$. There exists a solution, U, to the governing PDE:*

$$\begin{cases}\frac{\partial U}{\partial t}+\beta(\mathbf{x})\frac{\partial U}{\partial\xi}=D_n\nabla^2U, & \mathbf{x}\in\mathbb{R}^n,\ \xi\in[0,\infty),\ t>0,\\ U=\phi(\mathbf{x},\xi), & \mathbf{x}\in\mathbb{R}^n,\ \xi\in[0,\infty),\ t=0,\\ \lim_{|\mathbf{x}|\to\infty}U=0, & \mathbf{x}\in\mathbb{R}^n,\ \xi\in[0,\infty),\ t>0,\end{cases}\tag{5.20}$$

such that, for any $t\ge0$, $U\in L^1(\mathbb{R}^n\times[0,\infty))$.

Proof. Choose any $\mathbf{x} \in \mathbb{R}^n$, $\xi \in [0, \infty)$, and any $t > 0$. Suppose $\phi \in L^1(\mathbb{R}^n \times [0, \infty))$ and define $z_{m,\tau}(\mathbf{x}, \xi) = G(\mathbf{x}, \tau) *^m \phi(\mathbf{x}, \xi - \beta(\mathbf{x})m\tau)$ for any $m \in \mathbb{N}$, $\tau > 0$. By Lemma 1 and Lemma 3 we know that $z_{m,t/m} \in L^1(\mathbb{R}^n \times [0, \infty))$ is a Cauchy sequence. On account of L^1 being complete, there exists a $\mathcal{U} \in L^1(\mathbb{R}^n \times [0, \infty))$ such that $\lim_{m\to\infty} ||z_{m,t/m}(\mathbf{x}, \xi) - \mathcal{U}(\mathbf{x}, t, \xi)||_1 = 0$. Since $z_{m,t/m}(\mathbf{x}, \xi)$ satisfies the operator-split PDE for all $m \in \mathbb{N}$, we know that $\mathcal{U}(\mathbf{x}, t, \xi)$ satisfies the operator-split PDE. Therefore $\mathcal{U}(\mathbf{x}, t, \xi)$ satisfies the time-continuous PDE. □

5.2.4 Uniqueness & Continuous Dependence on Initial Data

Theorem 6. *(Uniqueness) The solution to PDE* (5.6) *is unique.*

Proof. Suppose we have two solutions, $U_1, U_2 \in L^1(\mathbb{R}^n \times [0, \infty))$ to the PDE (5.6). We define $W = U_2 - U_1$. Given (5.6) is linear, we know $W(\mathbf{x}, t, \xi)$ solves the PDE:

$$\begin{cases} \frac{\partial W}{\partial t} + \beta(\mathbf{x})\frac{\partial W}{\partial \xi} = D_n \nabla^2 W, & x \in \mathbb{R}^n,\ \xi \in [0, \infty),\ t > 0, \\ W = 0, & x \in \mathbb{R}^n,\ \xi \in [0, \infty),\ t = 0, \\ \lim_{|\mathbf{x}|\to\infty} W = 0, & x \in \mathbb{R}^n,\ \xi \in [0, \infty),\ t > 0. \end{cases} \tag{5.21}$$

From the energy argument in Theorem 3, we know that

$$0 \le E_w(t) \le E_w(0).$$

Since $E_w(0) = \frac{1}{2}\int_{\mathbb{R}^n}\int_0^\infty W(\mathbf{x}, 0, \xi)^2\, d\xi\, d\mathbf{x} = 0$, we know that $E_w(t) = 0$ for all t. By definition of $E_w(t)$, we demonstrated that

$$0 \le \int_{\mathbb{R}^n}\int_0^\infty \left(U_1(\mathbf{x}, t, \xi) - U_2(\mathbf{x}, t, \xi)\right)^2\, d\xi\, d\mathbf{x} = E_w(t) = 0.$$

Therefore, $U_1(\mathbf{x}, t, \xi) = U_2(\mathbf{x}, t, \xi)$ almost everywhere. □

Theorem 7. *(Continuous Dependence on Initial Data) Consider any $\epsilon > 0$. Suppose U_1 satisfies the PDE*

$$\begin{cases} \frac{\partial U}{\partial t} + \beta(\mathbf{x})\frac{\partial U}{\partial \xi} = D_n \nabla^2 U, & \mathbf{x} \in \mathbb{R}^n,\ \xi \in [0, \infty),\ t > 0, \\ U = \phi_1(\mathbf{x}, \xi), & \mathbf{x} \in \mathbb{R}^n,\ \xi \in [0, \infty),\ t = 0, \\ \lim_{|\mathbf{x}|\to\infty} U = 0, & \mathbf{x} \in \mathbb{R}^n,\ \xi \in [0, \infty),\ t > 0,, \end{cases} \tag{5.22}$$

and U_2 satisfies the PDE

$$\begin{cases} \frac{\partial U}{\partial t} + \beta(\mathbf{x})\frac{\partial U}{\partial \xi} = D_n \nabla^2 U, & \mathbf{x} \in \mathbb{R}^n,\ \xi \in [0, \infty),\ t > 0, \\ U = \phi_2(\mathbf{x}, \xi), & \mathbf{x} \in \mathbb{R}^n,\ \xi \in [0, \infty),\ t = 0, \\ \lim_{|\mathbf{x}|\to\infty} U = 0, & \mathbf{x} \in \mathbb{R}^n,\ \xi \in [0, \infty),\ t > 0, \end{cases} \tag{5.23}$$

where $||\phi_1(\mathbf{x}, \xi) - \phi_2(\mathbf{x}, \xi)||_2 < \epsilon$. Then $||U_1 - U_2||_2 < \epsilon$.

Proof. We define $W = U_1 - U_2$. As (5.22) and (5.23) are both linear, W solves the PDE

$$\begin{cases} \frac{\partial W}{\partial t} + \beta(\mathbf{x})\frac{\partial W}{\partial \xi} = D_n \nabla^2 W, & \mathbf{x} \in \mathbb{R}^n,\ \xi \in [0,\infty),\ t > 0, \\ W = \phi_1(\mathbf{x},\xi) - \phi_2(\mathbf{x},\xi), & \mathbf{x} \in \mathbb{R}^n,\ \xi \in [0,\infty),\ t = 0, \\ \lim_{|\mathbf{x}|\to\infty} W = 0, & \mathbf{x} \in \mathbb{R}^n,\ \xi \in [0,\infty),\ t > 0. \end{cases} \tag{5.24}$$

Let us define the energy of (5.24) as

$$E_w(t) = \frac{1}{2}\int_{\mathbb{R}^n}\int_0^\infty W^2\, d\xi\, d\mathbf{x} = \frac{1}{2}||W(t)||_2.$$

By the same argument in the proof of Theorem 3, we have that $0 \le ||W(\mathbf{x},t,\xi)||_2 \le ||W(\mathbf{x},0,\xi)||_2$. Since $||W(\mathbf{x},0,\xi)||_2 = ||\phi_1(\mathbf{x},\xi) - \phi_2(\mathbf{x},\xi)||_2 < \epsilon$ and $||W(\mathbf{x},t,\xi)||_2 = ||U_1(\mathbf{x},,t,\xi) - U_2(\mathbf{x},t,\xi)||_2$, we have that

$$0 \le ||U_1(\mathbf{x},t,\xi) - U_2(\mathbf{x},t,\xi)||_2 \le ||\phi_1(\mathbf{x},\xi) - \phi_2(\mathbf{x},\xi)||_2 < \epsilon.$$

□

From the energy argument in Theorem 3, we know that the PDE for V also satisfies the properties of uniqueness and continuous dependence on initial data. Thus, the model for V is also well-posed.

5.2.5 Explicit Solution for Constant Absorption Case

Suppose that the absorption term, $\beta > 0$, for the free-space 1-d cumulative absorption equation 5.5 is constant. We can find an explicit solution to the equation.

Theorem 8. *Let $\beta \ge 0$ be constant and let $\phi \in L^1(\mathbb{R})$ for any $\xi > 0$. Then $U(x,t,\xi) = G(x,2t) * \phi(x,\xi - 2\beta t)$ solves (5.5) exactly, where $G(x,t)$ is the fundamental solution to the diffusion equation in $\mathbb{R}$,*

$$G(x,t) = \frac{1}{\sqrt{4\pi D_n t}}\exp\left\{-\frac{x^2}{4Dt}\right\}, \qquad t > 0.$$

Proof. By definition, $G \in L^1(\mathbb{R})$ for any $t \ge 0$. We can then compute the following:

$$\frac{\partial U}{\partial t} = \frac{\partial}{\partial t}\left[G(x,2t) * \phi(x,\xi-2\beta t)\right] = \frac{1}{2}\left[2\frac{\partial G(x,2t)}{\partial t}\right] * \phi(x,\xi-2\beta t) + \frac{1}{2}G(x,2t) * \left[-2\beta\frac{\partial \phi(x,\xi-2\beta t)}{\partial t}\right]$$

$$\frac{\partial U}{\partial \xi} = \frac{\partial}{\partial \xi}\left[G(x,2t) * \phi(x,\xi-2\beta t)\right] = G(x,2t) * \frac{\partial \phi(x,\xi-2\beta t)}{\partial \xi}$$

$$\frac{\partial U}{\partial t} = \frac{\partial}{\partial t}\left[G(x,2t) * \phi(x,\xi-2\beta t)\right] = \frac{\partial^2 G(x,2t)}{\partial x^2} * \phi(x,\xi-2\beta t)$$

Inserting the above expressions into (5.5) gives us

$$\left\{\frac{\partial G(x,2t)}{\partial t} * \phi(x,\xi-2\beta t) + G(x,2t) * \left[-\beta\frac{\partial \phi(x,\xi-2\beta t)}{\partial t}\right]\right\} + \beta\left\{G(x,2t) * \frac{\partial \phi(x,\xi-2\beta t)}{\partial \xi}\right\} = D\left\{\frac{\partial^2 G(x,2t)}{\partial x^2} * \phi(x,\xi-2\beta t)\right\}.$$

After rearranging and grouping terms, we have

$$\left\{\frac{\partial G(x,2t)}{\partial t} * \phi(x,\xi-2\beta t) - D\left[\frac{\partial^2 G(x,2t)}{\partial x^2} * \phi(x,\xi-2\beta t)\right]\right\} + \left\{G(x,2t) * \left[-\beta\frac{\partial \phi(x,\xi-2\beta t)}{\partial t}\right] + \beta\left[G(x,2t) * \frac{\partial \phi(x,\xi-2\beta t)}{\partial \xi}\right]\right\} = 0.$$

Since D, β are constants, we can insert them into the convolutions. Using the linearity of integration helps us recover:

$$\phi(x,\xi-2\beta t)*\left\{\frac{\partial G(x,2t)}{\partial t} - D\frac{\partial^2 G(x,2t)}{\partial x^2}\right\}+G(x,2t)*\left\{-\beta\frac{\partial \phi(x,\xi-2\beta t)}{\partial t} + \beta\frac{\partial \phi(x,\xi-2\beta t)}{\partial t}\right\}.$$

Since G is the fundamental solution of the diffusion equation, the first term is 0. Therefore, $U(x,t,\xi) = G(x,2t) * \phi(x,\xi-2\beta t)$ solves (5.5) exactly. □

Note that the constant absorption coefficient, β, acts like a delay term in the ξ variable.

5.3 Numerical Approximation

5.3.1 Fully Discrete Derivation

We are primarily interested in calculating the spatially-variable, total density of agents in the live state, p. While demonstrating that the PDE models for U and V are both well-posed, we explain how the only difference in approximate solutions was multiplying by an indicator function $\mathbf{1}_{[0,\xi_c)}(\xi)$. This leads to the fact that the value of $p(\mathbf{x},t)$ using either method is identical. So for our numerical computation, we compute the spatially-variable, total density of agents in the initial live state with $p(\mathbf{x},t) = \int_0^{\xi_c} U(\mathbf{x},t,\xi)\,d\xi$. We derive this numerical approximation within the spatial domain in 1-d, but the method can easily extend to higher dimensions. Considering that we first solve (5.6) for U and then integrate to solve for p, we discretize the region $\mathbb{R}\times[0,\infty)$ using cell volumes (as opposed to discrete nodes). This spatial discretization ensures that we can compute an exact integral for p. We divide the spatial component into M bins[7] of width δx and the absorption component into K bins of width $\delta\xi$; the cell volumes have area $\delta x\delta\xi$. We denote the numerical time-step as δt.

These cell volumes are defined as $\omega_{i,k} = B(x_i,\delta x/2)\times[\xi_k,\xi_{k+1})$, where δx is the spatial discretization step-size and $B(x_i,\delta x/2) = \{y\in\mathbb{R} : |x_i - y| < \delta x/2\}$. For the following derivations, the spatial location is indexed by i and the cumulative absorption amount is indexed by k. We then define $u_{i,k}^m \approx U^m(x_i,\xi_k)$ as

$$u_{i,k}^m = \frac{1}{\delta x\,\delta\xi}\int_{\omega_{i,k}} U^m(y,z)\,dy\,dz, \tag{5.25}$$

[7] The analytic solution requires the spatial domain to be $\mathbb{R}$. However, numerically, we need to choose a finite domain. We choose M such that $G(M\,\delta x/2,\delta t)$ is bounded close to 0. Similarly, the absorption domain is $[0,\infty)$. Our solution of interest is within the domain $[0,\xi_c)$ and hence, we choose K such that $K\delta\xi$ is larger than ξ_c.

the average value of U^m in the cell volume $\omega_{i,k}$ as used in finite volume methods [76]. Note that the continuous and semi-discrete solution is capitalized, $U(x,t,\xi)$ or $U^m(x,\xi)$, whereas the fully discrete solution is in lower-case, $u^m_{i,k}$.

We know the semi-discrete recurrence relation $U^{m+1}(x,\xi) = G(x,\tau) * U^m(x,\xi-\beta(x)\tau)$ from equation (5.17). This solution is fully discretized by integrating over the cell volume $\omega_{i,k}$ and assigning δt as the numerical time-step. By recalling that $u^m_{i,k}$ is piece-wise continuous over $\omega_{i,k}$, we can solve the convolution exactly with the approximated solution:

$$\begin{aligned}
\int_{\omega_{i,k}} G(x,\delta t) * U^m(x,\xi-\beta(x)\delta t)\,d\xi\,dx &= \int_{\omega_{i,k}}\int_{\mathbb{R}} G(y,\delta t)U^m(x-y,\xi-\beta(x)\delta t)\,dy\,d\xi\,dx \\
&= \sum_{j\in\mathbb{Z}} \int_{B(x_j,\delta x/2)}\int_{B(x_i,\delta x/2)}\int_{\xi_k}^{\xi_{k+1}} G(y,\delta t)U^m(x-y,\xi-\beta(x)\delta t)\,d\xi\,dx\,dy \\
&= \sum_{j\in\mathbb{Z}} \int_{B(x_j,\delta x/2)} \left[G(y,\delta t)\int_{B(x_i,\delta x/2)}\int_{\xi_k}^{\xi_{k+1}} U^m(x-y,\xi-\beta(x)\delta t)\,d\xi\,dx \right] dy \\
&= \sum_{j\in\mathbb{Z}} \delta x\,\delta\xi\, u^m_{i-j,k} \int_{B(x_j,\delta x/2)} G(y,\delta t)\,dy.
\end{aligned}$$

Since $u^{m+1}_{i,k} = \frac{1}{\delta x\,\delta\xi}\int_{\omega_{i,k}} U^m(y,z)\,dy\,dz$, we have

$$u^{m+1}_{i,d_i} = \sum_{j\in\mathbb{Z}} u^m_{i-j,k} \int_{B(x_j,\delta x/2)} G(y,\delta t)\,dy,$$

where $d_i = \lfloor k + \beta(x_i)\delta t \rfloor$, the new absorption index. By calculation[8], we find that

$$G_j = \int_{B(x_j,\delta x/2)} G(y,\delta t)\,dy = \frac{1}{2}\left\{ erf\left(\frac{x_j+\delta x/2}{\sqrt{4D\delta t}}\right) - erf\left(\frac{x_j-\delta x/2}{\sqrt{4D\delta t}}\right)\right\}. \tag{5.26}$$

Our numerical method is then

$$u^{m+1}_{i,d_i} = \frac{1}{2}\sum_{j\in\mathbb{Z}} u^m_{i-j,k}\left\{ erf\left(\frac{x_j+\delta x/2}{\sqrt{4D\delta t}}\right) - erf\left(\frac{x_j-\delta x/2}{\sqrt{4D\delta t}}\right)\right\}. \tag{5.27}$$

We discretize the density $p(x,t)$ as

$$p^m_i = \tfrac{1}{\delta x\,\delta\xi}\int_0^{\xi_c}\int_{B(x_i,\delta x/2)} U^m(y,z)\,dy\,dz \approx \tfrac{1}{\delta x\,\delta\xi}\textstyle\sum_{k\in\mathcal{A}}\int_{\omega_{i,k}} U^m(y,z)\,dy\,dz, \tag{5.28}$$

where $\mathcal{A} = \{k : k\delta\xi < \xi_c\}$. Therefore, we can represent p numerically as $p^m_i = \sum_{k\in\mathcal{A}} u^m_{i,k}$, the exact integral using our piece-wise constant approximate solutions.

[8] In 2-d, we calculate

$$G_{j,k} = \int_{B(\mathbf{x}_{j,k},\delta x/2)} G(\mathbf{y},\delta t)\,d\mathbf{y} = \frac{1}{4}\left\{ erf\left(\frac{x_j+\delta x/2}{\sqrt{4D\delta t}}\right) - erf\left(\frac{x_j-\delta x/2}{\sqrt{4D\delta t}}\right)\right\}\left\{ erf\left(\frac{y_k+\delta x/2}{\sqrt{4D\delta t}}\right) - erf\left(\frac{y_k-\delta x/2}{\sqrt{4D\delta t}}\right)\right\}.$$

5.3.2 Stability

To prove numerical stability, we use discrete energy methods [77]. We can break down the numerical method into two steps: a diffusive step where we perform the convolution,

$$v_{i,k}^{m+1} = \frac{1}{2}\sum_{j\in\mathbb{Z}} u_{i-j,k}^{m}\left\{erf\left(\frac{x_j+\delta x/2}{\sqrt{4D\delta t}}\right) - erf\left(\frac{x_j-\delta x/2}{\sqrt{4D\delta t}}\right)\right\}$$

and an absorption step $u_{i,d_i}^{m+1} = v_{i,k}^{m+1}$ where we change the indexing. Further, we define the discrete energy functional as

$$E^m = \sum_{k=0}^{K}\sum_{i=0}^{M-1}\left(u_{i,k}^{m}\right)^2.$$

To prove stability, we want to show $E^{m+1} - E^m \leq 0$. Note that due to the indexing change, for any i, $\sum_{k=0}^{K}\left(u_{i,k}^{m+1}\right)^2 \leq \sum_{k=0}^{K}\left(v_{i,k}^{m+1}\right)^2$.

We can rewrite our numerical scheme as a matrix-vector product, $\mathbf{v}_k^{m+1} = \mathbf{u}_k^m * G = \mathbf{A}\mathbf{u}_k^m$, where our discrete convolution matrix $\mathbf{A}$ and vector indexing of $\mathbf{u}_k^m$ are the following

$$\mathbf{A} = \begin{bmatrix} G_0 & G_{M-1} & \dots & G_2 & G_1 \\ G_1 & G_0 & G_{M-1} & \dots & G_2 \\ \vdots & G_1 & G_0 & \ddots & \vdots \\ G_{M-2} & & \ddots & \ddots & G_{M-1} \\ G_{M-1} & G_{M-2} & \dots & G_1 & G_0 \end{bmatrix} \quad \mathbf{u}_k^m = \begin{bmatrix} u_{0,k}^m \\ u_{1,k}^m \\ \vdots \\ u_{M-1,k}^m \end{bmatrix}, \tag{5.29}$$

given our definition of G_j, as defined in (5.26).

The difference between the energy functional at subsequent times, having absorbed $\xi \in [k\delta\xi, (k+1)\delta\xi]$ particles, is:

$$\begin{aligned} e_k^{m+1} - e_k^m &= \sum_{i=0}^{M-1}\left(u_{i,k}^{m+1}\right)^2 - \sum_{i=0}^{M-1}\left(u_{i,k}^{m}\right)^2 \\ &\leq \sum_{i=0}^{M-1}\left(v_{i,k}^{m+1}\right)^2 - \sum_{i=0}^{M-1}\left(u_{i,k}^{m}\right)^2 \\ &= \left(\mathbf{A}\mathbf{u}_k^m\right)^2 - \left(\mathbf{u}_k^m\right)^T\mathbf{u}_k^m \\ &= \left(\mathbf{u}_k^m\right)^T\left(\mathbf{A}^T\mathbf{A} - \mathbf{I}\right)\mathbf{u}_k^m, \end{aligned}$$

where $e_k^m \equiv \sum_{i=0}^{M-1}\left(u_{i,k}^m\right)^2$.

Theorem 9. *The spectrum of* $\mathbf{A}^T\mathbf{A} - \mathbf{I}$ *is* $s\left(\mathbf{A}^T\mathbf{A} - \mathbf{I}\right) \leq 0$*, with the matrix* $\mathbf{A}$ *defined in* (5.29) *and the scalars* G_j *defined in* (5.26)*.*

Proof. The discrete convolution matrix $\mathbf{A}$ is a circulant matrix, so it has eigenvalues

$$\lambda_j = G_0 + G_{M-1}\gamma_j + G_{M-2}\gamma_j^2 + \ldots + G_1\gamma_j^{M-1} = \sum_{\ell=0}^{M-1} G_\ell \gamma_j^{M-\ell},$$

for $j = 0, 1, \ldots, M_1$, where $\gamma_j = \exp\left\{\frac{2\pi j}{M}\sqrt{-1}\right\}$ (the M-th root of unity). It follows that the amplitude of the j-th eigenvalue is

$$|\lambda_j| = \left|\sum_{\ell=0}^{M-1} G_\ell \gamma_j^{M-\ell}\right| \leq \sum_{\ell=0}^{M-1} |G_\ell| \left|\gamma_j^{M-\ell}\right| = \sum_{\ell=0}^{M-1} |G_\ell| \,. \tag{5.30}$$

Given $G_\ell \geq 0$ for all ℓ, we have that $|\lambda_j| \leq \sum_{\ell=0}^{M-1} G_\ell$ for all j. Since

$$\begin{aligned} G_\ell &= \frac{1}{2}\left\{erf\left(\frac{x_\ell + \delta x/2}{\sqrt{4D\delta t}}\right) - erf\left(\frac{x_\ell - \delta x/2}{\sqrt{4D\delta t}}\right)\right\} \\ &= \frac{1}{2}\left\{erf\left(\frac{x_\ell + \delta x/2}{\sqrt{4D\delta t}}\right) - erf\left(\frac{x_{\ell-1} + \delta x/2}{\sqrt{4D\delta t}}\right)\right\}, \end{aligned}$$

we have that

$$|\lambda_j| \leq \frac{1}{2}\left\{erf\left(\frac{x_{M-1} + \delta x/2}{\sqrt{4D\delta t}}\right) - erf\left(\frac{x_0 - \delta x/2}{\sqrt{4D\delta t}}\right)\right\} < 1. \tag{5.31}$$

The strict inequality is due to $-1 \leq erf(x) \leq 1$ for all x and M being finite. It follows that the eigenvalues of $\mathbf{A}^T\mathbf{A}$ are $|\lambda_j|^2 < 1$. Therefore, the spectrum of $\mathbf{A}^T\mathbf{A} - \mathbf{I}$ is $s(\mathbf{A}^T\mathbf{A} - \mathbf{I}) < 0$. □

Therefore, $e_k^{m+1} - e_k^m \leq 0$. Consequently,

$$E^{m+1} - E^m = \sum_{k=0}^{K} \left\{e_k^{m+1} - e_k^m\right\} \leq 0,$$

which proves that the numerical method is stable.

5.4 Numerical Results

5.4.1 The 1-d Model

For our 1-dimensional simulations, we perform 10^5 realizations of the AB model with the agent initialized at $x_0 = 0.5$. The agent moves with spatial step size of $\triangle x = 0.01$ and time step $\triangle t = \triangle x^2/2$, so the PDE diffusivity constant is $D = \triangle x^2/(2\triangle t) = 1$. For the corresponding PDE model, we use the stable numerical algorithm detailed in Section 5.3 with a point source at $x_0 = 0.5$. We choose M so that $G_0, G_{M-1} < \varepsilon_{mach}$ and we assign the numerical step sizes as $\delta x = \triangle x$, $\delta t = \triangle t$, and $\delta\xi = \xi_c/2000$. In both the AB and

PDE models, we define the agent absorption function as $\beta(x) = \alpha \int_{B(x,\triangle x/2)} C(x)\, dx$. The α parameter defines the absorption rate of the agent's membrane and, since C has units of chemical particles per length, we see from the definition of $\beta(x)$ that α has units of time^{-1}. For the following examples, we let $\alpha = 0.1$. In each example, we see the solution initially undergoing pure diffusion, until some critical time where agents begin exiting their current state. This critical time can also be seen as the location of a cusp or turning point in the measure of spread graphs.

Example 1: Max Concentration at Starting Location For this example, the chemical concentration $C(x) = \frac{1}{1+10(x-0.5)^2}$ is symmetric and concave down around $x = 0.5$. A comparison of the AB model and our continuum PDE model is shown in Fig. 5.4, for a critical or tolerance threshold of $\xi_c = 10\triangle x\triangle t$. The distribution of cells or agents in the initial live state are shown in color with time on the vertical axis and spatial location on the horizontal axis. The values on Fig. 5.4b at location (x_i, t_m) are the numerical solutions p_i^m from (5.28), which are interpreted as the probability a cell is alive and located within region $B(x_i, \triangle x/2)$ at time t. Since the agents are all initialized at $x_o = 0.5$, we observe a high density of cells close to this point for small time intervals. We note that Fig. 5.4b is smoother than 5.4a since it is a continuous approximation whereas the AB model has agents moving discretely either to the left or right at each time step.

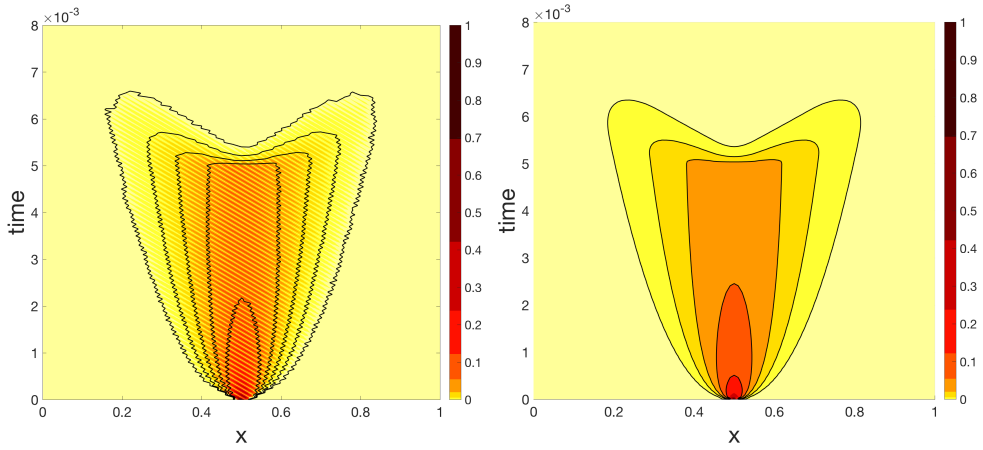

(a) AB Model Simulation (b) PDE Approximation

Figure 5.4: Comparison of the probability distribution of live agents (shown in color) at locations $x \in [0, 1]$ and at time points $t \in [0, 0.008]$. The AB model results are the mean over 10^5 simulations. For both, the chemical concentration is $C(x) = 1/(1+10(x-0.5)^2)$.

Additionally, since $C(x)$ has a max at $x = 0.5$, this causes the probability distribution $p(x, t)$ to become bimodal at approximately $t = 0.0055$. Those cells that have remained close to the initial starting location have absorbed more particles than those that have moved left or right. Hence, cells close to $x = 0.5$ are moving out of the initial live cell state when they reach their absorption capacitance ξ_c.

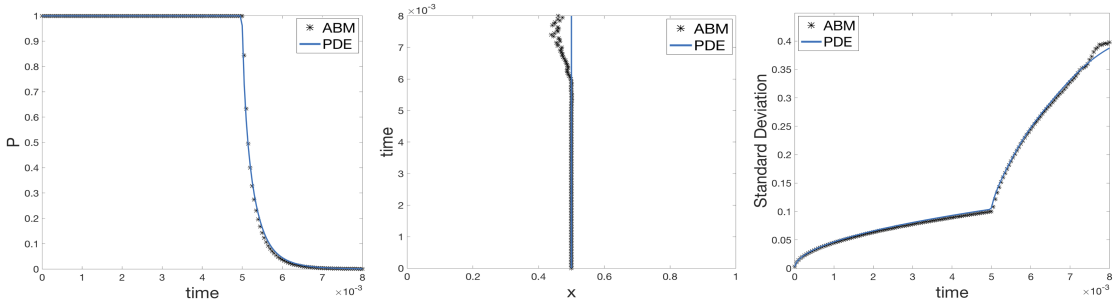

(a) Survival Probability (b) Mean Location (c) Standard Deviation

Figure 5.5: Comparison of the survival probability, as well as mean and standard deviation of the live agent locations, for the AB model (**black** $*$) and the numerical PDE solution (**blue** line) at each time-step for $C(x) = 1/(1 + 10(x - 0.5)^2)$.

The probability an agent is alive at a given time t is the survival probability $P(t)$, calculated as

$$P(t) = \int_{\mathbb{R}} p(x,t)\,dx. \tag{5.32}$$

In Fig. 5.5a, we observe that $P(t)$ for the AB model simulation and PDE approximations match; there is a sharp decrease in survival probability after $t = 0.005$ and the majority of the cells have died at $t = 0.007$.

The mean location of the live agents is calculated as $\mu(t) = \int_{\mathbb{R}} x\hat{p}(x,t)\,dx$, where $\hat{p}(x,t) = p(x,t)/P(t)$ is the normalized value of $p(x,t)$ at each time t. The numerical PDE solution solves for the average value in the interval centered at x_i with radius $\triangle x/2$, $B(x_i, \triangle x/2)$. This allows the calculation of $\mu_{PDE}(t)$, the mean at time $t = m\delta t$, as

$$\mu_{PDE}(t) = \int_{\mathbb{R}} x\hat{p}(x,t)\,dx = \frac{1}{P(t)} \sum_{i=1}^{M-1} p_i^m \int_{B(x_i,\triangle x/2)} x\,dx, \tag{5.33}$$

the exact integral of the approximate piece-wise constant solution. Just as we did when calculating the convolution, we can take p_i^m out of the integral since it is piece-wise constant. In a similar way, we can calculate $\sigma^2_{PDE}(t)$, the variance at time $t = m\delta t$, as

$$\sigma^2_{PDE}(t) = \int_{\mathbb{R}} (x - \mu_{PDE}(t))^2 \hat{p}(x,t)\,dx = \left\{ \tfrac{1}{P(t)} \textstyle\sum_{i=1}^{M-1} p_i^m \int_{B(x_i,\triangle x/2)} x^2\,dx \right\} - \mu_{PDE}(t)^2. \tag{5.34}$$

The mean location of the AB model simulation and PDE approximation is shown in Fig. 5.5b. The chemical concentration $C(x)$ is symmetric around $x = 0.5$, the location where the agents are initialized, and there is no bias in movement ($\ell(x) = r(x) = 0.5$). Hence, we would expect the mean location of agents in the initial state to be centered at $x = 0.5$. We see that until approximately $t = 0.006$, the PDE mean and the AB model mean are close to $x = 0.5$. For times $t > 0.006$, the number of agents in the AB model simulation is relatively small, as shown in Fig. 5.5a. This accounts for the increasing stochastic noise in the mean, as well as the standard deviation, which is shown in Fig. 5.5c.

At each iteration of the AB model simulation, the agent can move either left or right. We see that the agents that remain in the initial state are those that are furthest from $x = 0.5$, where $C(x)$ is smaller than at $x = 0.5$. As a result, the standard deviation is a monotonically increasing function, as seen in Fig. 5.5c. At approximately $t = 0.005$, many cells towards the center of the simulation change state, which causes the "corner" in the standard deviation graph.

Just like URW in Section 2.1.1, we may be interested in how the AB model simulation converges to the cumulative absorption PDE solution as the number of agents, N, increases. To get a sense of the trends, we find the total mean error for a simulation with N agents,

$$E_\mu(N) = \sum_{t_i} |\mu_{ABM}(t_i) - \mu_{PDE}(t_i)|\,,$$

as the summation over each iteration of the absolute difference between the AB model simulation mean and the PDE mean in the time interval $t_i \in [0, 0.008]$. Similarly, we find the total standard deviation error and total survival probability errors as

$$E_\sigma(N) = \sum_{t_i} |\sigma_{ABM}(t_i) - \sigma_{PDE}(t_i)| \text{ and}$$
$$E_P(N) = \sum_{t_i} |P_{ABM}(t_i) - P_{PDE}(t_i)|\,.$$

Similar to the URW, we see in Fig. 5.6 that the mean location data exhibits a log-linear trend. Performing a least-squares approximation on this data as derived in Appendix B, we find that $E_\mu(N) \approx e^{5.3902} N^{-0.5042}$. So the AB model mean converges to the PDE mean at a rate approximately $1/\sqrt{N}$. However, we see that $E_P(N)$ and $E_\sigma(N)$ do not have log-linear convergence. In fact, both error metrics seem to converge to fixed values for $N > 10^5$. This motivates the use of 10^5 agents in the examples.

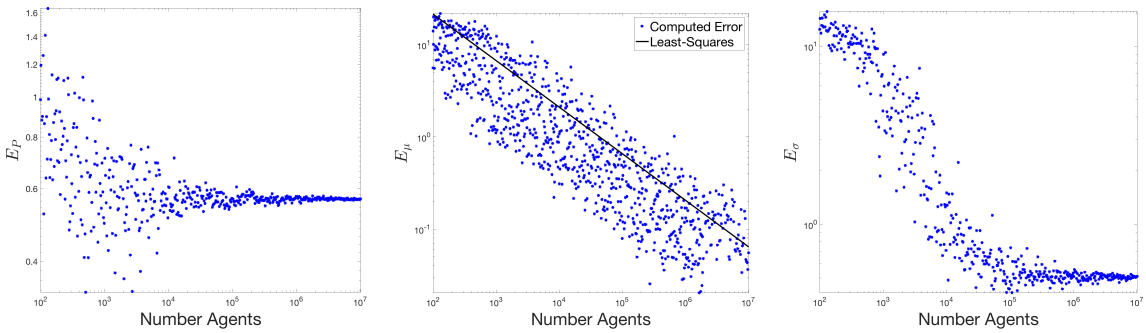

(a) Survival Probability Error (b) Mean Location Error (c) Standard Deviation Error

Figure 5.6: Total error between URW simulation and PDE approximation depending on the number of URW agents. **(a)** Total mean location error $E_P = \sum_{t_i} |P_{ABM}(t_i) - P_{PDE}(t_i)|$ **(b)** Total mean location error $E_\mu = \sum_{t_i} |\mu_{ABM}(t_i) - \mu_{PDE}(t_i)|$ **(c)** Total standard deviation error $E_\sigma = \sum_{t_i} |\sigma_{URW}(t_i) - \sigma_{PDE}(t_i)|$.

Example 2: Decreasing Concentration The chemical concentration is $C(x) = \exp(-x^2)$, which is monotonically decreasing in the interval $[0, 1]$ and all agents or cells are initialized at $x_o = 0.5$. We expect that the agents which tend to move to the right within this interval have a higher probability of remaining in the initial state. As shown in Fig. 5.7, the cells that remain in the initial state tend to be further to the right and again, we have excellent qualitative agreement between the AB model and the new PDE continuum model. In Fig. 5.7a we observe a striped pattern, which is a result of the AB model agents moving only left or right at any given iteration. At a critical threshold of $\xi_c = 10\triangle x\triangle t$, cells are able to achieve a cumulative chemical absorption $\xi > \xi_c$, causing the cell to transition states or die. The survival probability shows this trend in Fig. 5.8a, where there is a sharp decrease in survival probability at $t = 0.055$.

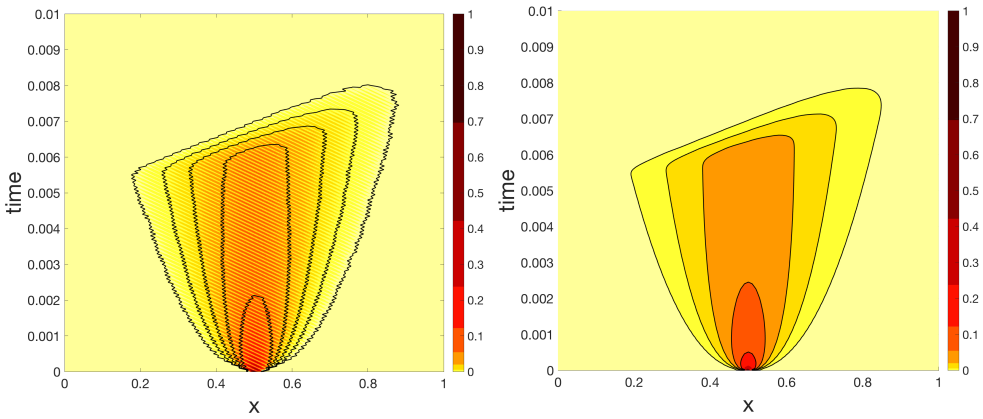

(a) AB Model Simulation (b) PDE Approximation

Figure 5.7: Comparison of the probability distribution of live agents (shown in color) at locations $x \in [0, 1]$ and at time points $t \in [0, 0.1]$. The AB model results are a mean of 10^5 simulations. For both, the chemical concentration is $C(x) = \exp(-x^2)$.

To further characterize the agreement between the AB model simulation and our PDE approximation, we again look at the mean and standard deviation of the location of live cells (with cumulative absorption $\xi < \xi_c$). In Fig. 5.8b, we observe that the mean location (calculated using (5.33)) does move to the right of the initial location $x_o = 0.5$ due to the decreased concentration $C(x)$ to the right of $x = 0.5$ (allowing cells to live in this region for a longer period of time). Again, we see that there is noise in the AB model mean for times $t > 0.008$, when there are relatively few agents in the initial state.

As shown in Fig. 5.8c, the standard deviation of the agents locations is increasing for $0 \leq t \leq 0.005$, which corresponds to the time interval where most cells are alive (see survival probability in Fig. 5.8a). At $t = 0.005$, agents with a cumulative absorption reaching ξ_c begin to change state. Cells to the right of $x_o = 0.5$ tend to remain in the initialized state, which moves the mean to the right and reduces the variance. A majority of the cells have changed state by $t = 0.008$, where the cells that remain are those that continued to move right. Thus, the standard deviation approaches zero. Similar to

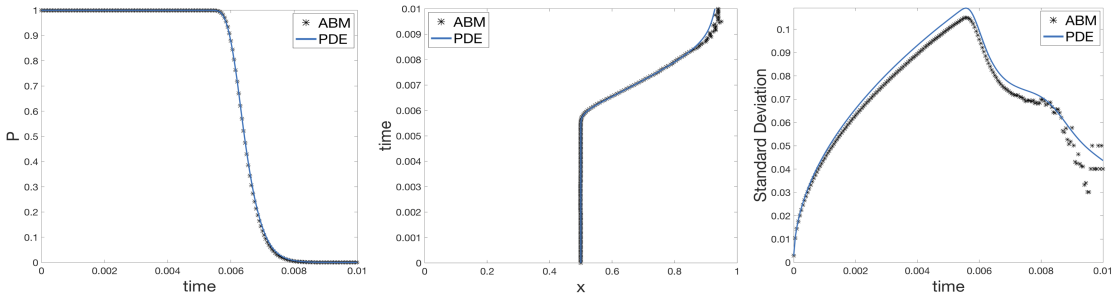

(a) Survival Probability (b) Mean Location (c) Standard Deviation

Figure 5.8: Comparison of the survival probability, as well as mean and standard deviation of the live agent locations, for the AB model (**black** $*$) and the numerical PDE solution (**blue** line) at each time-step for $C(x) = \exp(-x^2)$.

Example 1, we see that as the number of agents in the AB model simulation approaches zero, the stochastic noise influences the variance (Fig. 5.8c).

Example 3: Biased Random Walk Suppose the RW has a constant bias, where ℓ and r denote the probabilities of moving left or right, respectively. Our absorption model is the following PDE

$$\begin{cases} \frac{\partial U}{\partial t} + \beta(x)\frac{\partial U}{\partial \xi} = a\frac{\partial U}{\partial x} + D\frac{\partial^2 U}{\partial x^2}, & x \in \mathbb{R},\ \xi \in [0,\infty),\ t > 0, \\ U = \phi(x,\xi), & x \in \mathbb{R},\ \xi \in [0,\infty),\ t = 0, \\ \lim_{|x|\to\infty} U = 0, & x \in \mathbb{R},\ \xi \in [0,\infty),\ t > 0, \end{cases} \tag{5.35}$$

where $a = \triangle x(\ell - r)/\triangle t$ and $D = \triangle x^2(\ell + r)/(2\triangle t)$. Note that the existence proof also holds if the agent moves with a constant bias. After splitting the linear operator, the only difference between Eq. (5.35) and our initial cumulative absorption model equation in Eq. (5.5) is the form of the Green's function

$$G(x,t) = \frac{1}{4\pi D t}\exp\left\{-\frac{(x-at)^2}{4Dt}\right\}, \quad a = \frac{\triangle x(\ell - r)}{\triangle t},$$

as derived in Appendix A.1.3. Replacing the diffusion Green's function with this advection-diffusion Green's function does not affect the existence proof in Section 5.2.3. Further, by integration by parts and using our free-space boundary condition, we can show that $\int_{\mathbb{R}}\int_0^\infty aUU_x\, d\xi\, dx = 0$. Therefore, the biased model (5.35) satisfies Theorem 1, so we can prove that the PDE (5.35) is well-posed.

We set the chemical concentration as $C(x) = 1/(1 + 10(x - 0.5)^2)$ and the absorption capacitance as $\xi_c = 10\triangle x\triangle t$, the same as in Example 1. However, in contrast to Example 1, we set the probability an agent moves left as $\ell = 0.4$ and the probability an agent moves right as $r = 0.6$. We note that a larger density of agents tend to move to the right. In fact, the graph in Fig. 5.10b initially moves to the right in a straight line at a rate of $0.2\triangle x$.

This is due to the fact that only the biased movement determines the agent locations. The graph of the mean location makes a sudden change around $t = 0.005$, which is when some agents absorb above the threshold ξ_c and begin leaving the live state. At that time, the chemical profile begins to influence the mean location of agents, which also explains the shapes of the distributions in Fig. 5.9.

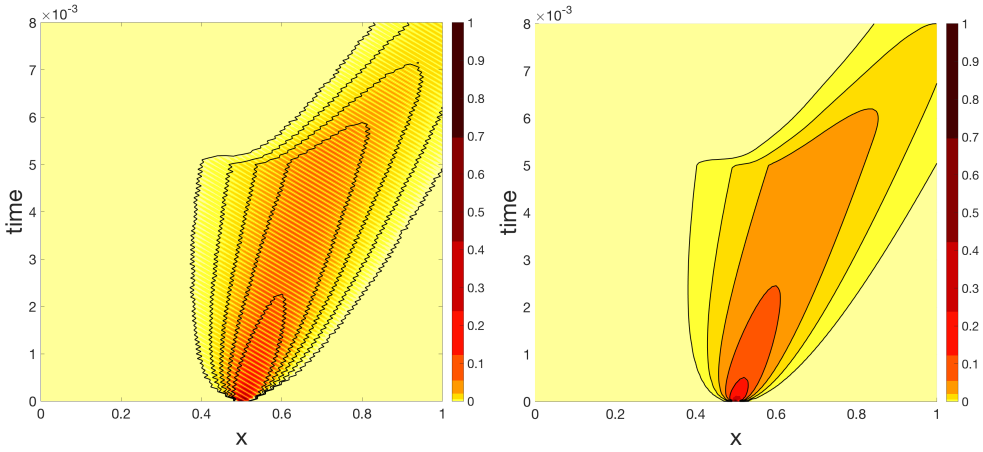

(a) AB Model Simulation (b) PDE Approximation

Figure 5.9: Comparison of the probability distribution of live agents (shown in color) at locations $x \in [0, 1]$ and at time points $t \in [0, 0.1]$. The AB model results are a mean of 10^5 simulations. For both, the chemical concentration is $C(x) = 1/(1 + 10(x - 0.5)^2)$ and movement is biased to the right.

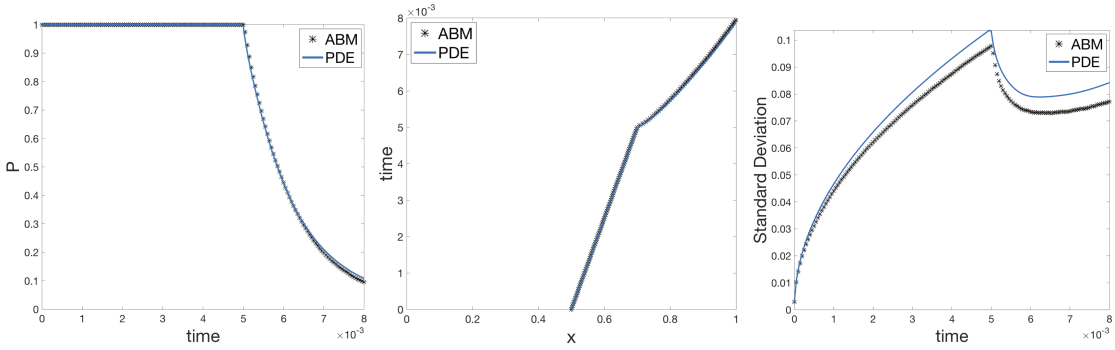

(a) Survival Probability (b) Mean Location (c) Standard Deviation

Figure 5.10: Comparison of the survival probability, as well as mean and standard deviation of the live agent locations, for the AB model (**black** $*$) and the numerical PDE solution (**blue** line) at each time-step for biased motion and $C(x) = 1/(1 + 10(x - 0.5)^2)$.

The survival probability for the AB model and continuum PDE model is shown in Fig. 5.10a, and again there is good agreement between the AB model and PDE solution. In

comparison to the unbiased movement case in Fig. 5.5a, Fig. 5.10a with biased movement begins decreasing at an earlier time, but then decreases at a slower rate.

5.4.2 The 2-d Model

We can readily extend the analysis and numerical methods in Sections 5.2-5.3 to the 2-dimensional case. To account for the increased stochasticity of adding an additional dimension, we initialize 10 million agents. In this example, the agents in the AB model move with spatial step size of $\triangle x = \triangle y = 0.01$ and time step $\triangle t = \triangle x^2/2$. Similarly, the PDE model utilizes a spatial step size of $\delta x = \delta y = \triangle x$, a time step of $\delta t = \triangle t$, and a cumulative absorption step of $\delta\xi = \xi_c/1000$. For both the AB model and PDE model, we set $\beta(\mathbf{x}) = \alpha \int_{B(\mathbf{x},\triangle x/2)} C(\mathbf{x})\, d\mathbf{x}$ where the chemical concentration is $C(x, y) = 0.5(\sin(4\pi x)\sin(4\pi y) + 1)$ and the chemical absorption threshold is $\xi_c = 2\triangle x\triangle y\triangle t$.

The surface plot of the concentration local to the initialized agents in $[0, 1] \times [0, 1]$ is shown in the dashed line contour plots in Fig. 5.11 and Fig. 5.12, where lighter colored lines denote a value closer to 0 and darker colored lines denote a value closer to 1. The concentration is symmetric along the lines $y = x$ and $y = 1-x$. Near the initial location at $(0.5, 0.5)$, there are local concentration minimums along the line $y = -x$. Thus, it makes sense that the probabilities for agents in the initial live state tend to be higher close to these chemical sinks, as shown in Figs. 5.11 and 5.12. In fact, Figs. 5.11(b)-(c) and 5.12(b)-(c) show the probability density function mode bifurcation. That is, the chemical distribution causes p_i^m to evolve into a bi-modal distribution, with each peak located on the line $y = 1 - x$ and equidistant to the line $y = x$. Again, when comparing the survival probability as a function of time, we observe excellent agreement between the AB model and continuum PDE (Fig. 5.13a).

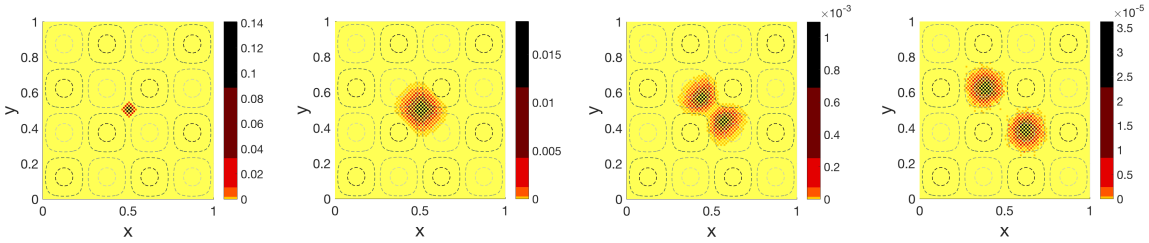

(a) $t = 0.0002$ (b) $t = 0.0017$ (c) $t = 0.0024$ (d) $t = 0.0050$

Figure 5.11: Probability distribution of live agents for the AB model (shown in color) in the region $[0, 1] \times [0, 1]$ at 4 different time points with $\alpha = 0.10$. The AB model results are a mean of 10 million agents. The dashed-line contour plot indicates the chemical concentration, $C(x, y)$.

For multi-dimensional models, we use the statistical measurement of mean squared deviation (MSD) rather than standard deviation. The MSD measures how much the

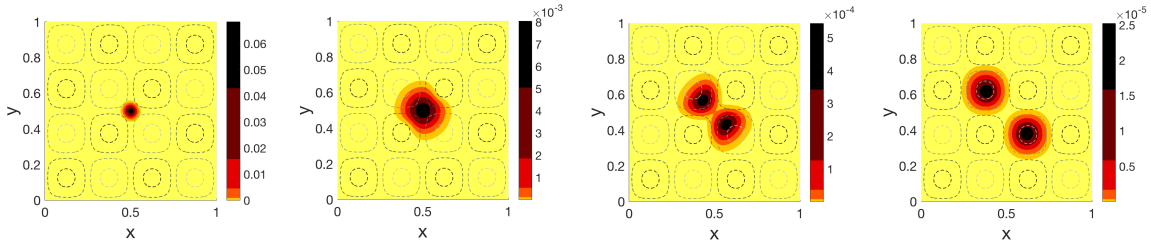

(a) $t = 0.0002$ (b) $t = 0.0017$ (c) $t = 0.0024$ (d) $t = 0.0050$

Figure 5.12: Probability distribution of live agents for the numerical PDE solution (shown in color) in the region $[0, 1]\times[0, 1]$ at 4 different time points with $\alpha = 0.10$. The dashed-line contour plot indicates the chemical concentration, $C(x, y)$.

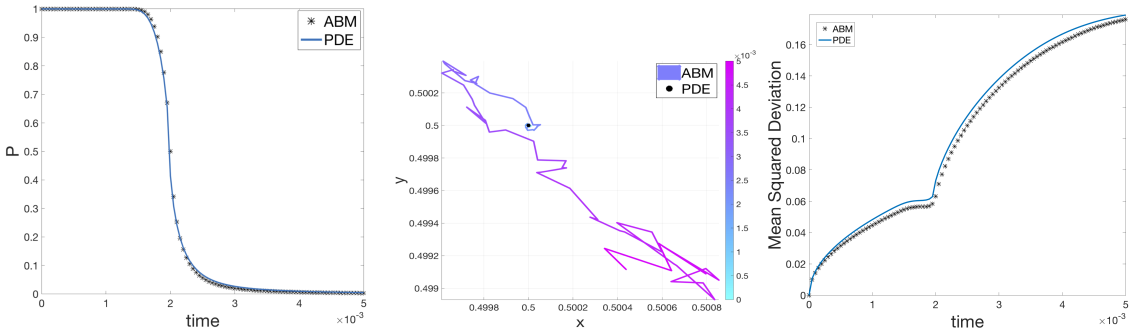

(a) Survival Probability (b) Mean Location (c) Mean Squared Deviation

Figure 5.13: Comparison of the survival probability, mean, and standard deviation of the AB model and the semi-discrete numerical PDE solution at each time-step. The color of the AB model mean in **(b)** corresponds to the time-step. Because the mean location of the numerical PDE approximation is located at (0.5,0.5) for every time-step, we label it using a **black** • to make a visual comparison with the AB model mean easier.

distribution spreads from the mean, $\bar{\mu}(t)$:

$$MSD(t) = \left(\int_{\mathbb{R}^d} (\mathbf{x} - \bar{\mu}(t))^2 \, \hat{p}(\mathbf{x}, t) \, d\mathbf{x} \right)^{1/2}.$$

Unlike the 2-D standard deviation, the MSD does not compute the spread along a given axis.

Fig. 5.13b demonstrates that the mean location of the PDE approximation remains constant at $(0.5, 0.5)$. The AB model mean is not constant. However, since the AB model mean is contained within the region $B((0.5, 0.5), \triangle x/2)$, and travels away from the PDE mean for times $t > 0.003$, we can assume that this is due to the greater influence of stochastic noise as the number of agents in the initial state becomes relatively small. Since there are sufficiently many agents towards the end of the simulation and the mean during this simulation is within the control region $B((0.5, 0.5), \triangle x/2)$, we see in Fig. 5.13c

the MSD of the AB model data is not unduly influenced by the stochastic noise. Hence, the AB model and PDE standard deviation curves match reasonably well throughout the simulations.

We can see the difference in how the model develops if we decrease the absorption proportion parameter to $\alpha = 0.01$ in Fig. 5.14 and Fig. 5.15. The agents diffuse for a longer time period before absorbing sufficient chemical to split. With $\alpha = 0.01$, the distribution forms two peaks around $t = 0.02$ (as shown in Fig. 5.14(d), 5.15(c)), whereas with $\alpha = 0.10$, the distribution forms two peaks around $t = 0.0024$ (as shown in Fig. 5.11(c), 5.12(c)). The pattern is different from $\alpha = 0.10$ as t increases further. Since p_i^m initially diffuses farther before changing states, the distribution eventually settles along additional chemical sinks (as shown in Fig. 5.14(d), 5.15(d)).

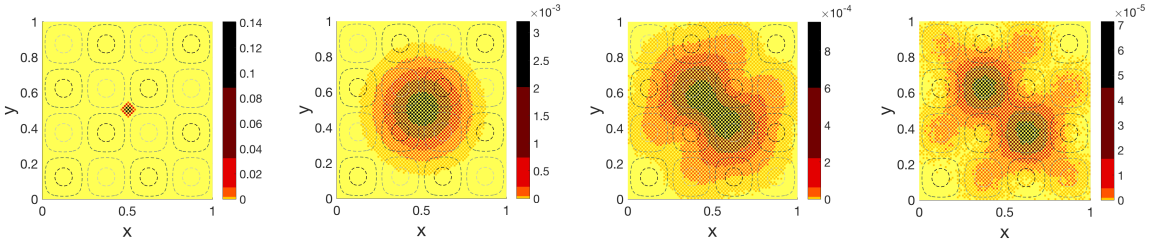

(a) $t = 0.0002$ (b) $t = 0.0100$ (c) $t = 0.0200$ (d) $t = 0.0375$

Figure 5.14: Probability distribution of live agents for the AB model (shown in color) in the region $[0, 1] \times [0, 1]$ at 4 different time points with $\alpha = 0.01$. The AB model results are a mean of 10 million agents. The dashed-line contour plot indicates the chemical concentration, $C(x, y)$.

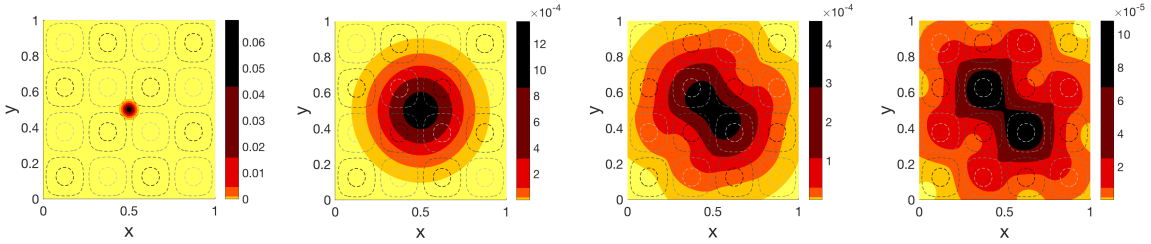

(a) $t = 0.0002$ (b) $t = 0.0100$ (c) $t = 0.0200$ (d) $t = 0.0375$

Figure 5.15: Probability distribution of live agents for the numerical PDE solution (shown in color) in the region $[0, 1] \times [0, 1]$ at 4 different time points with $\alpha = 0.01$. The dashed-line contour plot indicates the chemical concentration, $C(x, y)$.

If we instead choose an $\alpha \ll 1$, the diffusion time of the agents is much faster than the time for the agents to absorb chemical to capacitance. In that case, we can simplify and re-frame the model as a diffusion-dominant absorption model. The derivation and examples of such a model are further developed in Section 5.5.

5.4.3 Mean Occupancy Time

Derivation

We may be interested in the mean time an agent is in the initial live state, which is denoted as the mean occupancy time (MOT). In a manner similar to deriving the mean first passage time in Section 2.1.2, this is the first moment of the total flux out of a particular state.

The total flux out of the initial state can be computed as

$$F(\mathbf{x}, t) = -\frac{\partial}{\partial t} \int_{\mathbb{R}^n} p(\mathbf{x}, t)\, d\mathbf{x}.$$

The negative sign is due to the fact that we are tracking the density exiting the initial state. It follows that the MOT is

$$M = \int_0^\infty tF(\mathbf{x}, t)\, dt. \tag{5.36}$$

Since $p \in L^1(\mathbb{R}^n)$ and for any finite location $\mathbf{x} \in \mathbb{R}^n$, $\lim_{t\to\infty} p(\mathbf{x}, t) = 0$, we can use integration by parts to derive the MOT,

$$M = \int_0^\infty \int_{\mathbb{R}^n} p(\mathbf{x}, t)\, dx\, dt. \tag{5.37}$$

Inverse Problem: Approximating α

We may not be able to explicitly measure the absorption rate α, which may be a useful parameter for other experiments or applications [46]. However, using our cumulative absorption model, we develop an indirect method of measuring an agent's absorption rate. We define the forward problem as $\mathbf{y} = \mathcal{G}(\mathbf{x})$, where we denote $\mathcal{G}$ as the cumulative absorption model, $\mathbf{y}$ as the distribution of live agents (data), and $\mathbf{x}$ as the parameters (input). The inverse problem solves for an unknown input $\mathbf{x}$, given the data $\mathbf{y}$. Suppose we have experimental data, $\mathbf{y}$, of the spatial distribution of live agents in time and we want to solve for the unknown parameter $x = \alpha$. To accomplish this, we approach this parameter approximation in an indirect manner by using the MOT. This offers two advantages: the MOT is relatively easy to calculate from distributional time-series data and our inverse problem does not require any manipulation with the spatial variable.

We can use Eq. (5.37) to compare the MOT for various values of permeability, α, and initial point source, x_0. In Fig. 5.16a, we illustrate the MOT for various permeability parameters, α, and initial locations x_0. The data points were collected by numerically solving for p (as in Section 5.4.1) and then summing over the spatial and time dimensions. As one would predict, the MOT is shorter as α approaches 1. The concavity of the graph depends on the initial location of the agent, since the simulation has a spatially-variable chemical concentration. We also see that for each initial location, the numerical MOT data, $M(\alpha|x_0)$, follows a power law, $A\alpha^{-k}$ which is common for biological applications [137]. Using the least squares formulation[9] in Appendix B, we can approximate values

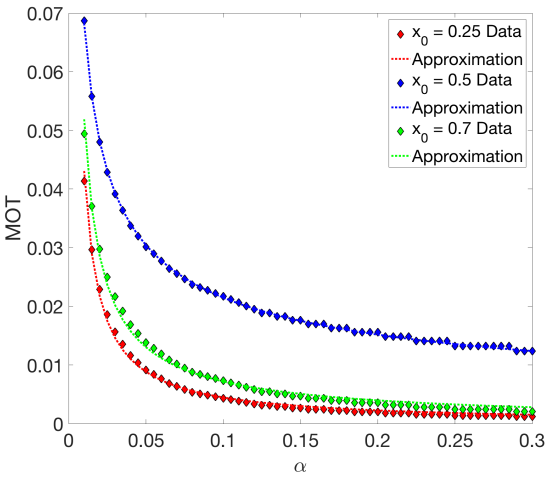

(a) The mean occupancy time (MOT) in the live state, $M(\alpha|x_0)$, for various starting locations x_0 plotted as a function of absorption permeability, α. The approximations are determined by fitting data to a power law, $A\alpha^{-k}$.

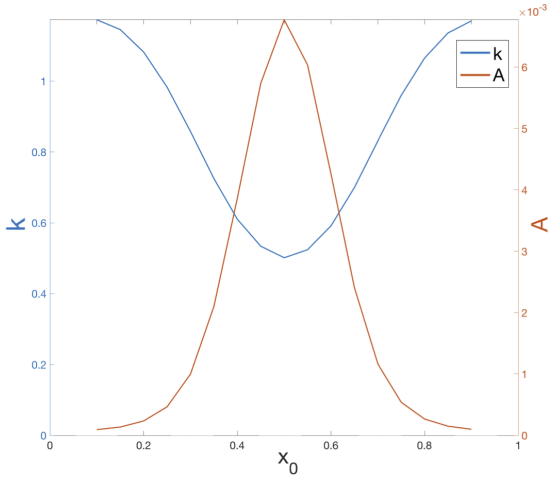

(b) We have solved for $A(x_0)$ and $k(x_0)$ for different MOT curves, where we assume a power law, $A(x_0)\alpha^{-k(x_0)}$, for a known MOT profile.

Figure 5.16: Mean occupancy time (MOT) data in the live state, $M(\alpha|x_0)$, corresponding to a chemical concentration $C(x) = 1 - \sin(\pi x)$, spatial-step size $\triangle x = 0.01$, time-step size $\triangle t = \triangle x^2$, and absorption capacitance $\xi_c = 10\triangle x\triangle t$.

for A and k. We see that the parameters A and k depend on x_0. That is, $A \equiv A(x_0)$, $k \equiv k(x_0)$, and we can approximate the α-dependent MOT curves, assuming the form of the MOT is:

$$M(\alpha|x_0) = A(x_0)\alpha^{-k(x_0)}. \tag{5.38}$$

The curves in Figure 5.16b are a result of approximating $A(x_0)$ and $k(x_0)$ from MOT approximations for various x_0 on the interval $[0.1, 0.9]$. If one knows the relationship between α and the magnitude of the chemical concentration, $C(x)$, then it is possible to obtain the MOT curves similar to Fig. 5.16a. However, we do not need to know the exact values of α to make the power law approximations if we know the absorption relationship between α and $C(x)$. For our example, we know that $\beta(x) = \int_{B(x,\triangle x/2)} C(x)\,dx$. Thus, changing the value of α by a proportion while keeping $C(x)$ fixed yields the same results as changing the value of $C(x)$ by the same proportion while keeping α fixed. In this way, the experimentalist can obtain the power law parameters A and k without previously knowing the absorption rate.

So, for a known chemical concentration, C, and cell speed, we can create a graph like Fig. 5.16b. If we are given an initial location x_0, then we can approximate the parameters k and A. Knowing these parameters and MOT is sufficient to back out the corresponding absorption permeability parameter, $\alpha \approx \left(\frac{M}{A}\right)^{-1/k}$.

[9]There are other, more accurate non-linear least squares methods, such as the Gauss-Newton method [120, Ch.4]. However, using a logarithmic transformation was sufficient in this case for a proof of concept.

5.4.4 Measure of Chemical Effectiveness

Another question of interest may be, given the density of live agents in space and time, what is the underlying chemical concentration or chemical threshold. We demonstrated a way to measure the absorption rate, α, given an agent's initial location and the chemical profile. Now, we want to find a way to approximate the chemical profile, given an agent's initial distribution and a known chemical absorption rate. From the absorption model, we have that the probability an agent is alive and at location $\mathbf{x}$ at time t by the integral $p(\mathbf{x}, t) = \int_0^{\xi_c} U(\mathbf{x}, t, \xi)\, d\xi$. To solve this inverse problem, we first need to measure how effective the chemical is at transitioning agents from live to dead state.

Derivation of Effectiveness Measure

We know that without the chemical concentration, the agent would ceaselessly perform an URW. So, the role of the absorption term in the PDE is to essentially partition the URW solution into live agents and dead agents according to the dynamics imposed by the chemical concentration density, $C(\mathbf{x})$, absorption tolerance, ξ_c, and absorption rate, α. Let $W(\mathbf{x}, t)$ denote the probability that an agent undergoing an n-dimensional URW after being initialized at $\mathbf{x}_0$ is at location $\mathbf{x}$ at time t. That is, with the same free-space boundary conditions as the absorption model, the URW solution is $W(\mathbf{x}, t) = \frac{1}{(4\pi D t)^{n/2}} \exp\left\{-\frac{|\mathbf{x}-\mathbf{x}_0|^2}{4Dt}\right\}$. Note that we can also solve for W by calculating the integral $W(\mathbf{x}, t) = \int_0^{\infty} U(\mathbf{x}, t, \xi)\, d\xi$.

The effectiveness of the chemical to perform state transitions can be defined as the conditional probability that an agent is not in the live state, $\mathcal{U}$, at location x at time t given that the agent is at location x at time t. That is, we define the chemical effectiveness measure, $\varepsilon(\mathbf{x}, t)$, for $t > 0$ as

$$\varepsilon(\mathbf{x}, t) := \mathbb{P}(s_i^t \neq \mathcal{U} | \mathbf{x}_i^t = \mathbf{x}) = \frac{\int_{\xi_c}^{\infty} U(\mathbf{x}, t, \xi)\, d\xi}{\int_0^{\infty} U(\mathbf{x}, t, \xi)\, d\xi} = 1 - \frac{p(\mathbf{x}, t)}{W(\mathbf{x}, t)} \tag{5.39}$$

If $\varepsilon(\mathbf{x}, t) = 0$, then $p(\mathbf{x}, t) = W(\mathbf{x}, t)$ and the chemical concentration has no effect on the model at $(\mathbf{x}, t)$. However, if $\varepsilon(\mathbf{x}, t) = 1$, then $p(\mathbf{x}, t) = 0$ and the chemical concentration has changed the states of all the agents near $\mathbf{x}$ by time t. We examine two 1-d chemical effectiveness plots in Fig. 5.17. For both plots, we assign parameters $\delta x = \triangle x = 0.01$, $\delta t = \triangle t = \triangle x^2/2$, $\xi_c = 10 \triangle x \triangle t$, and $\delta\xi = \xi_c/2000$. In Fig. 5.17a, we assign the chemical concentration density as $C(x) = \frac{1}{1+10(x-0.5)^2}$. So $p(x, t)$ is the same as Example 1 in Section 5.4.1. The plot is of magnitude 1 until approximately $t = 0.0055$, when the agents close to the maximum of $C(x)$ at $x = 0.5$ begin to change state. We can see the same symmetry as Fig. 5.4. In Fig. 5.17b, we assign the chemical concentration density as $C(x) = \exp\{-x^2\}$. So $p(x, t)$ is the same as Example 2 in Section 5.4.1. In fact, we see the same trend as Fig. 5.7. Finally, in Fig. 5.17c, we assign the chemical concentration density as $C(x) = 0.5\,(\sin(4\pi x) + 1)$. Although the concentration density is periodic, the initial condition skews the graph surface.

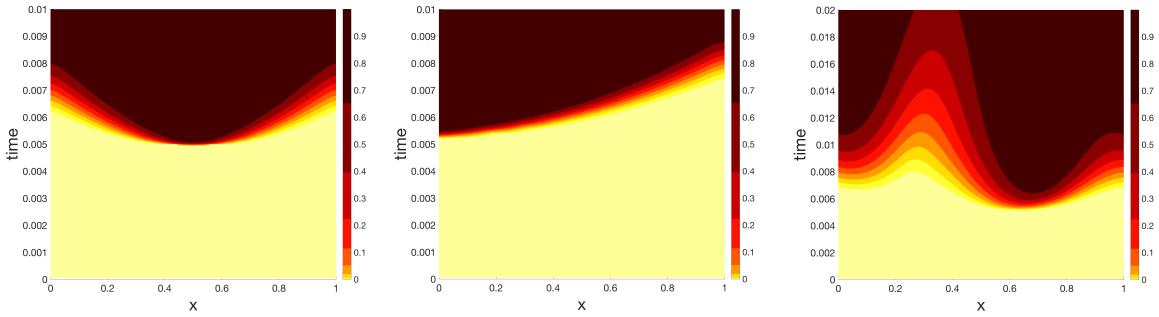

(a) $C(x) = \frac{1}{1+10(x-0.5)^2}$ (b) $C(x) = \exp\{-x^2\}$ (c) $C(x) = \frac{1}{2}(\sin(4\pi x) + 1)$

Figure 5.17: Conditional probability $\varepsilon(x,t) = \mathbb{P}(s_i^t \neq \mathcal{U} | x_i^t = x)$ surface plots for various chemical concentrations, $C(x)$ derived from the numerical PDE solution with $U(x, t = 0, \xi) = \delta(x - 0.5, \xi)$. If $\varepsilon(x,t) = 0$ then the PDE absorption solution matches the URW solution.

Inverse Problem: Approximating $C(x)$

The above examples compute the chemical effectiveness for initial condition $U(x, t = 0, \xi) = \delta(x - 0.5, \xi)$ as a point source. We acknowledge that the only difference between $p(\mathbf{x}, t)$ and $W(\mathbf{x}, t)$ is the state change due to the absorption of the chemical concentration. A natural question is whether there is a way to approximate the shape of the chemical concentration from the chemical effectiveness plots. As opposed to the previous example, the unknowns here are the spatially-dependent chemical concentration values, $C(x)$ (rather than α). The output is still the spatial time-series distribution of live agents, which can be used to obtain the chemical efficacy plots (and resulting separation curve).

To attempt this inverse problem, we first compute the chemical effectiveness for the absorption model with an initial uniform spatial distribution of agents at $\xi = 0$. That is, we solve the free-space absorption PDE[10] with initial condition $U(x, t = 0, \xi) = \delta(\xi)$. This initial condition allows the separation curve (which separates $\varepsilon(x,t) = 0$ from $\varepsilon(x,t) = 1$) in the plots of Fig. 5.18 to essentially recover the shape of the chemical concentrations (up to translation, reflection, and stretching). This shape distortion is related to the rate of absorption, α, and value of the absorption capacitance, ξ_c. If the agent remains in the same location, then the graphs would only have values of 0 or 1. Thus, the steepness of the boundary between 0 and 1 explains how much the agents move to regions of differing chemical concentration before changing state.

By the characteristic solution to the absorption operator, we know that if an agent at location x does not move in the spatial domain, then $t = \xi_c/\beta(x)$ is the time for the agent to change state. So, in the above simulations of Fig. 5.18, if we assume that the agents do not move, then we can find the time t^* in the plots that an agent initialized at location

[10]We run the PDE to generate data, which requires a known chemical concentration, $C(x)$. In practice, if we need to solve for $C(x)$, then we cannot explicitly know $C(x)$. However, we can gather the spatial distribution data from experimental results.

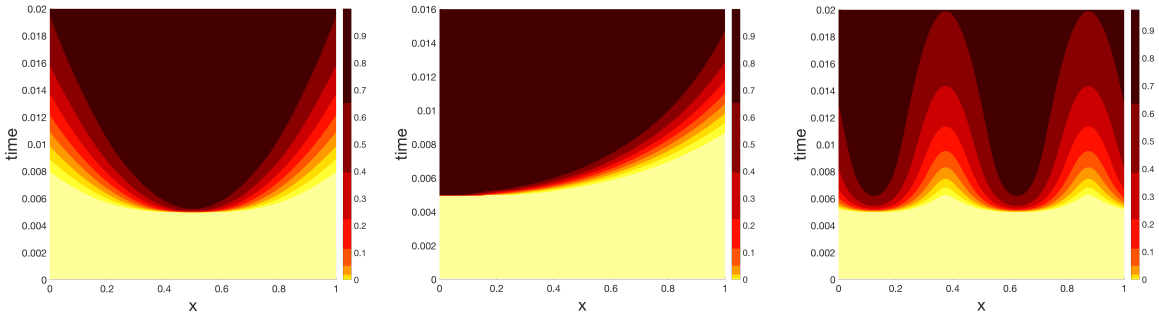

(a) $C(x) = \frac{1}{1+10(x-0.5)^2}$ (b) $C(x) = \exp\{-x^2\}$ (c) $C(x) = \frac{1}{2}(\sin(4\pi x) + 1)$

Figure 5.18: Conditional probability $\varepsilon(x,t) = \mathbb{P}(s_i^t \neq \mathcal{U} | x_i^t = x)$ surface plots for various chemical concentrations, $C(x)$ derived from the numerical PDE solution with $U(x, t = 0, \xi) = \delta(\xi)$.

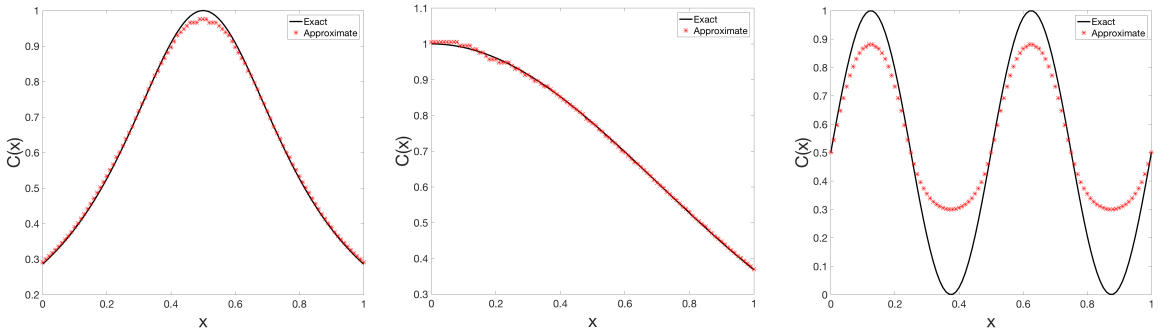

(a) $C(x) = \frac{1}{1+10(x-0.5)^2}$ (b) $C(x) = \exp\{-x^2\}$ (c) $C(x) = \frac{1}{2}(\sin(4\pi x) + 1)$

Figure 5.19: Comparison between the exact chemical concentration, $C(x)$, (**black** line) and the approximate chemical concentration, $C_{\text{approx}}(x)$, (**red** asterisk) derived from $\varepsilon(x,t)$ for various absorption model PDE numerical solutions.

x^* changes state. Since we approximate $\beta(x) \approx \alpha \triangle x C(x)$ by central finite differences, we can approximate the chemical concentration by solving

$$C_{\text{approx}}(x^*) = \frac{\xi_c}{\alpha \triangle x t^*}.$$

Of course, the agent does move, so we expect error to occur in our calculation of $C_{\text{approx}}(x^*)$. We compare the exact chemical concentration, $C(x)$, with the approximate chemical concentration, $C_{\text{approx}}(x)$, in Fig. 5.19. Since the agent moves, we find t^* by finding the time at which $\varepsilon(x^*) = 0.5$ from the plots in Fig. 5.18. The approximation error in Fig. 5.19c is much larger than the other approximation because the conditional probability transition from 0 to 1 in Fig. 5.18c is more gradual. This implies that the agents in the $C(x) = \frac{1}{2}(\sin(4\pi x) + 1)$ model moves along steeper chemical gradients than the other models. Thus, if the noise in the measurement of the chemical efficacy yields a non-

smooth separation curve, then this method for approximating $C(x)$ is not effective.

Inverse Problem: Approximating ξ_c

Experimentalists may be interested in calculating the chemical threshold. Using a similar approach as approximating $C(x)$, we can also approximate the chemical threshold, ξ_c. The unknown value here is ξ_c and the output is the spatial time-series distribution of live agents. Using the point source initial condition, $U(x, t = 0, \xi) = \delta(x - x_0, \xi)$, we develop the chemical efficacy surface plots like those shown in Fig. 5.17. We can then approximate the time t^* for the agent to change state by finding the time on the separation curve corresponding with $x = x_0$. We can approximate the chemical threshold by solving

$$\xi_{c,\text{approx}} \approx C(x_0)\alpha\triangle x t^*.$$

Since the value of $\xi_{c,\text{approx}}$ is explicitly dependent on the value t^*, large measurement errors in the chemical effectiveness separation curve at x_0 cause large approximation errors.

In Table 5.1 we compare the approximated chemical threshold values for the three chemical effectiveness plots in Fig. 5.17. The relative error is calculated by

$$\text{Relative Error} = \frac{|\xi_{c,\text{exact}} - \xi_{c,\text{approx}}|}{\xi_{c,\text{exact}}}.$$

We see that despite the skewness of Fig. 5.17c, the relative error is approximately the same order as the other figures.

$C(x)$	$\xi_{c,\text{exact}}$	$\xi_{c,\text{approx}}$	Relative Error
$\frac{1}{1+10(x-0.5)^2}$	5×10^{-6}	5.0250×10^{-6}	5.00×10^{-3}
$\exp\{-x^2\}$	5×10^{-6}	5.0038×10^{-6}	7.59×10^{-4}
$\frac{1}{2}(\sin(4\pi x) + 1)$	5×10^{-6}	4.9875×10^{-6}	2.50×10^{-3}

Table 5.1: Comparison between exact chemical threshold, $\xi_{c,\text{exact}}$, and the approximate chemical threshold, $\xi_{c,\text{approx}}$.

5.5 Relative Scaling Approximations

The above examples assumed a particular scaling of the absorption and movement parameters in (5.5) and (5.6). However, other scaling relations may be possible and we can further simplify the equations or analysis. First, let us non-dimensionalize the absorption variable, ξ, by using the scaling factor ξ_c to obtain $\bar{\xi} = \xi/\xi_c$. We can rewrite (5.5) as

$$\begin{cases} \frac{\partial U}{\partial t} + \frac{\beta(x)}{\xi_c}\frac{\partial U}{\partial \bar{\xi}} = D\frac{\partial^2 U}{\partial x^2}, & x \in \mathbb{R},\ \xi \in [0,\infty),\ t > 0, \\ U = \phi(x, \bar{\xi}), & x \in \mathbb{R},\ \xi \in [0,\infty),\ t = 0, \\ \lim_{|x|\to\infty} U = 0, & x \in \mathbb{R},\ \xi \in [0,\infty),\ t > 0, \end{cases} \tag{5.40}$$

with the agent changing state when $\xi \geq 1$. There are three different regimes based on the term $\beta(x)/(D\xi_c)$.

First, we investigate when $\beta(x)/(D\xi_c) \gg 1$. This occurs when the agent absorbs chemical above its capacitance before diffusion moves the agent, as can be observed in Fig 5.20(a). Assuming $\beta(x) > 0$ is continuous, we can asymptotically simplify (5.40) to

$$\begin{cases} \frac{\partial U}{\partial t} + \frac{\beta(x)}{\xi_c}\frac{\partial U}{\partial \bar{\xi}} = 0, & x \in \mathbb{R},\ \bar{\xi} \in [0,\infty),\ t > 0, \\ U = \phi(x,\bar{\xi}), & x \in \mathbb{R},\ \bar{\xi} \in [0,\infty),\ t > 0, \end{cases} \tag{5.41}$$

with a solution $U(x,t,\bar{\xi}) = \phi(x,\bar{\xi} - \beta(x)t/\xi_c)$ for all $x \in \mathbb{R}$. An example solution of the total density in the live state in an absorption-dominant parameter regime is shown in Fig 5.20(b). Note that as $\langle\beta(x)\rangle/(D\xi_c)$ approaches ∞, the AB model and PDE densities converge.

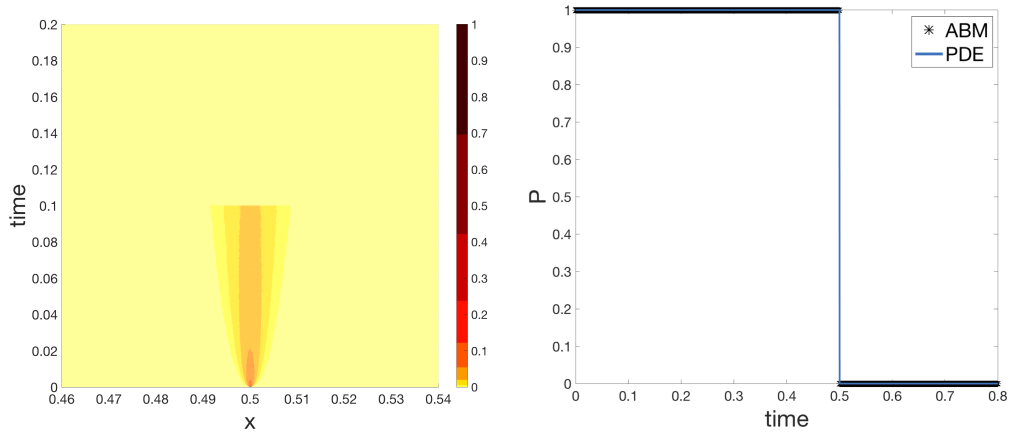

(a) AB model simulation surface plot.

(b) Comparison between AB model and PDE density in live state with respect to time.

Figure 5.20: Absorption-dominant parameter regime comparison between AB model and PDE density in live state with respect to time. Here $\triangle x = \triangle t = 10^{-4}$, $\beta(x) = \triangle x \frac{1}{20}(1 + \sin \pi x)$, $\xi_c = 10^{-6}$. Agents are initialized at $x_0 = 0.5$, so $\beta(x_0)/(D\xi_c) = 2 \times 10^5$.

Second, we investigate when $\beta(x)/(D\xi_c) \ll 1$. This occurs when the agent diffuses much faster than the agent absorbs chemical, as is shown in Fig 5.21(a). We cannot make an asymptotic argument, ignoring the absorption term, since that is our primary interest in this model. Thus, we make the assumption that the density of the agents in the live state quickly becomes uniform over the spatial coordinate. This assumption allows us to collapse the spatial coordinate and have a solution solely in absorption and time dimensions. We can define the PDE initial condition as $\bar{\phi}(\bar{\xi}) := \int_{\mathbb{R}} \phi(x,\bar{\xi})\,dx$ and we can redefine the PDE absorption term as the average value of β in the spatial domain, $\langle\beta(x)\rangle$,

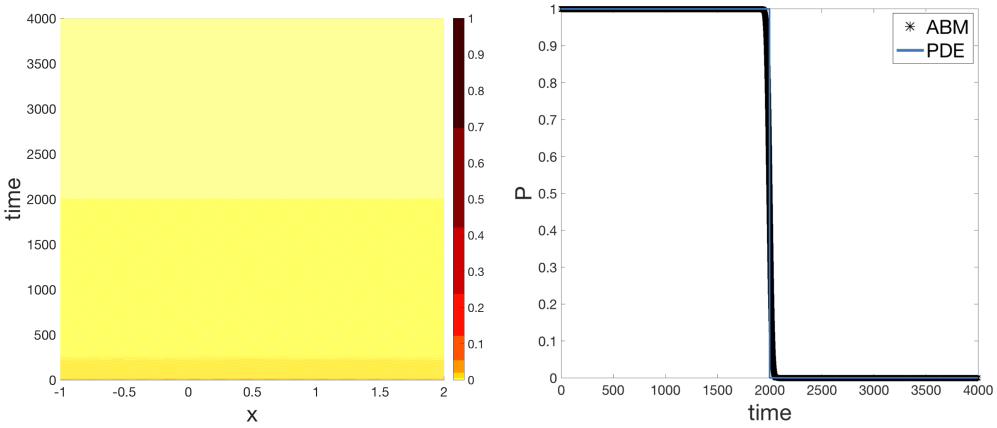

(a) AB model simulation surface plot.

(b) Comparison between AB model and PDE density in live state with respect to time.

Figure 5.21: Diffusion-dominant parameter regime comparison between AB model and PDE density in live state with respect to time. Here $\triangle x = 0.1$, $\triangle t = 0.01$, $\beta(x) = \triangle x \frac{1}{20}(1 + \sin \pi x)$, $\xi_c = 1$. Agents are initialized at $x_0 = 0.5$, so $\langle \beta(x) \rangle / (D\xi_c) = 10^{-3}$.

to obtain the following PDE,

$$\begin{cases} \frac{\partial U}{\partial t} + \frac{\langle \beta(x) \rangle}{\xi_c} \frac{\partial U}{\partial \bar{\xi}} = 0, & \bar{\xi} \in [0, \infty), t > 0 \\ U = \bar{\phi}(\bar{\xi}), & \bar{\xi} \in [0, \infty), t = 0. \end{cases} \tag{5.42}$$

The solution is $U(\bar{\xi}, t) = \bar{\phi}\left(\bar{\xi} - \langle \beta(x) \rangle t / \xi_c\right)$. An example solution of the total density in the live state in a diffusion-dominant parameter regime is shown in Fig 5.21(b). Note that as $\langle \beta(x) \rangle / (D\xi_c)$ approaches 0, the AB model and PDE densities converge.

Chapter 6

Absorption Model in Bounded Domain

The free space boundaries have illuminated interesting phenomenon with the absorption model. However, applying the cumulative absorption model to real world applications requires being able to solve the model in various bounded domains. It is important to understand how dynamics are affected by a boundary, so we need to investigate half-plane domains. Moreover, we know absorption occurs in blood vessels, so it would be useful to solve the model in an infinite strip. We may be interested in modeling cells in a petri dish or a microfluidic device, in which case solving in a bounded, convex shape is necessary. Finally, by adding a boundary, we may be interested in deriving the probability an agent escapes an absorption region before it absorbs a threshold level. In order to do this, we need to reexamine our free-space numerical scheme and adapt it to handle boundary conditions.

6.1 Numerical Green's Function in Bounded Regions

We use the method of images to use our stable numerical method in bounded domains. For this dissertation, we show examples of half-plane, infinite strip, and square domains. However, we can apply this numerical method to any domain that handles the method of images, such as triangular, circular, and annular domains. We formulate the numerical algorithms for the half-plane and infinite strip for the 1-d diffusion equation, with the understanding that they can extend to domains of higher dimensions.

Using Fourier transformations in Appendix A.1.2, we already know the exact solution to the free-space diffusion equation

$$\begin{cases} \frac{\partial U}{\partial t} = D\frac{\partial^2 U}{\partial x^2}, & x \in \mathbb{R}, t > 0, \\ U = \phi(x), & x \in \mathbb{R}, t = 0, \\ \lim_{|x|\to+\infty} U = 0, & x \in \mathbb{R}, t > 0 \end{cases}$$

is the convolution $U(x,t) = G * \phi(x)$, where $G(x,t) = \frac{1}{\sqrt{4\pi Dt}} \exp\left\{\frac{-x^2}{4Dt}\right\}$ is the 1-d fun-

damental solution to the diffusion equation. Further, in Section 5.3 we established a numerical method to solve this free space convolution solution numerically using cell volumes. We use the idea of the method of images in conjunction with our numerical Green's method solver to solve for other bounded domains.

6.1.1 Infinite Half-Line

We begin examining a bounded region with the infinite half-line. To derive the numerical method of images, we can consider the diffusion equation on the infinite half-line spatial domain $\Omega = [0, +\infty)$:

$$\begin{cases} \frac{\partial U}{\partial t} = D\frac{\partial^2 U}{\partial x^2}, & x \in \Omega, t > 0, \\ U = \phi(x), & x \in \Omega, t = 0, \\ \lim_{x\to+\infty} U = 0, & x \in \Omega, t > 0, \end{cases}$$

with either absorbing ($U(0,t) = 0$) or no-flux ($\frac{\partial U}{\partial x}\Big|_{x=0} = 0$) boundary conditions at the boundary $x = 0$.

We know from Appendix A.1.2 that $G(x,t|x_0) = \frac{1}{\sqrt{4\pi Dt}} \exp\left\{-\frac{(x-x_0)^2}{4Dt}\right\}$ is the solution to the 1-d diffusion equation with an initial point source at $x = x_0$ and free-space boundary equations. We use the vertical bar to explicitly denote the location of the initial point source. A common way to solve the diffusion equation in the domain of interest $\Omega = [0, +\infty)$ is by extending this domain to an image domain $(-\infty, 0)$ [41, Ch.2][125, Ch.3]. If we have no-flux boundary conditions at $x = 0$, then we reflect our Green's function solution across the boundary. Thus, the solution with an initial condition $U(x, t = 0) = \delta(x - x_0)$ is $U(x,t|x_0) = G(x,t|x_0) + G(x,t|-x_0)$. The point $-x_0$ is called the image point of x_0. However, if we have absorbing boundary condition at $x = 0$, then our solution is $U(x,t|x_0) = G(x,t|x_0) - G(x,t|-x_0)$. Since G is symmetric, it is clear that $U = 0$ at $x = 0$.

Numerical Method of Images for Half-Line: Suppose after discretizing the spatial domain, that the boundary is located at x_0, a cell center. Then, as seen in Fig. 6.1, our domain of interest contains half of the cell volume centered at x_0 as well as the cell volumes centered at $x_1, x_2, \ldots, x_M$. By the method of images, we want to reflect the data in the domain of interest over the boundary and into the image domain. We denote the cell centers of the image domain as the set $\{x_{-1}, x_{-2}, \ldots, x_{-M}\}$. With this notation, it is clear that information from the cell volume centered at x_i reflects to its image cell volume, which is centered at x_{-i}. In Fig. 6.1 the blue cell in the domain of interest is reflected to the orange image cell. For each time-step iteration of the numerical scheme, we reflect the current solution from the domain of interest over the boundary cell and into the image domain. The sign of the image solution depends on the type of boundary condition. That is, for absorbing boundary condition at x_0 we assign $u^m_{-i} = -u^m_i$ or for no-flux boundary condition at x_0 we assign $u^m_{-i} = u^m_i$. Once the image domain values are assigned, we compute the numerical Green's function convolution.

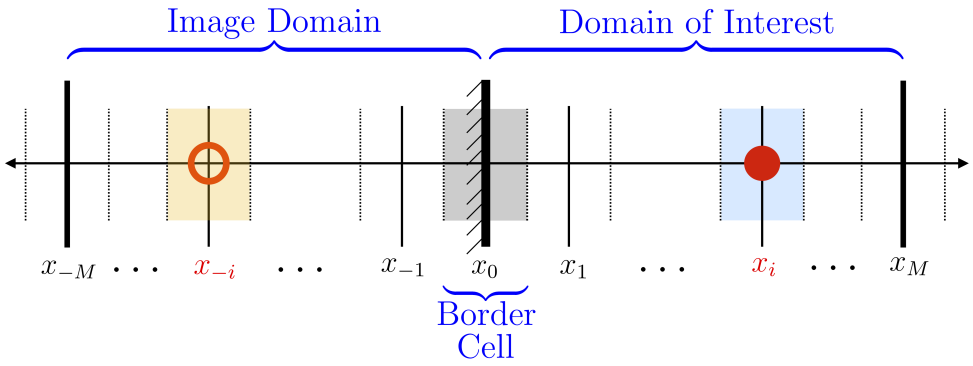

Figure 6.1: Numerical method of images method for half-line in 1-d. The numerical domain $\{x_0, x_1, \ldots, x_M\}$ is extended to the left of the border cell x_0 (depicted in **gray**), producing a mirror image of values in the extension $\{x_{-1}, x_{-2}, \ldots, x_{-M}\}$.

The half-line algorithm can be stated as:

- Initialize $u_i^0 = \phi_i$ for $i > 0$ and $u_0^0 = \begin{cases} 0 & : \text{ if absorbing boundary condition at } x_0 \\ 0.5\phi_0 & : \text{ if no-flux boundary condition at } x_0 \end{cases}$
- For $m = 0, 1, \ldots$:
  - $\diamond$ $\tilde{u}_0^m = \begin{cases} 0 & : \text{ if absorbing boundary condition at } x_0 \\ 2u_0^m & : \text{ if no-flux boundary condition at } x_0 \end{cases}$
  - $\diamond$ $\tilde{u}_{-i}^m = \begin{cases} -u_i^m & : \text{ if absorbing boundary condition at } x_0 \\ u_i^m & : \text{ if no-flux boundary condition at } x_0 \end{cases}$, (for $i = 1, 2, \ldots, M$)
  - $\diamond$ $u_i^m = \lambda_i \sum_{j=-M}^{M} \tilde{u}_{i-j}^m G_j$, (for $i = 0, 1, 2, \ldots, M$),

where G_j is defined in Section 5.3 as the fundamental solution integrated over the cell volume centered at x_j. After performing the discrete convolution, the parameter λ_i essentially deletes the image domain from the numerical solution at the boundary volume centered at x_0. To do this, we define λ_i as

$$\lambda_i = \begin{cases} 0.5 & : \text{ if } i = 0 \\ 1 & : \text{ if } i = 1, 2, \ldots, M. \end{cases}$$

Since only half the area of the border cell x_0 is in the domain of interest, we set $\lambda_0 = 1/2$.

6.1.2 Finite Line Segment

We may be interested in modeling cases in tubular regions, such as blood vessels or pipes. Using symmetry, we can reduce these models to infinite strips. To develop a reasonable

algorithm in this case, we can first consider the 1-d diffusion equation on a line segment $\Omega = [0, 1] \subset \mathbb{R}$:

$$\begin{cases} \frac{\partial U}{\partial t} = D\frac{\partial^2 U}{\partial x^2}, & x \in \Omega, t > 0, \\ U = \phi(x), & x \in \Omega, t = 0, \end{cases}$$

with either absorbing or no-flux boundary conditions at the boundaries $x = 0$ and $x = 1$.

Like the half-line, a common way to solve the diffusion equation in the line segment $\Omega = [0, 1]$ is by using method of images [41, Ch.2][125, Ch.3]. With the half-line we only had one image point, but for the line segment we need countably infinite image points. For example, if we take the point $x_0 \in (0, 1)$ and initially reflect it across $x = 1$ we have the image point $2 - x_0$. But then we need to reflect $2 - x_0$ across the boundary $x = 0$, which yields the image point $-2 + x_0$. However, we need to reflect this new image point across $x = 1$, which yields $4 - x_0$. This pattern continues countably infinite times. Thus, the solution with no-flux boundary conditions is $U(x, t|x_0) = \sum_{k\in\mathbb{Z}}[G(x, t|2k + x_0) + G(x, t|2k - x_0)]$. For absorbing boundary conditions, the solution is $U(x, t|x_0) = \sum_{k\in\mathbb{Z}}[G(x, t|2k + x_0) - G(x, t|2k - x_0)]$. We could also solve the diffusion equation in this domain using eigenvalue expansions with the method of separation of variables [41, Ch.4], but we want a method that can easily adapt the numerical method we used in Chapter 5.

Numerical Method of Images for Line Segment Domain: For notational simplicity, suppose the boundaries are located at $b_1 = x_{-M}$ and $b_2 = x_M$, where x_{-M} and x_M are numerical cell centers. Then our domain of interest contains half of each boundary cell as well as the cell volumes centered at $x_{-M+1}, x_{-M+2}, \ldots, x_{M-1}$. Similar to the half-line algorithm, we want to reflect the data in the domain of interest over each boundary and into the image domains. We denote the cell centers in the region reflected across x_{-M} as the image domain $\{x_{-M-1}, x_{-M-2}, \ldots, x_{-3M+1}\}$ and the cell centers in the region reflected across x_M as the image domain $\{x_{M+1}, x_{M+2}, \ldots, x_{3M-1}\}$. With this notation, the data from the cell volume centered at x_i reflects across x_{-M} to the cell volume $x_{-(i+2M)}$ and reflects across x_M to the cell volume x_{2M-i}. In Fig. 6.2 the blue cell in the domain of interest reflects to both orange image cells.

Other than reflecting across a second boundary, the numerical scheme is similar to the half-line algorithms:

- Initialize $u_i^0 = \phi_i$
- For $m = 0, 1, \ldots$:
  - $\diamond$ $\tilde{u}_{-M}^m = \begin{cases} 0 & : \text{ if absorbing boundary condition at } x_0 \\ 2u_{-M}^m & : \text{ if no-flux boundary condition at } x_0 \end{cases}$
  - $\diamond$ $\tilde{u}_{M}^m = \begin{cases} 0 & : \text{ if absorbing boundary condition at } x_0 \\ 2u_{M}^m & : \text{ if no-flux boundary condition at } x_0 \end{cases}$

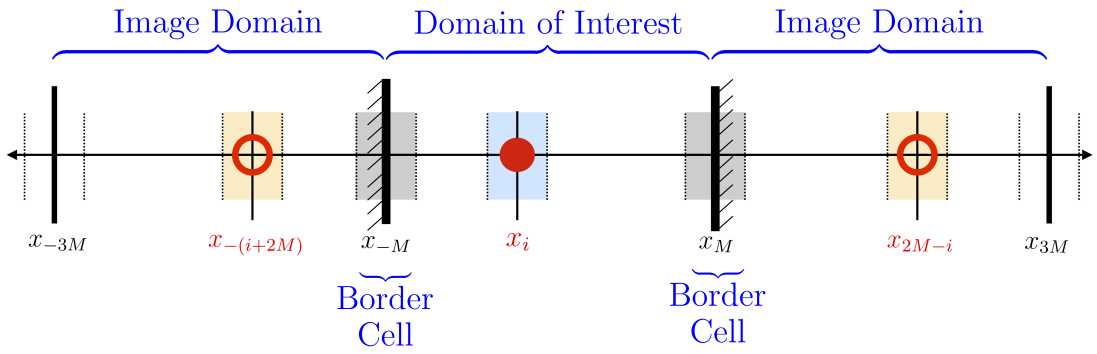

Figure 6.2: Numerical method of images method for line segment in 1-d. The numerical domain $\{x_{-M}, x_{-M+1}, \ldots, x_M\}$ is extended to the left of the border cell x_{-M} and to the right of border cell x_M (both depicted in **gray**), producing a mirror image of values in the extensions $\{x_{-M+1}, x_{-M+2}, \ldots, x_{-3M}\}$ and $\{x_{M+1}, x_{M+2}, \ldots, x_{3M}\}$. Because of the symmetry, it is notationally simpler to index the border cells as x_{-M} and x_M, rather than x_0 and x_M.

$$\diamond\ \tilde{u}^m_{-(i+2M)} = \begin{cases} -u^m_i & : \text{ if absorbing boundary condition at } x_{-M} \\ u^m_i & : \text{ if no-flux boundary condition at } x_{-M} \end{cases},$$
$$(\text{for } i = -M+1, -M+2, \ldots, M-1)$$
$$\diamond\ \tilde{u}^m_{2M-i} = \begin{cases} -u^m_i & : \text{ if absorbing boundary condition at } x_M \\ u^m_i & : \text{ if no-flux boundary condition at } x_M \end{cases},$$
$$(\text{for } i = -M+1, -M+2, \ldots, M-1)$$
$$\diamond\ u^m_i = \lambda_i \textstyle\sum_{j=-3M+1}^{3M-1} \tilde{u}^m_{i-j} G_j, \text{ (for } i = -M, -M+1, \ldots, M),$$

Just as it does with the half-line algorithm, the parameter λ_i deletes the image domain from the numerical solution. We define λ_i as

$$\lambda_i = \begin{cases} 0 & : \text{ if } i = -3M+1, -3M+2, \ldots, -M-1 \\ 0.5 & : \text{ if } i = -M \\ 1 & : \text{ if } i = -M+1, -M+2, \ldots, M-1. \\ 0.5 & : \text{ if } i = M \\ 0 & : \text{ if } i = M+1, M+2, \ldots, 3M-1. \end{cases}$$

The analytical method of images on a line segment requires infinite reflections, as the image points alternate reflecting across each boundary. We could extend the domain further to allow for more image domains. However, if $x_M - x_{-M}$ is large enough, then the Green's function is bounded close to zero outside the domain of interest. In that case, additional reflections would not decrease the error substantially.

6.1.3 Extension to Higher Dimensions

Half-Plane Domain: To extend the half-line to a half-plane, we simply add another spatial coordinate to the computational domain. Because free-space boundary conditions would be performed in the y-coordinate, we would not impose any image domains in the additional coordinate as seen in Fig. 6.3. The half-plane algorithm can be stated as:

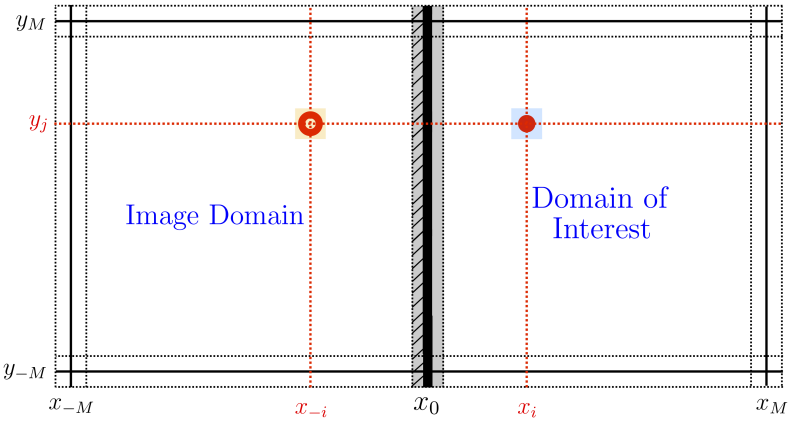

Figure 6.3: Numerical method of images method for half-plane in 2-d. The numerical domain x-coordinates, $\{x_0, x_1, \ldots, x_M\}$, are extended to the left of the border cells centered at $x = x_0$ (depicted in **gray**), producing a mirror image of values in the extension $\{x_{-1}, x_{-2}, \ldots, x_{-M}\}$.

- Initialize $u^0_{i,j} = \phi_{i,j}$
- For $m = 0, 1, \ldots$:
  - $\diamond$ $\tilde{u}^m_{0,j} = \begin{cases} 0 & : \text{ if absorbing boundary condition at } x_0 \\ 2u^m_{0,j} & : \text{ if no-flux boundary condition at } x_0 \end{cases}$, (for all j)
  - $\diamond$ $\tilde{u}^m_{-i,j} = \begin{cases} -u^m_{i,j} & : \text{ if absorbing boundary condition at } x_0 \\ u^m_{i,j} & : \text{ if no-flux boundary condition at } x_0 \end{cases}$, (for $i = 1, 2, \ldots, M$ and all j)
  - $\diamond$ $u^m_{i,j} = \lambda_i \sum_{k=-M}^{M} \sum_{\ell=-M}^{M} \tilde{u}^m_{i-k,j-\ell} G_{k,\ell}$, (for $i = 0, 1, 2, \ldots, M$ and all j),

where $G_{k,\ell}$ is defined in Section 5.3 as the 2-d fundamental solution integrated over the cell centered at (x_k, y_ℓ). Further, since the image cells only depend on the x-coordinate, we define λ_i as the same as the half-line algorithm.

$$\lambda_i = \begin{cases} 0 & : \text{ if } i = -M, -M+1, \ldots, -1 \\ 0.5 & : \text{ if } i = 0 \\ 1 & : \text{ if } i = 1, 2, \ldots, M. \end{cases}$$

Here, the y-dimension is partitioned into the same number of cells as the x-dimension. This is not a requirement for the above method.

Absorption Example $\mathbb{R} \times [0, \infty)$: We simulate an example of the absorption model in the upper half-plane, $\Omega = \mathbb{R} \times [0, \infty)$, with step-sizes $\triangle x = 0.02$ and $\triangle t = \triangle x^2/2$ along with reflecting boundary conditions at $y = 0$. The chemical density profile is $C(x, y) = 0.5(\cos(2\pi x)\sin(3\pi y) + 1)$ with absorption rate $\alpha = 0.1$. We initialize 5×10^5 agents in the live state at $\mathbf{x}_0 = (0.5, 0.5)$, and an agent changes state when it absorbs above the chemical threshold $\xi_c = 8\triangle t \triangle x \triangle y$. Histogram results for four time points of the AB model are shown in Fig. 6.4a.

We solve the following PDE numerically on the domain $[-2, 2] \times [-2, 2]$ using the method of images at $y = 0$

$$\begin{cases} \frac{\partial U}{\partial t} + \beta(\mathbf{x})\frac{\partial U}{\partial \xi} = D\frac{\partial^2 U}{\partial x^2}, & \mathbf{x} \in \Omega,\ \xi \in [0, \infty),\ t > 0, \\ U = \delta(\mathbf{x} - (0.5, 0.5), \xi), & \mathbf{x} \in \Omega,\ \xi \in [0, \infty),\ t = 0, \\ \lim_{y\to\infty} U = 0, & \mathbf{x} \in \Omega,\ \xi \in [0, \infty),\ t > 0, \\ \lim_{|x|\to\infty} U = 0, & \mathbf{x} \in \Omega,\ \xi \in [0, \infty),\ t > 0, \\ \frac{\partial U}{\partial y} = 0, & \mathbf{x} \in \mathbb{R} \times \{0\},\ \xi \in [0, \infty),\ t > 0, \end{cases} \tag{6.1}$$

where $D = \triangle x^2/4\triangle t$. The numerical scheme uses the same step-sizes as the AB model ($\delta x = \triangle x$ and $\delta t = \triangle t$) and absorption step-size $\delta\xi = \xi_c/300$. Numerical solution results for four time points of the PDE solution are shown in Fig. 6.4b.

Comparing the results of Fig. 6.4, we can easily see qualitative similarities. The initial point source is a local maximum of the chemical concentration, so as time progresses the agents near the initial source change state, and the agents which survive tend to be closer to the local minimums. For statistical comparison between the AB model and PDE solutions, we observe the quantitative agreement in Fig. 6.5. From the survival probability graph, agents in the AB model simulations and PDE solutions begin to change state around $t = 0.015$. The mean location is close to the initial point source until around 0.025. However, just like in Chapter 5, as the number of agents approaches 0 the simulation stochasticity exerts greater influence on the mean location. Additionally, we see agreement in the shape of the mean squared deviation (MSD), with a cusp appearing near $t = 0.017$, when agents begin changing state.

Infinite Strip Domain: To extend the line segment to an infinite strip, we essentially perform the same addendum as we did when extending the half-line to a half-plane as seen in Fig. 6.6. That is, we add a j index to the cell volumes and perform a 2-d convolution with $G_{k,\ell}$.

Absorption Example $\mathbb{R} \times [-1, 1]$: We simulate the absorption model in the infinite strip, $\Omega = \mathbb{R} \times [-1, 1]$, with step-sizes $\triangle x = 0.02$ and $\triangle t = \triangle x^2/2$ along with reflecting boundary conditions at $y = -1$ and $y = 1$. The chemical density profile is $C(x, y) = 0.5(\cos(\pi x)\sin(1.5\pi y) + 1)$ with absorption rate $\alpha = 0.1$. We initialize 5×10^5 agents in the live state at $\mathbf{x}_0 = (0, 0.64)$, and an agent changes state when it absorbs above the chemical threshold $\xi_c = 8\triangle t \triangle x \triangle y$. Histogram results for four time points of the AB model are shown in Fig. 6.7a.

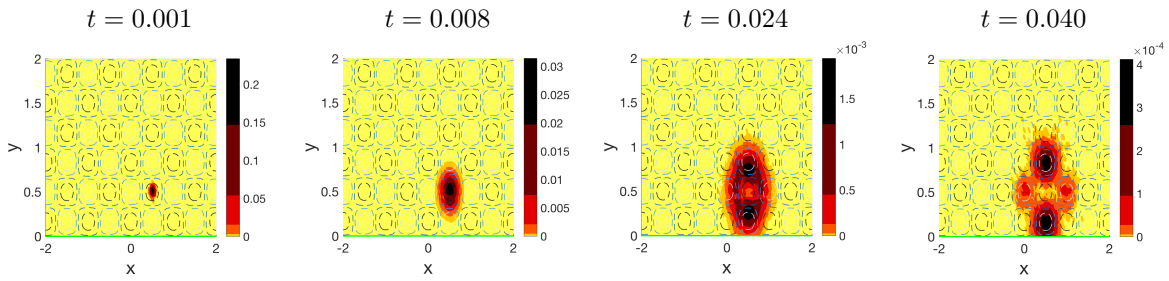

(a) AB Model Simulation

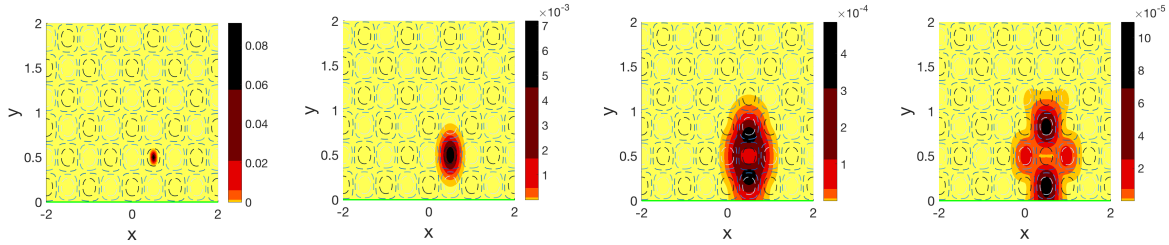

(b) PDE Numerical Solution

Figure 6.4: Probability distribution of agents (shown in color) in the upper half-plane region $[-2, 2] \times [0, 2]$ at four different time points. Agents are initialized at $(0.5, 0.5)$. The **blue** contour plot denotes the chemical concentration $C(\mathbf{x}) = \frac{1}{2}(\cos(2\pi x)\cos(3\pi y) + 1)$ and the **green** line denotes the reflective boundary at $y = 0$. The absorption capacitance is $\xi_c = 8\triangle t \triangle x \triangle y$. **(a)** AB model simulation 2-d histogram is average of 5×10^5 realizations with step sizes $\triangle x = 0.02$ and $\triangle t = \triangle x^2/2$. Histogram bin size is $2\triangle x \times 2\triangle x$. **(b)** PDE numerical solution is computed in the region $[-2, 2] \times [-2, 2]$ with numerical step sizes $\delta x = \triangle x$, $\delta t = \triangle t$, and $\delta\xi = \xi_c/300$.

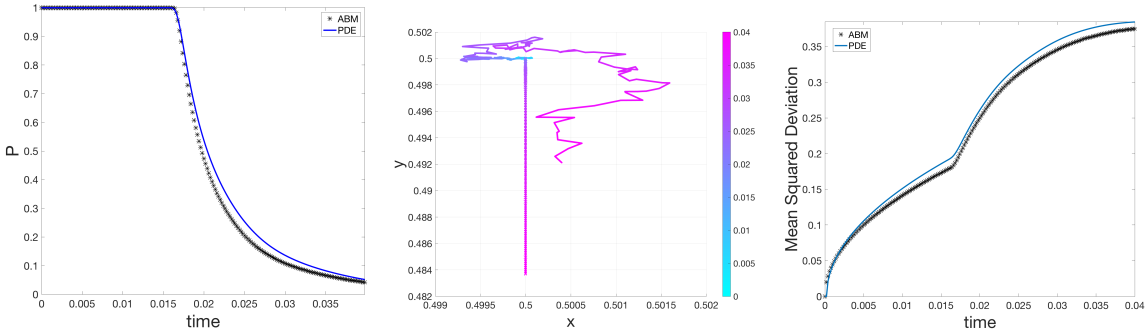

(a) Survival Probability (b) Mean Location (c) Mean Squared Deviation

Figure 6.5: Various statistical measures comparing the AB model and PDE **(a)** Survival probability, **(b)** Mean location, and **(c)** MSD.

We solve the following PDE numerically on the domain $[-3, 3] \times [-3, 3]$ using the

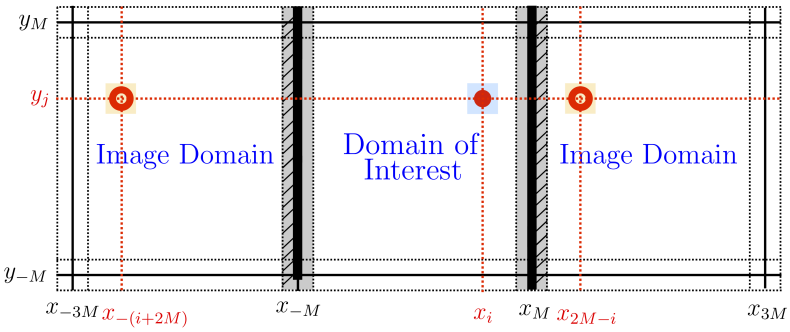

Figure 6.6: Numerical method of images method for an infinite strip in 2-d. The numerical domain x-coordinates, $\{x_{-M}, x_{-M+1}, \ldots, x_M\}$, are extended to the left of the border cells at $x = x_{-M}$ and to the right of border cells at $x = x_M$ (both depicted in gray), producing a mirror image of values in the extensions $\{x_{-M+1}, x_{-M+2}, \ldots, x_{-3M+1}\}$ and $\{x_{M+1}, x_{M+2}, \ldots, x_{3M-1}\}$.

method of images at $y = -1$ and $y = 1$

$$\begin{cases} \frac{\partial U}{\partial t} + \beta(\mathbf{x})\frac{\partial U}{\partial \xi} = D\frac{\partial^2 U}{\partial x^2}, & \mathbf{x} \in \Omega,\ \xi \in [0,\infty),\ t > 0, \\ U = \delta(\mathbf{x} - (0, 0.64), \xi), & \mathbf{x} \in \Omega,\ \xi \in [0,\infty),\ t = 0, \\ \lim_{|x|\to\infty} U = 0, & \mathbf{x} \in \Omega,\ \xi \in [0,\infty),\ t > 0, \\ \frac{\partial U}{\partial y} = 0, & \mathbf{x} \in \mathbb{R} \times \{-1, 1\},\ \xi \in [0,\infty),\ t > 0, \end{cases} \tag{6.2}$$

where $D = \triangle x^2/4\triangle t$. The numerical scheme uses the same step-sizes as the AB model ($\delta x = \triangle x$ and $\delta t = \triangle t$) and absorption step-size $\delta\xi = \xi_c/300$. Numerical results for the same four time points of the PDE solution are shown in Fig. 6.7b.

Comparing the results of Fig. 6.7, we can easily see qualitative similarities. The initial point source is vertically halfway between a local maximum and a local minimum of the chemical concentration. In fact, the closest local chemical minimum is at the boundary $y = 1$. So as time progresses the agents which survive tend to be close to the boundary. For statistical comparison between the AB model and PDE solutions, we observe the quantitative agreement in Fig. 6.8. From the survival probability graph, agents in the AB model simulations and PDE solutions begin to change state around $t = 0.01$. The mean location tends to move vertically. The AB model mean location is much less than a single spatial step $\triangle x = 0.02$ distance from the PDE mean location. As time approaches $t = 0.06$, we see that the AB model mean location varies wildly during each iteration due to the small number of agents in the live state. Finally, although the MSD graphs do not show exact agreement in magnitude, we can observe a qualitative agreement with their shapes. Each has a cusp appearing near $t = 0.013$, which is approximately when some agents begin changing state. The MSD graph magnitudes approach move closer after that time, since both the AB model simulation and PDE solution tend to be concentrated near a single local chemical minimum.

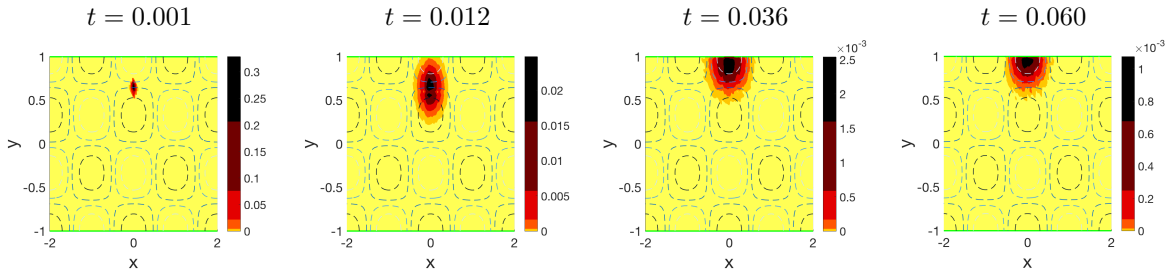

(a) AB Model Simulation

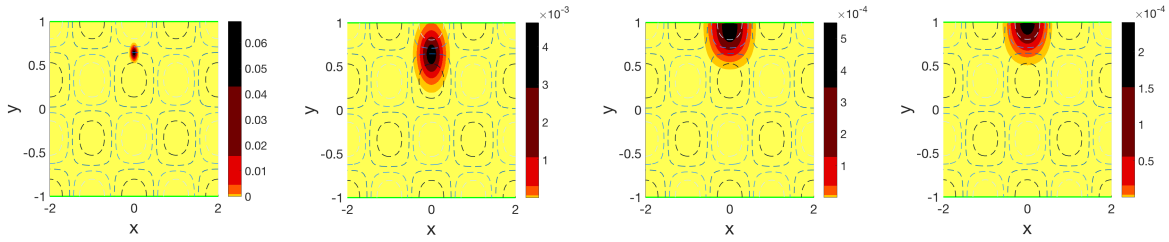

(b) PDE Numerical Solution

Figure 6.7: Probability distribution of agents (shown in color) in the infinite strip region $[-2, 2] \times [-1, 1]$ at four different time points. Agents are initialized at $(0, 0.64)$. The **blue** contour plot denotes the chemical concentration $C(\mathbf{x}) = \frac{1}{2}\left(\cos(\pi x)\sin\left(\frac{3}{2}\pi y\right) + 1\right)$ and the **green** line denotes the reflective boundary at $y = -1$ and $y = 1$. The absorption capacitance is $\xi_c = 8\triangle t \triangle x \triangle y$. **(a)** AB model simulation 2-d histogram is average of 5×10^5 realizations with step sizes $\triangle x = 0.02$ and $\triangle t = \triangle x^2/2$. Histogram bin size is $2\triangle x \times 2\triangle x$. **(b)** PDE numerical solution is computed in the region $[-3, 3] \times [-3, 3]$ with numerical step sizes $\delta x = \triangle x$, $\delta t = \triangle t$, and $\delta\xi = \xi_c/300$.

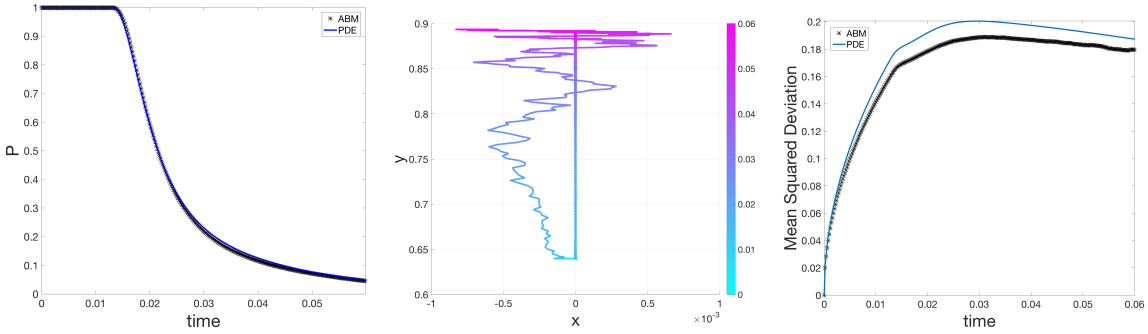

(a) Survival Probability (b) Mean Location (c) Mean Squared Deviation

Figure 6.8: Various statistical measures comparing the AB model and PDE **(a)** Survival probability, **(b)** Mean location, and **(c)** MSD.

Square Domain: To extend the infinite strip to a rectangular domain, we need to add another image step by imposing the numerical method of images to both the x-

and y-coordinates. Since adjacent boundaries in a rectangular domain are orthogonal, we can decompose the image domains as being a reflection of only one coordinate. So we essentially iterate the infinite strip method in each dimension. However, as we see in Fig. 6.9, we also need to account for the corner image domains, which are additional image extentions reflected from the image domains. Due to the added complexity, we state the

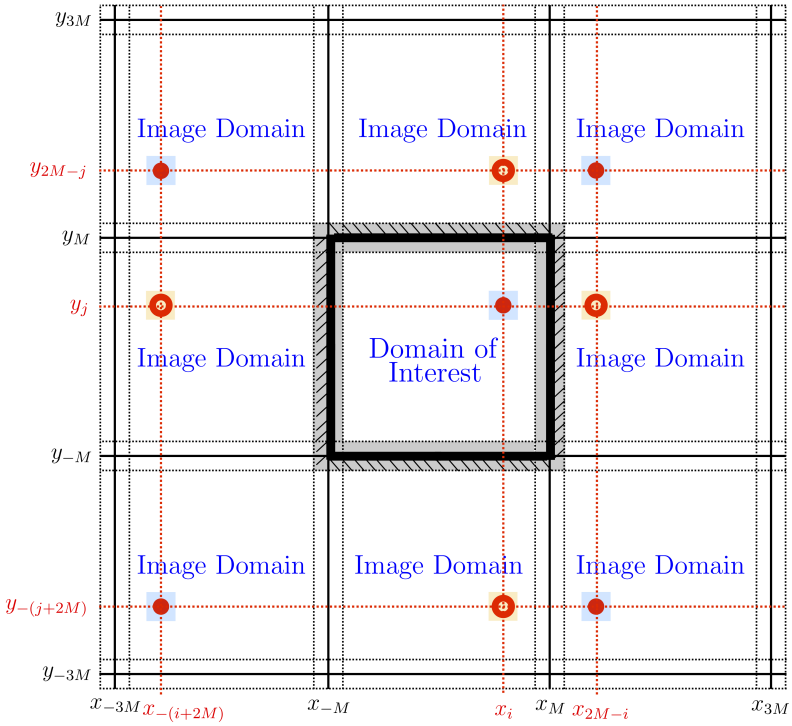

Figure 6.9: Numerical domain for a square domain of interest in 2-d. The numerical domain x-coordinates, $\{x_{-M}, x_{-M+1}, \ldots, x_M\}$, are extended to the left of the border cells at $x = x_{-M}$ and to the right of border cells at $x = x_M$ (both depicted in **gray**), producing a mirror image of values in the extensions $\{x_{-M+1}, x_{-M+2}, \ldots, x_{-3M+1}\}$ and $\{x_{M+1}, x_{M+2}, \ldots, x_{3M-1}\}$. Similarly, the numerical domain y-coordinates, $\{y_{-M}, y_{-M+1}, \ldots, y_M\}$, are extended to the left of the border cells at $y = y_{-M}$ and to the right of border cells at $y = y_M$ (both depicted in **gray**), producing a mirror image of values in the extensions $\{y_{-M+1}, y_{-M+2}, \ldots, y_{-3M+1}\}$ and $\{y_{M+1}, y_{M+2}, \ldots, y_{3M-1}\}$.

numerical algorithm for a square domain. However, to conserve space, we assume that the model has no-flux boundary conditions at each wall. By now, it is clear that absorbing boundary conditions require a sign change for each reflection.

- Initialize $u^0_{i,j} = \phi_{i,j}$
- For $m = 0, 1, \ldots$:
  - $\tilde{u}^m_{-M,j} = 2u^m_{-M,j}$, (for all j)

$\diamond$ $\tilde{u}^m_{i,-M} = 2u^m_{i,-M}$, (for all i)

$\diamond$ $\tilde{u}^m_{M,j} = 2u^m_{M,j}$, (for all j)

$\diamond$ $\tilde{u}^m_{i,M} = 2u^m_{i,M}$, (for all i)

$\diamond$ $\tilde{u}^m_{-(i+2M),j} = u^m_{i,j}$ (for $i, j = -M+1, -M+2, \ldots, M-1$)

$\diamond$ $\tilde{u}^m_{i,-(j+2M)} = u^m_{i,j}$ (for $i, j = -M+1, -M+2, \ldots, M-1$)

$\diamond$ $\tilde{u}^m_{2M-i,j} = u^m_{i,j}$ (for $i, j = -M+1, -M+2, \ldots, M-1$)

$\diamond$ $\tilde{u}^m_{i,2M-j} = u^m_{i,j}$ (for $i, j = -M+1, -M+2, \ldots, M-1$)

$\diamond$ $\tilde{u}^m_{-(i+2M),-(j+2M)} = u^m_{i,j}$ (for $i, j = -M+1, -M+2, \ldots, M-1$)

$\diamond$ $\tilde{u}^m_{-(i+2M),2M-j} = u^m_{i,j}$ (for $i, j = -M+1, -M+2, \ldots, M-1$)

$\diamond$ $\tilde{u}^m_{2M-i,-(j+2M)} = u^m_{i,j}$ (for $i, j = -M+1, -M+2, \ldots, M-1$)

$\diamond$ $\tilde{u}^m_{2M-i,2M-j} = u^m_{i,j}$ (for $i, j = -M+1, -M+2, \ldots, M-1$)

$\diamond$ $u^m_{i,j} = \lambda_{i,j} \sum_{k=-3M+1}^{3M-1} \sum_{\ell=-3M+1}^{3M-1} \tilde{u}^m_{i-k,j-\ell} G_{k,\ell}$, (for $i, j = -M, -M+1, \ldots, M$).

For the square domain, we define the domain of interest proportion parameter, $\lambda_{i,j}$, as

$$\lambda_{i,j} = \begin{cases} 0.5 & : \text{ if } i = -M \text{ and } j = -M+1, -M+2, \ldots, M-1 \\ 0.5 & : \text{ if } i = -M+1, -M+2, \ldots, M-1 \text{ and } j = -M \\ 0.25 & : \text{ if } i = M, -M \text{ and } j = -M \\ 1 & : \text{ if } i, j = -M+1, -M+2, \ldots, M-1 \\ 0.5 & : \text{ if } i = M \text{ and } j = -M+1, -M+2, \ldots, M-1 \\ 0.5 & : \text{ if } i = -M+1, -M+2, \ldots, M-1 \text{ and } j = M \\ 0.25 & : \text{ if } i = M, -M \text{ and } j = M \\ 0 & : \text{ otherwise.} \end{cases}$$

Note that $\lambda_{i,j} = 0.25$ at the corners of the domain of interest, since that is the proportion of each corner cell volume within the domain of interest.

Absorption Example $[-1,1] \times [-1,1]$**:** We simulate the absorption model in the square, $\Omega = [-1,1] \times [-1,1]$, with step-sizes $\triangle x = 0.02$ and $\triangle t = \triangle x^2/2$ along with reflecting boundary conditions at the boundary of the region $[-1,1] \times [-1,1]$. The chemical density profile is $C(x,y) = 0.5(\cos(4\pi x)\cos(3\pi y) + 1)$ with absorption rate $\alpha = 0.1$. We initialize 10^6 agents in the live state near the corner at $\mathbf{x}_0 = (0.76, 0.68)$, and an agent changes state when it absorbs above the chemical threshold $\xi_c = 2\triangle t \triangle x \triangle y$. Histogram results for four time points of the AB model are shown in Fig. 6.10a.

We solve the following PDE numerically on the extended numerical domain $[-3,3] \times$

$[-3, 3]$ using the method of images at the square boundary

$$\begin{cases} \frac{\partial U}{\partial t} + \beta(\mathbf{x})\frac{\partial U}{\partial \xi} = D\frac{\partial^2 U}{\partial x^2}, & \mathbf{x} \in \Omega,\ \xi \in [0, \infty),\ t > 0, \\ U = \delta(\mathbf{x} - (0.76, 0.68), \xi), & \mathbf{x} \in \Omega,\ \xi \in [0, \infty),\ t = 0, \\ \frac{\partial U}{\partial y} = 0, & \mathbf{x} \in [-1, 1] \times \{-1, 1\},\ \xi \in [0, \infty),\ t > 0, \\ \frac{\partial U}{\partial x} = 0, & \mathbf{x} \in \{-1, 1\} \times [-1, 1],\ \xi \in [0, \infty),\ t > 0, \end{cases} \tag{6.3}$$

where $D = \triangle x^2/4\triangle t$. The numerical scheme uses the same step-sizes as the AB model ($\delta x = \triangle x$ and $\delta t = \triangle t$) and absorption step-size $\delta\xi = \xi_c/300$. Numerical results for four time points of the PDE solution are shown in Fig. 6.10b.

Comparing the results of Fig. 6.10, we can easily see qualitative similarities. The initial point source is near a local chemical minimum. So the agents initially diffuse in the region, but as agents begin to change state the AB model and PDE histograms demonstrate that the the agents remain concentrated near that local chemical minimum. For statistical comparison between the AB model and PDE solutions, we observe the quantitative agreement in Fig. 6.11. From the survival probability graph, agents in the AB model simulations and PDE solutions begin to change state around $t = 0.008$. The mean location tends to move from the initial point source $(0.76, 0.68)$ to the point $(0.75, 0.667)$, the closest local chemical minimum. The AB model mean location is much less than the length of a single spatial step ($\triangle x = 0.02$) from the PDE mean location. As time approaches $t = 0.03$, we see that the AB model mean location varies wildly during each iteration due to the small number of agents in the live state. Finally, although the MSD graphs do not show exact agreement in magnitude, we can observe a qualitative agreement with their shapes. Each has a turning point near $t = 0.008$, when agents begin changing state. The MSD graph magnitudes approach move closer after that time, since both the AB model simulation and PDE solution tend to be concentrated near a single local chemical minimum. Moreover, we can see the stochasticity affecting the AB model MSD graph after $t = 0.03$.

6.2 Survival Probability

So far, in our model, the agent moves around the bounded spatial region (e.g. $\Omega = [0, \infty)$) via a random walk (RW), while absorbing chemical from the domain. Suppose that if the agent moves across $x = 0$, then the agent leaves the simulation alive. However, if the agent absorbs chemical above a threshold level, ξ_c, while still in the spatial region, then the agent dies. The domain of interest for this modeling problem is shown in Fig. 6.12.

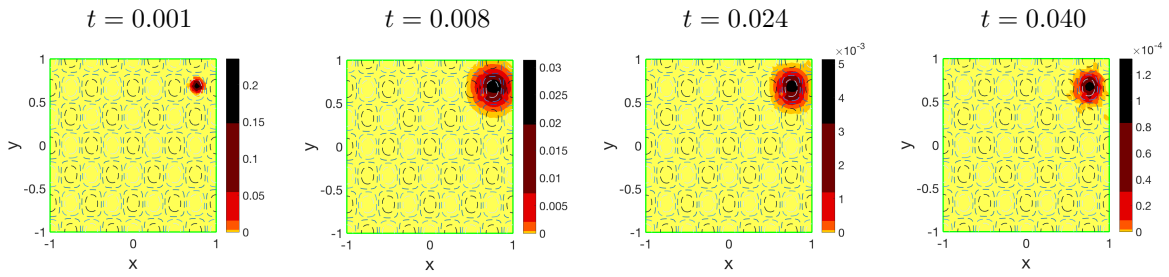

(a) AB Model Simulation

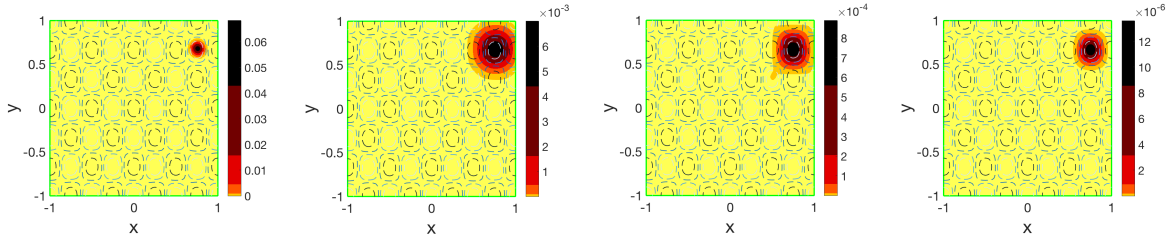

(b) PDE Numerical Solution

Figure 6.10: Probability distribution of agents (shown in color) in the square region $[-1,1] \times [-1,1]$ at four different time points. Agents are initialized at $(0.76, 0.68)$. The **blue** contour plot denotes the chemical concentration $C(\mathbf{x}) = \frac{1}{2}(\cos(4\pi x)\cos(3\pi y) + 1)$ and the **green** line denotes the reflective boundary at the square border. The absorption capacitance is $\xi_c = 2\triangle t \triangle x \triangle y$. **(a)** AB model simulation 2-d histogram is average of 10^6 realizations with step sizes $\triangle x = 0.02$ and $\triangle t = \triangle x^2/2$. Histogram bin size is $2\triangle x \times 2\triangle x$. **(b)** PDE numerical solution is computed in the region $[-3,3] \times [-3,3]$ with numerical step sizes $\delta x = \triangle x$, $\delta t = \triangle t$, and $\delta\xi = \xi_c/300$.

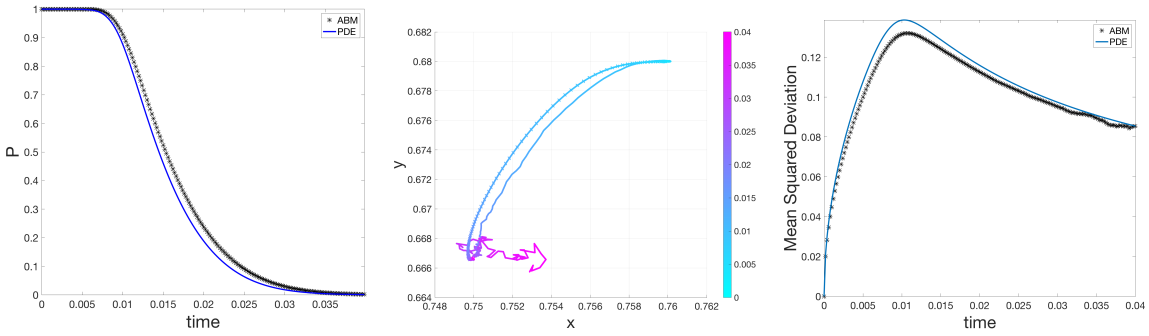

(a) Survival Probability (b) Mean Location (c) Mean Squared Deviation

Figure 6.11: Various statistical measures comparing the AB model and PDE **(a)** Survival probability, **(b)** Mean location, and **(c)** MSD.

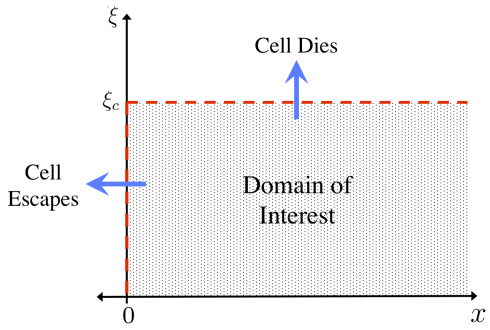

Figure 6.12: Domain of interest with the 1-d spatial domain in the horizontal axis and the absorption domain in the vertical direction. Agents moving across $x = 0$ are said to escape, whereas agents absorbing more than $\xi = \xi_c$ are said to die.

We know that the PDE system with these boundary conditions is:

$$\begin{cases} \frac{\partial U}{\partial t} + \beta(x)\frac{\partial U}{\partial \xi} = D\frac{\partial^2 U}{\partial x^2}, & x \in \Omega,\ \xi \in [0,\infty),\ t > 0, \\ U = \phi(x,\xi), & x \in \Omega,\ \xi \in [0,\infty),\ t = 0, \\ U = 0, & x = 0,\ \xi \in [0,\infty),\ t > 0, \\ \lim_{|x|\to\infty} U(x,t,\xi) = 0, & x \in \Omega,\ \xi \in [0,\infty),\ t > 0, \end{cases} \tag{6.4}$$

and, just like Section 5.1.2, we define

$$p(x,t) = \int_0^{\xi_c} U(x,t,\xi)\, d\xi \tag{6.5}$$

as the density of live agent at location x at time t. Recall that if $\int_\Omega \int_0^{\xi_c} \phi(x,\xi)\, dx\, d\xi = 1$ (such as is the case when the initial condition is a point source), then we can treat $p(x,t)$ as the probability an agent is in the domain at location x at time t and alive. A logical question to answer is: given an initial location and chemical profile, what is the probability an agent eventually escapes the simulation (rather than dies)?

6.2.1 Escape Probability

We can calculate the flux of live agents out of the domain at time t as $f(t) = \frac{\partial p}{\partial x}\Big|_{x=0}$. This concept is drawn from the calculation of splitting probabilities as derived in Section 2.1.3. Usually, splitting probabilities are calculated solely within the spatial dimensions, not between a spatial dimension and another (absorption) dimension.

Then, the total density of live agents that escape the domain after being initialized as

a point source at x_0 is

$$\begin{aligned} T(x_0) &= \int_0^\infty f(t)\,dt \\ &= \int_0^\infty \left.\frac{\partial p}{\partial x}\right|_{x=0} dt \\ &= \int_0^\infty \frac{\partial}{\partial x}\left[\int_0^{\xi_c} U(x,t,\xi)\,d\xi\right]_{x=0} dt \\ &= \int_0^\infty \int_0^{\xi_c} \left.\frac{\partial U}{\partial x}\right|_{x=0} d\xi\,dt \end{aligned}$$

Since $\int_0^\infty \int_0^{\xi_c} U(x,t,\xi)\,d\xi\,dx = 1$ we can consider U a probability distribution. So $T(x_0)$ is the probability an agent escapes the domain at x_0. However, if the initial condition $\int_0^\infty \int_0^{\xi_c} \phi(x,\xi)\,d\xi\,dx \neq 1$, then we can still calculate the escape probability by normalizing T:

$$T(x_0) = \frac{\int_0^\infty \int_0^{\xi_c} \left.\frac{\partial U}{\partial x}\right|_{x=0} d\xi\,dt}{\int_0^\infty \int_0^{\xi_c} \phi(x,\xi)\,dx\,d\xi}.$$

Since all agents in this model either die or escape, the probability that the agent dies is $1 - T(x_0)$. By treating the escape probability as a function $T : [0,\infty) \to [0,1]$ we can analyze what happens as we change the value of x_0.

6.2.2 Numerical Simulation

We simulate the absorption AB model with absorption rate $\alpha = 0.1$, absorption tolerance $\xi_c = 10^{-5}$, and step sizes $\triangle x = 0.01$, $\triangle t = \triangle x^2/2$. We initialize the agents at x_0 and run the simulation until 0.9999 of the agents either escape or transition. Fig. 6.13(a) compares the proportion of agents which are alive, dead, or escaped from the AB model simulation and PDE solutions with chemical density $C(x) = x$. Whereas, Fig. 6.13(b) compares those with chemical density $C(x) = \frac{1}{2}(\sin(x) + 1)$. Part of the discrepancy between the AB model and PDE escape probabilities we see in Table 6.1 is due to the numerical scheme setting dirichlet-zero boundary condition on the entire volume at $[0, \triangle x/2)$. The other is that there is zero waiting probability, as detailed in Section 2.1.1.

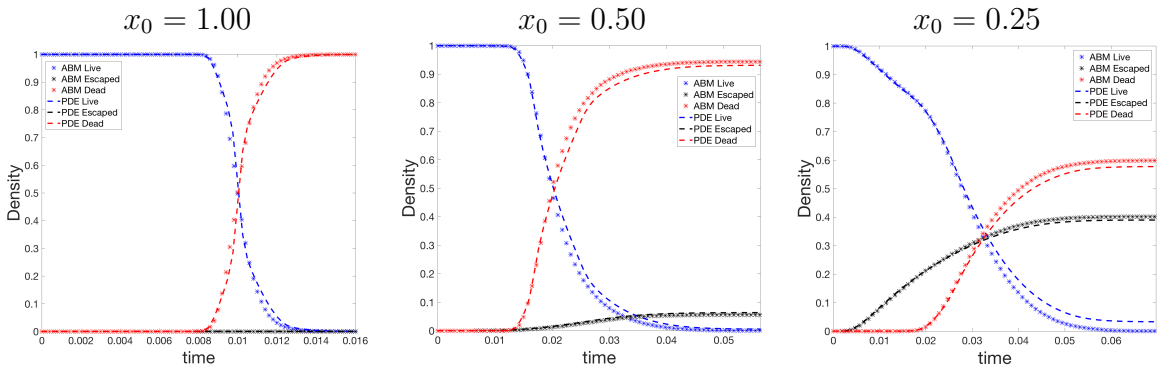

(a) $C(x) = x$

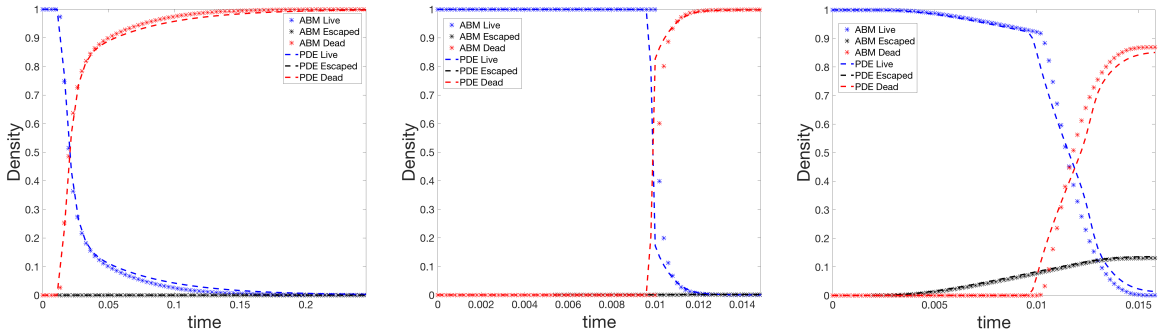

(b) $C(x) = 0.5\,(\sin(\pi x) + 1)$

Figure 6.13: We initialize 10^5 agents at three different point sources at x_0 with chemical profile $C(x)$ and boundary at $x = 0$. The lines and stars denote AB model and PDE solutions, respectively, with colors denoting **Live**, **Dead**, and **Escaped** agents.

$C(x) = x$

	Died		Escaped	
x_0	ABM	PDE	ABM	PDE
1.00	0.9999	0.9999	0	0
0.50	0.9440	0.9313	0.0559	0.0634
0.25	0.5984	0.5776	0.4015	0.3898

$C(x) = 0.5(\sin(\pi x) + 1)$

	Died		Escaped	
x_0	ABM	PDE	ABM	PDE
1.00	0.9999	0.9999	0	0
0.50	0.9987	0.9981	0.0012	0.0017
0.25	0.8695	0.8527	0.1304	0.1357

Table 6.1: Tables of survival probabilities corresponding to end behavior of Fig. 6.13.

Chapter 7

Absorption Model in Fluid Flow

Along with fixed boundaries, agent-based (AB) models can be influenced by dynamic environments. A natural environment for biological organisms to absorb chemical is in a fluid flow. We may be interested in modeling species survival in regions where radioactive particles are spread by atmospheric processes [97], organisms in streamwater currents [40], or chemicals and platelets in blood flow [74]. Recent engineering apparatuses, such as microfluidic devices, allow for experimentation of small scale organisms in controlled fluid profiles [129, 68]. In this chapter, we further adapt the random walk (RW) and cumulative absorption models by immersing the agents in a fluid with a steady (time-independent) profile.

7.1 RW Biased By Fluid

Up to this chapter, we assume that the environment had no explicit effect on the motility of the agents or the chemical concentration, other than the effect that the state changes or boundaries have on the mean location. This is a valid assumption when the agent and chemical are immersed in a static fluid or when the mass of the agent is large enough that the fluid does not exert sufficient force to influence the agent movement. However, in this chapter we examine the cumulative absorption model in cases where the agent and chemical are immersed in a moving fluid, which affects agent and chemical motility. We assume the fluid is steady. That is, the fluid velocity profile, $\mathbf{v}(\mathbf{x})$, is not time dependent, as seen in the examples from Fig. 7.1. But, the RW and cumulative absorption models in this chapter can easily be extended to account for time-dependent fluid velocity profiles. Moreover, the fluid velocity examples in this chapter are incompressible, $\nabla \cdot \mathbf{v} = 0$ [1, Ch.1].

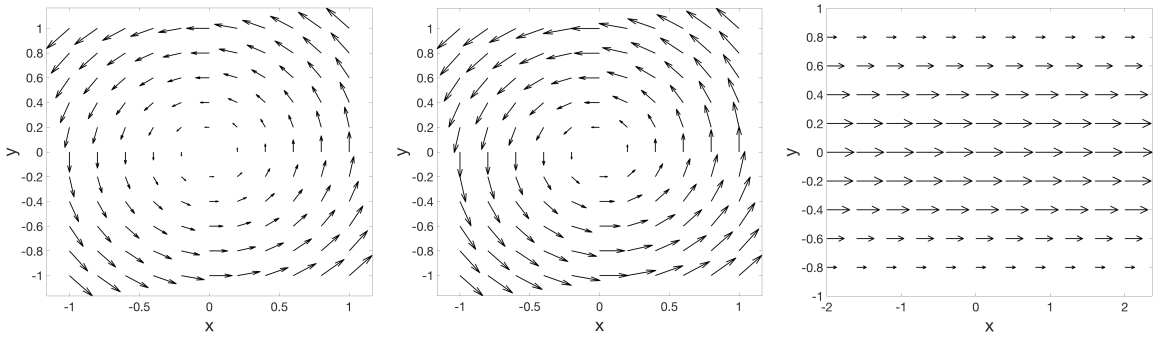

(a) $\mathbf{v}(\mathbf{x}) = \begin{pmatrix} -y \\ x \end{pmatrix}$ (b) $\mathbf{v}(\mathbf{x}) = (3 - ||\mathbf{x}||_2) \begin{pmatrix} -y \\ x \end{pmatrix}$ (c) $\mathbf{v}(\mathbf{x}) = \frac{1}{4} \begin{pmatrix} 1 - y^2 \\ 0 \end{pmatrix}$

Figure 7.1: Fluid velocity fields used in RW and absorption model examples.

7.1.1 Derivation

Assume that an agent's movement is affected by a fluid velocity[1] $\mathbf{v}(\mathbf{x}) = (v_1(\mathbf{x}), v_2(\mathbf{x}))^T$ in some 2-d spatial domain $\Omega \subset \mathbb{R}^2$. We acknowledge that this influence can occur directly, by the fluid forces physically transporting the agent, or indirectly, by biasing the agent's movement. Semantically, we demarcate the terms transport and movement. Transport implies the agent changes location through some external force and independent of an agent's actions, whereas movement refers to change in location due to an agent's self-agency, even though the movement may be biased by the same forces that transport the agent.

Direct Fluid Influence: Transport Due to Fluid Forces

The agent may be transported by the fluid, the influence of which may be dampened by friction or drag forces [58]. During a given time-step interval $[t, t+\triangle t)$, the fluid transports an agent the distance $\int_t^{t+\triangle t} a\mathbf{v}(\mathbf{x})\, dt = a\mathbf{v}(\mathbf{x})\triangle t$, where the parameter $a \in [0, 1]$ is the influence (or force) of the steady fluid flow to move the agent. If $a = 0$ then the agent does not move due to the fluid, but only from its self-agency. If $a = 1$, then the agent moves with the fluid, so the reference frame of the agent is the same as a fluid particle in the flow. This parameter correlates to the mechanical notion of drag or friction forces impeding an agent's movement. For example, a sphere moving through a viscous fluid has a drag force $F_d = 6\pi\mu r\mathbf{v}$, where μ is the viscosity, r is the sphere radius, and $\mathbf{v}$ is the fluid velocity relative to the sphere [1, Ch.7]. The drag force is directly proportional to the sphere radius. So, in a random walk model, the fluid transport influence, a, would decrease as the agent's radius, r, increases.

[1]For this particular section, the variables $\mathbf{v}(\mathbf{x}) = (v_1(\mathbf{x}), v_2(\mathbf{x}))^T$ are used to denote fluid velocities. Velocities $v_1(\mathbf{x})$ and $v_2(\mathbf{x})$ denote the fluid velocity in the x and y coordinates, respectively. As in previous chapters, U denotes the density of live cells.

Indirect Fluid Influence: Movement Biased by Fluid

The fluid flow may affect the agent's decision to move, which reveals itself in our model by changing the RW movement probabilities. This is similar to modeling chemotaxis by a biased random walk [3]. However, in this case the movement probabilities are not manipulated by chemical gradients, but rather by the fluid velocities. We define the normalized velocities as

$$\hat{v}_1(\mathbf{x}) = \frac{v_1(\mathbf{x})}{\sup_{\hat{\Omega}} |v_1(\mathbf{x})|}, \qquad \hat{v}_2(\mathbf{x}) = \frac{v_2(\mathbf{x})}{\sup_{\hat{\Omega}} |v_2(\mathbf{x})|},$$

where $\hat{\Omega} \subset \Omega$ is the numerical or simulation boundary. In an unbounded case we may find that $\sup_{\Omega} |v_k(\mathbf{x})| = +\infty$. So, we need to restrict the domain Ω to a region, $\hat{\Omega}$, local to the agent's initial location and such that the agent cannot exit during the simulation run-time. This provides a normalized bound $0 \leq |\hat{v}_1(\mathbf{x})|, |\hat{v}_2(\mathbf{x})| \leq 1$ for all $\mathbf{x} \in \hat{\Omega}$.

Suppose the agent can move in one of four directions n, s, e, w. We assign biasing in each direction as probabilistic functions $n(\mathbf{x}, \mathbf{v}), s(\mathbf{x}, \mathbf{v}), e(\mathbf{x}, \mathbf{v})$, and $w(\mathbf{x}, \mathbf{v})$ such that $0 \leq n(\mathbf{x}, \mathbf{v}), s(\mathbf{x}, \mathbf{v}), e(\mathbf{x}, \mathbf{v}), w(\mathbf{x}, \mathbf{v})$ and $0 \leq (n(\mathbf{x}, \mathbf{v}) + s(\mathbf{x}, \mathbf{v}) + e(\mathbf{x}, \mathbf{v}) + w(\mathbf{x}, \mathbf{v})) \leq 1$. Given these contraints, the choice of biasing functions is not unique. In this chapter, we define the biasing probability functions as

- $e(\mathbf{x}) = \frac{1}{4} \{1 + b\hat{v}_1(\mathbf{x})\}, \qquad w(\mathbf{x}) = \frac{1}{4} \{1 - b\hat{v}_1(\mathbf{x})\},$
- $n(\mathbf{x}) = \frac{1}{4} \{1 + b\hat{v}_2(\mathbf{x})\}, \qquad s(\mathbf{x}) = \frac{1}{4} \{1 - b\hat{v}_2(\mathbf{x})\}.$

The parameter $b \in [-1, 1]$ is the influence of the fluid to bias the agent's movement. If $b = 0$, the agent moves itself according to an unbiased RW. As $|b| \to 1$, the fluid exerts greater influence on an agent's decision. The sign of b determines whether the agent desires to travel with or against the fluid flow.

For example, sperm cells and several species of nematodes tend to swim against the flow direction (positive rheotaxis), so we would use $b < 0$ [9, 66]. In contrast, young salmon tend to swim with the flow direction (negative rheotaxis), so we would use $b > 0$ [40]. Although the sign of the biasing parameter b may be known from observation, the exact value is experiment-dependent and may require an inverse problem methodology to tune properly. It is worth noting that some animals, such as *Planaria alpina* choose positive or negative rheotaxis based on the temperature and alkalinity of the fluid [10]. To model this, one can make b a function dependent on the local chemical concentration, however in this chapter we only focus on the constant case.

Derivation of Biased Movement PDE

As in Chapter 2, let $U(x, y, t)$ be the probability an agent is at location (x, y) at time t. We begin with a difference equation, which defines the agent's movement

$$\begin{aligned} U(x,&y, t + \triangle t) \\ &= e(x - a\triangle tv_1 - \triangle x, y - a\triangle tv_2)U(x - a\triangle tv_1 - \triangle x, y - a\triangle tv_2, t) \\ &+ w(x - a\triangle tv_1 + \triangle x, y - a\triangle tv_2)U(x - a\triangle tv_1 + \triangle x, y - a\triangle tv_2, t) \\ &+ n(x - a\triangle tv_1, y - a\triangle tv_2 - \triangle x)U(x - a\triangle tv_1, y - a\triangle tv_2 - \triangle x, t) \\ &+ s(x - a\triangle tv_1, y - a\triangle tv_2 + \triangle x)U(x - a\triangle tv_1, y - a\triangle tv_2 + \triangle x, t). \end{aligned} \tag{7.1}$$

The right side of Eq. (7.1) accounts for both transport and biasing. We assume the flow velocity profile is such that these are the only four locations at time t that can move to location (x, y) at time $t + \triangle t$. As we did in previous chapters, we can expand in a Taylor series and simplify to obtain the movement PDE

$$\frac{\partial U}{\partial t} + a\mathbf{v} \cdot \nabla U + bc\nabla \cdot (\hat{\mathbf{v}}U) = D\nabla^2 U, \tag{7.2}$$

where $\hat{\mathbf{v}} = (\hat{v}_1, \hat{v}_2)^T$, $c = \frac{\triangle x}{2\triangle t}$, and $D = \frac{\triangle x^2}{4\triangle t}$. Suppose the fluid is incompressible, which means $\nabla \cdot \mathbf{v} = 0$. Then, by vector Calculus identities, $\nabla \cdot (\hat{\mathbf{v}}U)$ can be rewritten as

$$\nabla \cdot (\hat{\mathbf{v}}U) = U(\nabla \cdot \hat{\mathbf{v}}) + \hat{\mathbf{v}} \cdot (\nabla U) = \hat{\mathbf{v}} \cdot (\nabla U).$$

It follows that (7.2) simplifies to $\frac{\partial U}{\partial t} + (a\mathbf{v} + bc\hat{\mathbf{v}}) \cdot \nabla U = D\nabla^2 U$. For notational simplicity, we can define the variable

$$\mathbf{w} = a\mathbf{v} + bc\hat{\mathbf{v}} = \begin{bmatrix} av_1 + bcv_1/\sup_{\hat{\Omega}} |v_1| \\ av_2 + bcv_2/\sup_{\hat{\Omega}} |v_2| \end{bmatrix}, \quad \text{with } c = \frac{\triangle x}{2\triangle t}.$$

Note that the fluid biasing proportion, b, and the fluid transport proportion, a, appear in the advection parameter $\mathbf{w}$. Then we just need to solve the following advection-diffusion equation

$$\frac{\partial U}{\partial t} + \mathbf{w} \cdot \nabla U = D\nabla^2 U \tag{7.3}$$

to know the density of agents at $(\mathbf{x}, t)$. It may seem obvious that movement advected by fluid is in the form (7.3), but, in general, the form of $\mathbf{w}$ is not necessarily known. By deriving (7.3) from the RW model, we know the form of $\mathbf{w}$ in terms of how the fluid influences movement bias, b, and the influence of fluid force on the agent's transport, a.

7.1.2 Numerical Method

The PDE (7.3) may not have an explicit analytic solution for general fluid flow $\mathbf{v}$, initial, and boundary conditions. We solve the linear PDE with an operator-split numerical method, similar to that which we introduced in Section 5.2.2. We derive the operator-split system of PDEs in the following subsection. Due to the fluid flow advection term, this system has an additional transport equation, which we need to solve numerically.

Operator-Splitting Algorithm

Suppose our RW has initial condition $U(\mathbf{x}, 0) = \phi(\mathbf{x})$ and free-space boundary condition, $\lim_{|\mathbf{x}|\to\infty} U(\mathbf{x}, t) = 0$. We do not know a closed form solution to this for general fluid velocities $\mathbf{v}(\mathbf{x})$. To solve the PDE approximation, we follow the same method as Chapter 5, where we restate the problem by splitting the operator at discrete time-steps of length τ and then solve each step over discrete control volumes. The algorithm for solving the operator-split PDE problem is adapted from Section 5.2.2 to include the transport term in (7.4), and is defined as:

- $U^0(\mathbf{x}) = \phi(\mathbf{x})$
- For $m = 1, 2, \ldots$
  - $\diamond$ $\bar{U}^{m-1}(\mathbf{x}) = U^{m-1}(\mathbf{x})$
  - $\diamond$ $\hat{U}^{m-1/2}(\mathbf{x}) = G(\mathbf{x}, \tau) * \bar{U}^{m-1}(\mathbf{x})$
  - $\diamond$ $U^m(\mathbf{x}) = \hat{U}^{m-1/2}(x - (bv_1 + ac\hat{v}_1)\tau, y - (bv_2 + ac\hat{v}_2)\tau)$.

Note that the last equation is the same as $U^m(\mathbf{x}) = \hat{U}^{m-1/2}(\mathbf{x} - \mathbf{w}\tau)$. For the numerical solution of the diffusion equation, we use the same Green's function convolution as Section 5.2.2. Due to variations in the magnitude of the advection function throughout the domain, we derive an advection numerical method from a Lagrangian perspective to ensure the accuracy of the advection operator.

Lagrangian Advection Numerical Method

Assume we know the average fluid velocity in each numerical volume $B(x_i, \delta x/2) \times B(y_j, \delta y/2)$. That is, we can compute $\mathbf{v}_{i,j} = \frac{1}{\delta x\, \delta y} \int_{B(x_i,\delta x/2)} \int_{B(y_j,\delta y/2)} \mathbf{v}(\mathbf{x})\, dy\, dx$. We want to numerically solve the 2-d advection equation

$$\frac{\partial U}{\partial t} + (bv_{1_{i,j}} + ac\hat{v}_{1_{i,j}})\frac{\partial U}{\partial x} + (bv_{2_{i,j}} + ac\hat{v}_{2_{i,j}})\frac{\partial U}{\partial y} = 0, \tag{7.4}$$

whose solution in our operator-split PDE problem is found as $U^m(\mathbf{x}) = \hat{U}^{m-1/2}(x-(bv_{1_{i,j}}+ ac\hat{v}_{1_{i,j}})\tau, y - (bv_{2_{i,j}} + ac\hat{v}_{2_{i,j}})\tau)$.

The advection operator numerical solution method should be robust, so that the stability does not depend on the ratio between the numerical spatial step, δx, and numerical time step, δt. This stability ratio may be spatially-dependent, since the ratio of the advection and diffusion parameters, $\mathbf{w}/D$ may be of different orders throughout the computational domain. Thus, we might need a different method in advective regimes, $|\mathbf{w}|/D \gg 1$, than the method in diffusive regimes, $0 < |\mathbf{w}|/D \ll 1$. We resolve this issue by tracking where the information in each control volume travels.

Generally, finite difference methods choose a particular node and calculate the proportion of information that each neighboring node transfers to that node [75, Ch.1]. In contrast, finite volume methods choose a particular control volume and calculate the fluxes

from surrounding control volumes. The Gudonov method refines this by using characteristics to calculate the proportion of information that enters and exits the cell volumes [76, Ch.4]. However, if the fluid is very fast we would require very small time steps to ensure we do not lose information (i.e. information would travel further than a control volume width during a time increment of length δt). So, we adapt the idea behind the Gudonov method and solve the advection operator from a Lagrangian perspective.

We can think of the advection operator as a means of transporting information across the domain at prescribed directions and speeds. A certain proportion of the information that originated in the control volume centered at $\mathbf{x}_{i,j}$ at time t_n is then propagated to the control volumes near $\mathbf{x}_{i,j} - \mathbf{w}_{i,j}\delta t$ at time t_{n+1}. Although we eventually need a method to advect in 2-d, we can initially derive this numerical method in 1-d and then implement it by iterating the method in both the x and y coordinates.

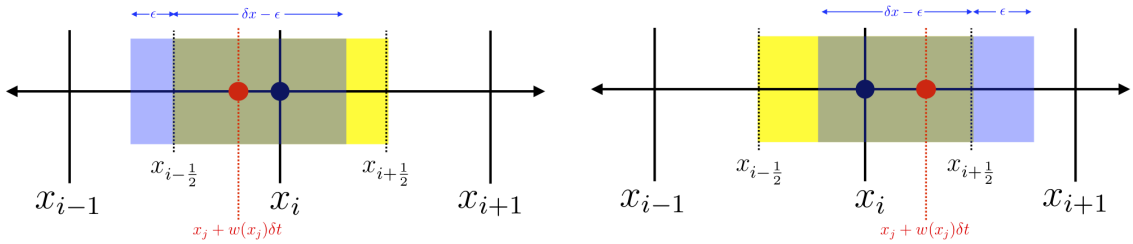

(a) Advected to Left of Cell Center

(b) Advected to Right of Cell Center

Figure 7.2: How information propagates from the control volume at x_j (shown as a **blue rectangle**). The advected x_j is at $x_j + w(x_j)\delta t$ (shown as a **red circle**) and the closest cell volume to the advected x_j is centered at x_i (shown as a **yellow rectangle**). Unless that is the cell center, a proportion of u_j^n is propagated to the cell on either the left or the right of x_j.

Suppose we wanted to solve the 1-d transport PDE:

$$\frac{\partial U}{\partial t} + w(x)\frac{\partial U}{\partial x} = 0.$$

In 1-d, we know the characteristics of the transport equation at x_j move a distance $w(x_j)\delta t$ during the time interval $[t, t+\delta t)$ for every t. So the new location after time-step δt becomes $\hat{x}_j = x_j + w(x_j)\delta t$. But, we cannot guarantee that this new location is centered at a cell grid for every cell center x_j and numerical time step δt. To account for this error, we calculate the proportion of information from the cell centered at x_j that advects to the cell centered at x_i by looking at the characteristics. We encode this information into the characteristic proportion factor γ_j^i for every x_j, x_i in our numerical domain. Denote $idx(\hat{x}_j)$ the index of the closest cell center to $\hat{x}_j$. From Fig. 7.2 we see that we define the characteristic proportion factor as

$$\gamma_j^i = \begin{cases} 1 - \epsilon/\delta x & : \text{ if } i = idx(\hat{x}_j) \\ \epsilon/\delta x & : \text{ if } i = idx(\hat{x}_j) + sgn[\hat{x}_j - idx(\hat{x}_j)] \\ 0 & : \text{ otherwise,} \end{cases}$$

where the sign function, $sgn(x)$, returns 1 if $x \geq 0$ or returns -1 if $x < 0$. Our proposed 1-d Lagrangian numerical scheme, with $u_k^m = \frac{1}{\delta x} \int_{B(x_i, \delta x/2)} U(x, m\delta t)\, dx$, is

$$u_i^{m+1} = \sum_j \gamma_j^i u_j^m.$$

This Lagrangian method can easily extend to higher dimensions, by solving for the proportion iteratively in each dimension. Note that if the flow is steady (w does not depend on time), the characteristic proportion factors, γ_j^i, can be precomputed in a sparse matrix to save computational time.

7.1.3 Examples

Before adding a chemical concentration and absorption dynamics into the model, we want to examine how well the RW simulation agrees with the PDE approximation. Our insights here help us better understand any error that we may incur by adding absorption based state changes to the model. We examine the RW in different domains, both free-space and bounded, with prescribed steady fluid velocity fields.

Free-Space Domain

We begin examining the RW in the free-space domain with the biasing parameter, $b = 1$, held constant for three different fluid advection parameter, a, regimes. For these free-space examples, the fluid velocity profile is defined as

$$\mathbf{v}(x, y) = 50 \left(3 - \sqrt{x^2 + y^2}\right) \begin{pmatrix} -y \\ x \end{pmatrix}$$

as shown in Fig. 7.1b. It is easy to calculate that $\nabla \cdot \mathbf{v} = 0$, so we know that the fluid flow is incompressible. We initialize 10^6 agents at $\mathbf{x}_0 = (0, 0.4)$, advect the agent a distance proportional to a and then move the agent with spatial step-size $\triangle x = 0.01$ with biasing parameter b. Each time-step is defined as $\triangle t = \triangle x^2/2$. For the numerical PDE approximation, we define step-sizes $\delta x = \triangle x$ and $\delta t = \triangle t$ and solve the PDE in the numerical domain $[-4, 4] \times [-4, 4]$. The three regimes are $a = 0$ (biasing only), $a = 1/50$ (maximum fluid transport distance is roughly the same order as the estimated URW mean squared deviation for one time-step), and $a = 1$ (maximum fluid transport distance is much larger than the the estimated URW mean squared deviation for one time-step).

No fluid transport ($a = 0$): Here we experiment with just a passive fluid influence by assigning $a = 0$. That is, we model a RW biased by fluid flow, but the fluid does not actively move each agent, such as what occurs when the agent has large mass. We see in Fig. 7.3a and 7.3b that the pdf spreads almost symmetrically from a center point. But, in contrast to the graphs from Chapter 2, the distribution translates due to the fluid biasing. We can see this translation in the mean location graph of Fig. 7.4. The mean

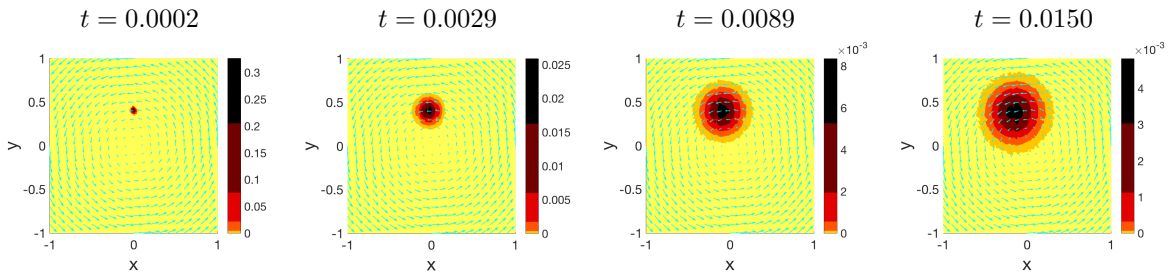

(a) AB Model Simulation

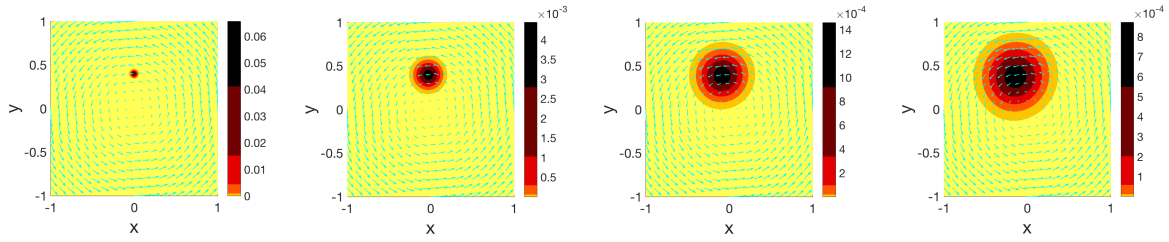

(b) PDE Numerical Solution

Figure 7.3: Probability distribution of agents (shown in color) in the region $[-1,1]\times[-1,1]$ at four different time points. Agents are initialized at $(0, 0.4)$ and move with parameters $b = 1$, $a = 0$. The fluid velocity field is denoted in **cyan**. **(a)** AB model probability distribution is average of 10^6 realizations with step sizes $\triangle x = 0.01$ and $\triangle t = \triangle x^2/2$ and is depicted as a 2-d histogram with bin size $2\triangle x \times 2\triangle x$. **(b)** PDE numerical solution is computed in the region $[-4, 4] \times [-4, 4]$ with numerical step sizes $\delta x = \delta y = \triangle x$ and $\delta t = \triangle t$.

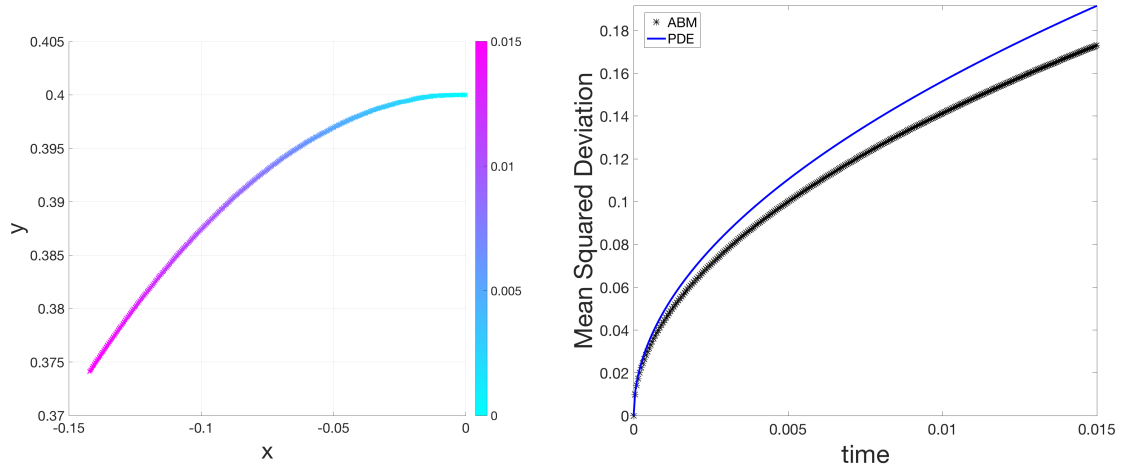

(a) Mean Location

(b) Mean Squared Deviation

Figure 7.4: Plots of various statistical measures comparing the AB model and PDE **(a)** Mean location (time shown in colorbar) and **(b)** MSD.

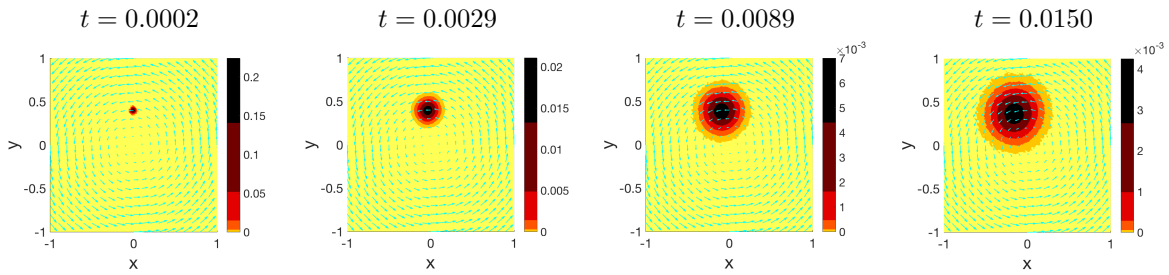

(a) AB Model Simulation

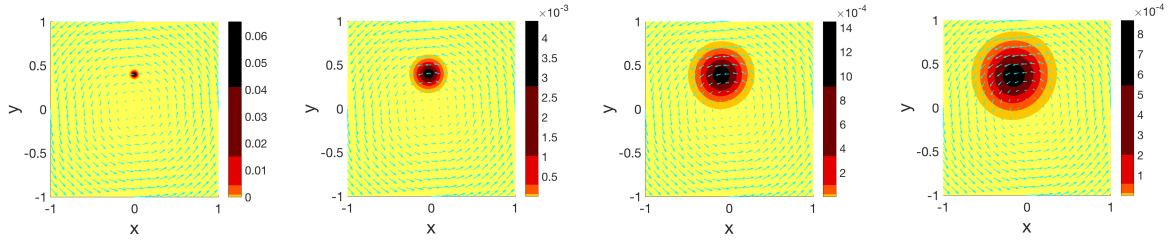

(b) PDE Numerical Solution

Figure 7.5: Probability distribution of agents (shown in color) in the region $[-1,1]\times[-1,1]$ at four different time points. Agents are initialized at $(0, 0.4)$ and move with parameters $b = 1$, $a = 1/50$. The fluid velocity field is denoted in **cyan**. **(a)** AB model probability distribution is average of 10^6 realizations with step sizes $\triangle x = 0.01$ and $\triangle t = \triangle x^2/2$ and is depicted at each time as a 2-d histogram with bin size $2\triangle x \times 2\triangle x$. **(b)** PDE numerical solution is computed in the region $[-4, 4] \times [-4, 4]$ with numerical step sizes $\delta x = \delta y = \triangle x$ and $\delta t = \triangle t$.

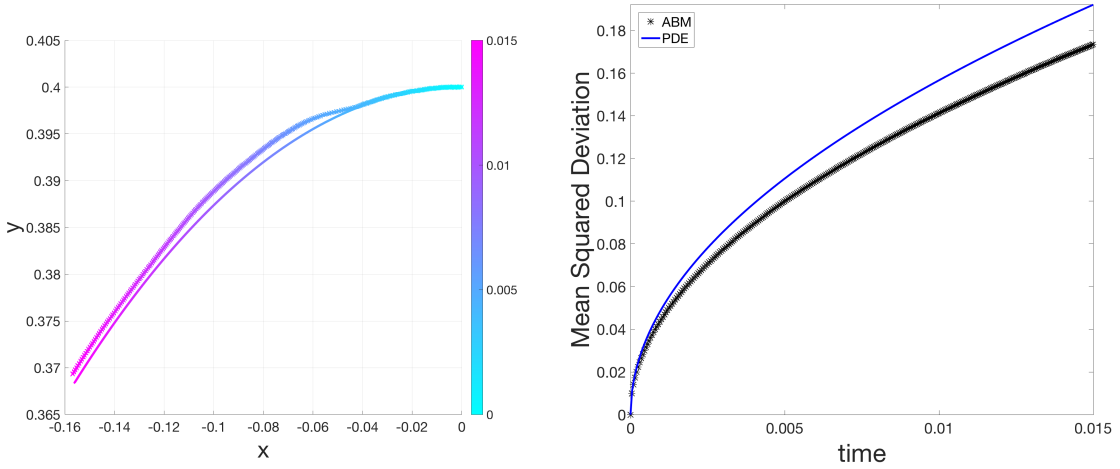

(a) Mean Location

(b) Mean Squared Deviation

Figure 7.6: Plots of various statistical measures comparing the AB model and PDE **(a)** Mean location (time shown in colorbar) and **(b)** MSD.

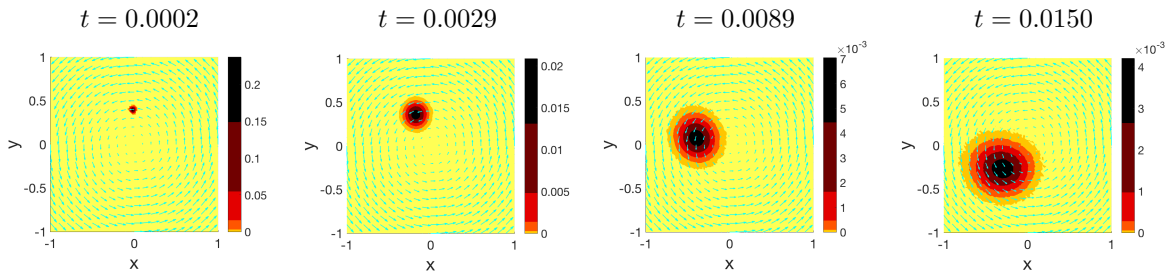

(a) AB Model Simulation

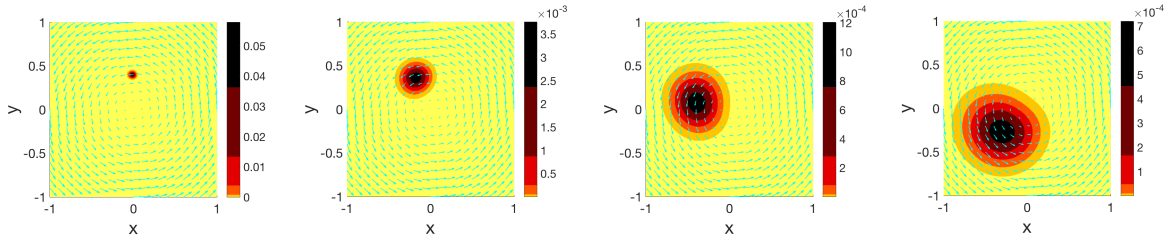

(b) PDE Numerical Solution

Figure 7.7: Probability distribution of agents (shown in color) in the region $[-1,1]\times[-1,1]$ at four different time points. Agents are initialized at $(0, 0.4)$ and move with parameters $b = 1$, $a = 1$. The fluid velocity field is denoted in **cyan**. **(a)** AB model probability distribution is average of 10^6 realizations with step sizes $\triangle x = 0.01$ and $\triangle t = \triangle x^2/2$ and is depicted at each time as a 2-d histogram with bin size $2\triangle x \times 2\triangle x$. **(b)** PDE numerical solution is computed in the region $[-4, 4] \times [-4, 4]$ with numerical step sizes $\delta x = \delta y = \triangle x$ and $\delta t = \triangle t$.

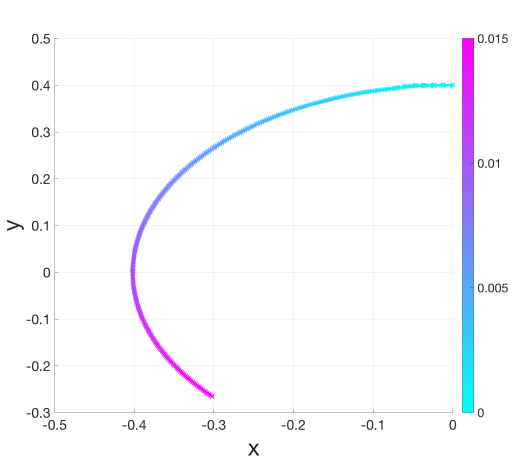

(a) Mean Location

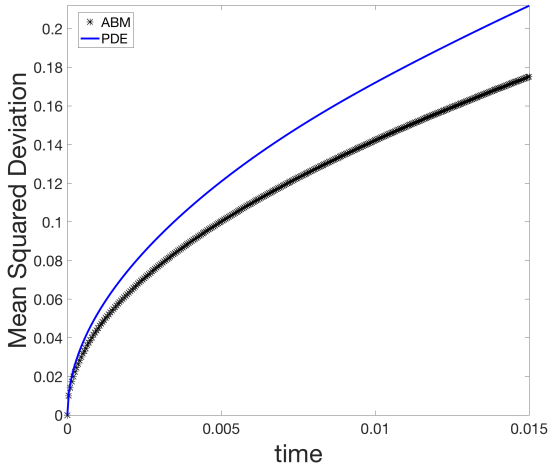

(b) Mean Squared Deviation

Figure 7.8: Plots of various statistical measures comparing the AB model and PDE **(a)** Mean location (time shown in colorbar) and **(b)** MSD.

location starts at $(0, 0.4)$, the initial point source, and terminates around $(-0.14, 0.374)$ at $t = 0.015$ due to the fluid biased movement.

In contrast with the URW graphs, there is less agreement with the mean squared deviation (MSD). Note that the RW, as defined in Section 7.1.1, has zero waiting probability. So, the movement is not as smooth as the PDE approximation. The advection is spatially dependent, causing these smoothing approximation errors to accumulate as time increases.

Large Friction or Drag Forces ($a = 1/50$): In this case, we add active fluid transport by increasing the fluid transport parameter to $a = 1/50$. So we may interpret the mass of the agent in this example as being less than the previous example. We maintain the biasing parameter as $b = 1$ so we can more easily compare both examples. We see in Fig. 7.6 that the agents advect faster than the previous case. The curved trend from $(0, 0.4)$ at $t = 0$ to $(-0.155, 0.369)$ at $t = 0.015$ is due to the fluid biased movement and slight fluid transport. The AB model and PDE MSDs have similar trends, but the difference is due to the spatially dependent fluid velocity.

No Friction or Drag Forces ($a = 1$): In this case, we add active fluid transport by increasing the fluid transport parameter to $a = 1$. That is, the model agents move with the fluid without friction or drag forces, which occurs for infinitesimally small particles (such as pollen grains). We keep the biasing parameter $b = 1$ so we can compare with the previous free-space examples. It is clear in Fig. 7.7a and 7.7b that the increase in fluid force skews the resulting distributions. We see in Fig. 7.8 that the agents advect much faster than the previous case. The curved trend from $(0, 0.4)$ at $t = 0$ to $(-0.3, -0.28)$ at $t = 0.015$ is due to the fluid biased movement and large fluid transport. Moreover, because of the increase in advection speed, the difference in MSD increases. But, we can see that the general shape is the same. Despite this difference in spread, the mean for the AB model and PDE solutions agree fairly well.

Bounded Domains

We provide examples of RW movement biased and advected by fluid velocity profiles in the half-plane, infinite strip, and square bounded regions. We interpret this model as similar to a filter where the filter wall is permeable to the fluid, but obstructs passage of solid particles. The fluid profiles, initial point-source location, and domains may be different in each case, but each bounded simulation initializes 5×10^5 agents at a point source and moves the agents with spatial step $\triangle x = 0.02$ and time-step $\triangle t = \triangle x^2/2$.

Infinite Half-Plane Domain: First, we examine the infinite half-plane domain $\Omega = \mathbb{R} \times [0, \infty)$, enforcing no-flux boundary conditions for the agents at $y = 0$. Agents are initialized at location $(0.5, 0.5)$. The fluid velocity profile is the same as the free-space

case,

$$\mathbf{v}(x,y) = 50(3 - \sqrt{x^2+y^2}) \begin{pmatrix} -y \\ x \end{pmatrix},$$

with simulation biasing parameter $b = 1/5$ and transport parameter $a = 1/50$. To solve this numerically in the bounded domain Ω, we need to use the numerical method of images introduced in Section 6.1.3. However, to ensure that the data is advecting correctly in the image domain, we need to make the transformation for $x \in \mathbb{R}$ and $y < 0$:

$$\begin{aligned} v_1(x,y) &= v_1(x,-y) \\ v_2(x,y) &= -v_2(x,-y). \end{aligned}$$

It is important to note that this image transformation is done to compute the numerical solution, the fluid velocity profile in the model does not reflect across the y-axis. The PDE is then solved in the extended domain $[-2,2] \times [-2,2]$. Note that the fluid velocity $v_2(x,0)$ is non-zero when $x \neq 0$, but the agents reflect off the wall at $y = 0$. Recall that the wall is permeable to the fluid, but not the solid particles.

In Fig. 7.9a and 7.9b that the shape of the distribution is similar. Further, we see in Fig. 7.10 that the mean location agrees up to some small stochastic perturbations. The mean location begins at $(0.5, 0.5)$ and terminates around $(0.2, 0.68)$ at $t = 0.04$ due to the fluid biased movement and slight fluid transport. The AB model and PDE MSDs have similar trends, but the difference is due to the spatially dependent fluid velocity.

Infinite Strip Domain: Suppose there are two infinite planes at $y = -1$ and $y = 1$ bounding the spatial domain. The agents are initialized at $(-1, 0)$. In this infinite strip, we assume the incompressible flow is pressure driven with a constant pressure gradient $\nabla P = -1$ and viscosity $\mu = 1$. The fluid velocity profile is that for a Poiseuille flow [1, Ch.2]:

$$\mathbf{v}(x,y) = \begin{pmatrix} \frac{-\nabla P}{4\mu}(1-y^2) \\ 0 \end{pmatrix},$$

as shown in Fig. 7.1c. Agents are biased with parameter $b = 1/5$ and advected with a moderate friction parameter $a = 1/5$.

The PDE is solved numerically using the numerical method of images, which is introduced in Section 6.1.3. Just as we do for the half-plane case, we need to ensure that the fluid flow in the image domains is flowing correctly. Since $v_2(x,y) = 0$ we do not have to manipulate the vertical velocity in the image domain. The fluid velocity used in the image domain becomes

$$\begin{aligned} v_1(x,y) &= v_1(x,-2-y), \quad \text{if } x \in \mathbb{R}, y \in (-1,-3) \\ v_1(x,y) &= v_1(x,2-y), \quad \text{if } x \in \mathbb{R}, y \in (1,3). \end{aligned}$$

Just as in the half-plane, this reflection is solely done to compute a numerical solution and the reflected fluid flow in the image domains does not represent the actual fluid flow

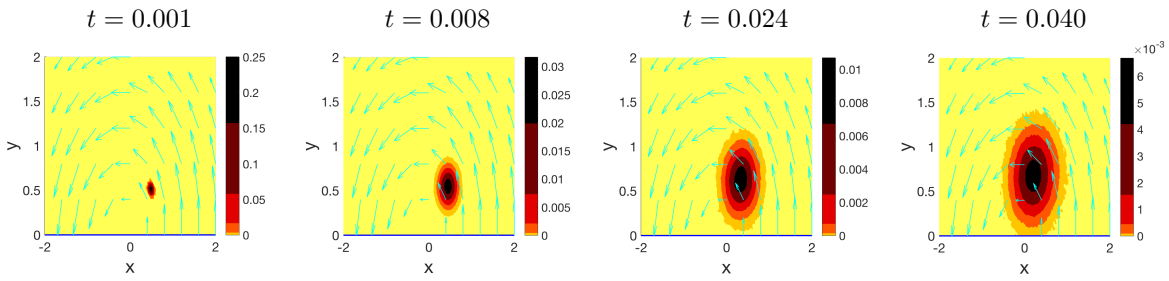

(a) AB Model Simulation

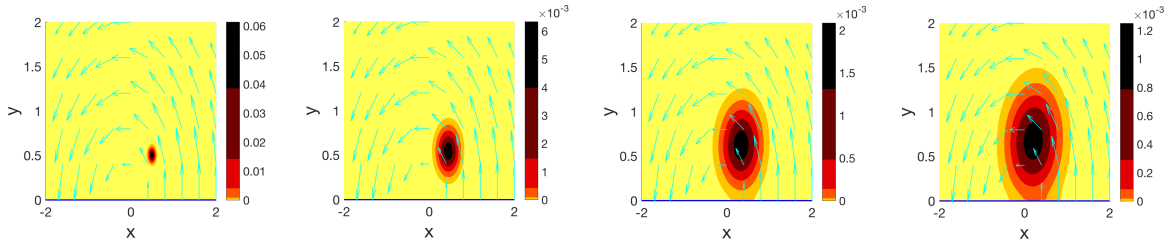

(b) PDE Numerical Solution

Figure 7.9: Probability distribution of agents (shown in color) in the upper half-plane region $[-2, 2] \times [0, 2]$ at four different time points. Agents initialize at $(0.5, 0.5)$ and move with parameters $b = 1/5$, $a = 1/50$. The fluid velocity field is denoted in **cyan** and the boundary is denoted as **blue lines**. **(a)** AB model probability distribution is average of 10^6 realizations with step sizes $\triangle x = 0.02$ and $\triangle t = \triangle x^2/2$ and is depicted at each time as a 2-d histogram with bin size $2\triangle x \times 2\triangle x$. **(b)** PDE numerical solution is computed in the region $[-2, 2] \times [-2, 2]$ with numerical step sizes $\delta x = \delta y = \triangle x$ and $\delta t = \triangle t$.

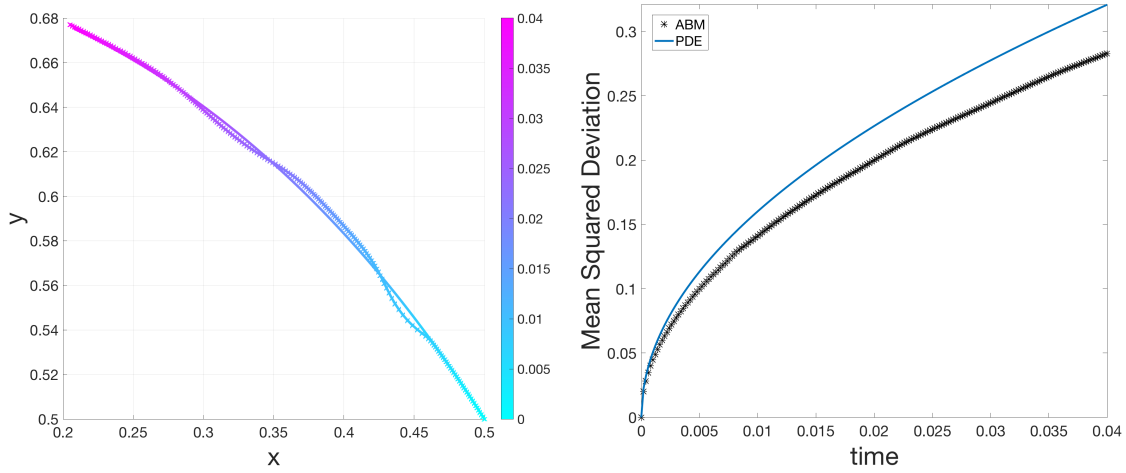

(a) Mean Location

(b) Mean Squared Deviation

Figure 7.10: Plots of various statistical measures comparing the AB model and PDE **(a)** Mean location (time shown in colorbar) and **(b)** MSD.

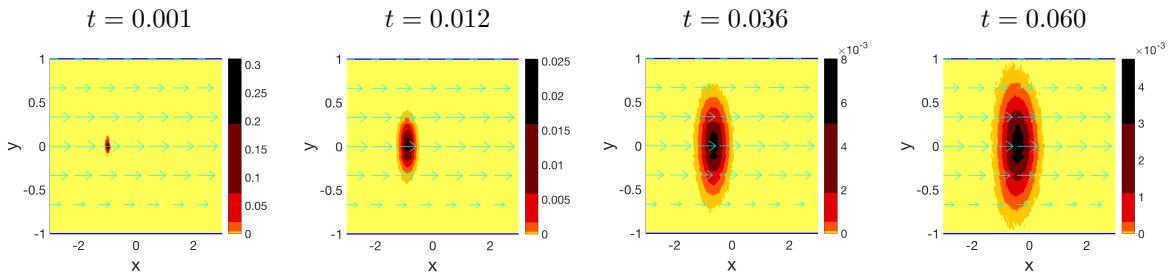

(a) AB Model Simulation

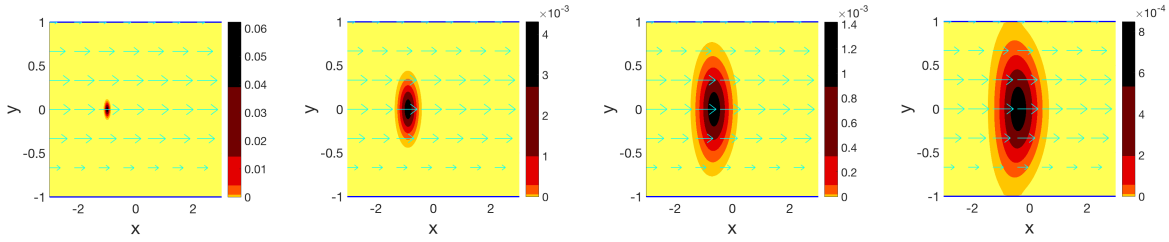

(b) PDE Numerical Solution

Figure 7.11: Probability distribution of agents (shown in color) in the infinite strip region $[-3, 3] \times [-1, 1]$ at four different time points. Agents are initialized at $(-1, 0)$ and move with parameters $b = 1/5$, $a = 1/5$. The fluid velocity field is denoted in **cyan** and the boundary is denoted as **blue lines**. **(a)** AB model probability distribution is average of 10^6 realizations with step sizes $\triangle x = 0.02$ and $\triangle t = \triangle x^2/2$ and is depicted at each time as a 2-d histogram with bin size $2\triangle x \times 2\triangle x$. **(b)** PDE numerical solution is computed in the region $[-3, 3] \times [-3, 3]$ with numerical step sizes $\delta x = \delta y = \triangle x$ and $\delta t = \triangle t$.

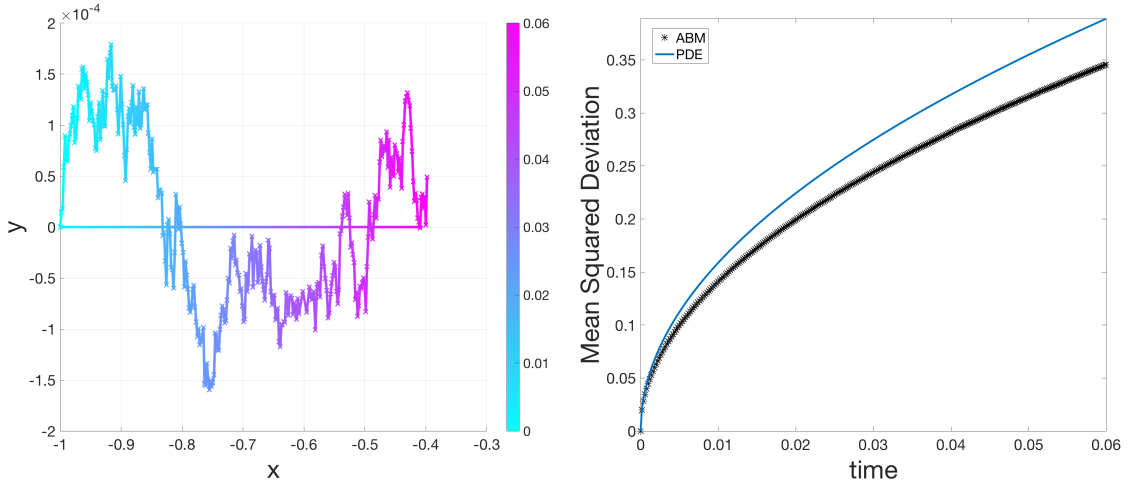

(a) Mean Location

(b) Mean Squared Deviation

Figure 7.12: Plots of various statistical measures comparing the AB model and PDE **(a)** Mean location (time shown in colorbar) and **(b)** MSD.

of the model in the extended domain. We solve the PDE in the extended numerical domain, which is $[-3,3] \times [-3,3]$.

It is clear from Fig. 7.11a and 7.11b that the solution shape appears similar in both cases. The flow has a periodic profile tangential to the x-axis, which accounts for the distribution shape evolution as $t = 0.06$. We see that the solution front has an almost parabolic shape due to the biasing and advection. The mean location, as seen in Fig. 7.12 remains close to $y = 0$. The linear trend for the PDE mean location from $(-1, 0)$ at $t = 0$ to $(-0.4, 0)$ at $t = 0.06$ is due to the fluid biased movement and slight fluid transport. The AB model mean location is noisier due to the RW stochasticity. However, this experimental noise is bounded within a hundredth of the step-size $\triangle x = 0.02$. The AB model and PDE MSDs have similar trends, but the difference is due to the spatially dependent fluid velocity and RW stochasticity.

Square Domain: Finally, we examine the RW in a square domain. We initialize the agents at $\mathbf{x}_0 = (0.2, 0.2)$. We use the same fluid profile as well as the same fluid bias and transport parameters as the infinite half-plane example. Additionally, we also assume that the fluid can pass the boundary without obstruction but the agents reflect off the boundary walls. The simulation domain is $[-1,1]\times[-1,1]$. However, due to the numerical method of images as derived in Section 6.1.3, the extended numerical domain becomes $[-3,3] \times [-3,3]$. To compute the numerical solution, we reflect the fluid velocity profile across the boundaries in a similar way as the infinite half-plane and the infinite strip.

In Fig. 7.13a and 7.13b we see that even when the solution reaches the boundary at $t = 0.04$, the solution shape is relatively symmetrical. We expect this after modeling the free-space solution with large friction forces. The mean and MSD match fairly well in Fig. 7.14. The curved trend from $(0.2, 0.2)$ at $t = 0$ to $(0.04, 0.28)$ at $t = 0.04$ is due to the fluid biased movement and slight fluid transport. The AB model and PDE MSDs have similar trends, but the difference is due to the spatially dependent fluid velocity.

Now that we examined the RW in fluid, we want to add a chemical concentration and absorption-based state change to the model. We first derive the PDE model. Then, we compare the AB model and PDE models in free-space and bounded domains.

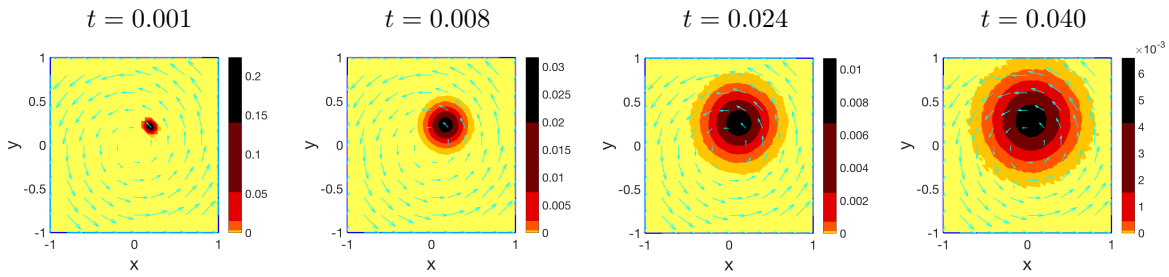

(a) AB Model Simulation

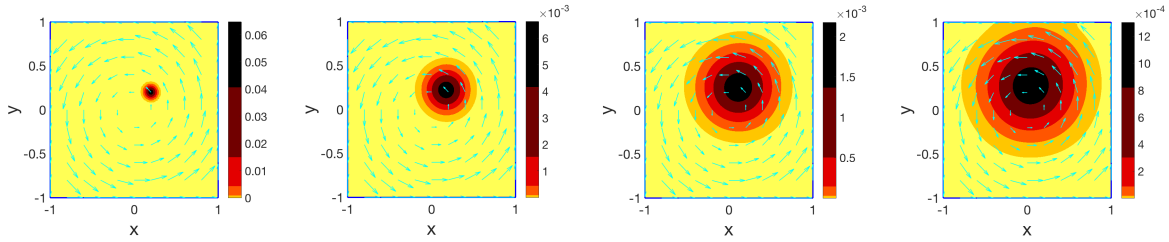

(b) PDE Numerical Solution

Figure 7.13: Probability distribution of agents (shown in color) in the square region $[-1,1]\times[-1,1]$ at four different time points. Agents are initialized at $(0.2, 0.2)$ and move with parameters $b = 1/5$, $a = 1/50$. The fluid velocity field is denoted in **cyan** and the boundary is denoted as **blue lines**. **(a)** AB model probability distribution is average of 10^6 realizations with step sizes $\triangle x = 0.02$ and $\triangle t = \triangle x^2/2$ and is depicted at each time as a 2-d histogram with bin size $2\triangle x \times 2\triangle x$. **(b)** PDE numerical solution is computed in the region $[-3,3]\times[-3,3]$ with numerical step sizes $\delta x = \delta y = \triangle x$ and $\delta t = \triangle t$.

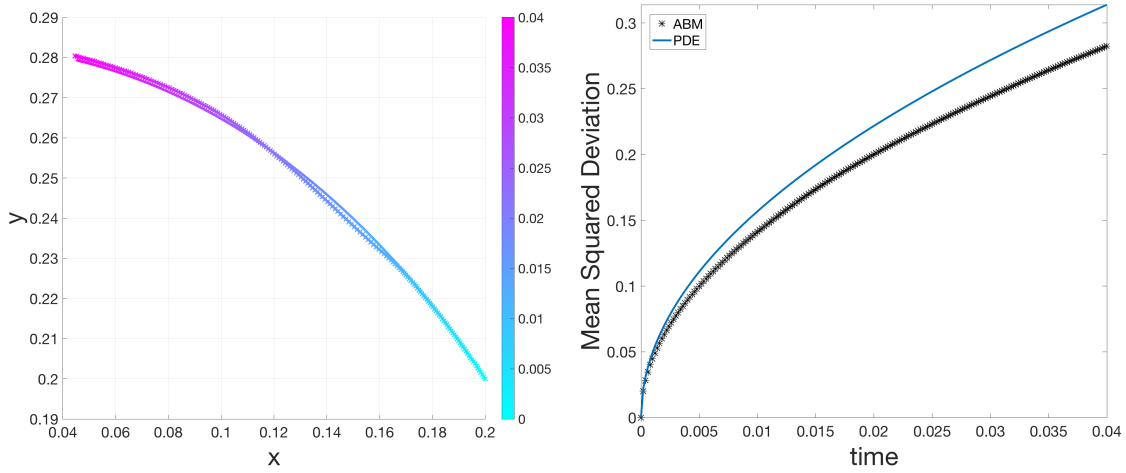

(a) Mean Location

(b) Mean Squared Deviation

Figure 7.14: Plots of various statistical measures comparing the AB model and PDE **(a)** Mean location (time shown in colorbar) and **(b)** MSD.

7.2 Absorption Model in Fluid

We developed methods for modeling cumulative advection as well as a method for modeling RW in a fluid flow. In this section, we combine both models to develop a framework to model cumulative chemical absorption state changes in cases where the fluid affects motility. The flowchart in Fig. 7.15 depicts the logic of the AB model. Not only are the agents moving, but the chemical profile can also change in time due to the fluid flow.

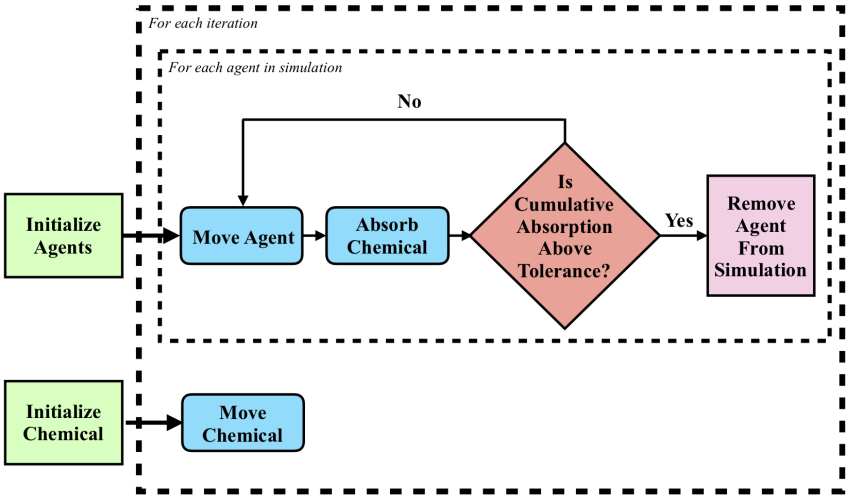

Figure 7.15: Flowchart depicting agent and chemical moving in fluid. The agent absorbs chemical and dies, if cumulative absorption is above tolerance ξ_c.

7.2.1 Derivation

Let $\Omega \subset \mathbb{R}^2$. Suppose we have an incompressible steady fluid profile $\mathbf{v}(\mathbf{x}) = (v_1(\mathbf{x}), v_2(\mathbf{x}))^T$. Just as in Chapter 5, we derive our governing PDE equation by first formulating a difference equation. From Sections 5.1.1 and 7.1.1, we know the difference equation is of the form

$$\begin{aligned} &U(x,y,t+\triangle t, \xi+\hat{\beta}(\mathbf{x},t)) \\ &\quad = e(x-a\triangle tv_1-\triangle x, y-a\triangle tv_2)U(x-a\triangle tv_1-\triangle x, y-a\triangle tv_2, t, \xi) \\ &\quad + w(x-a\triangle tv_1, +\triangle x, y-a\triangle tv_2)U(x-a\triangle tv_1+\triangle x, y-a\triangle tv_2, t, \xi) \\ &\quad + n(x-a\triangle tv_1, y-a\triangle tv_2-\triangle x)U(x-a\triangle tv_1, y-a\triangle tv_2-\triangle x, t, \xi) \\ &\quad + s(x-a\triangle tv_1, y-a\triangle tv_2+\triangle x)U(x-a\triangle tv_1, y-a\triangle tv_2+\triangle x, t, \xi), \end{aligned} \tag{7.5}$$

where e, w, n, and s are defined in the the same way as in Section 7.1.1. In fact, other than the inclusion of the absorption variable, ξ, the right hand side of the difference equation is the same as (7.1). We can also see that the left hand side of the difference equation is similar to our simple absorption model in Section 5.1.1, except here the chemical concentration is also transported by the fluid. So $\hat{\beta}$ depends on time in addition to space. That is, $\hat{\beta}(\mathbf{x},t) = \alpha\triangle t \int_{B(\mathbf{x},\triangle x/2)} C(\mathbf{x},t)\, d\mathbf{x}$, where α is the absorption porosity. Expanding this

difference equation in a Taylor series and simplifying results in the following governing PDE:

$$\frac{\partial U}{\partial t} + \mathbf{w} \cdot \nabla U + \left[\beta(\mathbf{x}, t) + \triangle t \frac{\partial \beta(\mathbf{x}, t)}{\partial t} \right] \frac{\partial U}{\partial \xi} = D_u \nabla^2 U, \tag{7.6}$$

where $D_u = \triangle x^2/(4\triangle t)$ and $\mathbf{w} = a\mathbf{v} + bc\hat{\mathbf{v}}$. In order to solve this PDE, we have to couple it with the equation for chemical concentration.

In a manner similar to Section 7.1.1, we can find the governing PDE of the chemical concentration as:

$$\frac{\partial C}{\partial t} + a_c \mathbf{v} \cdot \nabla C = D_c \nabla^2 C, \tag{7.7}$$

where D_c is the diffusion coefficient. This is the same PDE form as (7.4) with fluid transport parameter $a = a_c$ and fluid biasing parameter $b = 0$, since we assume the chemical has no self-agency. So, we can use the method detailed in Section 7.1 to numerically solve this PDE. Depending on the properties of the chemical, there may be a resistance force causing $a < 1$.

Numerically, we solve the concentration as the average concentration over each spatial control volume

$$c_{i,j}^m = \frac{1}{\delta x \, \delta y} \int_{B(\mathbf{x}_{i,j}, \delta x/2)} C^m(\mathbf{x}) \, d\mathbf{x},$$

where $C^m(\mathbf{x}) = C(\mathbf{x}, m\delta t)$. It follows that for numerical time step $\delta t \ll 1$, we can approximate the time derivative as

$$\frac{\partial}{\partial t} \int_{B(\mathbf{x}_{i,j}, \delta x/2)} C^m(\mathbf{x}) \, d\mathbf{x} \approx \delta x \, \delta y \frac{c_{i,j}^m - c_{i,j}^{m-1}}{\delta t}.$$

As in Section 5.2.2, we solve the PDE (7.6) using an operator-splitting method. The following iterative algorithm solves the semi-discrete, operator-splitting system:

- $U^0(\mathbf{x}, \xi) = \phi(\mathbf{x}, \xi)$
- For $m = 1, 2, \ldots$
  - $\diamond$ $\bar{U}^{m-1}(\mathbf{x}) = U^{m-1}(\mathbf{x})$
  - $\diamond$ $\hat{U}^m(\mathbf{x}, \xi) = \bar{U}^{m-1}(\mathbf{x}, \xi - \beta(\mathbf{x}, m\tau)\tau)$
  - $\diamond$ $\tilde{U}^m(\mathbf{x}, \xi) = G(\mathbf{x}, \tau) * \hat{U}^m(\mathbf{x}, \xi)$
  - $\diamond$ $U^m(\mathbf{x}, \xi) = \tilde{U}^{m-1/3}(x - (bv_1 + ac\hat{v}_1)\tau, y - (bv_2 + ac\hat{v}_2, \xi)\tau)$,

where $\beta(\mathbf{x}, m\tau) = \alpha \left[\int_{B(\mathbf{x}, \triangle x/2)} C^m(\mathbf{x}) \, d\mathbf{x} + \triangle t \frac{\partial}{\partial t} \int_{B(\mathbf{x}, \triangle x/2)} C^m(\mathbf{x}) \, d\mathbf{x} \right]$.

7.2.2 Examples

Free-Space Absorption Fluid Examples

Just as we did in Section 7.1, we first examine the fluid advected absorption model in $\mathbb{R}^2$. For each free-space example we initialize 10^6 agents at $\mathbf{x}_0 = (0, 0.2)$. Agents move with step-size $\triangle x = 0.01$ and $\triangle t = \triangle x^2/2$. The fluid biases movement with parameter $b = 1/5$ and transports the agents with parameter $a = 1/25$. The chemical concentration is initialized as the function $C(\mathbf{x}, 0)$, diffuses at the rate $D_c = 0.2$, and is transported by the fluid with chemical transport parameter $a_c = 1$. Each iteration, the agents absorb chemical with rate $\alpha = 0.1$ until the agent absorbs its chemical capacitance $\xi_c = 10\triangle t\triangle x\triangle y$. The model is solved numerically with numerical steps $\delta x = \delta y = \triangle x$, $\delta t = \triangle t$, and $\delta\xi = \xi_c/300$. The numerical domain in which the solution is solved is $[-3, 3] \times [-3, 3]$.

Free-Space Example 1: In the first free-space example, we define the fluid velocity field as $\mathbf{v}(\mathbf{x}) = 25(-y, x)^T$ and initialize the chemical concentration as $C(\mathbf{x}, 0) = 0.5\,(\sin(4\pi x)\sin(4\pi y))$. Fig. 7.16a and 7.16b show AB model simulation and the PDE solution, respectively, for four time-points. We see the chemical concentration, denoted by blue contour lines, diffusing and rotating. At $t = 0.015$, the solution surface shows that the agents which are still in the live state exist at locations of low concentration.

Similar to the other absorption model examples, Fig. 7.17 shows the survival probability, mean location, and standard deviation. We can see that the survival probability curve is not as steep as our previous models. This may be due to the diffusion of the chemical concentration. The mean location, in contrast to the free-space advection RW model in the previous section, does not simply follow the fluid streamlines. In fact, we can partition the behavior into an initial fluid advected phase and a later state-change phase. The curved trend from $(0, 0.2)$ at $t = 0$ to $(-0.17, 0.04)$ at $t = 0.015$ is initially only due to the fluid biased movement, but after $t = 0.006$ the mean location is also influenced by state changes around regions of higher chemical density. The noise in the AB model mean location is much smaller than a spatial-step $\triangle x = 0.01$. Agents begin to exit the live state around $t = 0.006$, which is the location of the cusp in the mean location graph (around $(-0.01, 0.2)$). This cusp marks the moment in the model where agent state change begins to influence the mean location.

Similar to the standard deviation graphs of the free-space fluid RW models, the MSD initially accumulates error. The AB model and PDE mean squared deviations have a similar trend, but the difference is due to the spatially dependent fluid velocity. The RW has zero waiting probability, and the lack of smoothness coupled with the fluid profile account for the error of this dispersion metric. We can see that as the proportion of cells in the live state changes concavity near $t = 0.01$, and the concentration of cells become localized to one local minimum in the chemical surface, that the difference between the AB model and PDE MSD graphs begin to decrease.

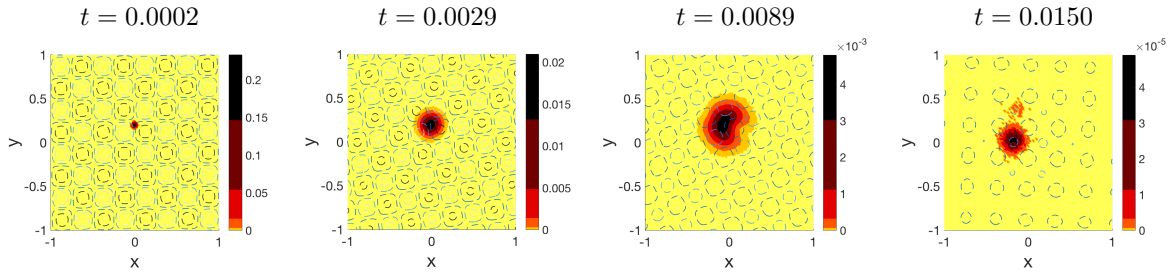

(a) AB Model Simulation

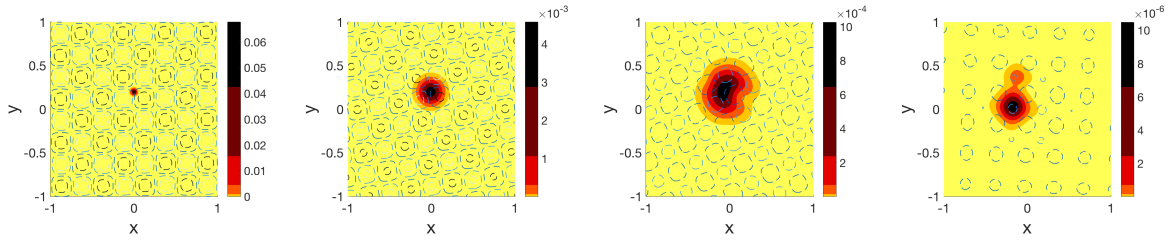

(b) PDE Numerical Solution

Figure 7.16: Probability distribution of agents (shown in color) in the free-space region $[-1,1] \times [-1,1]$ at four different time points. Agents are initialized at $(0, 0.2)$ and move with parameters $b = 1/5$, $a = 1/25$. The **blue** contour plot denotes the chemical concentration $C(\mathbf{x}, t)$. The absorption parameters are $\alpha = 0.1$ and $\xi_c = 10\triangle t \triangle x \triangle y$. **(a)** AB model probability distribution is average of 10^6 realizations with step sizes $\triangle x = 0.01$ and $\triangle t = \triangle x^2/2$ and is depicted at each time as a 2-d histogram with bin size $2\triangle x \times 2\triangle x$. **(b)** PDE numerical solution is computed in the region $[-3, 3] \times [-3, 3]$ with numerical step sizes $\delta x = \delta y = \triangle x$, $\delta t = \triangle t$, and $\delta\xi = \xi_c/300$.

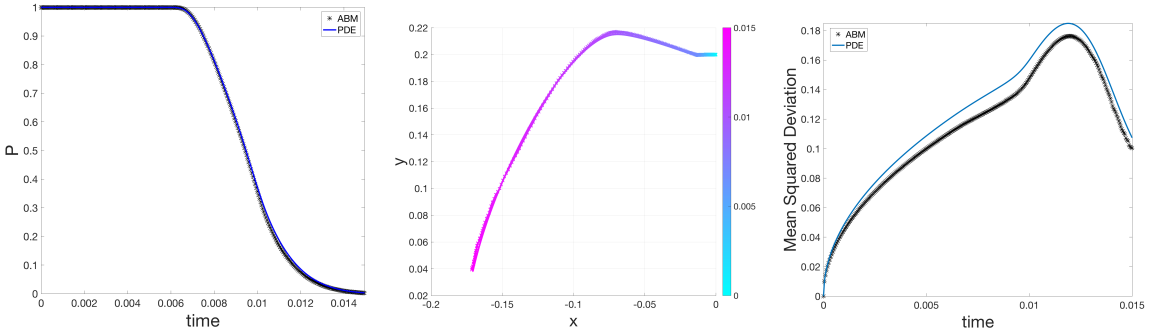

(a) Survival Probability (b) Mean Location (c) Mean Squared Deviation

Figure 7.17: Plots of various statistical measures comparing the AB model and PDE **(a)** Survival probability, **(b)** Mean location (time shown in colorbar), and **(c)** MSD.

Free-Space Example 2: Here, we change the flow field from the previous example to $\mathbf{v}(\mathbf{x}) = 25(3 - \sqrt{x^2 + y^2})(-y, x)^T$, but keep the same initial chemical profile. The

dynamics appear similar to the previous example, with the main concentration of live cells at $t = 0.015$ concentrating near a local minimum of the chemical concentration plot. The curved trend in the mean location graphs of Fig. 7.19 from $(0, 0.2)$ at $t = 0$ to $(-0.14, 0.105)$ at $t = 0.015$ is initially due to the fluid biased movement but after $t = 0.007$ it is also due to state changes around regions of higher chemical density. The error between the AB model and PDE mean locations is much smaller than a spatial-step $\triangle x = 0.01$. The AB model and PDE mean squared deviations have a similar trend, but the difference is due to the spatially dependent fluid velocity. The survival probability plots begin to decrease around $t = 0.007$, which is the same time that a cusp forms in the mean location graph (around point $(-0.035, 0.2)$). This fluid moves faster than the previous example, which is why the cusp appears further from $\mathbf{x}_0$. The AB model simulation and PDE approximations appear to match well in the survival probability and mean location graphs. Again, the mean squared deviation accumulates errors until around $t = 0.012$, which is where the survival probability changes concavity and the live cell surface plot contracts around a single chemical concentration local minimum.

Free-Space Example 3: Here, we keep the same fluid velocity as the previous example, but we change the initial chemical profile to $C(\mathbf{x}, 0) = 0.5\,(\sin(2\pi x)\cos(3\pi y))$. In contrast to the previous two examples, we see in Fig. 7.20a and 7.20b that the chemical concentration causes the agent density to have two separate peaks at $t = 0.015$. These peak centers correspond to local chemical concentration minimums at that time. The curved trend in the mean location in Fig. 7.21 from $(0, 0.2)$ at $t = 0$ to $(-0.085, 0.37)$ at $t = 0.015$ is initially due to the fluid biased movement but after $t = 0.008$ it is also due to state changes around regions of higher chemical density. The error between the AB model and PDE mean locations is much smaller than a spatial-step $\triangle x = 0.01$. The AB model and PDE mean squared deviations have a similar trend, but the difference is due to the spatially dependent fluid velocity. Because the surface plot has two local maximums, the mean squared deviation curves do not begin to converge. Also, the change in the initial chemical profile, $C(\mathbf{x}, t)$, causes the survival probability graphs to begin decreasing at $t = 0.008$. This corresponds to the sharp curve in the mean location graphs around point $(-0.06, -0.2)$. It took longer for the agents to start to accumulate ξ_c chemical, so the fluid was the only influence on the mean location for a longer interval of time.

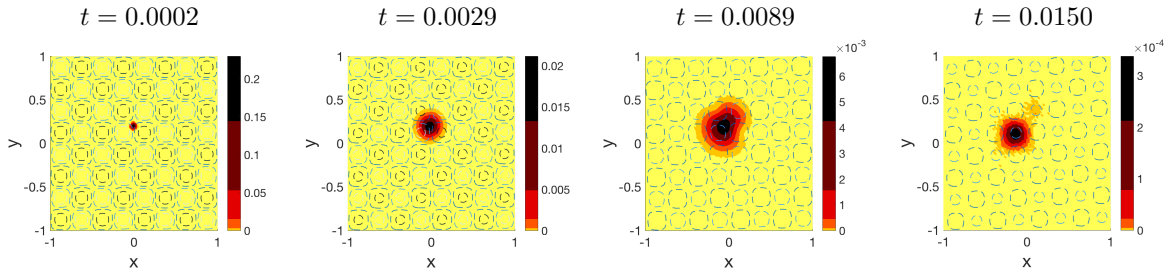

(a) AB Model Simulation

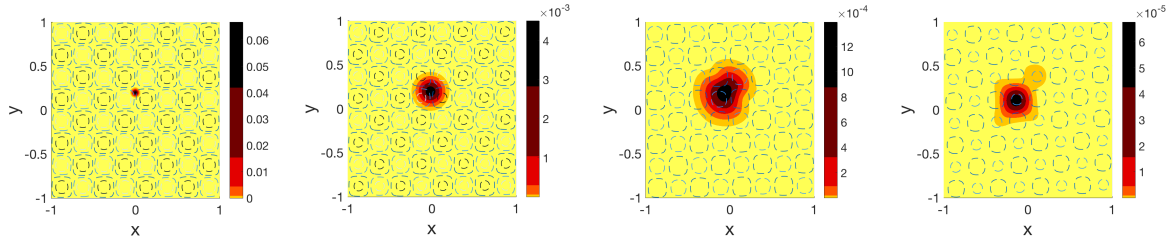

(b) PDE Numerical Solution

Figure 7.18: Probability distribution of agents (shown in color) in the free-space region $[-1,1] \times [-1,1]$ at four different time points. Agents are initialized at $(0, 0.2)$ and move with parameters $b = 1/5$, $a = 1/25$. The **blue** contour plot denotes the chemical concentration $C(\mathbf{x}, t)$. The absorption parameters are $\alpha = 0.1$ and $\xi_c = 10\triangle t \triangle x \triangle y$. **(a)** AB model probability distribution is average of 10^6 realizations with step sizes $\triangle x = 0.01$ and $\triangle t = \triangle x^2/2$ and is depicted at each time as a 2-d histogram with bin size $2\triangle x \times 2\triangle x$. **(b)** PDE numerical solution is computed in the region $[-3, 3] \times [-3, 3]$ with numerical step sizes $\delta x = \delta y = \triangle x$, $\delta t = \triangle t$, and $\delta\xi = \xi_c/300$.

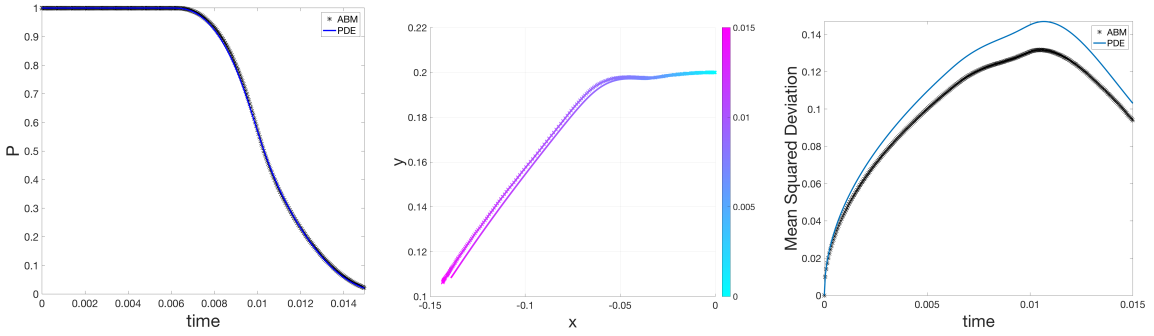

(a) Survival Probability (b) Mean Location (c) Standard Deviation

Figure 7.19: Plots of various statistical measures comparing the AB model and PDE **(a)** Survival probability, **(b)** Mean location (time shown in colorbar), and **(c)** MSD.

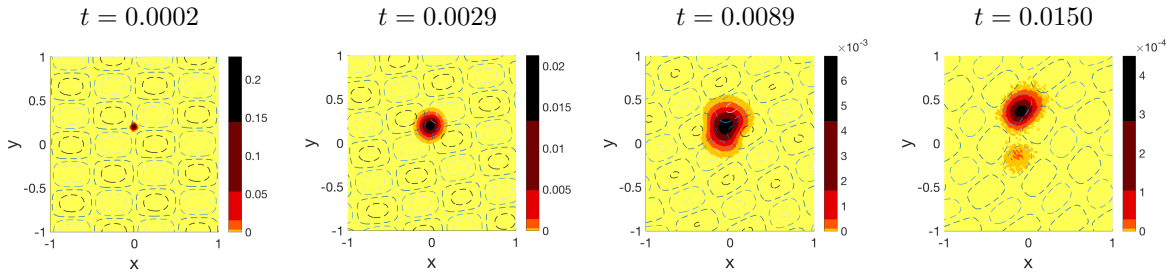

(a) AB Model Simulation

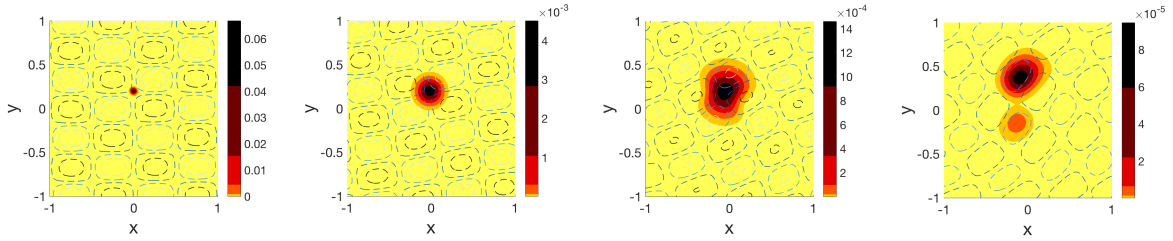

(b) PDE Numerical Solution

Figure 7.20: Probability distribution of agents (shown in color) in the free-space region $[-1,1] \times [-1,1]$ at four different time points. Agents are initialized at $(0, 0.2)$ and move with parameters $b = 1/5$, $a = 1/25$. The **blue** contour plot denotes the chemical concentration $C(\mathbf{x}, t)$. The absorption parameters are $\alpha = 0.1$ and $\xi_c = 10\triangle t \triangle x \triangle y$. **(a)** AB model probability distribution is average of 10^6 realizations with step sizes $\triangle x = 0.01$ and $\triangle t = \triangle x^2/2$ and is depicted at each time as a 2-d histogram with bin size $2\triangle x \times 2\triangle x$. **(b)** PDE numerical solution is computed in the region $[-3,3] \times [-3,3]$ with numerical step sizes $\delta x = \delta y = \triangle x$, $\delta t = \triangle t$, and $\delta\xi = \xi_c/300$.

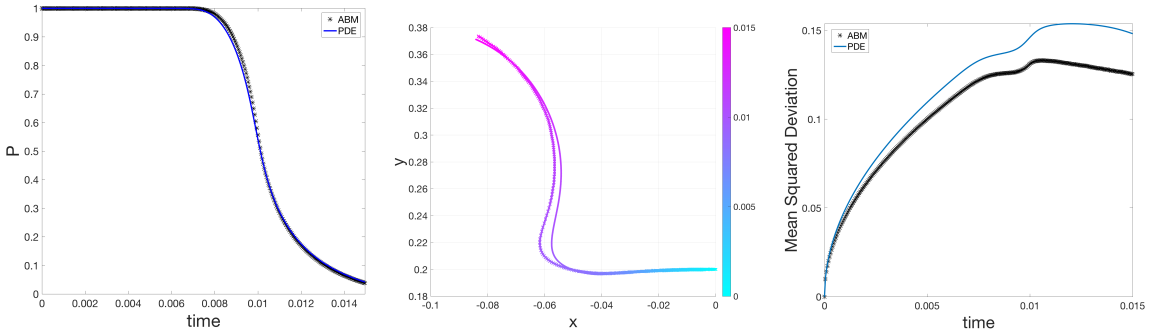

(a) Survival Probability (b) Mean Location (c) Mean Squared Deviation

Figure 7.21: Plots of various statistical measures comparing the AB model and PDE **(a)** Survival probability, **(b)** Mean location (time shown in colorbar), and **(c)** MSD.

Bounded Absorption Fluid Examples

If we want to apply the absorption model to specific real-world situations, we need to verify it in bounded regions. We examine the same three bounded regions as Section 7.1.3: an infinite half-plane, an infinite strip, and a square. In each case we initialize 10^6 agents at a point $\mathbf{x}_0$. The agents move with spatial step-size $\triangle x = 0.02$ and temporal step size $\triangle x^2/2$. The chemical concentration is initialized with an initial chemical profile, $C(\mathbf{x}, 0)$, which is transported by the fluid with transport parameter $a_c = 1$ and diffusivity parameter $D_c = 0.2$. Numerically, we solve the PDE with step-sizes $\delta x = \delta y = \triangle x$, $\delta t = \triangle t$, and $\delta\xi = \xi_c/300$.

Infinite Half-Plane Domain: First, we examine the half-plane region $\Omega = \{(x, y) \subset \mathbb{R}^2 : y > 0\}$ with fluid velocity profile

$$\mathbf{v}(\mathbf{x}) = 2\left(3 - \sqrt{x^2 + y^2}\right)\begin{pmatrix} -y \\ x \end{pmatrix}$$

and initial chemical profile $C(\mathbf{x}, 0) = 0.5\left(\sin(2\pi x)\cos(2\pi y) + 1\right)$. The agents and chemical have no-flux boundary conditions at $y = 0$, but we assume that the fluid passes through the boundary without obstruction. We initialize the agents at $\mathbf{x}_0 = (0.24, 0.5)$, which are transported by the fluid with transport parameter $b = 1/5$ and biased by the fluid with biasing parameter $a = 1/2$. The agent's chemical capacitance is $\xi_c = 5\triangle t\triangle x\triangle y$ with an absorption rate of $\alpha = 0.1$. We solve the PDE in the numerical domain $[-3, 3] \times [-3, 3]$ using the numerical method of images for an infinite half-plane.

There is agreement between the plots in Fig. 7.22a and 7.22b. The agents diffuse from $\mathbf{x}_0$ and we can observe from the density plots that the agents reflect off the wall at $y = 0$. Eventually, the agents which are still in the live state at $t = 0.045$ are centered around a single local chemical minimum.

We see general agreement in Fig. 7.23 with the survival probability. The curved trend from $(0.24, 0.2)$ at $t = 0$ to $(0.13, 0.545)$ at $t = 0.04$ is initially due to the fluid biased movement, but after $t = 0.02$ the curve is also influenced by state changes around regions of higher chemical density. The noise in the AB model mean location is smaller than a spatial-step $\triangle x = 0.02$. The AB model and PDE mean squared deviations have a similar trend, but the difference is due to the spatially dependent fluid velocity. Agents begin exiting the live state around $t = 0.02$ at an almost linear rate, which corresponds to the point $(0.19, 0.52)$ in the mean location graphs. The PDE mean location shows a change of concavity at that point, demonstrating the influence of cells leaving the live state on the mean location. Although there is more noise in the AB model mean location graph, it is much smaller than the spatial step size, $\triangle x$. We further see that even though the error between the AB model and PDE mean squared deviations initially increases, until around $t = 0.025$ when the error begins to contract. This corresponds to the moment in the model where agents in locations of high chemical densities leave the state faster than the agents near local chemical minimums.

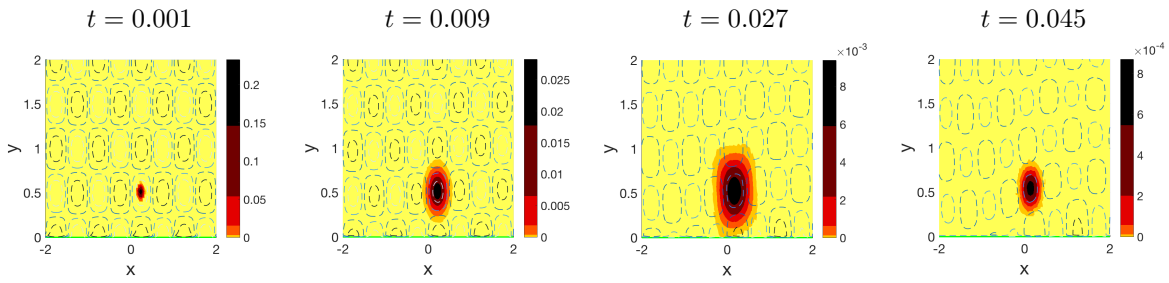

(a) AB Model Simulation

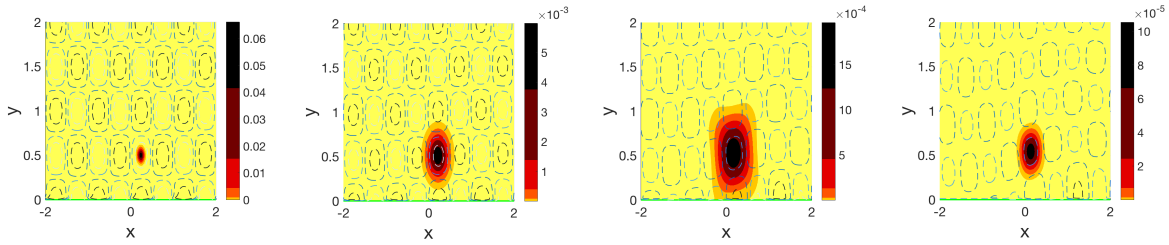

(b) PDE Numerical Solution

Figure 7.22: Probability distribution of agents (shown in color) in the half-plane region $[-2, 2] \times [0, 2]$ at four different time points. Agents are initialized at $(0.24, 0.5)$ and move with parameters $b = 1/5$, $a = 1/2$. The **blue** contour plot denotes the chemical concentration $C(\mathbf{x}, t)$ and the **green** line denotes the reflective boundary at $y = 0$. The absorption parameters are $\alpha = 0.1$ and $\xi_c = 5\triangle t \triangle x \triangle y$. **(a)** AB model probability distribution is average of 10^6 realizations with step sizes $\triangle x = 0.02$ and $\triangle t = \triangle x^2/2$ and is depicted at each time as a 2-d histogram with bin size $2\triangle x \times 2\triangle x$. **(b)** PDE numerical solution is computed in the region $[-3, 3] \times [-3, 3]$ with numerical step sizes $\delta x = \delta y = \triangle x$, $\delta t = \triangle t$, and $\delta \xi = \xi_c/300$.

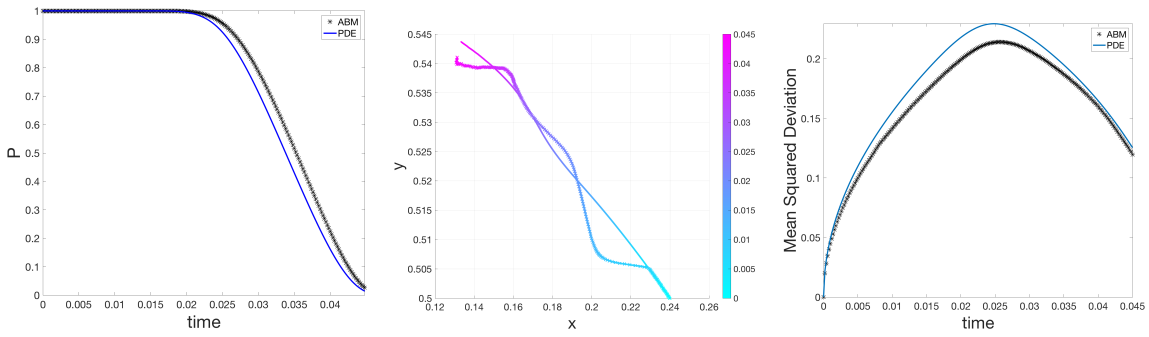

(a) Survival Probability (b) Mean Location (c) Mean Squared Deviation

Figure 7.23: Plots of various statistical measures comparing the AB model and PDE **(a)** Survival probability, **(b)** Mean location (time shown in colorbar), and **(c)** MSD.

Infinite Strip Domain: Now we consider the case of the infinite strip region $\Omega = \{(x, y) \subset \mathbb{R}^2 : -1 \leq y \leq 1\}$ with fluid velocity profile

$$\mathbf{v}(\mathbf{x}) = \frac{5}{4}\begin{pmatrix} 1 - y^2 \\ 0 \end{pmatrix}$$

and initial chemical profile $C(\mathbf{x}, 0) = 0.5\,(\sin(1.5\pi x)\cos(\pi y) + 1)$. The agents and chemical have no-flux boundary conditions at $y = -1$ and $y = 1$. The Poiseuille flow (with viscosity $\mu = 1$ and constant pressure gradient $\nabla P = -5$) has zero velocity on the walls and corresponds to the type of fluid profile seen in tubes where the cross-section is much shorter than the length. We initialize the agents at $\mathbf{x}_0 = (-1, 0)$, which are transported by the fluid with transport parameter $b = 1/5$ and biased by the fluid with biasing parameter $a = 1/25$. The agent's chemical capacitance is $\xi_c = 10\triangle t\triangle x\triangle t$ with an absorption rate of $\alpha = 0.1$. We solve the PDE in the numerical domain $[-3, 3] \times [-3, 3]$ using the numerical method of images for an infinite strip.

The plots in Fig. 7.24a and 7.24b are phenomenologically similar. The agent is initialized at $\mathbf{x}_0$ and is biased and transported by the right-moving fluid flow. Eventually, agents absorb above their capacitance and begin leaving the live state. We see a brief bimodality in the PDE surface plot at $t = 0.03$, where the cells towards the left are still in the live state because they are located near a region of low chemical density. However, the flow biases those agents towards the higher chemical concentration to their right, which quickly causes those cells to absorb above their capacitance. We see a few AB model agents in that region, but we would need to initialize many more agents to see a similar density as the PDE numerical solution. The cells which survive to $t = 0.06$ appear to be centered at a local chemical minimum around $(-0.2, 0)$.

Given the vertical scale in the mean location graph is much less than $\triangle x$, we see general agreement in the survival probability and mean location graphs in Fig. 7.25. The linear trend from $(-1, 0)$ at $t = 0$ to $(-0.15, 0)$ at $t = 0.06$ is initially due to the fluid biased movement but after $t = 0.02$ state changes begin to influence the mean location. The noise in the AB model mean location is much smaller than a spatial step $\triangle x = 0.02$. The AB model and PDE MSDs have a similar trend, but the difference is due to the spatially dependent fluid velocity. Agents begin exiting the live state around $t = 0.02$, which is the maximum of the mean squared deviation. After that time, the agents which survive tend to be located around a single local minimum, which is why the difference between the AB model and PDE MSD graphs decreases. Unlike the previous examples in this Section, we do not see a cusp in the mean location graph suggesting a time when state change begins to influence the mean location. This is due to the symmetry in the numerical domain at $y = 0$ and the fact that the vertical fluid velocity, $v_2(\mathbf{x})$, is constantly zero everywhere in Ω.

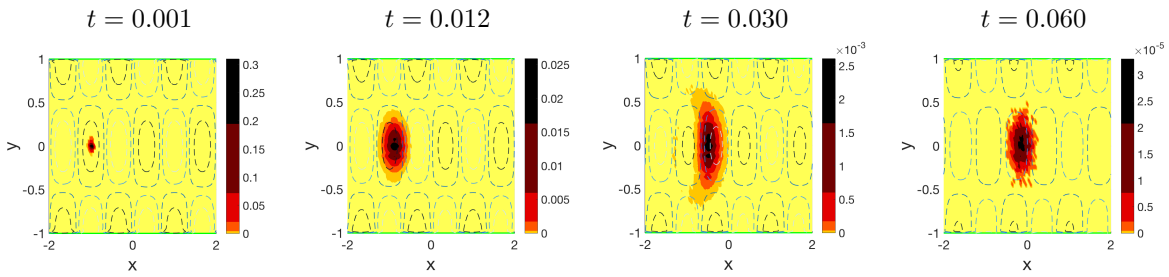

(a) AB Model Simulation

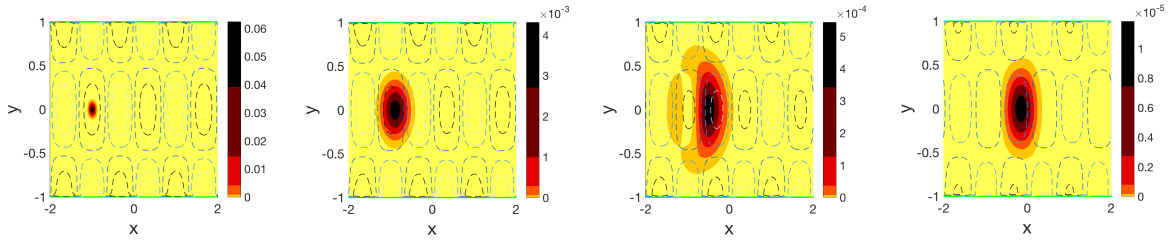

(b) PDE Numerical Solution

Figure 7.24: Probability distribution of agents (shown in color) in the infinite strip region $[-2, 2] \times [-1, 1]$ at four different time points. Agents are initialized at $(-1, 0)$ and move with parameters $b = 1/5$, $a = 1/25$. The **blue** contour plot denotes the chemical concentration $C(\mathbf{x}, t)$ and the **green** line denotes the reflective boundary at $y = -1$ and $y = 1$. The absorption parameters are $\alpha = 0.1$ and $\xi_c = 10\triangle t\triangle x\triangle y$. **(a)** AB model probability distribution is average of 10^6 realizations with step sizes $\triangle x = 0.02$ and $\triangle t = \triangle x^2/2$ and is depicted at each time as a 2-d histogram with bin size $2\triangle x \times 2\triangle x$. **(b)** PDE numerical solution is computed in the region $[-3, 3] \times [-3, 3]$ with numerical step sizes $\delta x = \delta y = \triangle x$, $\delta t = \triangle t$, and $\delta\xi = \xi_c/300$.

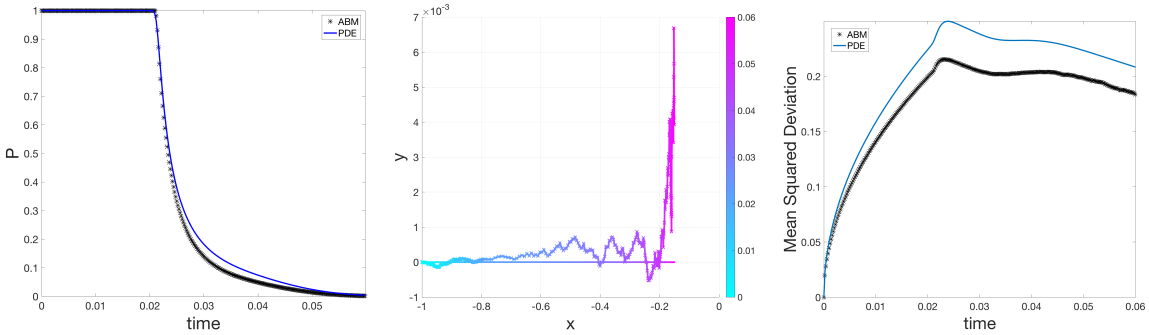

(a) Survival Probability (b) Mean Location (c) Mean Squared Deviation

Figure 7.25: Plots of various statistical measures comparing the AB model and PDE **(a)** Survival probability, **(b)** Mean location (time shown in colorbar), and **(c)** MSD.

Square Domain: Finally, we consider the case of the square region $\Omega = \{(x, y) \subset \mathbb{R}^2 : -1 \leq x \leq 1, -1 \leq y \leq 1\}$ with fluid velocity profile

$$\mathbf{v}(\mathbf{x}) = 25(3 - \sqrt{x^2 + y^2}) \begin{pmatrix} -y \\ x \end{pmatrix}$$

and initial chemical profile $C(\mathbf{x}, 0) = 0.5\,(\sin(2\pi x)\cos(2\pi y) + 1)$. This spatial domain can be seen in microfluidic devices for biofilm experimentation [129, 68]. The agents and chemical have no-flux boundary conditions at the edge of the square, and in this example the fluid can move through the boundary without any obstruction. We initialize the agents at $\mathbf{x}_0 = (-0.24, 0)$, which are transported by the fluid with transport parameter $b = 1/5$ and biased by the fluid with biasing parameter $a = 1/25$. The agent's chemical capacitance is $\xi_c = 5\triangle t \triangle x \triangle t$ with an absorption rate of $\alpha = 0.1$. We solve the PDE in the numerical domain $[-3, 3] \times [-3, 3]$ using the numerical method of images for a square.

We can see from Fig. 7.26 that the AB model simulations and the PDE numerical solutions agree qualitatively. The agents initialize at $\mathbf{x}_0$, diffuse outward and are biased as well as translated by the fluid. Eventually, agents begin switching states, which causes the avocado-looking shape at $t = 0.024$, before contracting to a region of low chemical concentration. Moreover, it is clear that in this example the chemical concentration is transported by the fluid and a much faster rate than the agents.

The survival probability and mean location graphs in Fig. 7.27 show good agreement. The curved trend from $(-0.24, 0)$ at $t = 0$ to $(0.14, -0.18)$ at $t = 0.04$ is initially due to the fluid biased movement, but after $t = 0.02$ state changes exert influence on the mean location. The AB model and PDE mean squared deviations have a similar trend, but the difference is due to the spatially dependent fluid velocity. At around $t = 0.02$, agents begin changing state. This time corresponds to the cusp around $(-0.23, -0.075)$ in the mean location graph, which again demonstrates when state change begins influencing the mean location. The mean squared deviation reaches a maximum around $t = 0.025$, when the survival probability changes concavity. This shows the contraction of the density surface plots to a single local chemical minimum region. Just like the infinite half-plane example, the difference between the AB model and PDE MSD curves begins to decrease at this point.

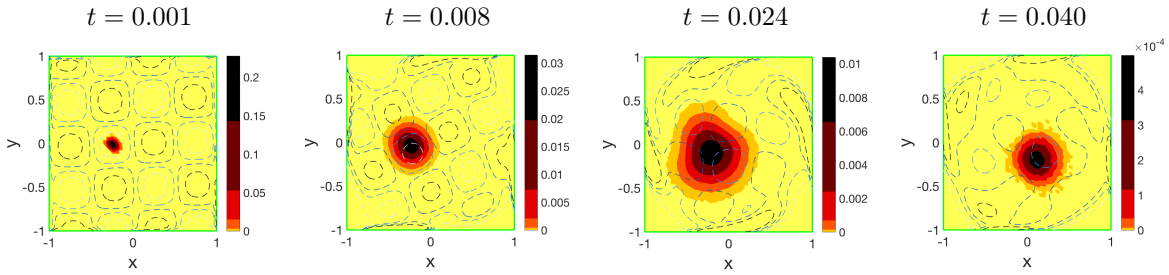

(a) AB Model Simulation

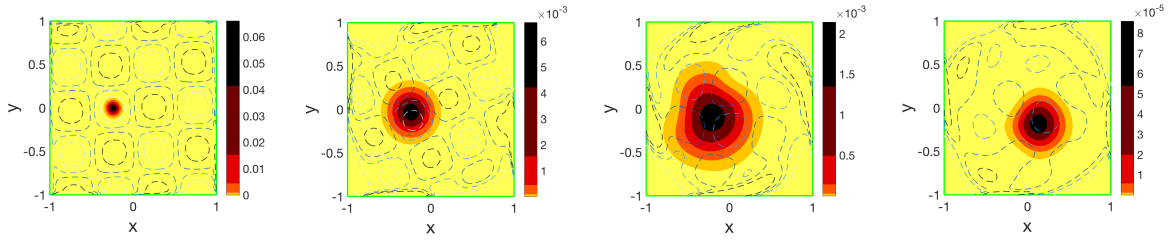

(b) PDE Numerical Solution

Figure 7.26: Probability distribution of agents (shown in color) in the square region $[-1,1] \times [-1,1]$ at four different time points. Agents are initialized at $(-0.24, 0)$ and move with parameters $b = 1/5$, $a = 1/25$. The **blue** contour plot denotes the chemical concentration $C(\mathbf{x}, t)$ and the **green** line denotes the reflective boundary at the square border. The absorption parameters are $\alpha = 0.1$ and $\xi_c = 5\triangle t \triangle x \triangle y$. **(a)** AB model probability distribution is average of 10^6 realizations with step sizes $\triangle x = 0.02$ and $\triangle t = \triangle x^2/2$ and is depicted at each time as a 2-d histogram with bin size $2\triangle x \times 2\triangle x$. **(b)** PDE numerical solution is computed in the region $[-3,3] \times [-3,3]$ with numerical step sizes $\delta x = \delta y = \triangle x$, $\delta t = \triangle t$, and $\delta \xi = \xi_c/300$.

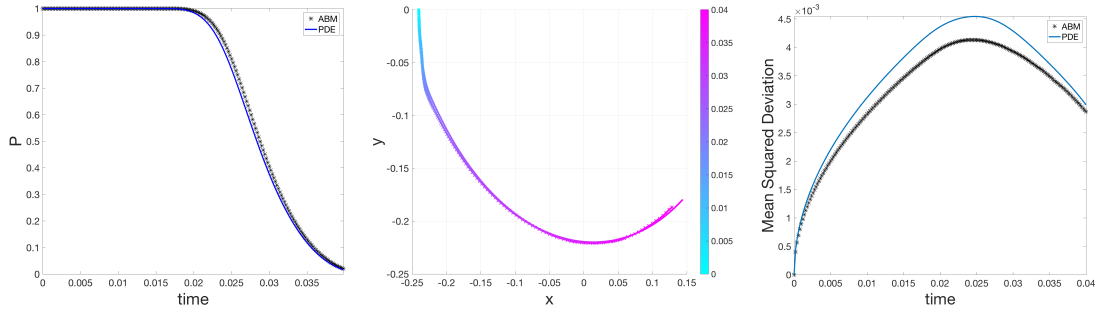

(a) Survival Probability (b) Mean Location (c) Mean Squared Deviation

Figure 7.27: Plots of various statistical measures comparing the AB model and PDE **(a)** Survival probability, **(b)** Mean location (time shown in colorbar), and **(c)** MSD.

Chapter 8

Conclusion

8.1 Discussion

In this dissertation, we develop a continuum PDE approximation to a stochastic agent-based (AB) model that has a cumulative coupling to the environment. Through simulations, we see that the AB model agrees qualitatively with the governing PDE. We analyze the newly developed PDE, showing that the equation is stable and well-posed. In our examples, we use point sources as initial conditions to validate the model. However, by superposition, we know that we can extend this to account for any initial condition in $L^2(\Omega \times [0, \infty))$, where Ω denotes the spatial domain. Further, we see agreement when we add reflecting boundary conditions and bias the agents' movement with a fluid velocity profile.

Having a PDE approximation of the cumulative absorption AB model gives us the ability to adapt previously developed PDE theory and applications. Experimentalists may not know the absorption rate, α, and the chemical threshold, ξ_c. In Section 5.4.3, we used the PDE formulation to derive a method for calculating α using mean occupancy times (MOTs) for various proportions of $C(x)$. Once α is known, we can use the chemical effectiveness measure, introduced in Section 5.4.4, to approximate ξ_c. This approach may not have been as clear without first obtaining a PDE.

Although we use cell biology as a motivating example, in an abstract way the cumulative absorption model demonstrates how to add memory-dependent dynamics to any PDE by use of the ξ-coordinate. We merely assume that an agent moves by an unbiased (or a biased) random walk (RW) and that cumulative accumulation of some particles in the environment leads to a state change. Simply by changing the parameters and initial conditions, this model can be adapted to specify many different physical situations, such as: chemical uptake, chemical filtering, and engineered material lifespan (where the stress on the material is what is "absorbed").

The modeling framework developed assumes that the cells have cumulative exposure, but the chemical or substance is not being removed from the environment. This setup can be used to model morphogens (signaling molecules) that often act directly on a cell by binding to a receptor. It is well established that exposure to high levels of transforming

growth factor (TGF)-β leads to cell death [47]. In this scenario, morphogens bind and initiate a secondary process in the cell that accumulates and leads to cell death. After a small period of time (smaller than the scale of movement or time to cell death), the morphogen is released from the receptor and thus the relative morphogen concentration can be assumed constant in time.

We assumed that there is sufficient chemical such that the density does not change from agents' absorption. We may want to adapt the model to account for situations where the amount of chemical absorbed is of a similar order as the chemical density in the absorption region. To update the continuum chemical density, we would need to evaluate an "ensemble" average over all possible realizations by leveraging the agent's spatially-dependent density solution. With such a model, we can attempt to solve for the parameter space where there is a non-trivial steady state.

8.2 Future Work

A limitation of the current cumulative absorption model is an inability to directly compare the AB model probability distribution with the PDE solution. Instead, we relied on comparing statistical measures, such as the survival probability, mean location, and location spread. The movement part of the PDE is parabolic and has an infinite wave speed. It would be interesting to adapt the movement to the correlated RW, as detailed in Section 2.3. We saw that the biased RW parameter assumptions imposed error in the standard deviation graphs. It would be of interest to investigate how (or whether) a hyperbolic model could mollify such errors. Doing so would require a different proof of well-posedness as well as a different numerical scheme.

Along with adapting the movement, the absorption model can be further modified to model probabilistic state change dynamics. In our current cumulative absorption model, we assumed that there is a deterministic state change when an agent has absorbed ξ_c chemical. However, to approximate more realistic dynamics, a model may want to express this change as probabilistic with the expected cumulative chemical absorption to induce a state transition to be ξ_c. The absorption tolerance, ξ_c, may be known in terms of statistical ranges through experimentation rather than a single fixed number [95], so our model should be capable of handling this data. Additionally, we see complex state changes when studying drug-induced resistance [122]. Cells undergo behavioral changes at discrete exposure lengths, that can be modeled as different states, which can be reversed upon drug release.

In Section 5.1.2, we derived a PDE for absorption using a Heaviside function at ξ_c. However, we could replace the Heaviside function with any function $q(\xi|\xi_c)$, which represents the probability of switching states having absorbed ξ chemical given that the mean

threshold is ξ_c:

$$\begin{cases} \frac{\partial V}{\partial t} + \beta(x)\frac{\partial V}{\partial \xi} = D\frac{\partial^2 V}{\partial x^2} - q(\xi|\xi_c)V, & x \in \mathbb{R},\ \xi \in [0,\infty),\ t > 0, \\ V = \phi(x,\xi), & x \in \mathbb{R},\ \xi \in [0,\infty),\ t = 0, \\ \lim_{|x|\to\infty} V = 0, & x \in \mathbb{R},\ \xi \in [0,\infty),\ t > 0. \end{cases}$$

A preliminary comparison of this model is shown in Fig. 8.1 with the same chemical concentration, $C(x) = \exp(-x^2)$ and parameters as Example 2 in Section 5.4.1. This example uses the probability function $q(\xi) = \frac{\exp[(10/\xi_c)(\xi-\xi_c)]}{1+\exp[(10/\xi_c)(\xi-\xi_c)]}$. We can see that the survival probability curve is smoother than that of Fig. 5.8a, which uses the same simulation and numerical parameters. More work needs to be employed as to what restrictions need to be placed on q in this framework as well as how the shape of q effects the comparison errors.

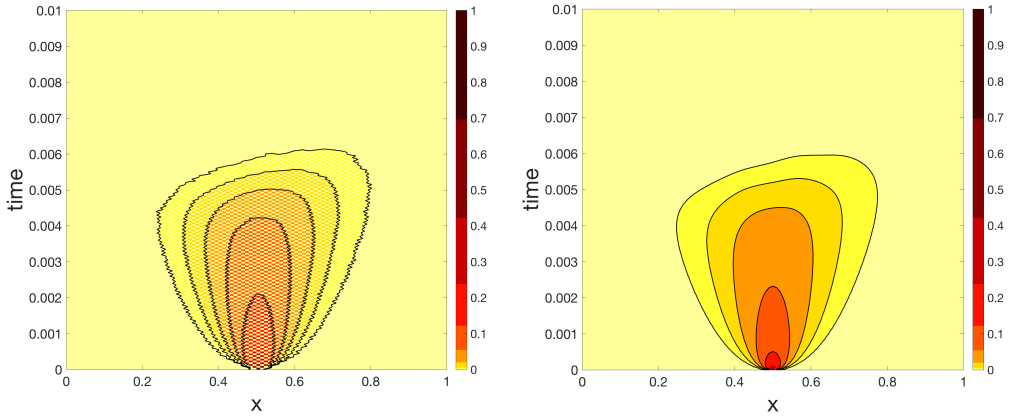

AB Model Simulation PDE Approximation

(a) Solution Comparison

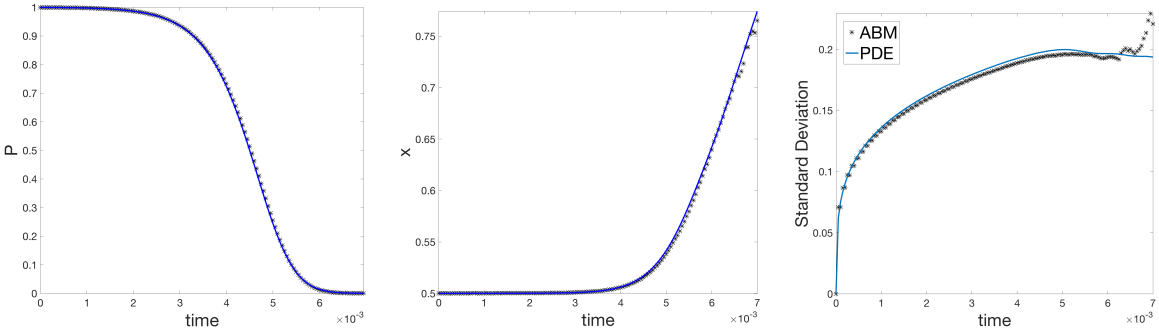

Survival Probability Mean Location Standard Deviation

(b) Statistical Measures

Figure 8.1: Comparison between AB model ($N = 10^5$ agents) and PDE solution with probabilistic cumulative absorption state change. This uses the same simulation and numerical parameters as Example 2 in Section 5.4.1.

Our initial framework modeled one cell and one chemical concentration. One natural extension would be to examine the dynamics of multiple competing chemical concentrations, where each chemical can cause the agent to transition to a distinct state. It would increase the value of this modeling framework to further modify the model to account for a transition to multiple states due to different chemical concentrations. In fact, extending the model in this way can be used to help model combination therapy, a pharmacological treatment of HIV, lupus, and certain aggressive forms of multiple sclerosis [48, 82], and further investigate drug interactions. Thus, we could model the competition or cooperation of different memory-dependent dynamics.

We performed a preliminary derivation of these dynamics using two chemical concentrations, C_1 and C_2. If an agent in state $\mathcal{U}$ absorbs a cumulative amount of the chemical C_1 above ξ_c, then the agent transitions to state $\mathcal{V}$. However, if an agent in state $\mathcal{U}$ absorbs a cumulative amount of the chemical C_2 above γ_c, then the agent transitions to state $\mathcal{W}$. The PDE system for this two-concentration model is the following:

$$\begin{cases} \frac{\partial U}{\partial t} + \beta_1(x)\frac{\partial U}{\partial \xi} + \beta_2(x)\frac{\partial U}{\partial \gamma} = \frac{\triangle x^2}{\triangle t}\frac{\partial^2 U}{\partial x^2} - \frac{H(\xi-\xi_c)+H(\gamma-\gamma_c)}{\triangle t}U, & x\in\mathbb{R}, \xi\in[0,\infty), \gamma\in[0,\infty), t>0, \\ \frac{\partial V}{\partial t} = \frac{1}{\triangle t}\int_0^\infty H(\xi-\xi_c)U(x,t,\xi,\gamma)\,d\xi, & x\in\mathbb{R}, \xi\in[0,\infty), \gamma\in[0,\infty), t>0, \\ \frac{\partial W}{\partial t} = \frac{1}{\triangle t}\int_0^\infty H(\gamma-\gamma_c)U(x,t,\xi,\gamma)\,d\gamma, & x\in\mathbb{R}, \xi\in[0,\infty), \gamma\in[0,\infty), t>0, \\ U = \delta(x-x_0), & x\in\mathbb{R}, \xi\in[0,\infty), \gamma\in[0,\infty), t=0, \\ V = 0, & x\in\mathbb{R}, \xi\in[0,\infty), \gamma\in[0,\infty), t=0, \\ W = 0, & x\in\mathbb{R}, \xi\in[0,\infty), \gamma\in[0,\infty), t=0, \\ \lim_{|x|\to\infty} U = 0, & x\in\mathbb{R}, \xi\in[0,\infty), \gamma\in[0,\infty), t>0, \\ \lim_{|x|\to\infty} V = 0, & x\in\mathbb{R}, \xi\in[0,\infty), \gamma\in[0,\infty), t>0, \\ \lim_{|x|\to\infty} W = 0, & x\in\mathbb{R}, \xi\in[0,\infty), \gamma\in[0,\infty), t>0, \end{cases}$$

where H denotes the Heaviside function. We examined this system in Fig. 8.2 using the same chemical concentrations, $C_1(x) = \frac{1}{1+10(x-0.5)^2}$ and $C_2(x) = \exp(-x^2)$, as well as the same parameters as the first two examples in Section 5.4.1.

Another extension, for practical considerations, would be to add finitely many interacting agents or obstructions. Having agents reflect off each other adds complexity to the movement and an added layer of difficulty in deriving the PDE. First, we derive a PDE for RW movement through a porous medium, and then we adapt that model by replacing the porous medium with another agent. Let $f(x)$ be the probability an agent encounters an obstruction at location x. We know that if the agent is at location x at time t and there is an obstruction at $x \pm \triangle x$, then the agent returns to location x at time $t + \triangle t$. Assuming the probability of moving left or right is $\ell = r = 1/2$, the difference equation for this porous medium RW is:

$$\begin{aligned} U(x,t+\triangle t) = &\frac{1}{2}\left(1-f(x)\right)U(x-\triangle x,t) + \frac{1}{2}\left(1-f(x)\right)U(x+\triangle x,t) \\ &+ \frac{1}{2}\left(f(x-\triangle x)+f(x+\triangle x)\right)U(x,t). \end{aligned}$$

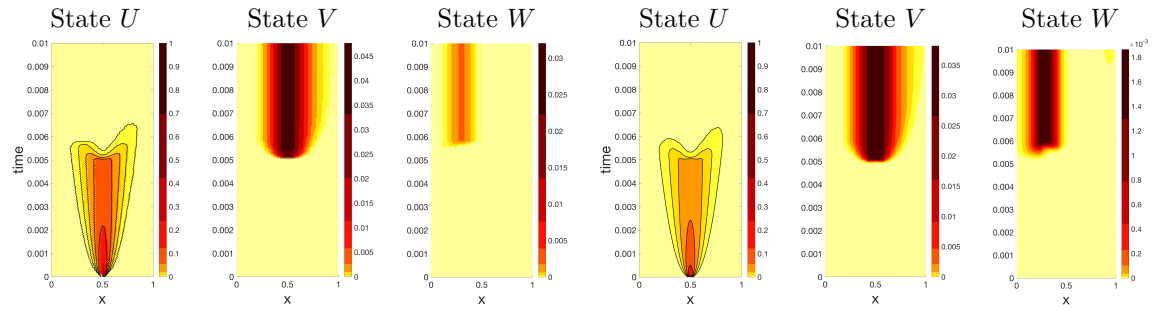

AB Model Simulation PDE Approximation

(a) Solution Comparison

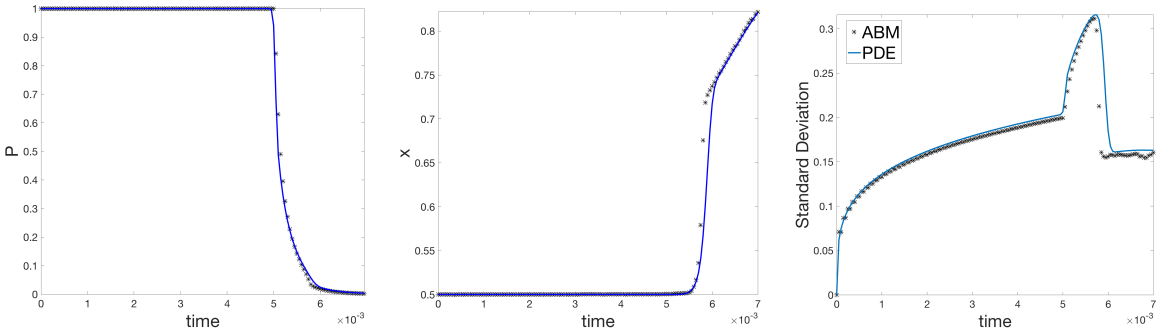

Survival Probability Mean Location Standard Deviation

(b) Statistical Measures For State $\mathcal{U}$

Figure 8.2: Comparison between AB model ($N = 10^5$ agents) and PDE solution with probabilistic cumulative absorption state change. This uses the same simulation and numerical parameters as Example 2 in Section 5.4.1.

If we assume $U \in \mathcal{C}^2(\mathbb{R}, [0, \infty))$ and $f \in \mathcal{C}^2(\mathbb{R})$, then, by using a Taylor series, the PDE for the porous medium RW becomes

$$\frac{\partial U}{\partial t} = D\frac{\partial^2 f}{\partial x^2}U + D(1-f)\frac{\partial^2 U}{\partial x^2}, \qquad x \in \Omega,\ t > 0,$$

where $D = \triangle x^2/(2\triangle t)$.

For two interacting agents, the PDE becomes the system:

$$\begin{cases} \frac{\partial U}{\partial t} = D\frac{\partial^2 f}{\partial x^2}U + D(1-f)\frac{\partial^2 U}{\partial x^2}, & x \in \Omega,\ t > 0, \\ \frac{\partial V}{\partial t} = D\frac{\partial^2 g}{\partial x^2}V + D(1-g)\frac{\partial^2 V}{\partial x^2}, & x \in \Omega,\ t > 0, \end{cases}$$

for $f, g : \Omega \times [0, \infty) \to [0, 1]$. If U and V are initialized as point sources, then we can treat $U(x, t)$ and $V(x, t)$ as probability density functions for any fixed $t \geq 0$. Since we are interested in agent interaction, we need to define f as the probability agent U is obstructed by V given that there is an obstruction at x. Assuming agents centered at x

take up finite length $B(x,\epsilon)$, we can define:

$$f(x,t) = \eta \frac{\int_{B(x,\epsilon)} V(y,t)\,dy}{\int_{B(x,\epsilon)}[U(y,t)+V(y,t)]}\,dy, \qquad g(x,t) = \eta \frac{\int_{B(x,\epsilon)} U(y,t)\,dy}{\int_{B(x,\epsilon)}[U(y,t)+V(y,t)]\,dy},$$

where $\eta \in [0,1]$ is some permitivity constant. In Fig. 8.3, we compare the AB model with the PDE approximation in $\Omega = [0,1]$, with $dx = \triangle x = 0.01$, $dt = \triangle t = \triangle x^2$, $\epsilon = \triangle x/2$, $\eta = 1/2$, and no-flux boundary conditions.

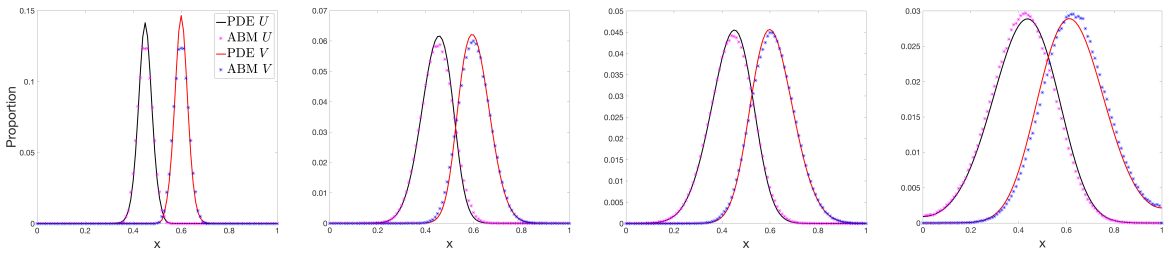

$t = 0.001$ $t = 0.005$ $t = 0.01$ $t = 0.025$

Figure 8.3: Comparison between 10^5 AB model realizations of two interacting agents (agents reflect off each other) and its PDE approximation. Agents perform RW with step-sizes $dx = \triangle x = 0.01$, $dt = \triangle t = \triangle x^2$. Agent width is $\epsilon = \triangle x/2$ and PDE permitivity constant is $\eta = 1/2$

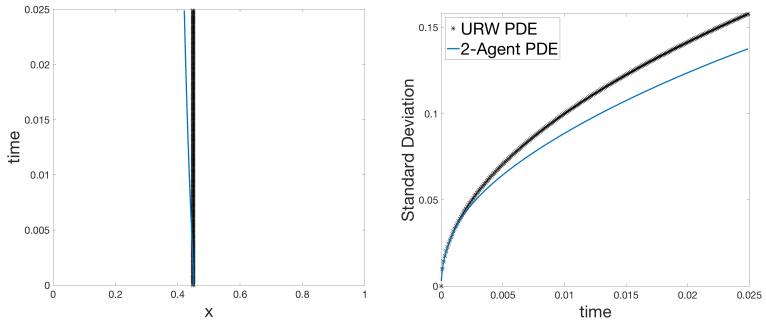

Mean Location Standard Deviation

Figure 8.4: Comparing URW PDE initialized at $x_0 = 0.45$ with two-agent PDE statistical measures for agent represented by U.

Although the example in Fig. 8.3 is simply a proof of concept, it shows that this model is subtly different than an URW model with no-flux conditions. At time $t = 0.025$ in Fig. 8.3, U appears as if it has a dirichlet boundary condition at $x = 1$, but this is a result of the reaction term (since that agent cannot move to the right of the agent represented by V). Statistical comparison between an URW initialized at $x_0 = 0.45$ and the two agent PDE variable U is shown in Fig. 8.4. Since U is initialized to the right of

V, it is not surprising that the interacting agent PDE drifts to the left and has a smaller standard deviation than the URW.

In the future, we need to examine the derivation of η in more depth, examine the origin of the experimental error, and prove the well-posedness conditions of the PDE. When that is accomplished, we can insert this PDE system into the cumulative absorption model framework. The three modifications to the cumulative absorption model briefly explored above can expand the model's utility for solving real world problems.

Part III

Appendix

Appendix A

PDE Solution Methods

A.1 PDE Fundamental Solution

We present a method for determining the fundamental solution to linear PDE problems using Fourier transformations [105, Ch.5][41, Ch.4][125, Ch.3]. Fourier transformation is a way to decompose a function into orthogonal trigonometric base frequencies. As such, it is widely used in signal theory and quantum mechanics due to its capability of separating frequencies with their corresponding amplitudes [69]. Fourier transforms are used in engineering applications, such as understanding beam vibrations [36] and refining infrared spectroscopy to determine chemical compositions [94]. Moreover, the transform has nice properties with Gaussian functions and convolutions [18, 67], which is why we use it to solve the diffusion equation.

A.1.1 Fourier Transform

We first must define the Fourier transform.

Definition. For any function $U \in L^1(\mathbb{R}) \cup L^2(\mathbb{R})$, the Fourier transform of U is defined as

$$\mathcal{F}(U) := \hat{U}(\xi, t) = \int_{\mathbb{R}} \exp(-2\pi i \xi x) U(x, t)\, dx. \tag{A.1}$$

The inverse Fourier transform is similarly defined as

$$\mathcal{F}^{-1}(U) := \check{U}(x, t) = \int_{\mathbb{R}} \exp(2\pi i \xi x) U(\xi, t)\, d\xi. \tag{A.2}$$

The ξ variable denotes the Fourier mode of U. For any integrable function, U, the Fourier transform is uniquely defined. That is,

$$\mathcal{F}\left(\mathcal{F}^{-1}(U)\right) = \mathcal{F}\left(\mathcal{F}^{-1}(U)\right) = U. \tag{A.3}$$

Now suppose we have a linear PDE, $\mathcal{L}U = f$, where $\mathcal{L}$ denotes any linear PDE operator. The general steps to solve the PDE using Fourier transformations are:

1. Take Fourier transformation of each side of the PDE ($\widehat{\mathcal{L}U} = \hat{f}$) and initial condition(s).
2. Solve the resulting time ODE for $\hat{U}(\xi, t)$
3. Solve for $U(x, t)$ by performing the inverse Fourier transform.

Here we solve the 1-D cases of the diffusion equation and the constant advection-diffusion equation. The method can be extended to higher dimensions. In our applications, we use two Fourier transform theorems: the convolution theorem and the derivative identity.

Convolution Theorem: A useful property of Fourier transforms is the ability to convert convolution into multiplication. We define and prove the convolution theorem [67], as stated below.

Theorem 10. *If $U, V \in L^1(\mathbb{R})$, then $\mathcal{F}(U * V) = \mathcal{F}(U)\mathcal{F}(V)$.*

Proof. We first need to show that $\exp(-2\pi i\xi x)(U * V)(x) \in L^1(\mathbb{R})$. By a calculation

$$\begin{aligned}
\int_{\mathbb{R}} |\exp(-2\pi i\xi x)(U * V)(x)|\, dx &= \int_{\mathbb{R}} |\exp(-2\pi i\xi x)|\, |(U * V)(x)|\, dx \\
&= \int_{\mathbb{R}} |U * V(x)|\, dx \\
&\leq \int_{\mathbb{R}} \int_{\mathbb{R}} |U(y)||V(x-y)|\, dy\, dx \\
&= \int_{\mathbb{R}} \left\{ |U(y)| \int_{\mathbb{R}} |V(x-y)|\, dx \right\} dy \\
&= \int_{\mathbb{R}} \{|U(y)|||V||_1\}\, dy \\
&= ||U||_1||V||_1.
\end{aligned}$$

Since $U, V \in L^1(\mathbb{R})$, we showed that $\exp(-2\pi i\xi x)(U * V)(x) \in L^1(\mathbb{R})$.

Now, by definition of the Fourier transform (A.1) and convolution,

$$\mathcal{F}(U * V) = \int_R \left\{ \exp(-2\pi i\xi x) \int_R U(y)V(x-y)\, dy \right\} dx.$$

Since $\exp(-2\pi i\xi x)(U * V)(x) \in L^1(\mathbb{R})$, we can use Fubini's theorem to rearrange the integrand as

$$\mathcal{F}(U * V) = \int_{\mathbb{R}} \left\{ U(y) \int_{\mathbb{R}} \exp(-2\pi i\xi x)V(x-y)\, dx \right\} dy.$$

We can change the variables by assigning $z = x - y$. By computation, we have

$$\begin{aligned}
\mathcal{F}(U * V) &= \int_R \left\{ U(y) \int_{\mathbb{R}} \exp(-2\pi i\xi(z+y))V(z)\, dz \right\} dy \\
&= \int_{\mathbb{R}} \exp(-2\pi i\xi y)U(y)\, dy \int_{\mathbb{R}} \exp(-2\pi i\xi z)U(z)\, dz \\
&= \mathcal{F}(U)\mathcal{F}(V).
\end{aligned}$$

Therefore, we showed that $\mathcal{F}(U * V) = \mathcal{F}(U)\mathcal{F}(V)$. □

For deriving exact solutions to the PDEs in the following subsections, we need to use a variation of the convolution theorem proved above. We first state this theorem and then prove it.

Theorem 11. *If $U, V \in L^1(\mathbb{R})$, then $\mathcal{F}^{-1}(UV) = \mathcal{F}^{-1}(U) * \mathcal{F}^{-1}(V)$.*

Proof. We want to show that

$$\mathcal{F}^{-1}(U) * \mathcal{F}^{-1}(V) = \mathcal{F}^{-1}(UV).$$

By Theorem 10 and the invertibility of the Fourier transform (A.3), we know that

$$\begin{aligned}\mathcal{F}\left(\mathcal{F}^{-1}(U) * \mathcal{F}^{-1}(V)\right) &= \mathcal{F}\left(\mathcal{F}^{-1}(U)\right)\mathcal{F}\left(\mathcal{F}^{-1}(V)\right) \\ &= UV \\ &= \mathcal{F}\left(\mathcal{F}^{-1}(UV)\right)\end{aligned}$$

Since $\mathcal{F}$ is uniquely defined, the above equality shows that $\mathcal{F}^{-1}(U) * \mathcal{F}^{-1}(V) = \mathcal{F}^{-1}(UV)$. □

Derivative Identity: Another useful property for our application is the derivative identity, which allows us to reduce PDEs into ODEs.

Theorem 12. *If $U, \frac{\partial U}{\partial x} \in L^1(\mathbb{R})$ and $\lim_{|x|\to\infty} U = 0$, then $\mathcal{F}\left(\frac{\partial U}{\partial x}\right) = (2\pi\xi i)\mathcal{F}(U)$.*

Proof. By definition (A.1), we know that

$$\mathcal{F}\left(\frac{\partial U}{\partial x}\right) = \int_{\mathbb{R}} \exp(-2\pi i\xi x)\frac{\partial U}{\partial x}\, dx.$$

By our theorem assumptions, we can perform integration by parts on the right side of the equation. This yields

$$\int_{\mathbb{R}} \exp(-2\pi i\xi x)\frac{\partial U}{\partial x}\, dx = \exp(-2\pi i\xi x)U\Big|_{-\infty}^{\infty} + \int_{\mathbb{R}} 2\pi i\xi \exp(-2\pi i\xi x)U\, dx.$$

Finally, since $\lim_{|x|} U = 0$ and by the definition of Fourier transform, we have

$$\begin{aligned}\mathcal{F}\left(\frac{\partial U}{\partial x}\right) &= \exp(-2\pi i\xi x)U\Big|_{-\infty}^{\infty} + \int_{\mathbb{R}} 2\pi i\xi \exp(-2\pi i\xi x)U\, dx \\ &= 2\pi i\xi \int_{\mathbb{R}} \exp(-2\pi i\xi x)U\, dx \\ &= (2\pi i\xi)\mathcal{F}(U).\end{aligned}$$

Therefore, we showed that $\mathcal{F}\left(\frac{\partial U}{\partial x}\right) = (2\pi i\xi)\mathcal{F}(U)$. □

We now have the requisite background to solve the diffusion and the advection-diffusion equations with constant coefficients.

A.1.2 Diffusion Equation

Suppose $G \in L^1(\mathbb{R}) \cup L^2(\mathbb{R})$ and satisfies the diffusion PDE

$$\begin{cases} \frac{\partial G}{\partial t} = D\frac{\partial^2 G}{\partial x^2}, & x \in \mathbb{R},\, t > 0, \\ G = \delta(x), & x \in \mathbb{R},\, t = 0, \\ \lim_{|x|\to+\infty} G = 0, & x \in \mathbb{R},\, t > 0, \end{cases} \tag{A.4}$$

where $\delta(x)$ denotes the Dirac delta distribution and $x_0 \in \mathbb{R}$. The notation $G(x,t)$ denotes that this is the fundamental solution, which we use to solve general free-space diffusion PDEs. By using definition (A.1) and Theorem 12, we calculate that the Fourier transform of both sides of the general equation are

$$\int_{\mathbb{R}} \exp(-2\pi i\xi x)\frac{\partial}{\partial t}G\,dx = \frac{\partial \hat{G}}{\partial t}$$
$$\int_{\mathbb{R}} D\exp(-2\pi i\xi x)\frac{\partial^2 G}{\partial x^2}\,dx = -D(2\pi\xi)^2\hat{G}.$$

The second equation is an explicit application of the Fourier derivative identity. Also, by definition of the Dirac delta distribution, the Fourier transform of the initial condition is

$$\hat{G}(\xi, 0) = 1.$$

This results in the following ODE for $\hat{G}(\xi,t)$:

$$\begin{cases} \frac{\partial \hat{G}}{\partial t} = -D(2\pi\xi)^2\hat{G}, & t > 0 \\ \hat{G} = 1, & t = 0. \end{cases} \tag{A.5}$$

Note that we used the free-space boundary conditions to justify being able to compute the Fourier transforms. It is clear that the solution to the ODE system (A.5) is

$$\hat{G}(\xi,t) = \exp(-D(2\pi\xi)^2 t) \tag{A.6}$$

Now, we use the inverse Fourier transform (A.2) to obtain an expression for $G(x,t)$ by calculating

$$\begin{aligned} G(x,t) &= \int_{\mathbb{R}} \exp(2\pi i\xi x)\exp(-Dt(2\pi\xi)^2)\,d\xi \\ &= \int_{\mathbb{R}} \exp\left\{2\pi i\xi x - Dt(2\pi\xi)^2\right\}\,d\xi. \end{aligned}$$

We can perform algebraic manipulations to obtain an exact solution to the above expression. By completing the square we know that

$$-(Dt(2\pi\xi)^2 - 2\pi\xi i(x - x_0)) = \frac{-(\xi - ix\pi\sqrt{Dt})^2}{2(1/8\pi^2 Dt)} - \frac{(x-x_0)^2}{4Dt}.$$

It follows that

$$G(x,t) = \int_{\mathbb{R}} \exp\left\{\frac{-(\xi - ix\pi\sqrt{Dt})^2}{2(1/8\pi^2 Dt)}\right\} \exp\left\{-\frac{x^2}{4Dt}\right\} d\xi$$
$$= \exp\left\{-\frac{x^2}{4Dt}\right\} \int_{\mathbb{R}} \exp\left\{\frac{-(\xi - ix\pi\sqrt{Dt})^2}{2(1/8\pi^2 Dt)}\right\} d\xi.$$

We know the identity $\int_{\mathbb{R}} \exp(-\xi^2)\, d\xi = \sqrt{\pi}$. Therefore, by substitution, we can calculate

$$\int_{\mathbb{R}} \exp\left\{\frac{-(\xi-\mu)^2}{2\sigma^2}\right\} d\xi = \sqrt{2\pi\sigma^2}. \tag{A.7}$$

In our integral expression for $G(x,t)$, the parameters are assigned as $\mu = ix\pi\sqrt{Dt}$ and $\sigma^2 = 1/4\pi^2 Dt$. Thus,

$$\int_{\mathbb{R}} \exp\left\{\frac{-(\xi - ix\pi\sqrt{Dt})^2}{2(1/8\pi^2 Dt)}\right\} d\xi = \sqrt{\frac{2\pi}{8\pi^2 Dt}} = \frac{1}{\sqrt{4\pi Dt}}.$$

Therefore, the solution to the PDE (A.5) is

$$G(x,t) = \frac{1}{\sqrt{4\pi Dt}} \exp\left\{-\frac{x^2}{4Dt}\right\}. \tag{A.8}$$

General Initial Condition Now, suppose the initial condition to the free-space diffusion PDE is $\phi(x) \in L^1(\mathbb{R}) \cup L^2(\mathbb{R})$. That is, we want to solve:

$$\begin{cases} \frac{\partial U}{\partial t} = D\frac{\partial^2 U}{\partial x^2}, & x \in \mathbb{R},\ t > 0, \\ U = \phi(x), & x \in \mathbb{R},\ t = 0, \\ \lim_{|x|\to+\infty} U = 0, & x \in \mathbb{R},\ t > 0. \end{cases} \tag{A.9}$$

By following the same reasoning as above, we solve the ODE

$$\begin{cases} \frac{\partial \hat{U}}{\partial t} = -D(2\phi\xi)^2 \hat{U}, & t > 0 \\ \hat{U} = \hat{\phi}(\xi), & t = 0. \end{cases}$$

The solution to the above ODE is

$$\hat{U}(\xi,t) = \hat{\phi}(\xi)\exp(-D(2\pi\xi)^2 t).$$

By convolution property of Fourier transforms [105, Ch.5],

$$\mathcal{F}^{-1}\left(\hat{\phi}(\xi)\exp(-D(2\pi\xi)^2 t)\right) = \mathcal{F}^{-1}\left(\exp(-D(2\pi\xi)^2 t)\right) * \mathcal{F}^{-1}\left(\hat{\phi}(\xi)\right).$$

The first inverse Fourier transform was calculated above as the fundamental solution of the diffusion PDE $G(x,t)$, and the second inverse Fourier transform is $\phi(x)$. Therefore, the solution to the PDE (A.9) is

$$U(x,t) = G(x,t) * \phi(x). \tag{A.10}$$

For example, if the initial condition is a point source centered at x_0, $\phi(x) = \delta(x - x_0)$, then

$$U(x,t) = G(x,t) * \delta(x - x_0) = \frac{1}{\sqrt{4\pi Dt}} \exp\left\{-\frac{(x-x_0)^2}{4Dt}\right\}.$$

A.1.3 Advection-Diffusion Equation (with constant advection term)

Now suppose $G \in L^1(\mathbb{R}) \cup L^2(\mathbb{R})$ satisfies the following 1-d advection-diffusion equation:

$$\begin{cases} \frac{\partial G}{\partial t} = c\frac{\partial G}{\partial x} + D\frac{\partial^2 G}{\partial x^2}, & x \in \mathbb{R},\ t > 0, \\ G(x,0) = \delta(x), & x \in \mathbb{R},\ t = 0, \\ \lim_{|x|\to+\infty} G(x,t) = 0, & x \in \mathbb{R},\ t > 0. \end{cases} \tag{A.11}$$

We perform similar steps as when solving the diffusion equation in Eq. (A.4). First, we use the Fourier transform (A.1) to each side of the PDE (A.11) to obtain

$$\begin{aligned} &\int_{\mathbb{R}} \exp(-2\pi i\xi x)\frac{\partial}{\partial t} G\, dx = \frac{\partial \hat{G}}{\partial t} \\ &\int_{\mathbb{R}} \exp(-2\pi i\xi x)\left[c\frac{\partial G}{\partial x} + D\frac{\partial^2 G}{\partial x^2}\right] dx = \left(2\pi ic\xi - D(2\pi\xi)^2\right)\hat{G}. \end{aligned}$$

Just as in the diffusion equation, the Fourier transform of the initial condition is $\hat{G}(\xi, 0) = 1$. This results in the following ODE for $\hat{G}(\xi, t)$:

$$\begin{cases} \frac{\partial \hat{G}}{\partial t} = \left(2\pi ic\xi - D(2\pi\xi)^2\right)\hat{G}, & t > 0, \\ \hat{G} = 1, & t = 0. \end{cases} \tag{A.12}$$

The free-space boundary conditions justify being able to compute the Fourier transforms. It is clear that the solution to the ODE system in (A.12) is

$$\hat{G}(\xi, t) = \exp\left\{\left[2\pi ic\xi - D(2\pi\xi)^2\right] t\right\}. \tag{A.13}$$

Now, we use the inverse Fourier transform (A.2) to obtain an expression for $G(x,t)$ by calculating

$$\begin{aligned} G(x,t) &= \int_{\mathbb{R}} \exp(2\pi i\xi x) \exp\left\{\left[2\pi ic\xi - D(2\pi\xi)^2\right] t\right\} d\xi \\ &= \int_{\mathbb{R}} \exp\left\{2\pi i\xi(x + ct) - Dt(2\pi\xi)^2\right\} d\xi. \end{aligned}$$

We can perform algebraic manipulations to obtain an exact solution to the above expression. By completing the square we know that

$$-(Dt(2\pi\xi)^2 - 2\pi\xi i(x + ct)) = \frac{-(\xi - i(x+ct)\pi\sqrt{Dt})^2}{2(1/8\pi^2 Dt)} - \frac{(x+ct)^2}{4Dt}.$$

It follows that

$$G(x,t) = \int_{\mathbb{R}} exp\left\{\frac{-(\xi - i(x+ct)\pi\sqrt{Dt})^2}{2(1/8\pi^2 Dt)}\right\} \exp\left\{-\frac{(x+ct)^2}{4Dt}\right\} d\xi$$
$$= \exp\left\{-\frac{(x+ct)^2}{4Dt}\right\} \int_{\mathbb{R}} \exp\left\{\frac{-(\xi - i(x+ct)\pi\sqrt{Dt})^2}{2(1/8\pi^2 Dt)}\right\} d\xi.$$

In our integral expression for $G(x,t)$, the parameters for identity (A.7) are assigned as $\mu = i(x+ct)\pi\sqrt{Dt}$ and $\sigma^2 = 1/8\pi^2 Dt$. Thus,

$$\int_{\mathbb{R}} \exp\left\{\frac{-(\xi - i(x+ct)\pi\sqrt{Dt})^2}{2(1/8\pi^2 Dt)}\right\} d\xi = \sqrt{\frac{2\pi}{8\pi^2 Dt}} = \frac{1}{\sqrt{4\pi Dt}}.$$

Therefore, the fundamental solution to the PDE (A.11) is

$$G(x,t) = \frac{1}{\sqrt{4\pi Dt}} \exp\left\{-\frac{(x+ct)^2}{4Dt}\right\}. \tag{A.14}$$

General Initial Condition: Now, suppose the initial condition to the free-space constant advection-diffusion PDE is $\phi(x) \in L^1(\mathbb{R}) \cup L^2(\mathbb{R})$. That is, we want to solve the PDE

$$\begin{cases} \frac{\partial U}{\partial t} = c\frac{\partial U}{\partial x} + D\frac{\partial^2 U}{\partial x^2}, & x \in \mathbb{R},\ t > 0, \\ U = \phi(x), & x \in \mathbb{R},\ t = 0, \\ \lim_{|x|\to+\infty} U = 0, & x \in \mathbb{R},\ t > 0. \end{cases} \tag{A.15}$$

We can apply the same convolution property of Fourier transforms to obtain the PDE solution

$$U(x,t) = G(x,t) * \phi(x), \tag{A.16}$$

where $G(x,t)$ is the fundamental solution of the constant advection-diffusion PDE.

A.2 Operator-Split, Semi-Discrete Formulation

The absorption PDE (5.5) is subtly difficult to solve due to the $\beta(x)$ term in front of the ξ partial derivative. To effectively deal with this problem, we chose to split the operator as detailed in Section 5.2.2. Operator-splitting techniques are used to solve difficult PDEs, such as fluid problems [13], advection-diffusion-reaction equations [117], and coupled PDE systems [116]. Moreover, similar to the Rothe methodology, we discretize in time [8]. However, since we know the exact solutions of the split operator we did not continue the Rothe method by directly discretizing in space. The following examples influenced my use of an operator-split, semi-discrete formulation.

A.2.1 Free-Space Diffusion Example

Suppose we want to solve the free-space diffusion equation with initial condition $U(x,t) = \phi(x) \in L^1(\mathbb{R})$ as shown in Eq. (A.9) by operator-splitting. This is a trivial example, since we know the exact solution is (A.10), however it provides insight into the process.

We begin by discretizing $U(x,t)$ in time as $U^n(x) := U(x, n\tau)$ for some time-step $\tau > 0$. Our algorithm for solving uses the Green's function solution:

- $U^0(x) = \phi(x)$
- For $m = 1, 2, \ldots$:
  - $\Diamond$ $U^m(x) = G(x,\tau) * U^{m-1}(x)$

Since we solved the equation exactly at each time step, we are interested in how close this algorithm is to the exact solution. Note that we have the following solutions at each time-step:

$$\begin{aligned}
U^0(x) &= \phi(x) \\
U^1(x) &= G(x,\tau) * U^0(x) = G(x,\tau) * \phi(x), \\
U^2(x) &= G(x,\tau) * U^1(x) = G(x,\tau) * G(x,\tau) * \phi(x), \\
&\vdots \\
U^m(x) &= G(x,\tau) * U^{m-1}(x) = G(x,\tau) *^m \phi(x).
\end{aligned}$$

Theorem 13. *The operator-split solution $G(x,\tau) *^m \phi(x) = U(x, m\tau) = G(x, m\tau) * \phi(x)$, the exact solution to the free-space diffusion equation.*

Proof. To prove this we need Lemma 4 to show that $G(x,\tau) * G(x,\tau) = G(x, 2\tau)$. By induction, we know that $G(x,\tau) *^m \delta(x) = G(x, m\tau)$. Therefore, $G(x,\tau) *^m \phi(x) = G(x, m\tau) * \phi(x)$. □

Now we need to prove the following lemma:

Lemma 4. *Let $G(x,t) = \frac{1}{\sqrt{4\pi D t}} \exp\left\{-\frac{x^2}{4Dt}\right\}$. Then for any $a, b \in \mathbb{R}$ and any $t_1, t_2 \in \mathbb{R}^+$, then $G(x-a, t_1) * G(x-b, t_2) = G(x-a-b, t_1+t_2)$ (with convolution on the x variable only).*

Proof. The lemma can be proven by computation.

$$
\begin{aligned}
G(x-a,t_1) * G(x-b,t_2) &= \int_{\mathbb{R}} G(x-y-a,t_1)G(y-b,t_2)\,dy \\
&= \frac{1}{\sqrt{4\pi D t_1}\sqrt{4\pi D t_2}} \int_{\mathbb{R}} \exp\left\{-\frac{(x-y-a)^2}{4Dt_1}\right\} \exp\left\{-\frac{(y-b)^2}{4Dt_2}\right\} dy \\
&= \frac{1}{4\pi D\sqrt{t_1 t_2}} \int_{\mathbb{R}} \exp\left\{-\frac{y^2-2(x-a)y+(x-a)^2}{4Dt_1} - \frac{y^2-2by+b^2}{4Dt_2}\right\} dy \\
&= \frac{1}{4\pi D\sqrt{t_1 t_2}} \exp\left\{-\frac{(x-a)^2}{4Dt_1} - \frac{b^2}{4Dt_2}\right\} \int_{\mathbb{R}} \exp\left\{-\frac{1}{4Dt_1t_2}(t_2y^2 - 2t_2(x-a)y + t_1y^2 - 2t_1by)\right\} dy \\
&= \frac{1}{4\pi D\sqrt{t_1 t_2}} \exp\left\{-\frac{(x-a)^2}{4Dt_1} - \frac{b^2}{4Dt_2}\right\} \int_{\mathbb{R}} \exp\left\{-\frac{(t_1+t_2)y^2 - 2(t_2(x-a)+t_1b)y}{4Dt_1t_2}\right\} dy \\
&= \frac{1}{4\pi D\sqrt{t_1 t_2}} \exp\left\{-\frac{t_2(x-a)^2+t_1b^2}{4Dt_1t_2}\right\} \exp\left\{\frac{(t_2(x-a)+t_1)^2}{4Dt_1t_2(t_1+t_2)}\right\} \int_{\mathbb{R}} \exp\left\{-\frac{(y-[(t_2(x-a)+t_1b)/(t_1+t_2)])^2}{4Dt_1t_2/(t_1+t_2)}\right\} dy \\
&= \frac{\sqrt{\pi 4Dt_1t_2}}{4\pi D\sqrt{t_1t_2(t_1+t_2)}} \exp\left\{-\frac{t_2x^2-2t_2ax+t_2a^2+t_1b^2}{4Dt_1t_2} + \frac{t_2^2x^2-2t_2^2ax+a^2t_2^2+t_1t_2x-t_1t_2a+t_1^2b^2}{4Dt_1t_2(t_1+t_2)}\right\} \\
&= \frac{1}{4\pi D(t_1+t_2)} \exp\left\{\frac{-t_1t_2x^2+2t_1t_2ax-t_1t_2a^2-t_1t_2b^2+2t_1t_2bx-t_1t_2ab}{4Dt_1t_2(t_1+t_2)}\right\} \\
&= \frac{1}{4\pi D(t_1+t_2)} \exp\left\{-\frac{x^2-2ax-2bx+a^2+b^2+ab}{4D(t_1+t_2)}\right\}
\end{aligned}
$$

Therefore, we showed that

$$
G(x-a,t_1) * G(x-b,t_2) = \frac{1}{4\pi D(t_1+t_2)} \exp\left\{-\frac{(x-a-b)^2}{4D(t_1+t_2)}\right\} = G(x-a-b,t_1+t_2).
$$

□

By Theorem 13 and Lemma 4, we showed that, for any $\tau > 0$, the solution to the operator-split, semi-discrete diffusion equation at any time-step is equal to the analytic solution.

A.2.2 Free-Space Advection-Diffusion Example

Suppose we want to solve the free-space advection-diffusion equation with initial condition $U(x,t) = \phi(x) \in L^1(\mathbb{R})$ as shown in Eq. (A.15) by operator-splitting. With constant coefficients, this PDE is slightly more complicated than the diffusion equation, but we still know the exact solution (A.16). This is an example where the operator-splitting semi-discrete method does not converge to the exact solution. However, it is important to see how this fails.

We begin by split the advection-diffusion operator of (A.15) into two problems, a diffusion problem and an advection problem. First, we examine the diffusion problem:

$$
\begin{cases}
\hat{U} = D\frac{\partial^2 \hat{U}}{\partial x^2}, & x \in \mathbb{R},\ t > 0, \\
\hat{U} = \hat{\phi}(x), & x \in \mathbb{R},\ t = 0, \\
\lim_{|x|\to\infty} U = 0, & x \in \mathbb{R},\ t > 0.
\end{cases}
\tag{A.17}
$$

By the Fourier transform method, we know that the solution is $\hat{U}(x,t) = G_d(x,t) * \hat{\phi}(x)$, where $G_d(x,t)$ is the fundamental solution of the diffusion equation (A.8). Next, we examine the advection problem:

$$\begin{cases} \frac{\partial \tilde{U}}{\partial t} + a\frac{\partial \tilde{U}}{\partial x} = 0, & x \in \mathbb{R},\, t > 0, \\ \tilde{U} = \tilde{\phi}(x), & x \in \mathbb{R},\, t = 0. \end{cases} \tag{A.18}$$

By the method of characteristics, we know that the solution is $\tilde{U}(x,t) = \tilde{\phi}(x - at)$.

We now discretize in time by denoting $U^n(x) := U(x, n\tau)$ for some time-step $\tau > 0$. Our algorithm for solving uses the Green's function solution:

- $U^0(x) = \phi(x)$
- For $m = 1, 2, \ldots$:
  - $\lozenge$ $\tilde{U}(x) = U^{m-1}(x - a\tau)$
  - $\lozenge$ $\hat{U}(x) = G(x,\tau) * U^{m-1}(x)$
  - $\lozenge$ $U^m(x) = \hat{U}(x)$

Since we solved the equation exactly at each time step, we are interested in how close this algorithm is to the exact solution. Note that we have the following solutions at each time-step:

$$\begin{aligned} U^0(x) &= \phi(x) \\ U^1(x) &= G(x,\tau) * U^0(x - a\tau) = G(x,\tau) * \phi(x - a\tau), \\ U^2(x) &= G(x,\tau) * U^1(x - a\tau) = G(x,\tau) * G(x - a\tau, \tau) * \phi(x - a2\tau), \\ &\vdots \\ U^m(x) &= G(x,\tau) * U^{m-1}(x - a\tau) = G(x,\tau) * G(x - a\tau,\tau) * \cdots * G(x - a(m-1)\tau)\phi(x - am\tau). \end{aligned}$$

Theorem 14. *The operator-split solution $G(x,\tau) * G(x - a\tau, \tau) * \cdots * G(x - a(m-1)\tau)\phi(x - am\tau) \neq U(x, m\tau) = G(x, m\tau) * \phi(x - am\tau)$, the exact solution to the free-space advection-diffusion equation, as $\tau \to 0$.*

Proof. Fix a time $t > 0$ and $x \in \mathbb{R}$. By Lemma 4 we know that $G(x-a, t_1) * G(x-b, t_2) = G(x - a - b, t_1 + t_2)$. Therefore, by induction and since $\sum_{k=0}^{m-1} k = \frac{m(m-1)}{2}$ we have

$$G(x,\tau) * G(x - a\tau, \tau) * \cdots * G(x - a(m-1)\tau) = G\left(x - a\frac{m(m-1)}{2}\tau, m\tau\right)$$

for any $m \in \mathbb{N}$. It is clear that $G\left(x - a\frac{m(m-1)}{2}\tau, m\tau\right) \neq G(x, m\tau)$ for $\tau > 0$.

Let us define $z_{m,\tau}(x) = G\left(x - a\frac{m(m-1)}{2}\tau, m\tau\right)$. Now we want to take the limit as $\tau \to 0$, but still evaluate the limit at the same time point, t. So, we let $\tau = t/m$ and take

the limit as $m \to \infty$. We then have

$$\begin{aligned}\lim_{m\to\infty} z_{m,t/m}(x) &= \lim_{m\to\infty} G\left(x - a\frac{m(m-1)}{2}\frac{t}{m}, m\frac{t}{m}\right) \\ &= \lim_{m\to\infty} G\left(x - a\frac{(m-1)t}{2}, t\right).\end{aligned}$$

Since $\lim_{|x|\to\infty} G(x,t) = 0$, we know that $\lim_{m\to\infty} z_{m,t/m}(x) = 0$ for all x. Thus, $G(x,\tau) * G(x - a\tau, \tau) * \cdots * G(x - a(m-1)\tau, \tau)\phi(x - am\tau) \neq U(x, m\tau) = G(x, m\tau) * \phi(x - am\tau)$ for all $t > 0$, $x \in \mathbb{R}$. □

The operator-split, semi-discrete method does not resolve the exact solution, even when $\tau \to 0$. We split the operator twice in the same coordinate system, which is why we saw error accumulation (as opposed to the absorption equation, where we split along the space-time and absorption-time coordinates). Note that we would achieve the same result if we reversed the order of the solution by solving for $\hat{U}$ before $\tilde{U}$.

A.2.3 Constant Absorption Example

In this example, we demonstrate how the cumulative absorption model is different from the advection-diffusion model with respect to the operator-splitting, semi-discrete method. We know the exact solution to the cumulative absorption model (5.5) in the case where the absorption coefficient, β, is constant. The solution, as proved in Section 5.2.5 is $U(x,t,\xi) = G(x,2t) * \phi(x, \xi - 2\beta t)$.

In Section 5.2.2, we derived the operator-split, semi-discrete algorithm as

- Initialize $U^0(x,\xi) = \phi(x,\xi)$
- For $m = 1, 2, \ldots$:
  - ◊ $\overline{U}^{m-1}(x|\xi) = U^{m-1}(x,\xi)$
  - ◊ $\widehat{U}^m(\xi|x) = \overline{U}^{m-1}(x|\xi - \beta\tau)$
  - ◊ $U^m(x,\xi) = G(x,\tau) * \widehat{U}^m(\xi|x)$.

Combining these solutions gives us the following solutions at each time-step:

$$\begin{aligned}U^0(x,\xi) &= \phi(x,\xi) \\ U^1(\mathbf{x},\xi) &= G(x,\tau) * U^0(x, \xi - \beta\tau) = G(x,\tau) * \phi(x,\xi) \\ U^2(\mathbf{x},\xi) &= G(x,\tau) * U^1(x, \xi - \beta 2\tau) = G(x,\tau) * G(x,\tau) * \phi(x,\xi) \\ &\vdots \\ U^m(\mathbf{x},\xi) &= G(x,\tau) * U^{m-1}(x, \xi - \beta m\tau) = G(x,\tau) *^m \phi(x, \xi - \beta m\tau).\end{aligned}$$

Theorem 15. *The operator-split solution $U^m(\mathbf{x},\xi) = G(x,\tau) *^m \phi(x, \xi - \beta m\tau)$ is the same as $U(x, m\tau, \xi) = G(x, m\tau) * \phi(x, \xi - \beta m\tau)$, the exact solution of the free-space cumulative absorption equation.*

Proof. Let $\tau > 0$, $x \in \mathbb{R}$, and $\xi \in [0, \infty)$ be given. By Lemma 4 and induction, we know that $G(x,\tau) *^m \delta(x) = G(x, m\tau)$ for any m. It follows that, $G(x,\tau) *^m \phi(x, \xi - \beta m\tau) = G(x, m\tau) * \phi(x, \xi - \beta m\tau)$ for any x, ξ, m. □

Since the operator is split in the (x,t) and (ξ,t) coordinates, we are able to recover the exact solution to the free-space cumulative absorption equation with constant absorption.

A.3 Regular Asymptotic Solution

In this section, we examine two regime choices for the PDE from Section 2.3.2:

$$\begin{cases} \frac{\triangle t}{2}\frac{\partial^2 U}{\partial t^2} + \frac{\partial U}{\partial t} = \frac{\triangle x^2}{2\triangle t}\frac{\partial^2 U}{\partial x^2}, & x \in \mathbb{R},\, t > 0, \\ U = \delta(x - x_0), & x \in \mathbb{R},\, t = 0, \\ \lim_{|x|\to\infty} U = 0, & x \in \mathbb{R},\, t > 0, \end{cases} \tag{A.19}$$

where $0 < \triangle t, \triangle x \ll 1$. We show that the above PDE exhibits different behaviors when $\triangle t \propto \triangle x^2$ or when $\triangle t \propto \triangle x$. In either case, the $\triangle t/2$ coefficient in the governing PDE (A.19) is a very small value, so we can set a parameter $\varepsilon = \triangle t/2$. Since $\varepsilon \ll 1$, we can use regular asymptotic methods [91] to find a solution. We first examine the case where $\triangle t \propto \triangle x^2$.

A.3.1 $\triangle t \propto \triangle x^2$

If we assume that $\triangle t \propto \triangle x^2$, then the diffusion parameter $D = \frac{\triangle x^2}{2\triangle t} = \mathcal{O}(1)$. Therefore, we can rewrite (A.19) as:

$$\begin{cases} \varepsilon\frac{\partial^2 U}{\partial t^2} + \frac{\partial U}{\partial t} = D\frac{\partial^2 U}{\partial x^2}, & x \in \mathbb{R},\, t > 0, \\ U = \delta(x - x_0), & x \in \mathbb{R},\, t = 0 \\ \lim_{|x|\to\infty} U = 0, & x \in \mathbb{R},\, t > 0. \end{cases} \tag{A.20}$$

To solve (A.20), we use the regular asymptotic expansion method.

First, we set

$$U(x,t) = U^{(0)}(x,t) + \varepsilon U^{(1)}(x,t) + \varepsilon^2 U^{(2)}(x,t) + \cdots . \tag{A.21}$$

Next, we insert the expansion (A.21) into (A.20) to obtain

$$\begin{cases} \varepsilon\left[\frac{\partial^2 U^{(0)}}{\partial t^2} + \varepsilon\frac{\partial^2 U^{(1)}}{\partial t^2}\right] + \left[\frac{\partial U^{(0)}}{\partial t} + \varepsilon\frac{\partial U^{(1)}}{\partial t} +\right] \approx D\left[\frac{\partial^2 U^{(0)}}{\partial x^2} + \varepsilon\frac{\partial^2 U^{(1)}}{\partial x^2}\right] \\ U^{(0)}(x, t=0) + \varepsilon U^{(1)}(x, t=0) \approx \delta(x - x_0) \\ \lim_{|x|\to\infty}\left[U^{(0)}(x,t) + \varepsilon U^{(1)}(x,t)\right] \approx 0. \end{cases} \tag{A.22}$$

We then solve (A.22) for each order.

$\mathcal{O}(1)$: We only keep the expansion terms from (A.22) that are of $\mathcal{O}(1)$. This yields the following PDE:

$$\begin{cases} \frac{\partial U^{(0)}}{\partial t} = D\frac{\partial^2 U^{(0)}}{\partial x^2}, & x \in \mathbb{R},\, t > 0, \\ U^{(0)} = \delta(x - x_0), & x \in \mathbb{R},\, t = 0, \\ \lim_{|x|\to\infty} U^{(0)} = 0, & x \in \mathbb{R},\, t > 0. \end{cases} \tag{A.23}$$

We know from Section A.1.2 that the solution to (A.23) is

$$U^{(0)}(x,t) = G(x - x_0, t), \tag{A.24}$$

where $G(x,t)$ is the fundamental solution of the diffusion equation (A.8).

$\mathcal{O}(\varepsilon)$: Now, we only keep the expansion terms from (A.22) that are of $\mathcal{O}(\varepsilon)$. This yields the following PDE:

$$\begin{cases} \frac{\partial^2 U^{(0)}}{\partial t^2} + \frac{\partial U^{(1)}}{\partial t} = D\frac{\partial^2 U^{(1)}}{\partial x^2}, & x \in \mathbb{R},\, t > 0, \\ U^{(1)} = 0, & x \in \mathbb{R},\, t = 0, \\ \lim_{|x|\to\infty} U^{(1)} = 0, & x \in \mathbb{R},\, t > 0. \end{cases} \tag{A.25}$$

If we rearrange the governing equation to

$$\frac{\partial U^{(1)}}{\partial t} - D\frac{\partial^2 U^{(1)}}{\partial x^2} = -\frac{\partial^2 U^{(0)}}{\partial t^2}$$

and recall that we know the form of $U^{(0)}(x,t)$, then this is just a diffusion equation with a sink term. From [41, Ch.2], we know that the solution is

$$U^{(1)}(x,t) = -\int_0^t \int_{\mathbb{R}} G(x - y, t - s)\frac{\partial^2 U^{(0)}}{\partial t^2}(y,s)\, dy\, ds, \tag{A.26}$$

where $G(x,t)$ is the fundamental solution of the diffusion equation (A.8).

Now, inserting (A.24) and (A.26) into (A.21), we have that the solution to (A.20) is

$$U(x,t) \approx G(x - x_0, t) - \varepsilon \int_0^t \int_{\mathbb{R}} G(x - y, t - s)\frac{\partial^2 G}{\partial t^2}(y - x_0, s)\, dy\, ds. \tag{A.27}$$

We see U has the diffusion solution with a correction term of order $\mathcal{O}(\varepsilon)$.

A.3.2 $\triangle t \propto \triangle x$

Now, if we assume that $\triangle t \propto \triangle x$, then $v = \triangle x/\triangle t = \mathcal{O}(1)$. So we can rewrite (A.19) as:

$$\begin{cases} \varepsilon\frac{\partial^2 U}{\partial t^2} + \frac{\partial U}{\partial t} = \varepsilon v^2\frac{\partial^2 U}{\partial x^2}, & x \in \mathbb{R},\, t > 0, \\ U = \delta(x - x_0), & x \in \mathbb{R},\, t = 0, \\ \lim_{|x|\to\infty} U = 0, & x \in \mathbb{R},\, t > 0. \end{cases} \tag{A.28}$$

Using the regular asymptotic expansion (A.21), and inserting it into (A.28) yields the following PDE:

$$\begin{cases} \varepsilon\left[\frac{\partial^2 U^{(0)}}{\partial t^2}+\varepsilon\frac{\partial^2 U^{(1)}}{\partial t^2}\right]+\left[\frac{\partial U^{(0)}}{\partial t}+\varepsilon\frac{\partial U^{(1)}}{\partial t}+\right]\approx \varepsilon v^2\left[\frac{\partial^2 U^{(0)}}{\partial x^2}+\varepsilon\frac{\partial^2 U^{(1)}}{\partial x^2}\right] \\ U^{(0)}(x,t=0)+\varepsilon U^{(1)}(x,t=0)\approx \delta(x-x_0) \\ \lim_{|x|\to\infty}\left[U^{(0)}(x,t)+\varepsilon U^{(1)}(x,t)\right]\approx 0. \end{cases} \tag{A.29}$$

$\mathcal{O}(1)$: Arranging the terms in (A.29) of $\mathcal{O}(1)$ is the PDE

$$\begin{cases} \frac{\partial U^{(0)}}{\partial t}=0, & x\in\mathbb{R},\, t>0, \\ U^{(0)}=\delta(x-x_0), & x\in\mathbb{R},\, t=0, \\ \lim_{|x|\to\infty} U^{(0)}=0, & x\in\mathbb{R},\, t>0. \end{cases} \tag{A.30}$$

The solution to the general equation is

$$U^{(0)}(x,t)=\delta(x-x_0). \tag{A.31}$$

$\mathcal{O}(\varepsilon)$: Arranging the terms in (A.29) of $\mathcal{O}(\varepsilon)$ is the PDE

$$\begin{cases} \frac{\partial^2 U^{(0)}}{\partial t^2}+\frac{\partial U^{(1)}}{\partial t}=v^2\frac{\partial^2 U^{(0)}}{\partial x^2}, & x\in\mathbb{R},\, t>0, \\ U^{(1)}=0, & x\in\mathbb{R},\, t=0, \\ \lim_{|x|\to\infty} U^{(1)}=0, & x\in\mathbb{R},\, t>0. \end{cases} \tag{A.32}$$

Rearranging the general equation yields $\frac{\partial U^{(1)}}{\partial t}=v^2\frac{\partial^2 U^{(0)}}{\partial x^2}$. This general solution is $U^{(1)}(x,t)=C(x)+v^2\frac{\partial^2 U^{(0)}}{\partial x^2}t$. The initial condition implies that $C(x)=0$. Then the boundary condition is satisfied since $\lim_{|x|\to\infty}\frac{\partial^2 U^{(0)}}{\partial x^2}=0$. Thus,

$$U^{(1)}(x,t)=v^2\frac{\partial^2 U^{(0)}}{\partial x^2}t. \tag{A.33}$$

Now, inserting (A.31) and (A.33) into (A.21), the solution to (A.28) is approximately

$$U(x,t)\approx\delta(x-x_0)+\varepsilon v^2\frac{\partial^2\delta(x-x_0)}{\partial x^2}t. \tag{A.34}$$

For $\varepsilon \ll 1$, this solution does not represent the actual model behavior. Thus, it is important to keep track of the parameter regime when developing the PDE model.

Appendix B

Least-Squares Approximations

Suppose we have a data set $\{(x_1, y_1), (x_2, y_2), \ldots (x_m, y_m)\}$ and want to find the function $f(x)$ that "best fits" the data. That is, we want to find the parameter set $\mathbf{p}$ of f that minimizes the squared residual error

$$E(\mathbf{p}) = \sum_{k=1}^{m} \left(y_k - f(x_k)\right)^2. \tag{B.1}$$

We want to derive the log-linear, $\log(y) = a\log(x) + b$, and exponential, $y = bx^a$ least-squares used in the dissertation. However, we begin by deriving the solution to the basic linear least-squares, $y = ax + b$, since both cases can transform to this basic case.

B.1 Linear Least-Squares: $y = ax + b$

Since $f(x) = ax + b$, we want to find parameters $a, b \in \mathbb{R}$ that minimize

$$E(a, b) = \sum_{k=1}^{m} \left(y_k - (ax_k + b)\right)^2. \tag{B.2}$$

To find the minimum, we need to set the partial derivatives with respect to the parameters equal to 0 and solve the resulting system of equations. We have

$$\frac{\partial E}{\partial a} = -2\sum_{k=1}^{m} x_k \left[y_k - (ax_k + b)\right] = 0,$$
$$\frac{\partial E}{\partial b} = -2\sum_{k=1}^{m} \left[y_k - (ax_k + b)\right] = 0.$$

Rearranging terms gives us the system of equations

$$a\sum_{k=1}^{m} x_k^2 + b\sum_{k=1}^{m} x_k = \sum_{k=1}^{m} x_k y_k,$$
$$a\sum_{k=1}^{m} x_k + b\sum_{k=1}^{m} 1 = \sum_{k=1}^{m} y_k.$$

We can rewrite the above as a matrix equation

$$\begin{bmatrix} \sum_{k=1}^{m} x_k^2 & \sum_{k=1}^{m} x_k \\ \sum_{k=1}^{m} x_k & \sum_{k=1}^{m} 1 \end{bmatrix} \begin{pmatrix} a \\ b \end{pmatrix} = \begin{pmatrix} \sum_{k=1}^{m} x_k y_k \\ \sum_{k=1}^{m} y_k \end{pmatrix}. \tag{B.3}$$

Solving (B.3) for a and b gives the line of "best fit" through the data. There is another way to solve for (B.3), by using the normal equations. If we want to find the line that "best fits" the data, we need to solve the system of equations:

$$\begin{aligned} y_1 &= ax_1 + b, \\ y_2 &= ax_2 + b, \\ &\vdots \\ y_m &= ax_m + b. \end{aligned}$$

We can rewrite this as a matrix equation $\mathbf{Ax} = \mathbf{y}$, where

$$\mathbf{A} = \begin{bmatrix} x_1 & 1 \\ x_2 & 1 \\ \vdots & \vdots \\ x_m & 1 \end{bmatrix}, \qquad \mathbf{x} = \begin{pmatrix} a \\ b \end{pmatrix}, \qquad \text{and } \mathbf{y} = \begin{pmatrix} y_1 \\ y_2 \\ \vdots \\ y_m \end{pmatrix}.$$

This system would only have an exact solution if the data rested on the same line. However, as seen in the error plots of Sections 2.1.1, 2.2.1, and 5.4.1, this may not be the case. However, if we multiply both sides of the matrix equation by $\mathbf{A}^T$, the transpose of the matrix, then we can solve the system. That is, we then solve $\mathbf{A}^T\mathbf{Ax} = \mathbf{A}^T\mathbf{y}$. It is worth noting that we can easily compute

$$\mathbf{A}^T\mathbf{A} = \begin{bmatrix} \sum_{k=1}^{m} x_k^2 & \sum_{k=1}^{m} x_k \\ \sum_{k=1}^{m} x_k & \sum_{k=1}^{m} 1 \end{bmatrix}, \qquad \text{and } \mathbf{A}^T\mathbf{y} = \begin{pmatrix} \sum_{k=1}^{m} x_k y_k \\ \sum_{k=1}^{m} y_k \end{pmatrix}.$$

So the (B.3) and normal equation formulations are equivalent. Now we have the necessary tools to solve the least-squares cases encountered in the dissertation.

B.2 Log-Linear Least-Squares: $\log(y) = a\log(x) + b$

In Figs. 2.7, 2.10, and 5.6 the data appears to follow a linear trend. However, the axes are spaced with log scaling. Thus, the data actually follows the equation $\log(y) = a\log(x) + b$. This looks non-linear, but we can transform the variables so that we can solve a linear least squares. Let $\hat{x}_k = x_k$ and $\hat{y}_k = \log(y_k)$ for all $k = 1, 2, \ldots, m$. We then can solve the linear least squares solution (B.3) of the line $\hat{y} = a\hat{x} + b$ for the points $\{(\hat{x}_1, \hat{y}_1), (\hat{x}_2, \hat{y}_2), \ldots, (\hat{x}_m, \hat{y}_m)\}$. Then the least-squares line is $y = e^b x^a$.

B.3 Exponential Least-Squares: $y = bx^a$

In Fig. 5.16a, the data appears to follow an exponential trend. We can perform a log transformation on the data, $\log(y) = \log(bx^a)$. By using logarithmic identities, we can rewrite this as $\hat{y} = a\hat{x} + \hat{b}$, where $\hat{y} = \log(y)$, $\hat{x} = \log(x)$, and $\hat{b} = \log(b)$. We then can solve the linear least squares solution (B.3) of the line $\hat{y} = a\hat{x} + \hat{b}$ for the points $\{(\hat{x}_1, \hat{y}_1), (\hat{x}_2, \hat{y}_2), \ldots, (\hat{x}_m, \hat{y}_m)\}$. Then the least-squares line is $y = e^{\hat{b}}x^a$.

Appendix C

2-d Perturbation Theorem

Here, we detail 2-d perturbation theorem as found in [34, 78]. Let $H(\mathbf{x}^{(k)}) = \mathbf{x}^{(k+1)}$ be a recursive rule. Suppose there exists a fixed point, $\hat{\mathbf{x}}$, to this recursive rule. That is, there exists an $\hat{\mathbf{x}}$ such that $\hat{\mathbf{x}} = H(\hat{\mathbf{x}})$. Now define δ_k such that $\delta^{(k)} = \mathbf{x}^{(k)} - \hat{\mathbf{x}}$. We then have that $\mathbf{x}_k = \hat{\mathbf{x}} + \delta_k$. Moreover,

$$\begin{aligned}\delta^{(k+1)} &= \mathbf{x}^{(k+1)} - \hat{\mathbf{x}} \\ &= H(\mathbf{x}^{(k)}) - \hat{\mathbf{x}} \\ &= H(\hat{\mathbf{x}} + \delta^{(k)}) - H(\hat{\mathbf{x}})\end{aligned}$$

Suppose that we choose a k such that $||\delta_k|| \ll 1$. By definition of the Jacobian, we have that

$$\mathbf{J}(\hat{\mathbf{x}})\delta^{(k)} \approx \delta^{(k+1)}. \tag{C.1}$$

Suppose $\mathbf{J}(\hat{\mathbf{x}})$ is diagonalizable with eigenpairs $\{(\lambda_i, \xi_i)\}$. That is, $\mathbf{J}(\hat{\mathbf{x}}) = \mathbf{M}\mathbf{\Delta}\mathbf{M}^{-1}$, where $\Delta = diag(\lambda_1, \lambda_2, ..., \lambda_N)$ and $\mathbf{M} = [\xi_1|\xi_2| \cdot |\xi_N]$. Rewriting Eq. (C.1) in this form gives us

$$\mathbf{M}\mathbf{\Delta}\mathbf{M}^{-1}\delta^{(k)} \approx \delta^{(k+1)}.$$

We then have that $\mathbf{M}^{-1}\delta^{(k+1)} = \mathbf{\Delta}\mathbf{M}^{-1}\delta_k$. By induction, we find that

$$\mathbf{M}\delta^{(k)} = \mathbf{\Delta}^k\mathbf{M}\delta_0$$

Thus, if the eigenvalue $|\lambda_j| < 1$, the fixed point $\hat{\mathbf{x}}$ is stable along the nullcline defined by its eigenvector ξ_j.

Appendix D

Sparse $\mu\left(\tilde{B}_t^{\mathcal{S},\mathcal{I}}\right)$ Formula For GRR

Let us assume, as we did when deriving the locally homogeneous region, that the infected agents are on the radial center of mass of the region $\tilde{B}_t^{\mathcal{S},\mathcal{I}} \setminus \tilde{B}_{t-1}^{\mathcal{S},\mathcal{I}}$, as shown in Figure 4.2. We assume that there are n newly infected agents that are uniformly distributed on the radial center of mass, a distance of r from the initially infected agent.

D.1 Deriving ζ_{k+1}

We want to find the total area $\mu\left(\bigcup_{i=1}^{n} A_i\right)$, where n is the expected number of infected agents in the region $\tilde{B}_t^{\mathcal{S},\mathcal{I}} \setminus \tilde{B}_{t-1}^{\mathcal{S},\mathcal{I}}$ and A_i is the region, illustrated in Figure 4.3, of the ith infected agent. For our expository purposes, we assume that the newly infected agents only exist in the edge of the expanding wave of infected agents, leading to the simplified derivation, $n = I_t - I_{t-1}$.

By the inclusion-exclusion principle [131] we find that

$$\mu\left(\bigcup_{i=1}^{n} A_i\right) = \sum_{i=1}^{n} \mu(A_i) - \sum_{i=1}^{n} \mu\left(A_i \cap A_{i+1}\right),$$

where $A_{n+1} = A_1$. Note that $\mu(A_i) = \mu(A_j)$ and that $\mu(A_i \cap A_{i+1}) = \mu(A_j \cap A_{j+1})$ for all $i, j = 1, 2, ..., n$. We then have that

$$\mu\left(\bigcup_{i=1}^{n} A_i\right) = n\Big(\mu(A) - \mu(A_1 \cap A_2)\Big). \tag{D.1}$$

First we find $\mu(A)$, the region shown in Figure D.1a.

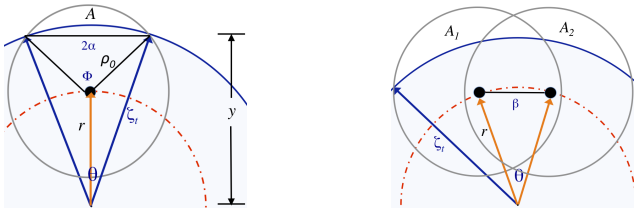

(a) (b)

Figure D.1: Newly infected agents (black circles) lie on the radial center of mass of the region $\tilde{B}_t^{\mathcal{S},\mathcal{I}} \setminus \tilde{B}_{t-1}^{\mathcal{S},\mathcal{I}}$, a distance r from the initially infected agent. **(a)** Solving for $\mu(A)$ as part of calculating how large the infection front becomes. The infectivity radius of the agent intersects the edge of region $\tilde{B}_t^{\mathcal{S},\mathcal{I}}$ at two points, creating an angle θ from the center of the region and an angle Φ from the agent. **(b)** Solving for $\mu(A_1) \cap \mu(A_2)$. The infected agents are a distance β apart and form an angle θ from the center of the region $\tilde{B}_t^{\mathcal{S},\mathcal{I}}$.

We already know r and ζ_t. By our assumption, $\theta = 2\pi/n$, we can find y by calculating the intersection of C_1 and C_2, defined by

$$C_1 : x^2 + (y - r)^2 = \rho_0^2,$$
$$C_2 : x^2 + y^2 = \zeta_t^2.$$

It follows that $y = \frac{\zeta_t^2 - \rho_0^2 + r^2}{2r}$. We can then find $\alpha = \sqrt{\zeta_t^2 - y^2}$ and $\Phi = 2 \arcsin\left(\frac{\alpha}{\rho_0}\right)$.

From Figure D.2 we know that $\mu(A) = \mu(R_2) - \mu(R_4)$. It is clear that $\mu(R_2) = \mu(R_1 \cup R_2) - \mu(R_1) = \frac{\Phi}{2}\rho_0^2 - \alpha\sqrt{\rho_0^2 - \alpha^2}$ and $\mu(R_4) = \mu(R_3 \cup R_4) - \mu(R_3) = \frac{\theta}{2}\zeta_t^2 - \alpha y$.

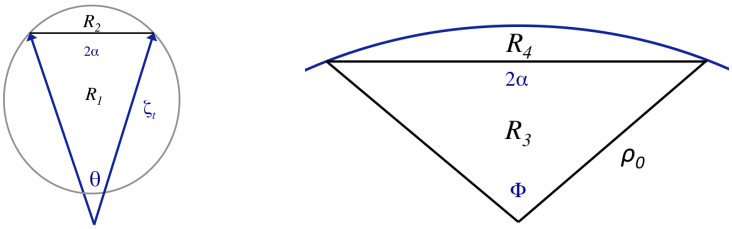

Figure D.2: We solve for region A by subtracting $\mu(R_4)$ from $\mu(R_2)$. We decompose solving for $\mu(A)$ in Figure D.1a by solving for the outer sector (left) and the inner sector (right).

We then have that

$$\mu(A) = \frac{1}{2}\left(\Phi\rho_0^2 - \theta\zeta_t^2\right) - \alpha\left(\sqrt{\rho_0^2 - \alpha^2} - y\right). \tag{D.2}$$

Now we can find $\mu(A_1) \cap \mu(A_2)$. From Figure D.1b we know θ, r, and ζ_t. We want to find the x-coordinate of the intersection of C_1 and C_2 defined as

$$\begin{aligned} C_1 &: (x+h)^2 + (y-k)^2 = \rho_0^2, \\ C_2 &: x^2 + y^2 = \zeta_t^2 \end{aligned}$$

with $h = \beta/2$ and $k = \sqrt{r^2 - (\beta/2)^2}$. The intersection is the larger solution $\hat{x}$ of the quadratic $4\left(h^2+k^2\right)\hat{x}^2 + 4h\left(2k^2+\eta\right)\hat{x} + \left(\eta^2 - 4k^2\left(\rho_0^2 - h^2\right)\right) = 0$, where $\eta = h^2 - k^2 + \zeta_k^2 - \rho_0^2$.

We then have that $\mu(A_1 \cap A_2) = 2\int_0^{\hat{x}} \left(k + \sqrt{\rho_0^2 - (x+h)^2} - \sqrt{\zeta_t^2 - x^2}\right) dx$ if $\hat{x} > 0$. After integrating, if $\hat{x} > 0$ we have

$$\begin{aligned} \mu(A_1 \cap A_2) = (h+\hat{x})\sqrt{\rho_0^2 - (h+\hat{x})^2} + \rho_0^2 \arctan\left(\frac{h+\hat{x}}{\sqrt{\rho_0^2 - (h+\hat{x})^2}}\right) - \zeta_t^2 \arctan\left(\frac{\hat{x}}{\sqrt{\zeta_t^2 - \hat{x}^2}}\right) \\ - \hat{x}\sqrt{\zeta_t^2 - \hat{x}^2} + 2k\hat{x} - \left[h\sqrt{\rho_0^2 - h^2} + \rho_0 \arctan\left(\frac{h}{\sqrt{\rho_0^2 - h^2}}\right)\right]. \end{aligned} \tag{D.3}$$

After inserting equations (D.2) and (D.3) into equation (D.1), we have a computable formula for $\mu(\cup_{k=1}^{n} A_k)$. Our new wavefront radius is

$$\zeta_{t+1} = \sqrt{\frac{\pi\zeta_t^2 + \mu(\cup_{i=1}^{n} A_i)}{\pi}}. \tag{D.4}$$

The above formulation works well for low density E-AB simulations, where agents in state $\mathcal{R}$ do not return to state $\mathcal{S}$ (T_R is longer than the time of the simulation). However, if recovered agents can become susceptible, then we must reformulate our calculation of the expected value of n.

Appendix E

Derivation of GRR Error Metric

Suppose we have a data set $(t_1, S_1), (t_2, S_2), ..., (t_N, S_N)$ and want to compute the error with another sequence of points $(\hat{t}_1, \hat{S}_1), (\hat{t}_2, \hat{S}_2), ..., (\hat{t}_M, \hat{S}_M)$. We assume that $t_1 < t_2 < \cdots < t_N$ and that $\hat{t}_1 < \hat{t}_2 < \cdots < \hat{t}_M$. We create a linear spline interpolant $f(t)$ from the first data set [120, Ch.2] by $f(t) = \frac{S_{k+1}-S_k}{t_{k+1}-t_k}(t - t_k) + S_k$, for $t_k \leq t \leq t_{k+1}$. Our error metric is a normalized least-square, where we find the minimum distance from each point in the second data set to the spline approximation of the first data set.

$$\nu = \frac{1}{M} \sum_{k=1}^{M} \inf_t \sqrt{(\hat{t}_k - t)^2 + (\hat{S}_k - f(t))^2}, \tag{E.1}$$

Consider a point $\hat{\mathbf{x}} = (\hat{t}, \hat{S})$. We need to derive an algorithm to calculate the following minimization:

$$d(\hat{\mathbf{x}}, f) = \inf_t \sqrt{(\hat{t} - t)^2 + (\hat{S} - f(t))^2}.$$

The line that intersects points (t_k, S_k) and (t_{k+1}, S_{k+1}) is given by

$$\ell_k(t) = \frac{S_{k+1} - S_k}{t_{k+1} - t_k}(t - t_k) + S_k. \tag{E.2}$$

To find the value $t_{\min}$ such that $d(\hat{\mathbf{x}}, \ell_k)$ is minimized, we must first find the line $\hat{\ell}$ that intersects $\hat{\mathbf{x}}$ and ℓ_k. This line is given by

$$\hat{\ell}(t) = -\frac{t_{k+1} - t_k}{S_{k+1} - S_k}(t - \hat{t}) + \hat{S}. \tag{E.3}$$

Setting (E.2) and (E.3) equal and solving for t, we find that

$$t_{\min} = \frac{(t_{k+1} - t_k)(S_{k+1} - S_k)}{(t_{k+1} - t_k)^2 + (S_{k+1} - S_k)^2} \left(\frac{t_{k+1} - t_k}{S_{k+1} - S_k} \hat{t} + \frac{S_{k+1} - S_k}{t_{k+1} - t_k} t_k + \hat{S} - S_k \right). \tag{E.4}$$

It follows that the location on the line ℓ_k that minimizes the distance to $\hat{\mathbf{x}}$ is $S_{\min,k} = \ell_k(t_{\min})$. We then calculate

$$d_k = \begin{cases} \sqrt{(\hat{t} - t_k)^2 + (\hat{S} - S_k)^2} & : \text{if } t_{\min} < t_k, \\ \sqrt{(\hat{t} - t_{k+1})^2 + (\hat{S} - S_{k+1})^2} & : \text{if } t_{k+1} < t_{\min}, \\ \sqrt{(\hat{t} - t_{\min})^2 + (\hat{S} - S_{\min,k})^2} & : \text{otherwise.} \end{cases} \tag{E.5}$$

Since $d(\hat{\mathbf{x}}, f) = \inf_t \sqrt{(\hat{t} - t)^2 + (\hat{S} - f(t))^2} = \min\{d_1, d_2, ..., d_{N-1}\}$, the minimum of the distance from $\hat{\mathbf{x}}$ to each of the line segments in f, we calculate the error by $\nu = \frac{1}{M} \sum_{k=1}^{M} d\left(\hat{\mathbf{x}}_k, f\right)$.

Appendix F

Path Dependent Absorption Formulation

The chemical absorption model developed in Chapter 5 is shown to be effective. Moreover, we see in Chapters 6 and 7 that the model is capable of being extended to incorporate more complex phenomena. However, for completeness I discuss my initial formulation of the model in this section. This was developed prior to realizing that the cumulative absorption variable, ξ, could be used a coordinate. This alternative way to model chemical absorption is accomplished by following the paths of the agents.

F.1 Path Model Development and Derivation

An agent is initialized in the domain Ω and travels within Ω, absorbing chemical. If the chemical concentration, $C(x)$, is heterogeneous, then the amount of chemical absorbed may change depending on the agent's path.

In Fig. F.1, we initialize four agents at $x_0 = 0.5$ and run the simulation with $C(x) = \exp\{-x^2\}$. The colored circles at each iteration denotes the particular agent (black, blue, red, or green) and the color of the path line denotes the cumulative amount of chemical the particular agent has absorbed at their respective times. The large colored circles denote the location and time in which each agent changes state. Since $C(x)$ is larger to the left, we see that the agents absorb chemical faster the farther left they move. In fact, at around $t = 0.005$ each agent's path line is a slightly different color. The black agent at the far left has a violet path line, whereas the green agent at the far right has a turquoise path line. This is because, except for a small amount of time at the beginning of the simulation, the green agent has moved randomly in a region of lower chemical concentration than the black agent.

From these AB Model observations, we propose approximating a path-dependent model for chemical absorption. Since the agent performs an unbiased random walk (URW), we can leverage the state-change modeling framework initially examined in Section 3.3. Define the function $f(x, t, C(x))$ as the proportion of all connected paths from

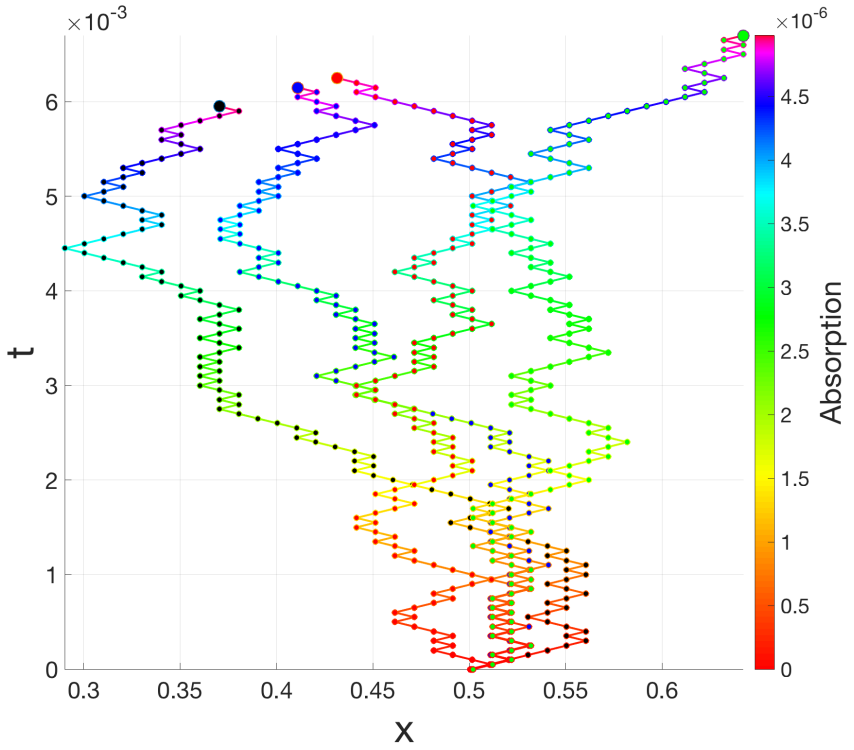

Figure F.1: Paths for four agents, each initialized at $x_0 = 0.5$ and distinguished by black, blue, red, and green circles at each iteration, where the horizontal axis represents location and the vertical axis represents time. The line colors denote the amount of chemical each agent absorbed, and the large circles denote where and when each agent changes state.

x_0 to x in time t from which the agent traveling along the path absorbs less than the absorption threshold, ξ_c. The difference equation for this model is:

$$U(x, t + \triangle t) = \frac{1}{2}U(x - \triangle x, t) + \frac{1}{2}U(x + \triangle x, t) - U(x, t)\left[1 - f(x, t, C(x))\right].$$

Expanding the above difference equation in a Taylor series and simplifying gives us

$$\frac{\partial U}{\partial t} = \frac{\triangle x^2}{2\triangle t}\frac{\partial^2 U}{\partial x^2} - \frac{1}{\triangle t}U(x, t)\left[1 - f(x, t, C(x))\right] + \mathcal{O}(\triangle x^3, \triangle t). \tag{F.1}$$

Using the asymptotic argument that $0 < \triangle x, \triangle t \ll 1$, we define the diffusion parameter $D = \frac{\triangle x^2}{2\triangle t}$ and state change proportion parameter $q(x, t) = \frac{1}{\triangle t}\left[1 - f(x, t, C(x))\right]$ to obtain the pdf that the agent is alive and at location x at time t:

$$\frac{\partial U}{\partial t} = D\frac{\partial^2 U}{\partial x^2} - q(x, t)U. \tag{F.2}$$

We now need a mathematical formulation of $f(x, t, C(x))$ in order to compute $q(x, t)$. Let $\varphi(t)$ be any connected path such that $\varphi(0) = x_0$ and $\varphi(t) = x$. Then the set of all such

connected paths is $A(x,t) = \{\varphi \subset \Omega : \varphi(0) = x_0, \varphi(t) = x\}$. The amount absorbed along each path can be found by an integral parameterized by time, $\int_0^t C(\phi(\tau))\, d\tau$. Therefore, we can calculate $f(x,t,C(x))$ by

$$f(x,t,C(x)) = \frac{\int_{\varphi \in A(x,t)} \chi(\varphi,t)\, \mathcal{D}\varphi}{\int_{\varphi \in A(x,t)} 1\, \mathcal{D}\varphi}, \tag{F.3}$$

where $\chi(\varphi,t) = \begin{cases} 1 & : \text{ if } \int_0^t C(\phi(\tau))\, d\tau < \xi_c \\ 0 & : \text{ otherwise} \end{cases}$ and $\mathcal{D}\varphi$ denotes the integrating measure over all connected paths in $A(x,t)$. The term $\int_{\varphi \in A(x,t)} 1\, \mathcal{D}\varphi$ in the denominator is a normalization constant computing the measure of $A(x,t)$. This notation is drawn from path integrals in Quantum Mechanics [30]. Therefore, $q(x,t) = \frac{1}{\triangle t}\left[1 - \frac{\int_{\varphi \in A(x,t)} \chi(\varphi,t)\, \mathcal{D}\varphi}{\int_{\varphi \in A(x,t)} 1\, \mathcal{D}\varphi}\right]$. Now we need a way of calculating (F.2).

F.2 Path Model Numerical Solution

In order to obtain our path absorption model's approximate solution, we need to solve the PDE

$$\begin{cases} \frac{\partial U}{\partial t} = D\frac{\partial^2 U}{\partial x^2} - q(x,t)U, & x \in \Omega,\ t > 0 \\ U = \delta(x - x_0), & x \in \bar{\Omega},\ t = 0 \\ \frac{\partial U}{\partial x} = 0, & x \in \partial\Omega, t > 0. \end{cases}$$

If we know q, then we can easily solve the above PDE using a finite difference method. So, it remains for us to solve (F.3).

The function $f(x,t,C(x))$ is a continuum integral over all possible paths. However, we know that the domain of an URW initialized at a point source with fixed step-size $\triangle x$ is essentially a discrete, finite lattice. In this absorption model, the lattice edges are weighted by the chemical concentration absorbed. Therefore, if $t = m\triangle t$, then we can approximate $\int_{\varphi \in A(x,t)} \chi(\varphi,t)\, \mathcal{D}\varphi$ by setting up a graph adjacency matrix to calculate the amount absorbed in each distinct m-step path from node x_0 to node x, if it exists.

We computed examples with different chemical profiles in Figs. F.2, F.3. The numerical calculation of $q(x,t)$ was inefficient, since the computational time required to solve over the space of all possible paths grows exponentially. This is why the domain $\Omega = [0,1]$ is only divided into 21 nodes, and this inefficiency is also why the simulations only ran for 21 iterations. Even though the solutions look somewhat reasonable given the large step-sizes, the computational cost of solving $q(x,t)$ was motivation for finding a different way to model chemical absorption, which eventually became the model in Chapter 5.

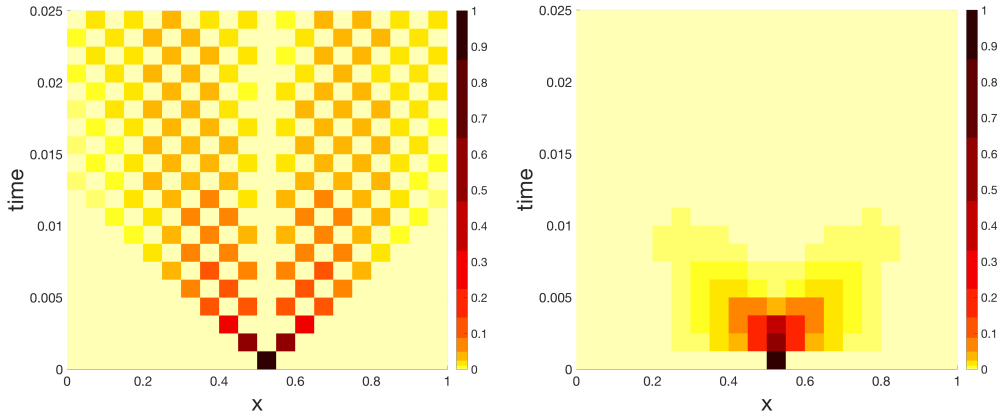

(a) AB Model Simulation (b) Numerical Solution

Figure F.2: Comparison between AB Model simulation and numerical approximation with chemical concentration $C(x) = \mathbf{1}_{[0.425,0.575]}(x)$ and threshold value $\xi_c = 3$. Agents initialized at $x_0 = 0.5$ in the region $\Omega = [0, 1]$ with no-flux boundary conditions. The agents move with spatial-step $\triangle x = 0.05$ and time-step $\triangle t = \triangle x^2/2$.

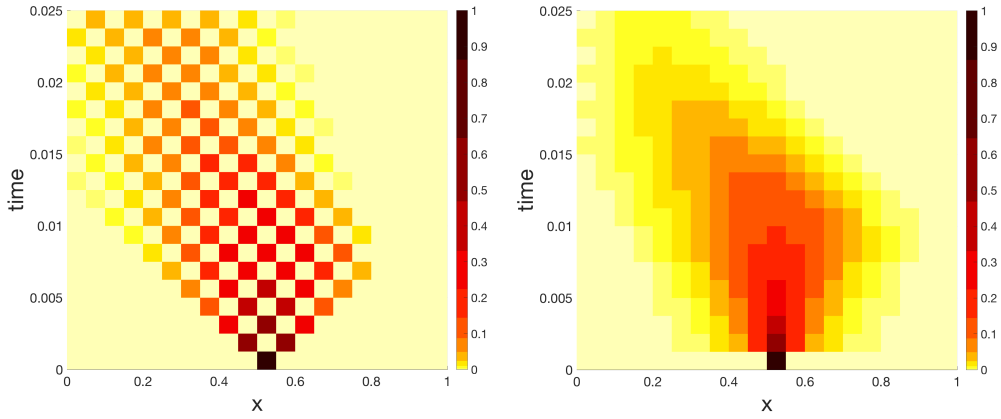

(a) AB Model Simulation (b) Numerical Solution

Figure F.3: Comparison between AB Model simulation and numerical approximation with chemical concentration $C(x) = x^2$ and threshold value $\xi_c = 3$. Agents initialized at $x_0 = 0.5$ in the region $\Omega = [0, 1]$ with no-flux boundary conditions. The agents move with spatial-step $\triangle x = 0.05$ and time-step $\triangle t = \triangle x^2/2$.

Appendix G

Numerical Method of Images Error

We are interested in how error is indroduced to the numerical method of images for the diffusion equation, as defined in Section 6.1.2. We examine no-flux and dirichlet boundary conditions for a known, explicit solution in the domain $\Omega = [-1, 1]$ with various spatial step-sizes. We also experimentally demonstrate that the no-flux method is conservative up to round-off errors.

G.1 No-Flux Boundary Condition Error

We solve the diffusion equation in the region $\Omega = [-1, 1] \subset \mathbb{R}$ with no-flux boundary conditions

$$\begin{cases} \frac{\partial U}{\partial t} = \frac{\partial^2 U}{\partial x^2}, & x \in (-1, 1),\ t > 0, \\ U = \sin\left(\frac{\pi}{2}x\right), & x \in [-1, 1],\ t = 0, \\ \frac{\partial U}{\partial x} = 0, & x \in \{-1, 1\},\ t > 0. \end{cases} \tag{G.1}$$

The exact solution to the PDE (G.1) is

$$U(x, t) = \exp\left\{-\frac{\pi^2 t}{4}\right\} \sin\left(\frac{\pi}{2}x\right). \tag{G.2}$$

This is clear, since the initial condition is an eigenfunction of the diffusion equation [105, Ch.2]. To compare the numerical solution with the exact solution, we integrate the solution (G.2) over each cell volume. That is, for spatial step-size δx, the exact solution integrated over the cell volume centered at x_i is

$$\begin{aligned} U_i(t) &= \int_{B(x_i, \delta x/2)} U(x, t)\, dx \\ &= -\frac{2}{\pi} \exp\left\{-\frac{\pi^2 t}{4}\right\} \left[\cos\left(\frac{\pi}{2}(x_i + \delta x/2)\right) - \cos\left(\frac{\pi}{2}(x_i - \delta x/2)\right)\right] \end{aligned}$$

We compute two types of error for various spatial step sizes, δx: absolute error and relative absolute error. The absolute error is computed as $E = \sum_{i=0}^{N} |u_i^m - U_i(m\delta t)|$,

and the relative absolute error is computed as $E_r = \sum_{i=0}^{N} \left| \frac{u_i^m - U_i(m\delta t)}{U_i(m\delta t)} \right|$. In each case, we compute the numerical method of images on the extended domain $[-3, 3]$ with time-step $\delta t = 5 \times 10^{-5}$.

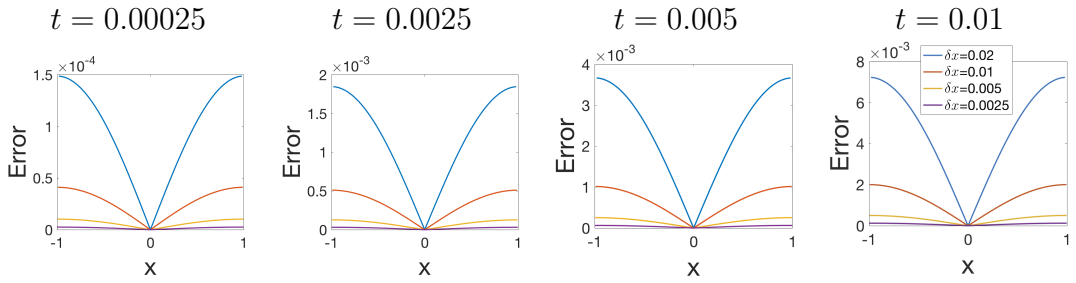

(a) Absolute Error

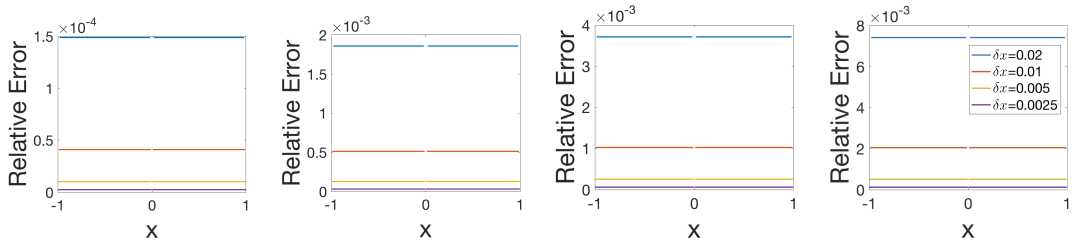

(b) Relative Absolute Error

Figure G.1: Absolute Error and Relative Absolute Error plots for method of images in a line segment with no-flux boundary conditions with various spatial step-sizes, δx.

We see in Fig. G.1 that even though the numerical method of images only performs one image reflection across each boundary, the boundary does not add additional error to the system. In fact, the numerical Green's function, G_i (as computed in Section 5.3), at the boundary is essentially 0. We can further observe that the numerical method appears to be second-order accurate in space, $\mathcal{O}(\delta x^2)$, and first-order accurate in time, $\mathcal{O}(\delta t)$.

Since the PDE (G.1) has no-flux boundary conditions at the endpoints, it is essential that the numerical method enforces this conservation. We calculate the average difference by $E_c = \frac{1}{N} \sum_{i=0}^{N} \left| u_i^m - \sum_{k=0}^{N} u_k^0 \right|$. Although Fig. G.2 appears very noisy, the important thing to observe

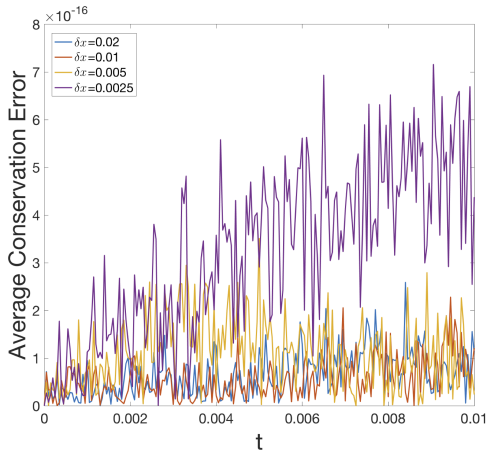

Figure G.2: Conservation error in time for method of images in a line segment with no-flux boundary conditions with various spatial step-sizes, δx.

is that the error for each δx is close to machine epsilon, $\varepsilon_{mach} = 10^{-16}$. Thus, the numerical method of images for no-flux boundary conditions enforces conservation up to rounding errors.

G.2 Absorbing Boundary Condition Error

We also want to examine the error when the numerical method of images uses absorbing boundary conditions. We solve the diffusion equation in the region $\Omega = [-1, 1] \subset \mathbb{R}$ with perfectly absorbing boundary conditions

$$\begin{cases} \frac{\partial U}{\partial t} = \frac{\partial^2 U}{\partial x^2}, & x \in (-1, 1),\ t > 0, \\ U = \cos\left(\frac{\pi}{2}x\right), & x \in [-1, 1],\ t = 0, \\ U(x, t) = 0, & x \in \{-1, 1\},\ t > 0. \end{cases} \tag{G.3}$$

The exact solution to the PDE (G.3) is

$$U(x, t) = \exp\left\{-\frac{\pi^2 t}{4}\right\} \cos\left(\frac{\pi}{2}x\right). \tag{G.4}$$

To compare the numerical solution with the exact solution, we integrate (G.4) over each cell volume. That is, for spatial step-size δx, the exact solution integrated over the cell volume centered at x_i is

$$\begin{aligned} U_i(t) &= \int_{B(x_i, \delta x/2)} U(x, t)\, dx \\ &= \frac{2}{\pi} \exp\left\{-\frac{\pi^2 t}{4}\right\} \left[\sin\left(\frac{\pi}{2}(x_i + \delta x/2)\right) - \sin\left(\frac{\pi}{2}(x_i - \delta x/2)\right)\right]. \end{aligned}$$

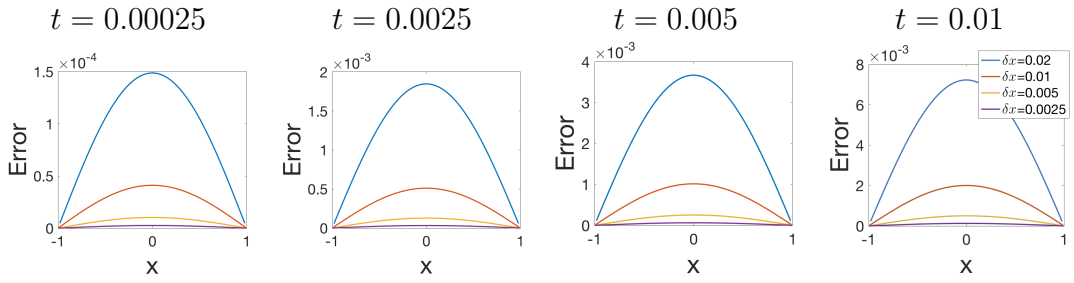

(a) Absolute Error

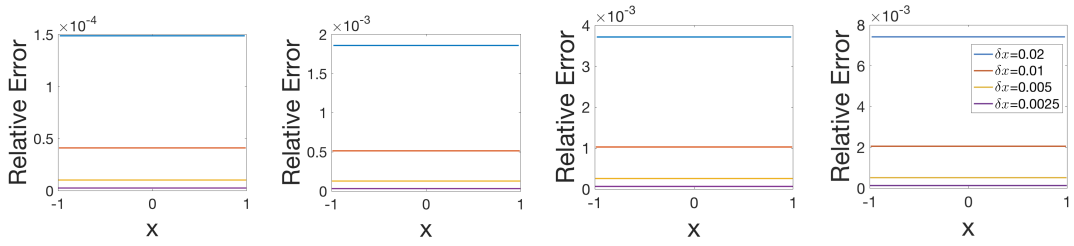

(b) Relative Absolute Error

Figure G.3: Absolute Error and Relative Absolute Error plots for method of images in a line segment with perfectly absorbing boundary conditions with various spatial step-sizes, δx.

We compute the absolute error, E, and the relative absolute error E_r between the exact solution and the numerical solution using the numerical method of images. Just as we see in the No-Flux example, Fig. G.3a demonstrates that the boundary does not affect the error. Again, we see that the numerical method appears to be second-order accurate in space, $\mathcal{O}(\delta x^2)$, and first-order accurate in time, $\mathcal{O}(\delta t)$.

Bibliography

[1] D.J. Acheson. *Elementary fluid dynamics*. ASA, 1st edition, 1991.

[2] K. Alden, M. Read, J. Timmis, P.S. Andrews, H. Veiga-Fernandes, and M. Coles. Spartan: a comprehensive tool for understanding uncertainty in simulations of biological systems. *PLoS Comput. Biol.*, 9:e1002916, 2013.

[3] W. Alt. Biased random walk models for chemotaxis and related diffusion approximations. *J. Math. Biol.*, 9:147–177, 1980.

[4] G. An, B.G. Fitzpatrick, S. Christley, P. Federico, A. Kanarek, R.M. Neilan, M. Oremland, R. Salinas, R. Laubenbacher, and S. Lenhart. Optimization and control of agent-based models in biology: A perspective. *Bull. Math. Biol.*, 79(1):63–87, 2017.

[5] B. Anvari, M.G.H. Bell, A. Sivakumar, and W.Y. Ochieng. Modelling shared space users via rule-based social force model. *Transport Res. C: Emer*, 51:83–103, 2015.

[6] A. Arnold and A.L. Lloyd. An approach to periodic, time-varying parameter estimation using nonlinear filtering. *Inverse Probl.*, 34(10):105005, 2018.

[7] A. Bartłomiejczyk and H. Leszczński. Method of lines for physiologically structured models with diffusion. *Appl. Numer. Math.*, 94:140–148, 2015.

[8] A. Bartłomiejczyk, H. Leszczński, and A. Marciniak. Rothe's method for physiologically structured models with diffusion. *Math. Slovaca*, 68(1):211–224, 2018.

[9] H.H. Bau, D. Raizen, and J. Yuan. Why do worms go against the flow? c. elegans behaviors explained by simple physics. In *WORM*, volume 4, page e1118606. Taylor & Francis, 2015.

[10] R.S.A. Beauchamp. Rate of movement and rheotaxis in planaria alpina. *J. Exp. Biol.*, 14(1):104–116, 1937.

[11] S. Benhamou. How to reliably estimate the tortuosity of an animal's path:: straightness, sinuosity, or fractal dimension? *J. Theor. Biol.*, 229(2):209–220, 2004.

[12] H. Berg. *Random walks in biology*. Princeton University Press, Princeton, 5th edition, 1993.

[13] B. Bermúdez, A. Nicolás, F.J. Sánchez, and E. Buendía. Operator splitting and upwinding for the navier-stokes equations. *Comput. Mech.*, 20(5):474–477, 1997.

[14] A.J. Bernoff and A.E. Lindsay. Numerical approximation of diffusive capture rates by planar and spherical surfaces with absorbing pores. *SIAM J. Appl. Math.*, 78:266–290, 2018.

[15] D. Bhaskar, A. Manhart, J. Milzman, J.T. Nardini, K.M. Storey, C.M. Topaz, and L. Ziegelmeier. Analyzing collective motion with machine learning and topology. *Chaos*, 29(12):123—125, 2019.

[16] I. Blank and P. Smith. Convergence of rothe's method for fully nonlinear parabolic equations. *J. Geom.*, 15(3):363–372, 2005.

[17] E. Bonabeau. Agent-based modeling: Methods and techniques for simulating human systems. *Proc. Natl. Acad. Sci. U.S.A.*, 99(suppl 3):7280–7287, 2002.

[18] R.N. Bracewell. *The Fourier Transform and Its Applications*, chapter 6, pages 105–135. McGraw-Hill, Boston, MA, 3rd edition, 2000.

[19] M. Burkitt, D. Walker, D.M. Romano, and A. Fazeli. Constructing complex 3d biological environments from medical imaging using high performance computing. *IEEE Transac. Computat. Bio. Bioinf.*, 9:643–654, 2012.

[20] M. Burkitt, D. Walker, D.M. Romano, and A. Fazeli. Using computational modeling to investigate sperm navigation and behavior in the female reproductive tract. *Theriogenology*, 77:703–716, 2012.

[21] A.Q. Cai, K.A. Landman, and B.D. Hughes. Modelling directional guidance and motility regulation in cell migration. *Bull. Math. Biol.*, 68:25, 2006.

[22] R. Carmona, J.P. Fouque, and L.H. Sun. Mean field games and systemic risk: a toy model. *Commun. Math. Sci.*, 13:911–933, 2015.

[23] D. Chakraborty. *Sample Efficient Multiagent Learning in the Presence of Markovian Agents*. Springer International Publishing, 1st edition, 2014.

[24] S. Chaturapruek, J. Breslau, D. Yazdi, T. Kolkolnikov, and S.G. McCalla. Crime modeling with lévy flights. *SIAM J. Appl. Math.*, 73(4):1703–1720, 2013.

[25] Q. Chen, J. Mao, and W. Li. Stability analysis of harvesting strategies in a cellular automata based predator-prey model. In S. El Yacoubi, Bastien Chopard, and Stefania Bandini, editors, *Cellular Automata*, pages 268–276, Berlin, Heidelberg, 2006. Springer Berlin Heidelberg.

[26] Y. Chen, S. Gottlieb, A. Heryudono, and A. Narayan. A reduced radial basis function method for partial differential equations on irregular domains. *J. Sci. Comput.*, 66(1):67–90, 2016.

[27] J. Chu, P. Magal, and R. Yuan. Hopf bifurcation for a maturity structured population dynamic model. *J. Nonlinear Sci.*, 21(4):521–562, 2011.

[28] E.A. Codling, J.W. Pitchford, and S.D. Simpson. Group navigation and the 'many wrongs principle' in models of animal movement. *Ecol.*, 88:1864–1870, 2007.

[29] E.A. Codling, M.J. Plank, and S. Benhamou. Random walk models in biology. *J. Royal Soc. Int.*, 5:813–834, 2008.

[30] E.G.D. Cohen. Properties of nonequilibrium steady states: a path integral approach. *J. Stat. Mech.: Theory Exp.*, 2008(07):P07014, 2008.

[31] J. Cosgrove, J. Butler, K. Alden, M. Read, V. Kumar, L. Cucurull-Sanchez, J. Timmis, and M. Coles. Agent-based modeling in systems pharmacology. *CPT Pharmacometrics Syst. Pharmacol.*, 4(11):615–629, 2015.

[32] J. Cosgrove, J. Butler, K. Alden, M. Read, V. Kumar, L. Cucurull-Sanchez, J. Timmis, and M. Coles. Agent-based modeling in systems pharmacology. *CPT Pharmacometrics Syst. Pharmacol.*, 4:615–629, 2015.

[33] B. Davis. Reinforced random walk. *Probab. Theory Relat. Fields*, 84(2):203–229, 1990.

[34] A. Deutsch and S. Dormann. *Cellular Automaton Modeling of Biological Pattern Formation*. Birkhäuser, Boston, 2nd edition, 2005.

[35] A. Devitt-Lee, H. Wang, J. Li, and B. Boghosian. A nonstandard description of wealth concentration in large-scale economies. *SIAM J. Appl. Math.*, 78(2):996–1008, 2018.

[36] H. Ding, G.C. Zhang, and L.Q. Chen. Supercritical vibration of nonlinear coupled moving beams based on discrete fourier transform. *Int. J. Nonlin. Mech.*, 47(10):1095–1104, 2012.

[37] U. Dobramysl and D. Holcman. Mixed analytical-stochastic simulation method for the recovery of a brownian gradient source from probability fluxes to small windows. *J. Comput. Phys.*, 355:22–36, 2018.

[38] C. Dombry. A weighted random walk model, with application to a genetic algorithm. *Adv. Appl. Probab.*, 39(2):550–568, 2007.

[39] B. Dybiec, E. Gudowska-Nowak, and P. Hänggi. Lévy-brownian motion on finite intervals: Mean first passage time analysis. *Phys. Rev. E*, 73(4):046104, 2006.

[40] E.C. Enders, M.H. Gessel, and J.G. Williams. Development of successful fish passage structures for downstream migrants requires knowledge of their behavioural response to accelerating flow. *Can. J. Fish Aquat. Sci.*, 66(12):2109–2117, 2009.

[41] L.C. Evans. *Partial Differential Equations*. American Mathematical Society, USA, 2nd edition, 2010.

[42] E. Fama. Random walks in stock market prices. *Financial Anal. J.*, 51(1):75–80, 1995.

[43] Y. Fang and Y. Liu. Design of automated control system based on improved e. coli foraging optimization algorithm. In *2008 IEEE International Conference on Automation and Logistics*, pages 238–243. IEEE, 2008.

[44] W. Feller. *An Introduction to Probability Theory and Its Applications*, volume 2, chapter XVI, pages 531–553. John Wiley & Sons, Inc., 2nd edition, 1971.

[45] A.M. Fofana and A. Hurford. Mechanistic movement models to understand epidemic spread. *Philos. T. R. Soc. B*, 372(1719):20160086, 2017.

[46] National Center for Biotechnology Information. PubChem Compound Database. Pubchem. `https://pubchem.ncbi.nlm.nih.gov/`. U.S. National Library of Medicine.

[47] E. Fosslien. The hormetic morphogen theory of curvature and the morphogenesis and pathology of tubular and other curved structures. *Dose Response*, 7:307–331, 2009.

[48] J. Fu, Z. Wang, K. Lee, C. Wei, Z. Liu, M. Zhang, M. Zhou, M. Cai, W. Zhang, P. Chuang, A. Ma'ayan, J. He, and Z. Liu. Transcriptomic analysis uncovers novel synergistic mechanisms in combination therapy for lupus nephritis. *Kidney Int.*, 93(2):416–429, 2018.

[49] M.A. Fuentes and M.N. Kuperman. Cellular automata and epidemiological models with spatial dependence. *Phys. A*, 267:471–486, 1999.

[50] C. Gardiner. *Stochastic methods*. Springer Berlin, 4th edition, 2009.

[51] L. Giuggioli and V.M. Kenkre. Consequences of animal interactions on their dynamics: emergence of home ranges and territoriality. *Mov. Ecol.*, 2(1):20, 2014.

[52] G.H. Goldsztein. Particles moving around a two-lane circular track in both directions. Avoiding collisions leads to self-organization. *SIAM J. Appl. Math.*, 76(4):1433–1445, 2016.

[53] D. Grebenkov. Universal formula for the mean first passage time in planar domains. *Phys. Rev. Lett.*, 117(26):260201, 2016.

[54] D. Grünbaum. Advection-diffusion equations for internal state-mediated random walks. *SIAM J. Appl. Math.*, 61(1):43–73, 2000.

[55] Y. Han and H. Liu. Modified social force model based on information transmission toward crowd evacuation simulation. *Physica A*, 469:499–509, 2017.

[56] P. He, L. Lu, X. Xu, K. Li, H. Qian, and W. Zhang. Confidence-based ant random walks. In *2014 IEEE Congress on Evolutionary Computation (CEC)*, pages 1721–1728. IEEE, 2014.

[57] D. Helbing and P. Molnar. Social force model for pedestrian dynamics. *Phys. Rev. E*, 51(5):42–82, 1995.

[58] N.A. Hill and D.P. Hader. A biased random walk model for the trajectories of swimming micro-organisms. *J. Theor. Biol.*, 186:503–526, 1997.

[59] F. Hinkelmann, D. Murrugarra, A.S. Jarrah, and R. Laubenbacher. A mathematical framework for agent based models of complex biological networks. *Bull. Math. Biol.*, 73(7):1583–1602, 2011.

[60] M. Holcombe, S. Adra, M. Bicak, S. Chin, S. Coakley, A.I. Graham, J. Green, C. Greenough, D. Jackson, M. Kiran, S. MacNeil, A. Maleki-Dizaji, P. McMinn, M. Pogson, R. Poole, E. Qwarnstrom, F. Ratnieks, M. D. Rolfe, R. Smallwood, T. Sun, and D. Worth. Modelling complex biological systems using an agent-based approach. *Integr. Biol.*, 4:53–64, 2012.

[61] A. Holko, M. Medrek, Z. Pastuszak, and K. Phusavat. Epidemiological modeling with a population density map-based cellular automata simulation system. *Expert Sys. Apps.*, 48:1–8, 2016.

[62] R. Interian, R. Rodriguez-Ramos, F. Valdeis-Ravelo, A. Ramirez-Torres, C.C. Ribeiro, and A. Conci. Tumor growth modelling by cellular automata. *Math. Mech. Complex Syst.*, 5(3-4):239–259, 2017.

[63] A. Ishihara, J.E. Segall, S.M. Block, and H.C. Berg. Coordination of flagella on filamentous cells of escherichia coli. *J. Bacteriol.*, 155(1):228–237, 1983.

[64] I. Jonsen, R. Myers, and J. Flemming. Meta-analysis of animal movement using state-space models. *Ecology*, 84(11):3055–3063, 2003.

[65] M. Kac. Random walk and the theory of brownian motion. *Amer. Math. Monthly*, 54(7):369–391, 1947.

[66] V. Kantsler, J. Dunkel, M. Blayney, and R.E. Goldstein. Rheotaxis facilitates upstream navigation of mammalian sperm cells. *eLife*, 3:e02403, 2014.

[67] Y. Katznelson. *An Introduction to Harmonic Analysis*, chapter 6, pages 132–200. Cambridge University Press, New York, NY, 3rd edition, 2002.

[68] J. Kim, H. Park, and S. Chung. Microfluidic approaches to bacterial biofilm formation. *Molecules*, 17(8):9818–9834, 2012.

[69] C.V. Kumar, H. Vardhan, C.S.N. Murthy, and N.C. Karmakar. Estimating rock properties using sound signal dominant frequencies during diamond core drilling operations. *J. Rock Mech. Geotech. Eng.*, 11(4):850–859, 2019-08.

[70] V. Kurella, J.C. Tzou, and D. Coombs. Asymptotic analysis of first passage time problems inspired by ecology. *Bull. Math. Biol.*, 77:83–125, 2015.

[71] J. Lasry and P. Lions. Mean field games. *Jap. J. Math.*, 2(1):229–260, 2007.

[72] R. Laubenbacher, A.S. Jarrah, H.S. Mortveit, and S.S. Ravi. Mathematical formalism for agent based modeling. In R.A. Meyers, editor, *Computational Complexity: Theory, Techniques, and Applications*, pages 88–104. Springer New York, New York, NY, 2012.

[73] L. Lehner, D. Neilsen, O. Reula, and M. Tiglio. The discrete energy method in numerical relativity: towards long-term stability. *Classical Quant. Grav.*, 21(24):5819–5848, 2004.

[74] K. Leiderman and A.L. Fogelson. Grow with the flow: a spatial–temporal model of platelet deposition and blood coagulation under flow. *Math. Med. Biol.*, 28(1):47–84, 2011.

[75] R.J. LeVeque. *Finite difference methods for ordinary and partial differential equations: steady-state and time-dependent problems*. Siam, 1st edition, 2007.

[76] R.J. LeVeque et al. *Finite volume methods for hyperbolic problems*. Cambridge university press, 1st edition, 2002.

[77] D. Levy and E. Tadmor. From semidiscrete to fully discrete: Stability of runge–kutta schemes by the energy method. *SIAM Rev.*, 40(1):40–73, 1998.

[78] C.C. Lin and L. A. Segel. *Mathematics Applied to Deterministic Problems in the Natural Sciences*, chapter 11, pages 321–345. Society for Industrial and Applied Mathematics, Philadelphia, 1 edition, 1988.

[79] A. Lindsay, A.J. Bernoff, and M.J. Ward. First passage statistics for the capture of a brownian particle by a structured spherical target with multiple surface traps. *Multiscale Model Sim.*, 15(1):74–109, 2017.

[80] A.L. Lloyd. Realistic distributions of infectious periods in epidemic models: Changing patterns of persistence and dynamics. *Theor. Popul. Biol.*, 60(1):59–71, 2001.

[81] J. Ma and D.J.D. Earn. Generality of the final size formula for an epidemic of a newly invading infectious disease. *Bull. Math. Biol.*, 68(3):679–702, 2006.

[82] V. Martinelli. Combination therapy. *J. Neurol. Sci.*, 27(5):s350–s354, 2006.

[83] V. Marziano, A. Pugliese, S. Merler, and M. Ajelli. Detecting a surprisingly low transmission distance in the early phase of the 2009 influenza pandemic. *Sci. Rep.*, 7(1), 2016.

[84] R. Mehran, A. Oyama, and M. Shah. Abnormal crowd behavior detection using social force model. In *2009 IEEE Conference on Computer Vision and Pattern Recognition*, pages 935–942. IEEE, 2009.

[85] R. Metzler, E. Barkai, and J. Klafter. Deriving fractional fokker-planck equations from a generalised master equation. *Europhys. Lett.*, 46(4):431–436, 1999.

[86] J.C. Miller. A note on the derivation of epidemic final sizes. *Bull. Math. Biol.*, 74(9):2125–2141, 2012.

[87] E.W. Montroll and M.F. Shlesinger. On the wonderful world of random walks. In J.L. Lebowitz and E.W. Montreal, editors, *Nonequilibrium phenomena II: from stochastics to hydrodynamics*, pages 1–121, Amsterdam, The Netherlands, 1984. North-Holland.

[88] J.R. Moraes and P. Stastny. A new antigen system expressed in human endothelial cells. *J. Clin. Invest.*, 60(2):449–454, 1977.

[89] M.M. Mousa. Efficient numerical scheme based on the method of lines for the shallow water equations. *J. Ocean. Eng. Sci.*, 3(4):303–309, 2018.

[90] J.D. Murray. *Mathematical Biology II: Spatial Models and Biomedical Applications*, chapter 13, pages 661–721. Springer, 3rd edition, 2003.

[91] J.D. Murray. *Asymptotic analysis*, chapter 6, pages 99–137. Springer Science & Business Media, 1st edition, 2012.

[92] J. Newby and J. Allard. First-passage time to clear the way for receptor-ligand binding in a crowded environment. *Phys. Rev. Let.*, 116:128101, 2016.

[93] M.J. North. A theoretical formalism for analyzing agent-based models. *Complex Adapt. Syst. Model.*, 2(1):3, 2014.

[94] Â. Novais, A. Freitas, C. Rodrigues, and L. Peixe. Fourier transform infrared spectroscopy: unlocking fundamentals and prospects for bacterial strain typing. *Eur. J. Clin. Microbiol. Infect. Dis.*, 38(3):427–448, 2019.

[95] National Institutes of Health. Hazardous substances data bank (hsdb). `https://toxnet.nlm.nih.gov/newtoxnet/hsdb.htm`. U.S. National Library of Medicine.

[96] A. Okubo and S.A. Levin. *Diffusion and ecological problems: modern perspectives*. Springer, Berlin, Germany, 2001.

[97] Committee on Meteorological Aspects of the Effects of Atomic Radiation. Meteorological aspects of atomic radiation. *Science*, 124(3212):105–112, 1956.

[98] H.G. Othmer, S.R. Dunbar, and W. Alt. Models of dispersal in biological systems. *J. Math. Biol.*, 26:263–298, 1988.

[99] H.G. Othmer and A. Stevens. Aggregation, blowup, and collapse: The ABC's of taxis in reinforced random walks. *SIAM J. Appl. Math.*, 57(4):1044–1081, 1997.

[100] N.H. Packard and S. Wolfram. Two-dimensional cellular automata. *J. Stat. Phys.*, 38(5):901–946, 1985.

[101] M.M. Palm, M.N. Steijaert, H.M.M. Ten Eikelder, and P.A.J. Hilbers. Modeling molecule exchange at membranes. In *Proceedings of the Third International Conference on the Foundations of Systems Biology in Engineering, Denver, Colorado*, 2009.

[102] L. Panait and S. Luke. A pheromone-based utility model for collaborative foraging. In *Proceedings of the Third International Joint Conference on Autonomous Agents and Multiagent Systems, 2004. AAMAS 2004.*, pages 36–43. IEEE, 2004.

[103] L. Pellis, F. Ball, K. Eames, T. House, V. Isham, and P. Trapman. Eight challenges for network epidemic models. *Epidemics*, 10:58 – 62, 2015.

[104] K.S. Perumalla and B.G. Aaby. Data parallel execution challenges and runtime performance of agent simulations on GPUs. In *Proceedings of the 2008 Spring simulation multiconference*, pages 116–123. Society for Computer Simulation International, 2008.

[105] M.A. Pinsky. *Partial differential equations and boundary-value problems with applications*. American Mathematical Soc., 3rd edition, 2011.

[106] M. Pogson, R. Smallwood, E. Qwarnstrom, and M. Holcombe. Formal agent-based modelling of intracellular chemical interactions. *Biosystems*, 85(1):37 – 45, 2006.

[107] S. Premžoe, T. Tasdizen, J. Bigler, A. Lefohn, and R.T. Whitaker. Particle-based simulation of fluids. In *Computer Graphics Forum*, volume 22, pages 401–410. Wiley Online Library, 2003.

[108] D. Prieto and T.K. Das. An operational epidemiological model for calibrating agent-based simulations of pandemic influenza outbreaks. *Health Care Manag. Sci.*, 19(1):1–19, 2016.

[109] C. Proulx, L. Proulx, and G. Blouin-Demers. Improving the realism of random walk movement analyses through the incorporation of habitat bias. *Ecol. Model*, 269:18–21, 2013.

[110] M. Read, P.S. Andrews, J. Timmis, and V. Kumar. Techniques for grounding agent-based simulations in the real domain: a case study in experimental autoimmune encephalomyelitis. *Math. Comp. Model Dyn.*, 18:67–86, 2012.

[111] M. Roberts, V. Andreasen, A. Lloyd, and L. Pellis. Nine challenges for deterministic epidemic models. *Epidemics*, 10(7):49 – 53, 2015.

[112] J. Sarma and K.A. De Jong. An analysis of local selection algorithms in a spatially structured evolutionary algorithm. In *ICGA*, pages 181–187. Citeseer, 1997.

[113] Y. Schwarzkopf, A. Rakos, and D. Mukamel. Epidemic spreading in evolving networks. *Phys. Rev. E*, 82:036112, 2010.

[114] S.V. Segbroeck, F.C. Santos, and J.M. Pacheco. Adaptive contact networks change effective disease infectiousness and dynamics. *PlOS Comp. Biol.*, 6:e1000895, 2010.

[115] B. Shraiman and D. Bensimon. Singularities in nonlocal interface dynamics. In *Dynamics of Curved Fronts*, pages 197–199. Elsevier, 1988.

[116] M.J. Simpson and K.A. Landman. Theoretical analysis and physical interpretation of temporal truncation errors in operator split algorithms. *Math. Comput. Simulat.*, 77(1):9–21, 2008.

[117] M.J. Simpson, K.A. Landman, and T.P. Clement. Assessment of a non-traditional operator split algorithm for simulation of reactive transport. *Math. Comput. Simulat.*, 70(1):44–60, 2005.

[118] R.D. Smith. Essential techniques for military modeling and simulation. In *1998 Winter Simulation Conference. Proceedings (Cat. No. 98CH36274)*, volume 1, pages 805–812. IEEE, 1998.

[119] A. Stevens. A stochastic cellular automaton modeling gliding and aggregation of myxobacteria. *SIAM J. Appl. Math.*, 61(1):172–182, 2000.

[120] J. Stoer and R. Bulirsch. *Introduction to Numerical Analysis*. Springer, New York, 3 edition, 2010.

[121] P. Stroud, S. Del Valle, S. Sydoriak, J. Riese, and S. Mniszewski. Spatial dynamics of pandemic influenza in a massive artificial society. *J. Artif. Soc. Soc. Simul.*, 10(4):9, 2007.

[122] Y. Su, W. Wei, L. Robert, M. Xue, J. Tsoi, A. Garcia-Diaz, B. Moreno, J. Kim, R. Ng, J. Lee, R. Koya, B. Comin-Anduix, T. Graeber, A. Ribas, and J. Heath. Single-cell analysis resolves the cell state transition and signaling dynamics associated with melanoma drug-induced resistance. *Proceedings of the National Academy of Sciences of the United States*, 114(52):13679–13684, 2017.

[123] Y. Taitel. On the parabolic, hyperbolic and discrete formulation of the heat conduction equation. *Int. J. Heat Mass Transf.*, 15(2):369–371, 1972.

[124] W. Talbott. Bayesian epistemology. In Edward N. Zalta, editor, *The Stanford Encyclopedia of Philosophy*. Metaphysics Research Lab, Stanford University, winter 2016 edition, 2016.

[125] M.E. Taylor. *Partial Differential Equations I Basic Theory*. Springer New York, New York, NY, 2nd edition, 2011.

[126] C.M. Topaz, L. Ziegelmeier, and T. Halverson. Topological data analysis of biological aggregation models. *PLoS One*, 10(5), 2015.

[127] R. Tranquillo, D. Lauffenburger, and S.H. Zigmond. A stochastic model for leukocyte random motility and chemotaxis based on receptor binding fluctuations. *J. Cell Biol.*, 106(2):303–309, 1988.

[128] J. Tzou and T. Kolokolnikov. Mean first passage time for a small rotating trap inside a reflective disk. *Multiscale Model Sim.*, 13(1):231–255, 2015.

[129] A. Valiei, A. Kumar, P.P. Mukherjee, Y. Liu, and T. Thundat. A web of streamers: biofilm formation in a porous microfluidic device. *Lab Chip*, 12(24):5133–5137, 2012.

[130] N.G. Van Kampen. Escape and splitting probabilities in diffusive and non-diffusive markov processes. *Prog. Theor. Phys. Supp.*, 64:389–401, 1978.

[131] J.H. van Lint and R. M. Wilson. The principle of inclusion and exclusion; inversion formulae. In *A Course in Combinatorics*, chapter 10, pages 89–97. Cambridge University Press, Cambridge, 2 edition, 2001.

[132] A. Vargha and H.D. Delaney. Critique and improvement of the CL common language effect size statistics of McGraw and Wong. *J. Educ. Behav. Stat.*, 25:101–132, 2000.

[133] E. Volz and Meyers L.A. Epidemic thresholds in dynamic contact networks. *J. R. Soc. Interface*, 6:233–241, 2009.

[134] E. Volz and L.A. Meyers. Susceptible-infected-recovered epidemics in dynamic contact networks. *Proc. Roy. Soc. B*, 274:2925–2933, 2007.

[135] S. Vuilleumier and R. Metzger. Animal dispersal modelling: handling landscape features and related animal choices. *Ecol. Mod.*, 190:159–170, 2006.

[136] G.H. Weiss. Random walks and their applications: widely used as mathematical models, random walks play an important role in several areas of physics, chemistry, and biology. *Amer. Sci.*, 71:65–71, 1983.

[137] X. Xiao, E. White, M. Hooten, and S. Durham. On the use of log-transformation vs. nonlinear regression for analyzing biological power laws. *Ecology*, 92(10):1887–1894, 2011.

[138] M.A. Yereniuk and S.D. Olson. Global density analysis for an off-lattice agent-based model. *SIAM J. Appl. Math.*, 79(5):1700–1721, 2019.

[139] M.A. Yereniuk and S.D. Olson. Computational framework to capture the spatiotemporal density of cells with a cumulative environmental coupling. *J. Comput. Appl. Math.*, 369:112572, 2020.

[140] V. Zaburdaev, S. Denisov, and J. Klafter. Lévy walks. *Rev. Modern Phys.*, 87(2):483, 2015.